· UNIVERSITY OF OXFORD ·

· DEPARTMENT OF ENGINEERING SCIENCE ·

Time-Dependent Phase Modulation in Liquid Crystal Photonics

· Thesis ·

Linpei Xue

St Hugh's College

Supervised by Prof. Stephen M. Morris and Prof Steve J. Elston

May 2025

To my family, whose unwavering support has lifted me every step of the way.

Abstract

Liquid crystal (LC) spatial light modulators (SLMs) have become essential components in various optical applications, enabling real-time and high-precision control over light properties such as phase, amplitude, and polarization. This thesis focuses on the optimization of LC-based optical phase modulators, aiming to enhance their response time, phase modulation depth, and polarization independence while maintaining low-voltage operation.

The study investigates two distinct nematic LC devices: a pi-cell-based phase modulator and a super-twisted nematic (STN) LC-based polarization-independent phase modulator. By applying optimized voltage waveforms, both devices achieve full 2π rad phase modulation within 1 ms, with the pi-cell operating in a reflective configuration and the STN device employing a four-pass configuration. To characterize and analyse the dynamic phase modulation behaviour, phase-shifting interferometry techniques are employed. Two phase-shifting interferometers are designed and constructed to provide high-resolution, accurate time-resolved phase measurements.

The theoretical framework is built upon Frank continuum theory and Ericksen-Leslie theory, which describe the elastic and hydrodynamic properties of nematic LCs. The free-energy density of the LC device is formulated and solved through Euler-Lagrange equations to determine the director profile, which is then used for phase modulation calculation. For twisted LC devices, Jones matrix formalism is utilized to compute phase modulation characteristics.

Furthermore, this work develops a computational optimization algorithm that integrates Jones matrix formalism and particle swarm optimization (PSO) to determine the optimal configuration of LC devices combined with additional waveplates. This approach results in an improved performance of phase modulation range and polarization independence beyond what is achievable with a single LC device. The optimization results validate that strategic combinations of LC devices and passive optical elements can significantly improve modulation performance within a voltage range or time scale.

The findings of this thesis contribute to the advancement of LC-based phase modulators by addressing the fundamental trade-offs between response time, phase modulation range, and applied voltage. The developed methodologies provide a robust foundation for designing next-generation LC optical modulators, with potential applications in adaptive optics, beam steering, holography, and AR/VR systems.

Acknowledgements

As I write this acknowledgment after completing my thesis, it feels surreal—almost as if I arrived in Oxford just yesterday, filled with curiosity and anticipation. Time truly flies. Through it all, this journey in Oxford has shaped me in ways I never expected.

First and foremost, I would like to express my deepest gratitude to my supervisors, Professor Stephen Morris and Professor Steve Elston. I consider myself incredibly fortunate to have had the guidance of both of them, and they have provided invaluable support in different aspects of my academic journey. They have not only shaped the direction of my research but also influenced my intellectual and personal growth. Their mentorship has inspired me to think critically, remain resilient, and strive for excellence, and for that, I will always be grateful.

I first met Professor Morris during my application interview. Later, he gave me a warm welcome on my first day in the lab, he guided me to the Engi-reception, helped me gain access to the labs and Engi-buildings, and extended a warm group welcome in Holder Cafe. Throughout my time here, he has been a constant and strong source of support, particularly during major milestones such as my publications, transfer of status, confirmation of status and so on. He has always been tremendously responsive to my research needs, offering valuable guidance, practical solutions, and constant encouragement, all of which have provided me with a strong foundation of support. In addition, his exceptional leadership in running such a large research group while fostering a collaborative and supportive atmosphere for us has been truly admirable. For all, I am sincerely grateful.

My research has been mostly close to Professor Elston, from whom I have gained not only technical knowledge but also invaluable wisdom—both of which will undoubtedly benefit me throughout my career and beyond. He has provided consistent supervision and guidance, introducing me to the world of optics, liquid crystals, and scientific exploration. Over the past four years, we have had countless hours of discussions about my research, during which I have accumulated thousands of handwritten notes, which reflects his extensive mentorship and invaluable insights. With this, I have developed not only technical expertise, but also the ability to think logically, critically, and to solve problems with a structured, systematic mindset. His passion for research has been truly inspiring, and I still vividly remember the moment he became genuinely excited about the research results we achieved. Beyond research, I am also grateful for the training he provided in scientific writing, presentations, and communication skills that will remain invaluable throughout my academic and

professional development. I am deeply thankful for his mentorship and support.

I am profoundly grateful to my family for their unwavering support, both financially and emotionally. Their presence and encouragement have been a constant source of warmth and strength, which illuminates my daily life and sustains me through the most challenging times. A special thanks to my sister for taking care of our family in my absence. This thesis would not have been possible without them.

I also extend my sincere gratitude to everyone I have met here. To the first group of friends who helped me settle into this new country and to the ones with whom I later shared countless moments of laughter and adventure—thank you for making my time here memorable. Especial thanks to Mengmeng Li, Fengning Yang, Yuxuan Lu, Yihan Jin, Ruohan Zhao, Peng Xie, Nathan Spiller and L Chen. To my research group, with whom I collaborated, discussed, and learned from—your inspiration and teamwork have been invaluable. To the staff at St Hugh's College and Department of Engineering Science, thank you for always being supportive and helpful throughout my time at Oxford. There are too many names and too many shared stories to list, and each one is held in my memory.

I want to express my heartfelt thanks to my teachers and friends in China who stayed connected with me, and offered countless remote support and endless encouragement. Especial thanks to Xuan Wang and Yuyu Yang. I also wish to extend my sincere gratitude to Miss Gao.

Finally, I would like to thank my assessors for their time, effort, and the invaluable feedback they have provided over the years. Their constructive comments and thoughtful insights have greatly contributed to the improvement of this work.

To everyone and everything that has been part of this journey—thank you! Each moment, each encounter, and each challenge has shaped this experience, and I carry them all with me.

Publications

➢ First-author Publications

1. **Xue, L**., Jin, Y., Elston, S. J., & Morris, S. M. (2023). Fast analogue 2π phase modulation using a liquid crystal Pi-Cell. ***Optics & Laser Technology***, 167, 109773.
2. **Xue, L.,** Elston, S. J., & Morris, S. M. (2025). Polarization-independent nematic liquid crystal phase modulators. ***ACS Photonics***.

➢ Co-authored Publications

3. Jin, Y., **Xue, L**., Zhao, Z, Elston, S.J., and Morris, S.M, (2025). Optical Phase Modulation of Fast Switching Flexoelectro-optic Liquid Crystal Devices. (Co-first, Under review)
4. Xie, P., **Xue, L.,** Li, M., Xia, M., ... & Zhang, X. (2025.). Artificial Intelligence-Driven Nanophotonic Devices. *ACS Nano*. (Under revision)
5. Han, Q., Elston, S. J., Kamal, W., **Xue, L**., & Morris, S. M. (2025). A switchable and rotatable chiral nematic liquid crystal diffraction grating for beam-steering technology. *Advanced Optical Materials*.
6. Han, Q., Elston, S. J., Kamal, W., **Xue, L**., & Morris, S. M. (2025). A nonlinear model of flexoelectric liquid crystal diffraction gratings. *Optics & Laser Technology*, 180, 111502.
7. Chen, B., Xie, P., Zhao, Z., Salter, P. S., Li, M., **Xue, L**., ... & Morris, S. M. (2024). Ultrafast laser writing of liquid crystal waveguides. *Ultrafast Science*, **4**, 0065.
8. Wang, X., Qiu, X., Liu, M., Liu, F., Li, M., **Xue, L.**, ... & Xie, P. (2023). Flat soliton microcomb source. *Opto-Electronic Science*, 2(12), 230024-1.

➢ Conferences Presentations

1. SPIE Photonics West, San Francisco, California, United States, 30th Jan to 1st Feb 2024 - **Linpei Xue,** Steve J. Elston, and Stephen M. Morris, Fast analogue 2π phase modulation using liquid crystal devices. **(Oral presentation)**
2. The 6th Optical Information and Optical Network Conference, Beijing, China, 1st Dec to 3rd Dec 2023 - **Linpei Xue**, Yihan Jin, Steve J. Elston, and Stephen M. Morris, Fast analogue 2π phase modulation using a liquid crystal Pi-Cell. **(Oral presentation and poster presentation)**
3. Oxford Photonics Day, Oxford, United Kingdom, 28th Sep 2022 - **Linpei Xue**, Yihan Jin, Steve J. Elston, and Stephen M. Morris, Nematic liquid crystal state with fast response and 2π phase modulation. **(Poster presentation)**
4. Oxford Photonics Day, Oxford, United Kingdom, 3rd Oct 2023 - **Linpei Xue**, Steve J. Elston, and Stephen M. Morris, Polarization-independent Phase Modulation based on Super-twisted nematic Liquid Crystal Devices. **(Poster presentation)**
5. British Liquid Crystal Society Annual Meeting, Oxford, United Kingdom, 10th Apr – 12th Apr 2024 - **Linpei Xue**, Steve J. Elston, and Stephen M. Morris, Time-Dependent Phase Modulation in Liquid Crystal Photonic Devices. **(Poster presentation)**

Contents

1. Introduction

1.1 Overview and Objectives

My D.Phil thesis focuses on the development of optical phase modulation technologies using liquid crystals (LC), the primary use of which is in Spatial light Modulators (SLMs). SLMs are compact devices that can be used to modulate the amplitude, phase and polarization (or a combination of these parameters) of an incident light beam along the two spatial dimensions of the modulator.

SLMs can be fabricated from micro-electromechanical systems (MEMS) or liquid crystal on silicon (LCOS). MEMS-based optical phase modulators consist of self-aligned mirrors and actuators. The advantages of these systems include mechanical stability, low cost and easy integration with fibre-based lasers and sensors or photonic microsystems [1]. However, optical MEMS switches require high driving voltage and have a high-power consumption. On the other hand, LCOS-based SLMs have the merits of real-time manipulation of incident light with unprecedented flexibility and precision, shaping optical wavefronts[2]. The architecture includes a glass layer with a transparent indium tin oxide (ITO) conductive layer, an LC layer aligned along the rubbing direction, and a reflective silicon backplane on one side. SLMs can be either transmissive or reflective devices, and LCOS is typically designed as a reflective SLM, and its silicon backplane prevents light transmission and provides reflection. The structure of a reflective device is shown in **Figure 1.1**.

LCOS SLMs can also be classified as electrically addressed or optically addressed [3], and in this work, we only consider electrically addressed SLMs. These devices are controlled

by an external electric field, which is applied through a silicon backplane. When a voltage is applied, the director in the LC layer reorients in response to the electric field. This reorientation alters the optical properties of the LC layer, thereby modulating the optical phase and amplitude of the output light, illustrated in **Figure. 1.2**. The ability to modulate the phase of light allows LCOS SLMs to perform various optical functions [2]. By creating controlled phase shifts in the output light, these devices can generate images through interference effects or correct optical aberrations in adaptive optics systems. This phase modulation capability is central to their widespread use in applications such as imaging and display systems, holography, beam shaping, and wavefront correction. Beyond these specific functionalities, LCOS SLM technology has been employed in a broad range of fields which require fast, high resolution and high-throughput optical modulators.

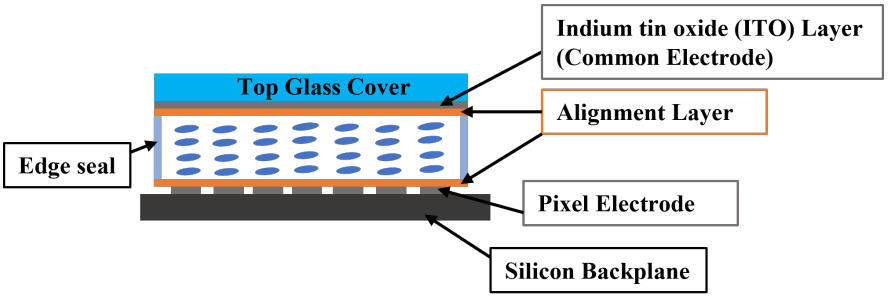

Figure 1.1. Schematic of a Liquid Crystal on Silicon (LCOS) cell where the vertical dimension has been exaggerated to show the different layers that make up the device. For such devices, the LC layer is usually only a few microns thick.

The first LC SLM was developed in the late sixties [4], and since then, these devices have become indispensable in applications such as optical signal processing [3][5], light detection and ranging (LiDAR) [6], beam steering [7], wavelength selective switch [8], hologram reconstruction [9]-[11], augmented reality and virtual reality displays [12][13], optical microscopes [14], real-time holography [15][16] and laser speckle reduction [17][18]. Because LCs do not generate light but instead modify incident light, LCOS SLMs consume

only a small amount of electrical energy. In addition, they have the merits of relatively low operation voltage, and low cost; and therefore, most commercially available SLMs are based upon LC technology.

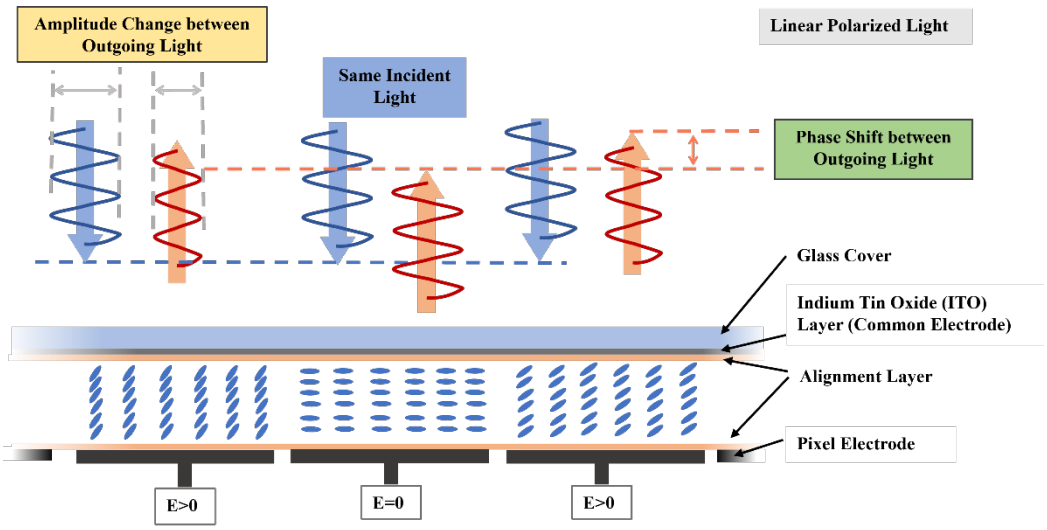

Figure 1.2. Schematic representation of the working principle of an LCOS SLM. Linear polarized light passes through the liquid crystal (LC) layer, which is modulated by the pixel electrode configuration. Regions with and without an applied electric field (E > 0 and E = 0) control the orientation of the LC director, resulting in amplitude and phase modulation of the outgoing light [23].

For many applications, the general requirements for an LCOS SLM are fast response time (ideally $\tau < 1$ ms), full analogue optical phase modulation ($\delta > 2\pi$ rad) and low operating voltage ($\leq$ 15 V). Each of these requirements is closely tied to the functionality and performance of LCOS SLMs in practical applications. A fast response time ensures high framing rates, which are crucial for applications such as augmented reality (AR), virtual reality (VR), and holographic displays. In these cases, low latency is essential to provide a seamless, realistic image and enhance user experience. Faster response times also enable higher refresh rates for dynamic wavefront shaping in optical communication systems and adaptive optics, where rapid adjustments are necessary for real-time beam control.

A phase range greater than 2π rad allows the SLM to handle complex wavefront modulations, which is critical for producing high-quality images and efficient beam steering. In holographic displays and laser beam shaping, controlling the phase over a full 2π rad or more ensures accurate reconstruction of the desired optical field and minimizes artifacts. This capability is also important for advanced optical applications, such as generating arbitrary light fields and improving diffraction efficiency in diffractive optical elements. A low operating voltage is a limitation of the silicon technology, where the maximum voltage supply for LC drives typically ranges between 15 and 20V. Additionally, low voltage operation is vital for energy efficiency and compatibility with portable devices, such as head-mounted AR/VR displays or battery-powered optical systems. Reduced power consumption not only extends device longevity but also minimizes thermal effects, which can degrade performance. Furthermore, it simplifies electronic driver circuits, making the device more compact and cost-effective for integration into consumer electronics.

The challenges in achieving those requirements simultaneously are that those requirements can involve in the trade-offs between each other. The first trade-off is between response time and phase modulation. For nematic LC devices, the response time is inherently limited by the viscoelastic properties of the material. The response time (τ) of a homogeneous (planar – the LC director lies in the plane of the device)) aligned cell can be expressed as:

$$\tau = \frac{\gamma_1 \, d^2}{K_{11} \, \pi^2} \qquad (1-1)$$

where γ_1 is the rotational viscosity, d is the thickness of the LC layer, and K_{11} is the splay elastic constant.

The maximum optical phase modulation (δ) is determined by:

$$\delta = \frac{2\pi d \Delta n}{\lambda} \qquad (1-2)$$

where Δn is the birefringence of the LC, and λ is the wavelength of light.

Optimizing the LC layer thickness (d) for a shorter response time (τ) requires reducing d, which in turn decreases the phase modulation range (δ). As a result, the device must balance between fast response and sufficient phase modulation to meet application-specific requirements, unless specialized designs are implemented to overcome these conventional limitations.

The second trade-off is between phase modulation and applied voltage. Accessing the full birefringence of the LC material requires, in principle, an infinite voltage. In practice, the effective birefringence (Δn_{eff}) experienced by the incident light depends on the applied voltage. Increasing the voltage amplitude improves the effective birefringence, thereby enhancing the phase modulation range. However, the silicon backplane of the LCOS device may not be capable of delivering the high voltages needed to fully exploit the material's birefringence, due to limitations in the maximum voltage supply and power handling capabilities [25][38].

In more complex scenarios, polarization independence is also required, meaning the polarization state of the incident light remains unchanged after passing through the LC device, and all polarizations experience the same phase shift. This capability is crucial and urgent in several advanced optical applications [19]-[21]. For example, in optical telecommunications systems, the polarization state of light is often unknown or fluctuating, which poses a significant challenge for polarization-sensitive components. As a result, achieving polarization-independent performance is critical to ensure system reliability and efficiency [22].

Additionally, in holographic systems, polarization independence is essential for maintaining the image quality [19]. Polarization inconsistencies can distort the wavefronts used to reconstruct the hologram, leading to reduced resolution, unwanted interference patterns, and degraded image fidelity. Through ensuring polarization-independent modulation, these systems can achieve uniform brightness, accurate colour reproduction, and enhanced visual performance [20]. In beam shaping systems, polarization independence is crucial for ensuring the modulated beam maintains a uniform intensity and phase profile. Polarization-dependent modulation can introduce unwanted asymmetries and irregularities in the shaped beam, compromising precision and reducing the effectiveness of the system. Ensuring polarization independence allows the system to function consistently, regardless of the input polarization state. Achieving polarization independence in LC-based devices is technically challenging because LCs are inherently birefringent, with phase modulation depending on the polarization state of the incident light [19].

In summary, designing an LCOS SLM that satisfies these conflicting requirements of fast response time, high phase modulation, and low voltage operation is inherently challenging due to the intrinsic trade-offs between these parameters. The need for polarization independence adds additional complexity, as it requires specialized designs or materials to ensure consistent performance regardless of the input polarization state. This further complicates the already delicate balance required to optimize these devices. Nevertheless, if these requirements can be met or even surpassed, such technology would represent a major breakthrough, driving advancements in both scientific research and industrial applications where SLMs play a critical role.

In the thesis, I aim to enhance the performance of LC-based optical phase modulators

and utilize phase-shift interferometry techniques to study the time-resolved phase modulation. Two distinct optical phase modulators based on nematic LC phases are investigated by applying optimised voltage waveforms. Furthermore, an optimization algorithm integrated with the optical simulation method is developed to identify the most effective device configurations. The primary objective is to significantly improve switching speed while maintaining analogue phase control (ranging from 0 to 2π rad) at room temperature under low voltage operation. Additionally, this work seeks to achieve polarization independence, a critical requirement for many advanced optical applications. The design process employs a comprehensive approach, including conceptualizing the modulator, conducting LC device simulations, characterizing device performance, developing phase measurement systems, and analysing experimental results. By integrating these techniques, this research aims to make a contribution to the development of high-performance LC-based optical phase modulators suitable for a wide range of scientific and industrial applications.

1.2 Layout of Thesis

Eight chapters constitute this thesis. These are summarised as follows.

Chapter 1 introduces the overview and objectives of the research work. The layout of the thesis is also contained herein.

Chapter 2 provides an overview of the relevant theory and background related to various LC materials, their properties, and the available LC based device configurations. It also discusses optical simulation methods and explores prospective optical phase modulators, including those based on chiral LCs and ferroelectric LCs. This foundational knowledge lays the groundwork for the exploration and analysis presented in the subsequent chapters.

Chapter 3 describes three optical phase measurement systems developed and used in my work: one indirect method based on transmission measurement and two direct, time-resolving measurement systems. The innovative working principles and the phase extraction methods of these systems are also discussed. Together, these measurement systems provide the experimental data analysed in the subsequent chapters.

Chapter 4 proposes an optical phase modulator based on nematic LCs filled in a pi-cell with anti-parallel pretilt angles. The chapter begins by discussing the challenges and the state-of-art technologies reported in the literature. The modulator concept and its characteristics are then explored, followed by a description of the simulation method based on continuum theory. The optical phase modulator designed in this Chapter can achieve a full 2π rad phase modulation within 1 ms in reflection. This work, in combination with the second measurement technique described in Chapter 3, has been written up and published in the journal article: Xue, L., Jin, Y., Elston, S. J., & Morris, S. M. (2023). Fast analogue 2π phase modulation using a liquid crystal Pi-Cell. *Optics & Laser Technology*, 167, 109773.

Chapter 5 proposes a polarization-independent phase modulator based on super-twisted nematic (STN) LCs. It first highlights the challenges associated with polarization independence and reviews cutting-edge technologies reported in the literature. The proposed phase modulator concept is then introduced, with a detailed explanation of the approach to achieve polarization independence, and a comparison with conventional twisted nematic (TN) LCs. The chapter proceeds to outline the simulation methodologies and provides an analysis of the simulation and experimental results. This work successfully demonstrates a polarization-independent optical phase modulator achieving full 2π rad phase modulation within 1 ms using a four-pass configuration. The work in this chapter, in combination with the third measurement technique

described in Chapter 3, has been written up and published in the journal article: Xue, L., Elston, S. J., & Morris, S. M. (2025). Polarization-independent nematic liquid crystal phase modulators. *ACS Photonics*.

Chapter 6 presents an optical optimization algorithm to explore the optimal combination of waveplates, such as quarter-waveplates and half-waveplates, with nematic LC devices. The primary goal is to identify a best configuration that meets specific performance criteria that are difficult to achieve with a single device, such as maximizing polarization independence phase modulation or attaining an improved phase modulation depth. This Chapter details the optical optimization methodology, providing illustrative examples and an in-depth discussion of the exploration results for several commonly used LC devices.

Finally, **Chapter 7** serves as a conclusion and discussion for all of the work presented in the previous chapters. In addition, it will plot a route forward for future work.

2. Background

This chapter provides the foundation and background on liquid crystals (LC) and optical phase modulator technologies necessary to understand the work presented in this thesis. It begins by outlining the key characteristics of nematic LCs, including their phase transitions and molecular ordering. The discussion then delves into their elastic properties and continuum theory, followed by an overview of their dielectric and optical properties. Furthermore, the chapter covers approaches for modelling LCs, the architecture of LC devices, and polymer stabilization processes using reactive mesogens.

2.1 Liquid Crystal Characteristics

2.1.1 Phase transitions

Liquid crystals (LCs) are phases of matter that exhibit properties intermediate between isotropic liquid phase and solid phase [24][25]. LC molecules can have different shapes, such as rod-like or disc-like forms, and present dielectric and optical anisotropies. There are two main types of LCs: thermotropic LCs, which form within a specific temperature range between a crystalline solid phase and an isotropic liquid phase, and lyotropic LC, whose formation depends on the concentration of the molecules in a solvent. Thermotropic LC are widely used in technological applications and so only this type is considered in this thesis.

Figure 2.1 illustrates the typical phase transitions of thermotropic LC as the temperature increases [24][25]. These transitions include the progression from a crystalline state to the Smectic C (SmC) phase, followed by the Smectic A (SmA) phase, the Nematic (N) phase, and finally the Isotropic (I) state at higher temperatures. Among these, the Nematic phase is arguably the most extensively studied LC phase, particularly for applications requiring

responsive and controllable optical properties. In this thesis, the nematic phase is primarily adopted for the design and analysis of LC devices. Specifically, the focus is on calamitic nematic LCs, which are characterized by their rod-like molecular shape. The term "nematic" originates from the ancient Greek word νῆμα, meaning "thread," likely referring to the thread-like texture observed under a polarizing optical microscope.

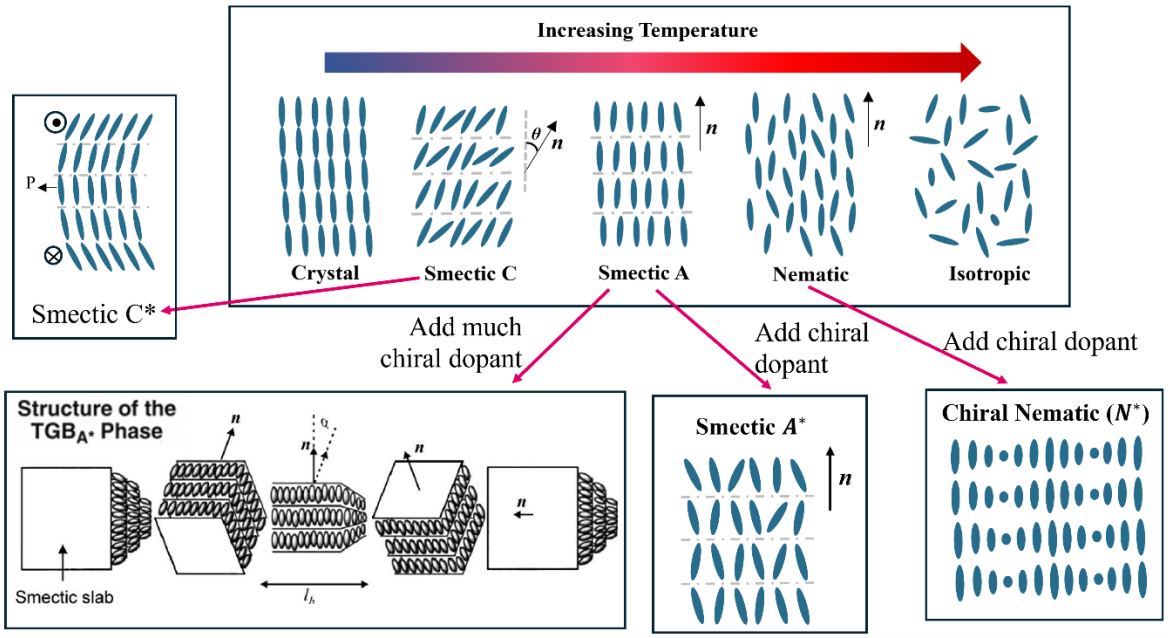

Figure 2.1. An example of the phase transitions of a thermotropic nematic LC as the temperature increases. This also illustrates the effect of adding a chiral dopant [24][25].

Most nematic LCs are uniaxial, meaning they possess one distinct preferred axis (the longitudinal axis), while the other two axes are equivalent. This uniaxial nature allows nematic LCs to be represented as rods or elongated ellipses. Their directional alignment and ease of reorientation under external fields (e.g., electric or magnetic), make nematic LCs the most commonly studied and widely applied type of LC. They are utilized in diverse technological applications, including displays, sensors, and optical devices. This thesis uses these properties to explore the design and functionality of nematic LC-based systems.

The smectic (Sm) phase can be sub-divided into several types, such as SmA, SmC, and others (e.g., SmB, SmF, SmK), based on the tilt angle of the LC director and the packing arrangement of the molecules [26]. Among these, the SmA and SmC phases are the most studied types and are illustrated in the Fig. 2.1. The smectic phase is distinguished by a layered structure, characterized by both orientational and positional order of the molecules. In the SmA phase, the LC molecules tend to be perpendicular to the layer planes, while in the SmC phase, the molecules are tilted at a fixed angle relative to the layer planes. This difference in molecular orientation within the layers leads to distinct physical properties and behaviours in the smectic phases [27]. Besides, compared to the nematic phase, the smectic phase is less fluid due to the presence of layers, which restricts the movement of molecules more than in the nematic phase.

In addition, Fig. 2.1 highlights the effects of introducing chiral dopants to LC phases. A chiral dopant is a chemical additive that induces a helical twist in the molecular alignment of the LC material. This twist occurs because chiral dopant molecules have an asymmetrical structure, lacking mirror symmetry, which produces chirality (handedness) to the LC phase. For example, when a small concentration of chiral dopant is added to a nematic LC, the nematic phase can transition into a chiral nematic (or cholesteric) phase [29], as illustrated in Fig. 2.1. In this phase, the LC molecules rotate continuously, forming a helical structure. The pitch of the helix - the distance over which the molecules complete a full 360° twist - depends on both the type and concentration of the chiral dopant.

Similarly, adding chiral dopants to the SmA phase produces chiral Smectic A* (SmA*) phase. In this phase, the molecules remain perpendicular to the layers, but the chirality causes the orientation of the molecules to rotate helically from layer to layer. At higher concentrations of chiral dopant, the SmA phase can transition into the TGBA* phase (Twisted Grain Boundary

Smectic A*). This phase features a broken-layer structure with embedded screw dislocations, resulting in a helical arrangement. Furthermore, when chiral dopants are added to the SmC phase, the phase transitions into the chiral Smectic C* (SmC*) phase. This phase is characterized by tilted molecules whose orientation also exhibits a helical arrangement due to chirality. Each of these transitions illustrates how chiral dopants expand the diversity of LC phases, enabling unique structural and optical properties for advanced applications.

2.1.2 The director and the order parameter

To specify the geometry and dynamics of the nematic LC phase, two macroscopic variables are used: the director and the order parameter. The average orientation of the LC molecules is known as the nematic director, $\vec{n}$, which is a unit vector aligned with the time-averaged axis of a single molecule (the direction will vary due to thermal fluctuations) or the average of an ensemble of molecules at a point in time, as indicated in Fig. 2.1. In nematic LCs, there exists an equivalence of $\vec{n} = -\vec{n}$ because of the symmetry of the phase. This means that the molecular alignment is invariant under a 180° rotation, reflecting the lack of a preferred directional polarity in the nematic phase. In contrast, in SmC LCs, this equivalence does not hold ($\vec{n} \neq -\vec{n}$) due to the asymmetry of the phase. The tilted molecular arrangement in the SmC phase creates a distinct directional polarity.

Due to the shape anisotropy of nematic LC, they exhibit a phenomenon known as nematic ordering, which is characterized by long-range orientational order but no positional order. It is possible to quantify how ordered the LC is by measuring how much the deviation of the molecules' orientation differs from that of the director ($\vec{n}$). The degree of orientational alignment is quantified by the order parameter, *S*, which is a scalar quantity introduced by Tsvetkov [30], and defined as:

$$S = \left\langle \frac{3}{2} cos^2 \theta - \frac{1}{2} \right\rangle \qquad (2-1)$$

where θ is the angle between the orientation of a molecule and the local director $\vec{n}$.

When all the molecules are well aligned with the director ($\theta = 0$), $S = 1$. In contrast, in the isotropic phase, $S = 0$ because in this case, θ refers to all directions, and the random orientation of molecules results in $\langle cos^2 \theta \rangle = \frac{1}{3}$herefore, the order parameter S typically ranges between 0 (random orientation) and 1 (perfectly ordered structure), depending on the LC. The order parameter S varies with temperature, generally increasing as the temperature decreases (since the structure becomes more ordered). In practical nematic phases, S often varies between approximately 0.4 and 0.7.

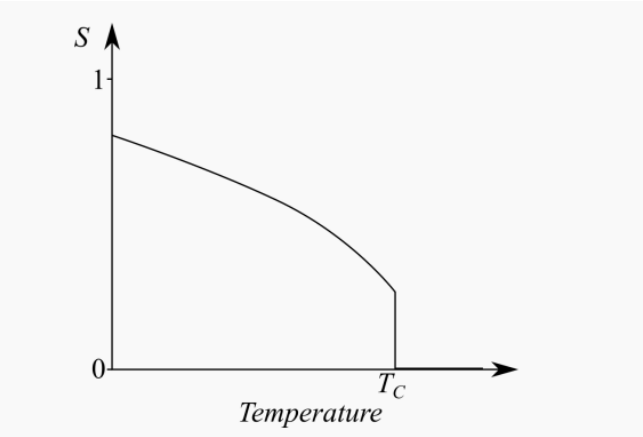

Figure 2.2. The temperature dependence of the scalar order parameter of nematic LCs [31].

Figure 2.2 illustrates the temperature dependence of the scalar order parameter S in nematic LC. As the temperature (T) increases, thermal energy disrupts the molecular alignment, causing a gradual decrease in S. Near the critical temperature (T_C), the nematic phase transitions to the isotropic phase, where the molecules become completely disordered, causing S to drop rapidly to zero. This sharp change at T_C signifies a first-order phase transition, characterized by a discontinuous change in the order parameter and the release or absorption of latent heat.

This transition often nucleates from impurities or defects in the liquid crystalline structure, which act as initiation points for the phase change.

In the nematic phase, the lack of positional order arises because thermal energy prevents the formation of a regular lattice structure, allowing the molecules to flow freely, similar to a liquid. However, unlike isotropic liquids, nematic LCs retain long-range orientational alignment of their molecules, making them distinct from liquid phase.

2.2 Elastic Properties and Continuum Theory

To better analyse an LC device, continuum theory [32][33] can serve as a foundation. This theory deals with the deformation and transmission of forces through LCs by modelling them as a continuous medium (a continuum) rather than discrete particles. By disregarding molecular-level details, this approach facilitates a macroscopic analysis of the LC behaviour. The concept of a continuous medium enables an intuitive understanding and the application of differential equations to describe bulk properties and interactions. The elastic free energy density model for LCs, which focuses on the various ways nematic LCs can deform, was initially developed by Carl Wilhelm Oseen [34] and later refined by Frederick Charles Frank [35]. This framework, commonly referred to as the Oseen-Frank theory, describes the elastic energy associated with different deformation modes in nematic LCs and remains fundamental in LC research [36].

As discussed previously, nematic LC molecules exhibit long-range orientational order but lack positional order. At thermodynamic equilibrium, these molecules tend to have random spatial distributions while maintaining a uniform orientation defined by the director, $\vec{n}$. Frank identified three fundamental modes of deformation from this lowest-energy state: splay, twist

and bend, as visualised in **Figure 2.3**. He demonstrated that all possible deformations in nematic LCs can be reduced to these three modes. According to the Oseen-Frank theory, deviations from equilibrium are analogous to stretching or compressing a spring, where the restoring forces are proportional to the distortion. The elastic free energy density associated with these deformations is given by:

$$f_d = \frac{1}{2}K_{11}[\nabla \cdot \vec{n}]^2 + \frac{1}{2}K_{22}[\vec{n} \cdot (\nabla \times \vec{n})]^2 + \frac{1}{2}K_{33}[\vec{n} \times (\nabla \times \vec{n})]^2 \quad (2-2)$$

where $\vec{n} = (n_x, n_y, n_z)$ is the director field, and K_{11}, K_{22}, and K_{33} are the Frank elastic constants for splay, twist and bend distortions, respectively. These constants, with units of [N], are analogous to spring constant in classical mechanics. Typically, the Frank elastic constants are on the order of 10 pN with the general relationship $K_{33} > K_{11} > K_{22}$. This hierarchy indicates that bend distortions are typically more energetically costly than splay and twist distortions.

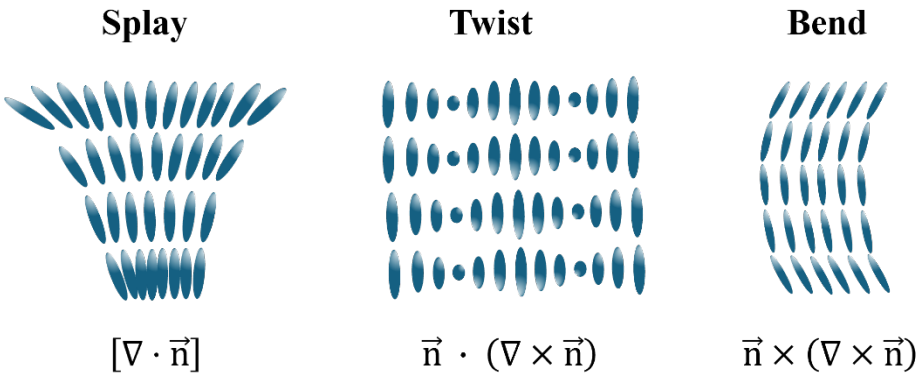

Figure 2.3. The three fundamental types of bulk elastic distortion in LCs: splay, twist, and bend.

The three distortion modes in Eq. (2-2) can be understood by examining the nature of the director field for each mode. As illustrated in Fig. 2.3, splay distortions occur when the director points outwards radially from a point, resulting in a non-zero divergence ($\nabla \cdot \vec{n} \neq 0$). For twist distortions, the curl ($\vec{n}$) of the director is parallel to the director ($\vec{n} \cdot (\nabla \times \vec{n}) \neq 0$), while in bend distortions, the curl ($\vec{n}$) of the director is perpendicular to the director ($\vec{n} \times (\nabla \times \vec{n}) \neq 0$). In continuum theory, this distortion free energy density expression describes the elastic energy

cost associated with deformations away from the equilibrium state, where all the molecules are aligned parallel to each other. This free energy provides a basis for calculating the director field by minimising the expression and solving the resulting differential equations. However, in practice, Eq. (2-2) is often too complex to solve analytically. To simplify the analysis, a common assumption is that $K_{11} = K_{22} = K_{33} = K$. Under this one-constant approximation, the elastic free energy density in Eq. (2-2) is simplified to:

$$f_d = \frac{1}{2}K[\nabla \cdot \vec{n}^2 + |\nabla \times \vec{n}|^2] \qquad (2-3)$$

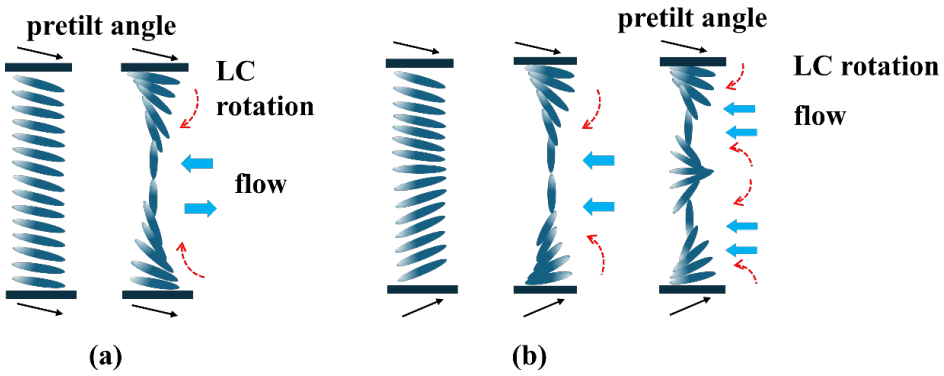

Figure 2.4 The influence of the flow on the LC device: (a) Fréedericksz LC device and (b) pi-cell device. The black arrows represent the pretilt angle of the device and the red dashed arrows represent the rotation direction of the LC director under voltage switch on. The flow effects of the LC are represented by the blue thick arrows in the switch on process.

To accurately simulate the LC devices in this thesis (e.g., in Section 4.3), it can also be important to consider the flow properties of LCs. LC devices are particularly sensitive to flow effects due to the anisotropic nature of LCs, and the flow is typically described by hydrodynamic equations that couple the fluid motion with the orientation of the LC molecules (director field). These flow effects influence the dynamic response, electro-optic properties, and stability of LC devices, particularly under external forces such as applied electric fields. The impact of flow effects varies depending on the device type and its operational state. For example, as shown in **Figure 2.4(a)**, flow-induced effects in a Fréedericksz device can

compromise stability. Reorientation of the LC director in the switching process generates flow forces in opposite directions, causing fluctuations in the central region. By contrast, flow effects are much less significant in a pi-cell device [86], as illustrated in Fig. 2.4 (b), especially when the LCs are in the vertically aligned state or the symmetric H state. In these states, the symmetric director distribution results in opposing flow directions that effectively cancel each other, thereby minimizing the flow-induced instability. This reduction in backflow effects enhances the overall stability and performance of pi-cell device.

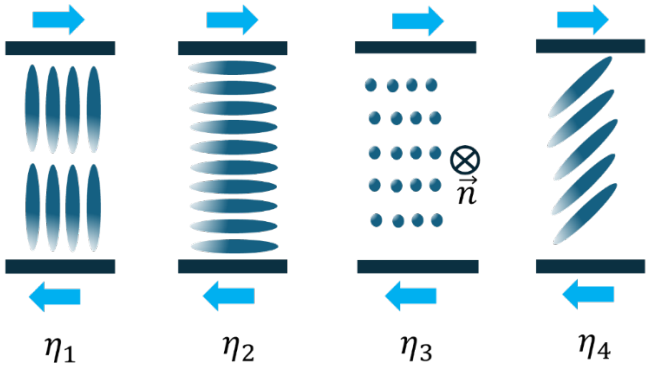

Figure 2.5. Illustration of the flow gradients and director orientations associated with the Miesowicz viscosities [41]. η_1 represents the viscosity when the director ($\vec{n}$) is perpendicular to both the flow direction and the velocity gradient. η_2 refers to the viscosity when the director ($\vec{n}$) is parallel to the flow direction. η_3 is the viscosity when the director ($\vec{n}$) is perpendicular to the flow direction but lies in the plane of the velocity gradient. η_4 is the viscosity in shear flow when the director ($\vec{n}$) lies in the flow plane and is at an oblique angle to the flow direction. The direction of flow in the LC is represented by the blue thick arrows.

Leslie proposed that LCs exhibit six independent viscosities [37] (α_1, α_2, α_3, α_4, α_5 and α_6), but Parodi later demonstrated that one of these can be expressed as a linear combination of two of the others [38] ($\alpha_6 - \alpha_5 = \alpha_2 + \alpha_3$). This simplification, widely accepted in LC theory, reduces the number of independent viscosities to five. In this study, we follow Parodi's theory and consider five independent viscosities in the simulation of LCs [39]. Additionally, there are two commonly used systems of notation for these viscosities: Leslie coefficients [37], which arise from theoretical discussions, and Miesowicz coefficients [40], which are defined

based on experimental measurements of shear flow under controlled conditions. The Miesowicz coefficients are more intuitive for experimental interpretation and can be expressed as combinations of the Leslie coefficients under specific conditions.

Figure 2.5 illustrates the flow gradients associated with the Miesowicz viscosities [41]. The notation for these viscosities includes one rotational viscosity (γ_1) and four shear viscosities (η_1, η_2, η_3, and η_4). Among these, the rotational viscosity dominates the switching behaviour in LC devices, since the rotation of the director is the primary mechanism responsible for the optical switching effect. Rotational viscosity characterizes friction between LC directors during molecular rotations, and its magnitude depends on temperature, intermolecular interactions, and the molecular structure [42]. The shear viscosities play secondary roles, contributing to flow-induced effects that influence stability and response time.

2.3 Electric properties

2.3.1 Dielectric energy

Liquid crystals are dielectric materials, meaning they do not conduct electricity like metals but can become polarized under an external electric field ($\vec{E}$). Polarization ($\vec{P}$) is the electric dipole moment per unit volume of the material. When subjected to an external electric field ($\vec{E}$), the LC director aligns in response, inducing dipole moments. The relationship between polarization ($\vec{P}$) and the electric field ($\vec{E}$) is given by:

$$\vec{P} = \varepsilon_0 \chi \vec{E} \qquad (2-4)$$

where ε_0 is permittivity of free space (8.85×10^{-12} $C^2/N\cdot m^2$), χ is the electric susceptibility, a dimensionless parameter.

As mentioned, LCs exhibit an anisotropic molecular structure, meaning their dielectric

properties vary depending on the direction of the applied electric field relative to their director ($\vec{n}$). In isotropic materials (like regular dielectrics), χ is scalar due to the uniformity of the material's structure, which ensures that its electric properties are the same in all directions. However, in LCs, χ is a tensor because the molecular alignment leads to direction dependent polarizability:

$$\chi = \begin{pmatrix} \chi_{\perp} & 0 & 0 \\ 0 & \chi_{\perp} & 0 \\ 0 & 0 & \chi_{\parallel} \end{pmatrix} \qquad (2-5)$$

where $\chi_{\perp}$ is the susceptibility when the electric field is perpendicular to the director, and $\chi_{\parallel}$ is the susceptibility when the electric field is parallel to the director.

The electric susceptibility (χ) is directly related to the material's relative permittivity (ε_r):

$$\varepsilon_r = 1 + \chi \qquad (2-6)$$

For LCs, this anisotropic susceptibility results in an anisotropic permittivity tensor, which can be expressed as:

$$\varepsilon_r = \begin{pmatrix} \varepsilon_{\perp} & 0 & 0 \\ 0 & \varepsilon_{\perp} & 0 \\ 0 & 0 & \varepsilon_{\parallel} \end{pmatrix} \qquad (2-7)$$

where $\varepsilon_{\perp}$ represents the relative permittivity when the electric field is applied perpendicular to the LC director ($\vec{n}$), and it is given by $\varepsilon_{\perp} = 1 + \chi_{\perp}$. Similarly, $\varepsilon_{\parallel}$ represents the relative permittivity when the electric field is applied parallel to the LC director and is expressed as: $\varepsilon_{\parallel} = 1 + \chi_{\parallel}$.

The difference between $\varepsilon_{\perp}$ and $\varepsilon_{\parallel}$ defines the dielectric anisotropy ($\Delta\varepsilon$), as expressed:

$$\Delta\varepsilon = \varepsilon_{\parallel} - \varepsilon_{\perp} \qquad (2-8)$$

The dielectric free energy density, which describes how the polarization responds to an external field to minimize the system's energy, can be expressed as:

$$f_{dielectric} = -\frac{1}{2}\Delta\varepsilon\varepsilon_0\left(\vec{n}\cdot\vec{\mathrm{E}}\right)^2 \qquad (2-9)$$

where $\Delta\varepsilon$ is the dielectric anisotropy, ε_0 is the vacuum permittivity, and $\vec{\mathrm{E}}$ is the applied electric field.

The sign of $\Delta\varepsilon$ determines the alignment of the director ($\vec{n}$) relative to the electric field. For positive dielectric anisotropy ($\Delta\varepsilon > 0$), the director aligns parallel to the electric field. This occurs because the LC director reorients to minimize energy by aligning the long molecular axes along the field direction. For negative dielectric anisotropy ($\Delta\varepsilon < 0$), the director aligns perpendicular to the electric field. Here, the molecules avoid alignment with the field direction, preferring a configuration perpendicular to it.

To fully describe the LC behaviour, this dielectric term must be incorporated into the elastic energy density described in Eq. (2-2) (or one-constant approximation described in Eq. (2-3)). The overall free energy density is then given by:

$$F = f_d + f_e \qquad (2-10)$$

Substituting the elastic and dielectric terms, the total free energy density becomes:

$$F = \frac{1}{2}K_{11}[\nabla\cdot\vec{n}]^2 + \frac{1}{2}K_{22}[\vec{n}\cdot(\nabla\times\vec{n})]^2 + \frac{1}{2}K_{33}[\vec{n}\times(\nabla\times\vec{n})]^2$$

$$-\frac{1}{2}\Delta\varepsilon\varepsilon_0\left(\vec{n}\cdot\vec{\mathrm{E}}\right)^2 \qquad (2-11)$$

For the one-constant approximation of the distortion free energy density, the overall free energy density simplifies to:

$$F = \frac{1}{2}K[\nabla\cdot\vec{n}^2 + |\nabla\times\vec{n}|^2] - \frac{1}{2}\Delta\varepsilon\varepsilon_0\left(\vec{n}\cdot\vec{\mathrm{E}}\right)^2 \qquad (2-12)$$

In summary, the orientation of the LC director ($\vec{n}$) under an electric field is determined by the balance among three key factors: dielectric coupling with the external field, elastic restoring forces arising from distortions (as described in Section 2.2), and minor anchoring forces. Surface anchoring refers to the interaction between the LC molecules and the device surface, which establishes a preferred molecular orientation at the boundary. The strength of this anchoring depends on surface treatment and material properties, and it can range from strong to weak. This interplay of forces governs the dynamic and equilibrium configurations of LC devices, ultimately shaping their electro-optic behaviour.

2.3.2 Fréedericksz threshold

In planar aligned LC devices, the director reorients in response to an applied electric field. The critical point at which this reorientation begins is known as the Fréedericksz threshold. The phase transition was first observed by Fréedericksz and Repiewa in 1927 [43]. This threshold occurs when the dielectric coupling energy becomes strong enough to overcome the elastic restoring forces of the LC. The corresponding critical field strength (E_c) represents the point where the LC director starts to reorient under the applied field. At this threshold, the dielectric coupling dominates, reorienting the director either to align with the electric field direction (for positive dielectric anisotropy, $\Delta\varepsilon > 0$) or perpendicular to it (for negative dielectric anisotropy, $\Delta\varepsilon < 0$). Below this threshold, the elastic forces dominate, and the director orientation remains unchanged. The critical field strength E_c is given by:

$$E_c = \frac{\pi}{d}\sqrt{\frac{K}{\Delta\varepsilon\ \varepsilon_0}} \qquad (2-13)$$

where d is thickness of the LC layer, K is the relevant elastic constant, $\Delta\varepsilon$ is the dielectric anisotropy, and ε_0 is the permittivity of free space. The specific elastic constant K depends on the type of deformation induced by the field. K_{11} is typically used for splay deformation, which occurs when the electric field is applied perpendicular to the initial planar alignment of the LC

devices. K_{22} is the relevant elastic constant for twist deformation, which occurs when an electric or magnetic field induces a twist in LC devices. Finally, K_{33} is used in the bend deformation, which occurs when the field is applied perpendicular to the initial homeotropic (vertical) alignment of the LC device.

We can express this threshold in terms of the critical voltage, V_c, which is independent of the LC layer thickness (d):

$$V_c = \pi \sqrt{\frac{K}{\Delta\varepsilon\ \varepsilon_0}} \qquad (2-14)$$

The Fréedericksz threshold defines the field strength or voltage required to initiate reorientation of LC director, fundamentally shaping the behaviour of LC-based devices. This threshold depends only on material properties, such as the elastic constant (K) and dielectric anisotropy ($\Delta\varepsilon$), providing a predictable and controllable framework for LC switching.

2.4 Director model and finite difference method

In the simulation, nematic LC molecules are modelled as ellipsoids, and a model of the LC device is developed to describe their orientation. The director ($\vec{n}$), as discussed, is defined in the modified spherical polar coordinates. In this framework, the orientation of the LC director (molecules) is represented by the tilt angle (θ), which represents the deviation from the surface plane, and the twist angle (φ), which indicates the rotation around the z-axis, as illustrated in **Figure 2.6**(a). During the switching process, the director's orientation changes along the z-axis, forming a twist structure, where both the tilt angle (θ) and the twist angle (φ) vary as functions of position. For an LC device dynamically oriented in one plane (e.g., constrained to the xz-plane), the twist angle (φ) is set to zero, as shown in Fig. 2.6(b). This simplifies the problem to

a model in which switching occurs solely along the *z*-axis, and only the tilt angle (θ) varies.

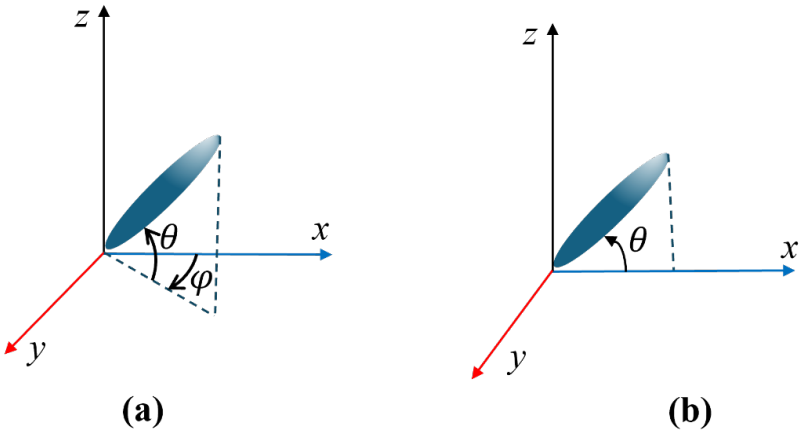

Figure 2.6. Schematic representation of a nematic LC molecule in modified spherical polar coordinates: (a) switching in the three dimensions, with the director defined by the tilt angle θ and twist angle φ and (b) switching constrained to the *xz*-plane, with the twist angle φ set to zero.

In this definition, the director $\vec{n}$ is expressed as follows: For the planar director model shown in Fig. 2.6(a), which includes both tilt and twist:

$$\vec{n} = \begin{pmatrix} cos\,\theta\, cos\varphi \\ cos\,\theta\, sin\varphi \\ sin\theta \end{pmatrix} \qquad (2-15)$$

For the model with all three director components shown in Fig. 2.6(b), where the twist angle (φ) is zero:

$$\vec{n} = \begin{pmatrix} cos\theta \\ 0 \\ sin\theta \end{pmatrix} \qquad (2-16)$$

The equilibrium configuration of the director field ($\vec{n}$) is determined by minimizing the free energy density of the LC. This is achieved using the Euler-Lagrange equation, a standard tool in the Calculus of Variations. If the free energy density is given by $F\left(y, \frac{\partial y}{\partial x_i}, x_i\right)$, the minimization condition is:

$$0 = \frac{\partial F}{\partial y} - \sum_i \frac{\partial}{\partial x_i}\left(\frac{\partial F}{\partial\left(\frac{\partial y}{\partial x_i}\right)}\right) \qquad (2-17)$$

where y is the dependent variable (e.g., θ, φ in spherical polar coordinates, or n_x, n_y, n_z in Cartesian coordinate), x_i are the independent spatial coordinates (e.g., x, y, z), and F is the free energy density.

For LCs, the Euler-Lagrange equations [44] for θ and ϕ are:

$$0 = \frac{\partial F}{\partial \theta} - \frac{\partial}{\partial x}\left(\frac{\partial F}{\partial\left(\frac{\partial \theta}{\partial x}\right)}\right) - \frac{\partial}{\partial y}\left(\frac{\partial F}{\partial\left(\frac{\partial \theta}{\partial y}\right)}\right) - \frac{\partial}{\partial z}\left(\frac{\partial F}{\partial\left(\frac{\partial \theta}{\partial z}\right)}\right) \qquad (2-18)$$

$$0 = \frac{\partial F}{\partial \phi} - \frac{\partial}{\partial y}\left(\frac{\partial F}{\partial\left(\frac{\partial \phi}{\partial x}\right)}\right) - \frac{\partial}{\partial y}\left(\frac{\partial F}{\partial\left(\frac{\partial \phi}{\partial y}\right)}\right) - \frac{\partial}{\partial z}\left(\frac{\partial F}{\partial\left(\frac{\partial \phi}{\partial z}\right)}\right) \qquad (2-19)$$

To model the dynamic behaviour of LC devices, the elastic free energy density (Eq. 2.11 or Eq. 2.12 for the one-constant approximation) is substituted into Eq. (2-18) and Eq. (2-19). We also incorporate the viscous dissipation term. This results in time-dependent partial differential equations (PDEs). To solve these equations, finite difference methods (FDM) along with an iterative relaxation approach are employed. FDM is a class of numerical analysis techniques that transform PDEs into a system of linear equations by discretizing the solution domain into a grid of discrete points. For derivatives with respect to z, the finite-difference approximations are: first derivative $\frac{\partial \theta}{\partial z}$ is expressed:

$$\left.\frac{\partial \theta}{\partial z}\right|_i \approx \frac{\theta_{i+1} - \theta_{i-1}}{2\Delta} \qquad (2-20)$$

second derivative $\frac{\partial^2 \theta}{\partial z^2}$ is expressed:

$$\left.\frac{\partial^2\theta}{\partial z^2}\right|_i \approx \frac{\theta_{i+1} - 2\theta_i + \theta_{i-1}}{\Delta^2} \qquad (2-21)$$

where *i* refers to the index of the grid point, and Δ is the grid spacing.

The iterative relaxation method is then used to solve the resulting system of equations. This involves iteratively updating the director configuration at each grid point based on a relaxation factor, proportional to the calculated torque acting on the director. Adjustments are made to the tilt angle (θ) and twist (ϕ) until convergence is achieved. Convergence is defined as a state where no significant change occurs in the director field, indicating the equilibrium configuration has been reached. By optimizing the director configuration for given conditions, this approach provides accurate modelling of LC behaviour under external forces and constraints, which facilitates detailed analysis of LC device performance.

2.5 Optical properties

2.5.1 Birefringence

Liquid crystals exhibit unique optical properties due to their anisotropic structure and birefringence, which arise from the alignment of their rod-like molecules along a preferred direction called the director ($\vec{n}$). The structural anisotropy leads to optical anisotropy, where the refractive index varies depending on the polarization and propagation direction of light. LCs are characterized by two distinct refractive indices: the extraordinary refractive index (n_e), and the ordinary refractive index (n_o). The extraordinary refractive index governs light polarized parallel to the director and is determined by the optical dielectric permittivity in the parallel direction ($\varepsilon_\parallel$). The ordinary refractive index governs light polarized perpendicular to the director and is determined by the optical dielectric permittivity in the perpendicular direction ($\varepsilon_\perp$).

The refractive indices are mathematically related to the dielectric permittivity by:

$$n = \sqrt{\varepsilon_r} \tag{2-22}$$

$$n_e = \sqrt{\varepsilon_{\parallel}} \qquad n_o = \sqrt{\varepsilon_{\perp}} \tag{2-23}$$

Birefringence (Δn) is a key property of LCs. It is defined as the difference between the extraordinary and ordinary refractive indices, expressed as:

$$\Delta n = n_e - n_o \tag{2-24}$$

When unpolarized light passes through a birefringent LC, its polarization components experience different refractive indices, and travel at different speeds. This results in a phase difference, $\Delta\delta$, between the *x*- and *y*-polarized components of the light, given by:

$$\Delta\delta = \Delta n k_0 z \tag{2-25}$$

where k_0 is the wavenumber and *z* represents propagation distance through the LC layer. This phase difference, $\Delta\delta$, alters the polarization state of the light, enabling LCs to act as polarization controllers.

By applying an external electric field, the orientation of the LC director can be dynamically adjusted, which in turn modifies the effective values of n_e and n_o of the device. For example, in a nematic Fréedericksz LC device, an applied external voltage modifies the tilt angle (θ) of the LC director while the twist angle (φ) remains unchanged, which leads to a change in the effective refractive indices. The effective extraordinary refractive index ($n_{eff_{n_e}}$) for light polarized along the direction of the surface alignment is calculated as:

$$n_{eff_{n_e}} = \frac{n_e n_o}{\sqrt{n_e^2 \sin^2\theta + n_o^2 \cos^2\theta}} \tag{2-26}$$

The effective ordinary refractive index ($n_{eff_{n_o}}$) for light polarized perpendicular to the direction of the surface alignment direction is calculated as:

$$n_{eff_{n_o}} = n_o \qquad (2-27)$$

Therefore, the effective birefringence Δn_{eff} can be expressed as:

$$\Delta n_{eff} = n_{eff_{n_e}} - n_{eff_{n_o}} \qquad (2-28)$$

This ability to dynamically control the effective birefringence enables precise manipulation of the polarization state of transmitted light. For instance, by controlling $\Delta n_{eff_{ne}}$ and the thickness (z) of the LC layer, linearly polarized light can be converted into elliptically or circularly polarized light, making LCs versatile for optical applications. Moreover, LCs are particularly suited for use as optical phase modulators due to their dynamic nature. In a nematic Fréedericksz LC device, the phase shift δ_V induced by the LC layer under varying voltages is determined by:

$$\delta_V = k_0 \int_0^d n_{eff_{ne}} dz \qquad (2-29)$$

where k_0 is the wavenumber and z represents propagation distance through the LC layer.

In summary, the effective birefringence of an LC layer can be modulated by applying a controlled voltage, which alters the relative phase difference between polarization components. This allows precise control over the polarization state of incident light. Additionally, the phase shift induced by the LC layer along a specific direction enables dynamic modulation of the optical phase of the incident light. This work focuses on investigating the dynamic optical phase modulation achieved using LC devices.

2.5.2 Jones matrix

In simulations, calculating the optical phase of light passing through an LC layer depends on the director configuration. When the LC director is oriented in a single plane without any twist — such as in a nematic Fréedericksz device — Eq. 2-29 is used. However, when the LC director

rotates in three dimensions, exhibiting a helical structure as in a super-twisted nematic (STN) device, Jones calculus, developed by R. C. Jones in 1941, is employed to determine the optical phase modulation [45], which will be detailed discussed in Section 5.3.

In Jones calculus, polarized light is represented by a Jones vector, while linear optical elements are described by Jones matrices. The polarization of light after passing through an optical element is obtained by multiplying the Jones matrix of the element with the Jones vector of the incident light. This method allows for precise analysis of polarization and phase changes in complex optical systems. As an example, the linearly polarised states of incident light are represented by:

$$J_H = \begin{pmatrix} 1 \\ 0 \end{pmatrix} \qquad J_V = \begin{pmatrix} 0 \\ 1 \end{pmatrix} \qquad (2-30)$$

Optical components, such as polarisers and waveplates, are represented as 2 × 2 matrices. For example, the matrices for horizontal (M_H) and vertical polarizers (M_V) are:

$$M_H = \begin{pmatrix} 1 & 0 \\ 0 & 0 \end{pmatrix} \qquad M_V = \begin{pmatrix} 0 & 0 \\ 0 & 1 \end{pmatrix} \qquad (2-31)$$

An LC device can be modelled as an optical retarder with a thickness of *d* using Jones calculus. The LC layer is subdivided into *N* ideally thin sub-layers, where it is assumed that the molecules in each sub-layer align along the extraordinary axis. The phase modulation introduced by each thin layer can be approximated as:

$$\delta_n = \frac{2\pi}{\lambda} \frac{n_{eff_{ne}}\, d}{N} \qquad (2-32)$$

where $n_{eff_{ne}}$ is the effective extraordinary refractive index, λ is the wavelength of the incident light, and *d* is the LC layer thickness, and *N* is the number of sub-layers.

The Jones matrix for a linear birefringent optical retarder with phase shift of δ_n with its

fast and slow axes aligned at an angle θ to the reference axis, can be written as:

$$J = R(-\theta)\begin{pmatrix} e^{i\delta_n/2} & 0 \\ 0 & e^{-i\delta_n/2} \end{pmatrix} R(\theta) \qquad (2-33)$$

where $R(\theta)$ is the rotation matrix and can be expressed as:

$$R(\theta) = \begin{pmatrix} cos\theta & -sin\theta \\ sin\theta & -cos\theta \end{pmatrix} \qquad (2-34)$$

By multiplying the Jones matrix of all the layers in the LC device, the optical effects of polarized light passing through the birefringent LC layers can be modelled. By combining Eqs. (2-32) - (2-34), the phase modulation of both twisted and untwisted LC layers can be accurately calculated.

2.6 Liquid Crystal Devices

As shown in Fig. 1.1, the schematic of a Liquid Crystal on Silicon (LCOS) cell illustrates reflective LC devices. The properties and performance of the LC device are determined by the type of LC used and the surface alignment technique employed [46]. Nematic LC can be made to align along a preferred direction using a surface alignment layer. Two main types of alignment techniques are commonly used, as depicted in **Figure 2.7**. The first is the planar alignment, which is obtained by mechanically rubbing a polymer-coated substrate (e.g., polyimide or polyvinyl alcohol) with a textile cloth. This process aligns the LC molecules parallel to the substrate surface. In traditional nematic LC device with planar alignment, a small pretilt angle (typically 3º to 5º) is introduced to prevent reverse tilt switching while maintaining the maximum depth of phase modulation [46]. For pi-cells, their anti-parallel pretilt angles on the two substrates cannot prevent reverse tilt switching, but they can counteract the effects of flow, as illustrated in Fig. 2.4. The second alignment technique is homeotropic alignment, where the LC molecules align perpendicular to the substrate. This is typically achieved by

coating the substrate with a surfactant containing an aliphatic tail (e.g. natural egg lecithin).

With those two types of surface alignment, four main configurations are widely used in optical phase modulator technologies:

1) **Fréedericksz cell**: pretilt angles on the surface are parallel, achieved through anti-parallel surface rubbing.
2) **pi-cell**: anti-parallel pretilt angles on the surface, achieved through parallel surface rubbing.
3) **hybrid aligned nematic (HAN) cell**: combines planar alignment on one substrate with a homeotropic alignment on the other.
4) **90º twisted nematic (TN) cell**: achieves a 90º twist in the LC director by aligning the two substrates perpendicularly.

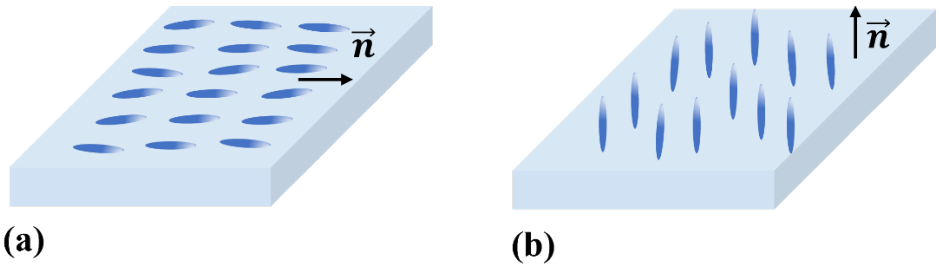

Figure 2.7. Schematic of two types of surface alignment for LC molecule orientation: (a) planar alignment where the director is parallel to the substrate and (b) homeotropic alignment where the director is perpendicular to the substrate.

These four configurations can be filled with various types of nematic LC mixtures, enabling diverse optical phenomena under suitable conditions. When applied to SLM technologies, they facilitate phase-only, amplitude-only, or combined phase-amplitude modulation when the polarization of the incident light and the polarization axis of the polarizers are well adjusted [11][48]. For devices filled with widely used nematic LCs, the corresponding director configurations are illustrated in **Figure 2.8**. These devices could exhibit different

electro-optic (EO) effects because the reorientation of the LC director varies depending on the initial alignment configuration when an external electric field is applied.

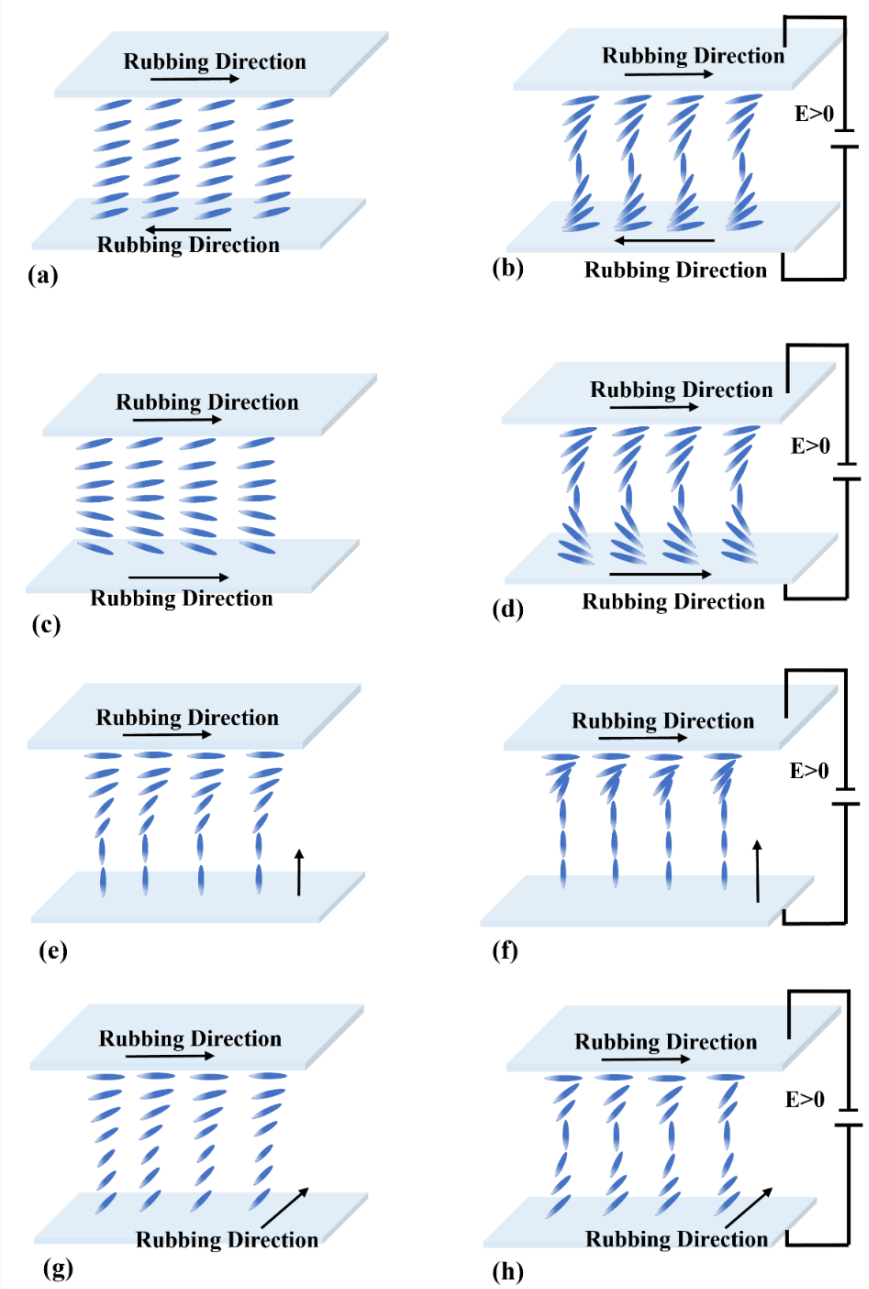

Figure 2.8. Schematics of four nematic LC devices, shown with and without an applied external voltage: (a) Fréedericksz cell with anti-parallel rubbing under no voltage and (b) Fréedericksz cell under applied voltage. (c) pi-cell with parallel rubbing under no voltage and (d) pi-cell under applied voltage. (e) HAN cell with homeotropic and planar alignment under no voltage and (f) HAN cell under applied voltage. (g) 90° twist nematic LC device under no voltage and (h) 90° twist nematic LC device under applied voltage.

As shown in Fig. 2.8(a)-(f), in devices such as the Fréedericksz cell, pi-cell, and HAN cell, there is no twist, and the light polarization lies in the plane of the director, which results in no optical polarization mixing. This makes them suitable for phase-only optical modulators for single polarized light. In particular, the majority of commercial spatial light modulators (SLMs) employ Fréedericksz cells as their phase modulation mechanism.

In a Fréedericksz device, when no voltage is applied, the LC molecules remain aligned parallel to each other due to the parallel pretilt angle, as illustrated in Fig. 2.8(a). As the applied voltage increases, the director gradually reorients along the direction of the electric field, shown in Fig. 2.8(b). This reorientation alters the birefringence, which results in an optical phase shift and forms the basis for applications in phase modulators. However, the Fréedericksz EO effect can suffer from backflow, where the coupling of torque and flow delays the relaxation response, as depicted in Fig. 2.4(a).

The pi-cell device forms a weakly splayed state due to its anti-parallel pretilt angle, as shown in Fig. 2.8(c). When applying a voltage across the device, the director transitions through states such as the asymmetric H (Ha) state, symmetric H (Hs) state, vertical (V) state and twist state (T state). The Hs state and V state are able to mitigate the backflow effects, as shown in Fig. 2.4(b), due to their symmetric structure. The Hs state, characterized by a sub-millisecond relaxation time, is ideal for fast-switching applications [46][47]. This state will be further discussed in Chapter 4.

In a HAN cell, the LC director near the homeotropic surface aligns perpendicular to the substrate, while the director near the planar surface aligns parallel, as shown in Fig. 2.8(e). Under an applied voltage, the LC molecules near the planar side reorient to align with the

electric field direction, as shown in Fig. 2.8(f).

In addition, twisted nematic (TN) devices, as shown in Fig. 2.8(g)-(h), introduce a twist in the director configuration. In a 90° TN-LC, the director twists smoothly through 90° between the two substrates, as shown in Fig. 2.8(g). When an external voltage is applied, the director tends to align along the field direction while retaining some degree of twist, as shown in Fig. 2.8 (h). The electro-optic effect of the TN LC device was first introduced by Schadt and Helfrich [51] and later applied in the display area by Fergason [52]. Over the years, the characteristics of TN-LC devices have been extensively studied. Initially designed for amplitude modulation, TN-LC devices can be adapted for phase-only modulation and polarization insensitive operation [53]. In applications requiring phase-only modulation, researchers have developed methods to minimize amplitude modulation. For instance, placing the device between two quarter wave plates and optimizing their configurations has shown promising results [54]-[56]. For example, Martínez *et al.* proposed a configuration with a reduced mean intensity transmission variation which can produce a 2π rad phase depth with 5% mean intensity transmission variation [54]. What's more, under high driving conditions, these devices can exhibit polarization-independent properties, making them suitable for a broader range of practical applications, as further discussed in Section 5.

Super-twisted nematic (STN) configurations extend the twist angle beyond 90º, such as 180º or 270º, with larger twist forming the Grandjean state. This thesis focuses on the 180º STN LC device, typically fabricated by doping a chiral additive to a nematic LC and filled into a pi-cell or Fréedericksz cell. 20 years ago, Shu-Hsia and Chiu-Lien investigated a 180º twist STN-LC pi-cell with fast optical response time of 2.2 ms [57]. They observed the back-flow-induced optical overshoot phenomena during both the switch on and switch off processes.

However, the potential continuous phase modulation in such LC configurations was not mentioned. To better stabilize these devices in the bend state without requiring a bias voltage, Tien-Jung *et al.* proposed using polymerization processes to produce a pretilt angle estimated to be 20º [58], facilitating a rapid transition to the bend state under low driving voltages. However, higher pretilt angles reduce the range over which LCs can reorient, limiting the achievable phase modulation. To solve this, the authors varied the LC pretilt angle by controlling the ultraviolet (UV) exposure time, achieving a stabilized π-twist state with sufficient phase retardation. The resulting device demonstrated a phase retardation over 200° at a driving voltage of 1.3 V and a total response of 4.9 ms when being switched on and off between 1 V and 6 V. However, the phase modulation of this device was not continuous, but instead varied between three different states.

2.7 Polymerization

To stabilize the LC molecules within a device, UV cross-linkable monomers, known as reactive mesogens, are often dissolved into an LC host. The device is then illuminated with UV light under specific voltages, which could initiate the formation of a polymer network through polymerization. The density of this polymer network is determined by the concentration of reactive mesogens and the intensity and duration of the UV light exposure. The polymer network provides bulk anchoring, which stabilizes the LC director in a specific state. For example, with a high-concentration polymer network, if the device is fully cured in the absence of an applied voltage, as shown in **Figure 2.9**(a), the polymer network stabilizes the LC director in its “relaxed state”, maintaining this configuration even when an external electric field is applied, as shown in Fig. 2.9(b). On the other hand, if the device is fully cured under a high voltage, as shown in Fig. 2.9(c), the polymer network preserves the director in the bend state, retaining this alignment even after the external voltage is removed, as shown in Fig. 2.9(d).

The influence of polymer networks on LC properties is complex and depends on the morphology of the polymer network. Polymer stabilization alters key LC parameters, such as dielectric anisotropy, rotational viscosity and elastic coefficients. These changes, in turn, affect the device's electro-optical performance, including response time and threshold voltage. Several studies suggest that polymer networks can effectively reduce the response time and enhance the switching speed of LC devices [59]-[61]. This improvement can be attributed to several factors. First, the polymer network reduces the LC domain size (d) to the nanoscale or microscale, resulting in faster switching dynamics [62]. Second, it increases the effective elastic constants due to the strong anchoring effects at the polymer–LC interface. In particular, an increase in splay elastic constant K_{11} has been shown to significantly decrease the response time [62]. Third, the polymer network can reduce the rotational viscosity (γ_1) through weak anchoring interactions between LC molecules and the polymer network [59]. According to Eq. (1-1), the LC response time is directly proportional to the square of the layer thickness (d^2) and rotational viscosity (γ_1), while being inversely proportional to the splay elastic constant K_{11}. Therefore, reducing d and γ_1, while increasing K_{11}, leads to faster switching speeds.

However, this faster switching comes at a cost. Trade-offs include limited phase modulation range, higher operation voltage, hysteresis effects, and increased light scattering loss [63]. Interestingly, contrary findings have suggested that polymer networks can impede LC reorientation [65] and bring an increase in the viscosities and slower flow velocity [66][67], which results in longer relaxation time to some extent. For example, a comparison between a conventional pi-cell and a polymer-stabilized pi-cell with the same switchable transmission range [67] indicated that the relaxation time increased by 1.7 times in the polymer-stabilized device.

Another challenge lies in the high voltages often required for polymer-stabilized LC devices, which can limit their practical applications. For example, polymer network LCs (PNLCs) used in phase modulator designs achieve a fast decay time of 49 μs and a rise time of 21 μs but required an operating voltage of 185 V_{rms} for 2π rad phase modulation [60]. Similarly, another LC mixture with a polymer network achieved 2π rad phase modulation in 3.6 ms, but with an applied voltage exceeding 105 V [64].

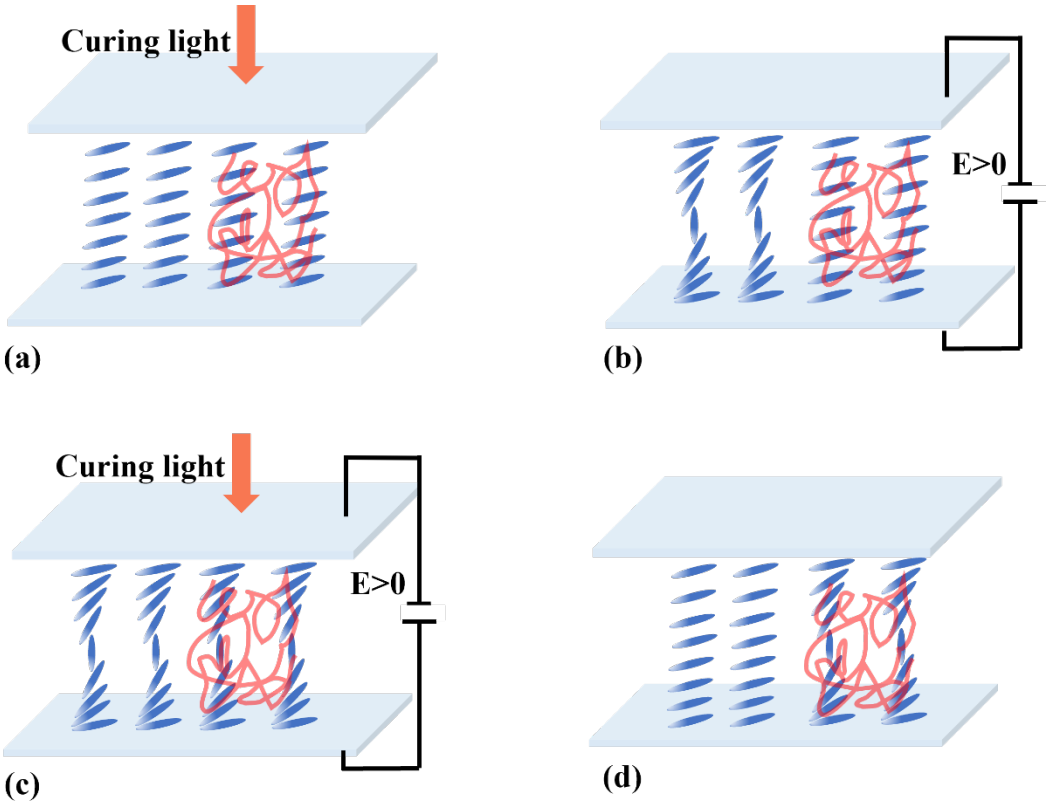

Figure 2.9. The effects of polymer network on the Fréedericksz LC device: (a) curing process under no voltage and (b) LC performance under voltage – it shows the area with dense polymer doesn't show much response to the electric field and remain in its relaxed state and (c) curing process under high voltage and (d) LC performance when the voltage is removed – it shows the area with dense polymer remains in the bend state even without external electrical field.

Polymer stabilization plays an important role in stabilizing specific LC states or configurations. For example, polymerizing without voltage application can enhance the lifetime of the Hs state [68]. In ferroelectric LCs (FLCs), polymer networks help reduce unfavourable geometric defects appearing in pure FLCs, improving vital parameters including

contrast ratio, viewing angle, rotational viscosity, and spontaneous polarization [69]. Additionally, polymer networks have been used in uniform lying helix (ULH) structures to avoid unwinding caused by dielectric coupling, surface interactions, or phase transitions [70]. Polymer stabilization techniques hold significant potential for advanced applications; however, it is essential to thoroughly investigate the effects of polymer networks on LC parameters and their influence on the electro-optical properties of different modulator configurations, considering the diverse impacts they may have.

2.8 Chiral Nematic Liquid Crystal Phase Modulators

Flexoelectro-optic (FEO) chiral nematic LCs have the merits of fast-switching speed and continuous phase modulation owing to analogue control of the tilt angle of the effective optic axis. Flexoelectricity in LCs was first proposed by Meyer in 1969 [71], which describes the relationship between curvature strains and electric polarization in LCs. This concept was further developed by Patel and Meyer with the realization of a linear flexoelectro-optic effect in short pitch chiral nematic LCs. In 1994, Rudquist and colleagues extended this work by incorporating dielectric coupling into the analysis [72]. The FEO effect occurs when an electric field is applied perpendicular to the helical axis of the LC. Under this condition, the optic axis is deflected away from the unperturbed helical axis within a plane, making it suitable for use as an optical phase modulator [29]. The response time of the FEO effect can reach the order of hundreds of microseconds for short-pitch chiral nematic LCs (<500 nm) [73].

The FEO effect is typically observed in a geometry known as the Uniform Lying Helix (ULH), where the helical axis is parallel to the plane of the substrate, as shown in **Figure 2.10 (a)**. In conventional ULH devices, electrodes are transverse, which generates an electric field perpendicular to the substrates. The effective optic axis in a ULH is parallel to the substrate,

and the applied voltage deforms the helical structure, producing a macroscopic rotation of the optic axis orientation within the plane of the LC cell, as shown in Fig. 2.10 (b) and (c). This optic axis rotation has been extensively studied under an external electric field [74]. The optical axis tilts inward when the electric field is applied in one direction and tilts outward when the field is reversed. The corresponding directors change are plotted in Fig. 2.10 (d) - (f).

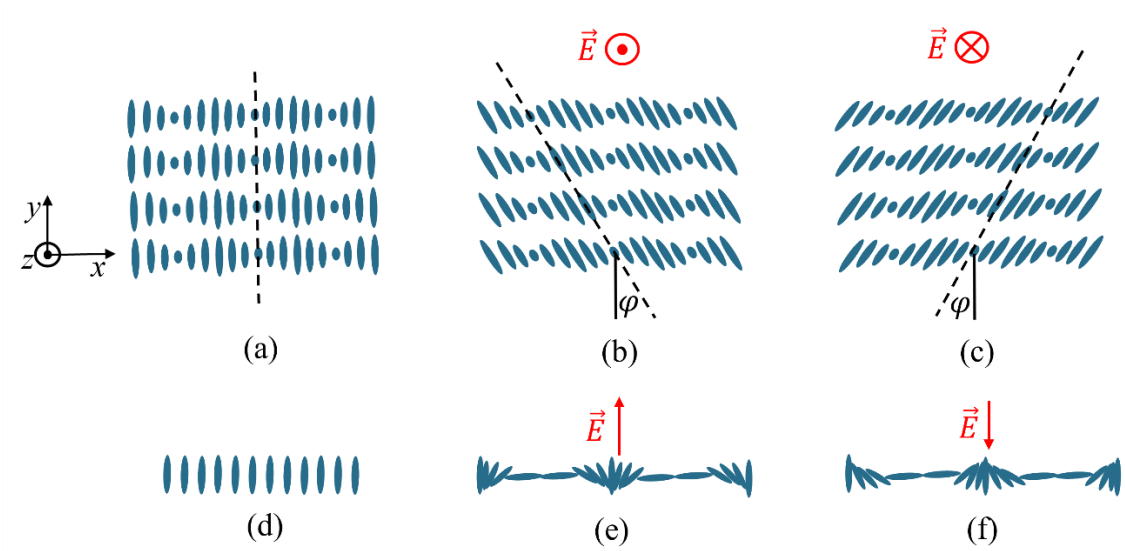

Figure 2.10. The illustration of FEO effect in ULH device. View from the top: (a) no voltage applied and the helical axis is along *x*-direction and (b) voltage applied out of the page (+*z* direction) and causes the directors to rotate by an angle of φ and (c) voltage applied into the page (-*z* direction) and causes the directors to rotate by an angle of -φ. The director structure along the dotted line in (a) - (c) are plotted in (d) - (f): (d) all directors behave same and (e) and (f) show the splay-bend pattern but with opposite direction, which results in a flexoelectric polarization [74].

The tilt angle Φ of the optic axis can be calculated as:

$$\mathrm{Tan}(\Phi) = \frac{e_f}{K}\frac{Ep_0}{2\pi} \qquad (2-35)$$

where E is the applied electric field, K is the effective elastic constant defined as $K = \frac{K_{11}+K_{33}}{2}$, with K_{11} and K_{33} representing the splay and bend elastic constants of the LC director, respectively. e_f is an effective flexoelectric constant and $e_f = \frac{e_1-e_3}{2}$, where e_1 and e_3 are the splay and bend flexoelectric coefficients introduced by Meyer, and p_0 is the equilibrium helical pitch of the LC.

The flexoelectric effect is inherently tied to the free energy density of the system, as it describes how the electric polarization ($\vec{P}_f$) arises from curvature strains in the LC director. The free energy density related to flexoelectric polarization can be written as:

$$f_{flexoelectric}(\vec{n}) = -\vec{P}_f \cdot \vec{E} \qquad (2-36)$$

where $\vec{P}_f$ is defined in terms of the LC director field and the associated gradients:

$$\vec{P}_f = e_1\vec{n}(\nabla \cdot \vec{n}) + e_3(\nabla \times \vec{n}) \times \vec{n} \qquad (2-37)$$

Optical phase modulation based on the FEO effect can be achieved by placing a ULH device between two quarter waveplates in a transmissive configuration or using a reflective configuration with a mirror. In the reflection configuration, when the optic axis tilts by an angle of Φ under an applied voltage, the resulting optical phase modulation is four times the tilt angle, Φ. This relationship has been verified both theoretically using Jones matrices and experimentally through direct measurement of tilt angles and phase modulation [75][76]. To achieve a full 2π rad optical phase modulation, the LC tilt angle needs to be more than ± 45º, ideally at low applied voltages and room temperature.

Studies have demonstrated that the flexoelectric properties of the LC compound CBC7CB can achieve a tilt angle of ± 45° in polymer stabilized ULH chiral nematic LCs, with an electric field of 4.5V/μm and sub-millisecond electro-optic switching times [77]. Similarly, another study proposed a design by filling the LC mixture of CBC7CB and chiral dopant R5011 in a 5 μm-thick ULH mode cell. This device dynamically achieved a tilt angle of ± 54° at voltages up to ± 25V at 106°C [75], and tilt angles of ±45° at ±85 V at 108°C driven by a 1 kHz waveform [76]. While both devices demonstrated full 2π rad phase modulation and fast electro-optic response, their high operating voltages and temperatures pose significant challenges. Moreover, maintaining stable alignment in these devices is difficult, and strategies

such as polymer stabilization have been proposed to address this issue.

In summary, the FEO effect offers promising opportunities for high-speed, continuous optical phase modulation, and is typically implemented by positioning the device between quarter-waveplates to function as an optical phase modulator. Its practical application requires addressing challenges such as high operating voltages, elevated temperatures, and alignment stability.

2.9 Smectic Ferroelectric Liquid Crystals

Smectic ferroelectric liquid crystals (FLCs) are another class of LC that hold significant potential for optical phase modulation, particularly due to their super-fast response time of the order of μs. FLCs exhibit a so-called bookshelf structure, as shown in Fig. 2.1, where the molecules are organized into smectic layers, and within each layer, the molecules generally align in the same direction unless influenced by external forces. In recent years (around 2017–2020), scientists discovered ferroelectric behavior in nematic LCs, and molecules in ferroelectric nematic LCs (N_F) are aligned in the same general direction (called the director) but do not form layers. This N_F phase does not have any spontaneous polarization, but presents macroscopic polarization. In this section, we will focus exclusively on the former smectic FLCs.

In 1974, Meyer demonstrated that chiral smectic C and smectic H liquid crystals possess ferroelectric properties, including spontaneous polarization [26]. Later, Clark and Lagerwall presented the surface-stabilized smectic C (SSSC) geometry, which exhibits two distinct polarization states corresponding to opposite ferroelectric polarizations. These states are associated with different LC director orientations and can be switched rapidly under an external electric field. The dynamic switching process between these two states demonstrates sub-

microsecond electro-optic responses, making FLCs highly suitable for fast applications [78]. This rapid switching is driven by the strong coupling between the applied electric field and the spontaneous polarization. However, this switching mechanism is inherently binary, allowing only two distinct phase states, which significantly limits its applicability for analogue phase modulation in advanced optical systems. To overcome this limitation, two established theoretical approaches have been proposed for achieving continuous phase modulation with FLCs: the ferroelectric twisted smectic (FETS) structure and the distorted helix ferroelectric (DHF) effect.

The FETS structure was proposed by Pertuis and Patel in 1993 [79]. In this design, FLCs are incorporated into a twisted configuration, where the rubbing directions on the two alignment surfaces are perpendicular to each other. This results in a gradual twist of the molecular orientation from one surface to the other. When an electric field is applied, the twisted structure reorients toward a switched state. This reorientation enables continuous changes in light transmission, which suggests that with suitable modifications, the FETS structure could be used as a phase modulator capable of both fast switching and continuous phase modulation. However, practical implementation and optimization of the FETS structure for phase modulation remain areas for further research.

The DHF effect relies on smectic FLCs with very short pitch, where the smectic layers adopt a “bookshelf” arrangement, and the helical axis aligns parallel to the device surface [80]-[82]. Because the helix pitch is much smaller than the spacing between the two substrates, the structure is largely free from surface-induced distortions. When an electric field is applied across the device, it interacts with the spontaneous dipole moment in each molecular layer. This interaction deforms the helical structure, which results in a change in the effective orientation

of the optic axis and, consequently, the birefringence. As a result, the DHF structure can be positioned between two quarter waveplates, offering the potential for continuous phase modulation while maintaining a fast-switching speed.

Both the FETS structure and the DHF effect demonstrate the feasibility of achieving analogue phase modulation with FLCs, which addresses the limitations of binary phase modulation inherent in conventional FLC configurations. However, further advancements are needed to optimize these designs for practical applications, including improved alignment techniques, reduced operating voltages, and enhanced stability under various environmental conditions.

2.10 Summary

In summary, this chapter serves as a general introduction to the theoretical and practical aspects of LCs and their applications in optical phase modulation, covering the key physical properties and numerical modelling techniques. It began by introducing the characteristics of LCs, emphasizing the significance of the order parameter and its relationship to temperature during phase transitions. Next, the elastic properties and continuum theory were discussed, which describes deformations of the LC director field using three deformations: splay, twist, and bend. These elastic properties were then integrated with the electric properties of LCs, including the concept of dielectric energy and the critical electric field required for director reorientation, known as the Fréedericksz threshold. Together, these models establish an understanding of how external forces influence LC configurations.

Following this, the director model and the finite difference method were introduced as numerical tools for simulating the equilibrium configurations of LC under various conditions.

The director distribution can be obtained by solving the equations iteratively. This chapter then explored the optical properties of LCs, particularly focusing on birefringence, which is a direct result of the anisotropic optical dielectric permittivity of LCs. This enables the LCs to modulate the phase and polarization of light. Jones matrix formalism was introduced as a mathematical tool for describing the interaction of polarized light with anisotropic LCs.

Finally, the chapter provided an overview of LC-based optical phase modulators, with particular attention to devices based on nematic LCs. In addition, the chapter introduced two other types of LC-based optical phase modulators—those utilizing chiral nematic LC and ferroelectric smectic LCs—highlighting their distinct features and potential uses.

3. Dynamic Phase Measurement Systems

In the chapter, we investigate various optical phase measurement techniques used for evaluating the optical phase modulators during our experiments. Firstly, we provide a literature review of widely used phase measurement methods in the introduction, establishing a theoretical foundation for our work. Following this, this chapter presents two well-designed measurement systems, including detailed working principles and corresponding optical phase data extraction methods. This detailed clarification ensures a clear understanding of the approaches that were used to accurately assess the performance of optical phase modulators in various experimental conditions**.**

3.1 Introduction

To evaluate the optical phase modulator devices and technologies outlined in Section 2.1, it is of great necessity to measure the phase modulation in the time domain, which requires an accurate investigation of the optical phase modulation and dynamic switching capability of the designed spatial light modulators (SLMs). Several methodologies have been developed to achieve high accuracy in phase measurement, with particular attention to reducing environmental sensitivities like vibration and air turbulence. In this chapter, we mainly discuss three different methods to determine the phase modulation experimentally: 1) rough assessment based on the optical transmission behavior between crossed polarizers, which is introduced in Section 3.2; 2) diffraction-based methods, such as the Ronchi grating [83][84]; 3) interference methods based on Michelson or Mach-Zehnder interferometers, together with phase-shifting interferometry [85][86].

The first approach involves deducing an approximate value of the phase modulation by

measuring the transmission response when the device is placed at a 45º angle between two orthogonally oriented polarizers. The transmission curves obtained in this configuration are directly influenced by the optical properties of the liquid crystal (LC) device. A particular advantage of this setup is that it allows the simultaneous utilization of a microscope, enabling the real-time observation of the dynamic state transformations occurring within the device. By analysing these transmission curves, we can make preliminary predictions about the LC device's potential optical phase modulation performances and ensure that the corresponding response is indeed produced by the specific states of interest. This method provides a convenient and efficient means of assessing the device's capabilities before proceeding to more complex phase measurement procedures. Consequently, it was employed as an initial evaluation step in our testing of the LC device, as detailed in Section 3.2.

Moreover, several studies have optimized this transmission-based measurement for the dynamic characterization of LC devices [87][88]. For instance, this approach can be used to characterize the dynamic phase retardation and optic-axis orientation of birefringent devices, such as a LC device. For example, Fells *et al.* (2018) presented a measurement setup [87], as shown in **Figure 3.1**. In this arrangement, a laser emits linearly polarized light, which is converted to circular polarization after passing through a quarter-wave plate (QWP) set at ±45°. The circularly polarized light then passes through the device under test (DUT), whose phase retardation, $\delta(t)$, and optic-axis angle, $\varphi(t)$, vary over time due to an applied modulation. An output polarizer (P2), rotated to different angles, θ, analyses the modified polarization, with the resulting intensity detected by a photodetector. The detected intensity, expressed by Eq. 3-1, is related to the phase retardation of the DUT.

$$S(\theta, t) = \frac{1}{2} S_0 \left[1 + \sin\big(\delta(t)\big) \sin\big(2\theta - 2\varphi(t)\big)\right] \tag{3-1}$$

By sampling the intensity at multiple angles and times, $\delta(t)$ and $\varphi(t)$ can be extracted, providing time-resolved data on the DUT's birefringent behaviour. This system successfully characterized a chiral nematic LC device in the uniform lying helix (ULH) mode at a fast-switching frequency of 3 kHz, providing precise time-resolved measurements at high speeds. Building on this, O'Neill *et al.* (2019) [88] addressed the issue of alignment quality in measuring the flexoelectro-optic effects of chiral nematic LC using a similar measurement setup. Together, these studies underscore the potential of the transmission-based method in developing dynamic phase measurement systems. It can be accurate and resilient to alignment imperfections, with broad applications in the field of high-speed optical phase characterization for birefringent devices.

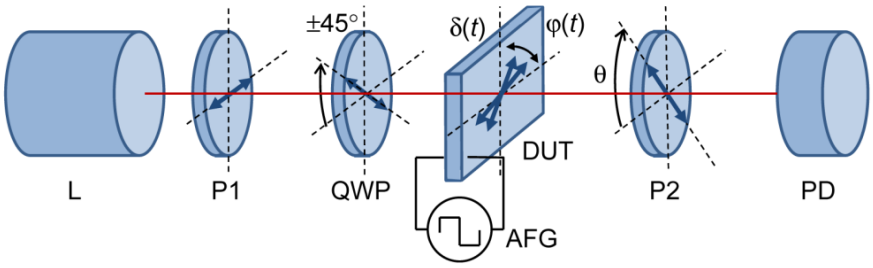

Figure 3.1. A schematic of the transmission-based measurement in [84]. L: Laser, P1: input polarizer, QWP: quarter-wave plate (on a motorized rotation mount), DUT: device under test, AFG: arbitrary function generator, P2 output polarizer (on a motorized rotation mount), PD: photodetector.

Diffraction-based methods are another effective approach for optical phase calibration and measurement [83][84][89]. In these techniques, patterns such as Ronchi gratings or binary amplitude masks are projected onto the LC modulator, and the resulting diffraction pattern is analysed. Phase information is extracted from the intensity variations of the diffraction orders, which are related to the phase modulation, as illustrated in Eq. 3-2 and 3-3.

$$I_0 \propto cos^2\left(\frac{\delta}{2}\right) \tag{3-2}$$

$$I_1 \propto sin^2\left(\frac{\delta}{2}\right) \tag{3-3}$$

For example, Zhang *et al.* (1994) [84] employs a Ronchi grating pattern projected onto a liquid crystal television (LCTV) panel to analyse phase modulation through diffraction intensities. By examining the diffraction orders, the authors were able to quantify phase shifts introduced by the LCTV, providing a straightforward calibration method that is sensitive to changes in modulation depth. In addition, Ronchi grating methods are particularly useful in the optical phase calibration and dynamic calibration for SLMs. For instance, Otón *et al.* proposed to employ the use of Ronchi gratings to measure the intensities in the diffraction pattern at the Fourier plane at a frame rate of 205 Hz [83]. By analysing the intensity of the diffraction orders, phase shifts can be identified: maximum intensity occurs for phase shifts that are multiples of π rad, while minimum intensity appears for phase shifts that are multiples of 2π rad.

Both studies highlight the versatility of Ronchi gratings as a practical and robust tool for measuring phase shifts in LC devices, as well as the phase calibration. However, it can be influenced by factors such as the specific design parameters of the gratings, variations in the light source, and the sensitivity of the detection system. These factors may introduce systematic errors or calibration uncertainties that need careful consideration.

The third method, based on interferometry, is a well-developed approach for measuring phase variations. The basic schematic of interferometry is shown in **Figure 3.2**. The light from the laser is split into two beams by a beam-splitter. The two beams then pass through two arms of unequal length in the interferometer, where each is reflected by a mirror separately before being recombined at the beam splitter. The combined beam is then received by the photodiode. The electric field, E, can be expressed as:

$$E = A(t)\cos(\omega t + kd_1) + B(t)\cos(\omega t + kd_2) \tag{3-4}$$

The intensity, I, is proportional to the time-averaged square of the electric field E, and can be expressed as:

$$I = \frac{(A(t))^2}{2} + \frac{(B(t))^2}{2} + A(t)B(t)\cos\big(k(d_1 - d_2)\big) \tag{3-5}$$

where ω is the angular frequency of the light, k is the wave number, d_1 and d_2 represent the distance of the two paths, respectively, kd_1 and kd_2 are the continuous phase produced by the distance, and $A(t)$ and $B(t)$ are the amplitudes of the two beams.

From Eq. 3-5, received intensity is the sum of the self-intensity contributions of the two beams and an interference term that depends on the phase difference ($k(d_1 - d_2)$). Therefore, by placing the device in one arm, the signal received by the photodiode, in principle, can be used to extract the phase information. However, this setup has several disadvantages, including inherent ambiguities, the need for precise alignment, and sensitivity to environmental vibrations, all of which may introduce measurement errors.

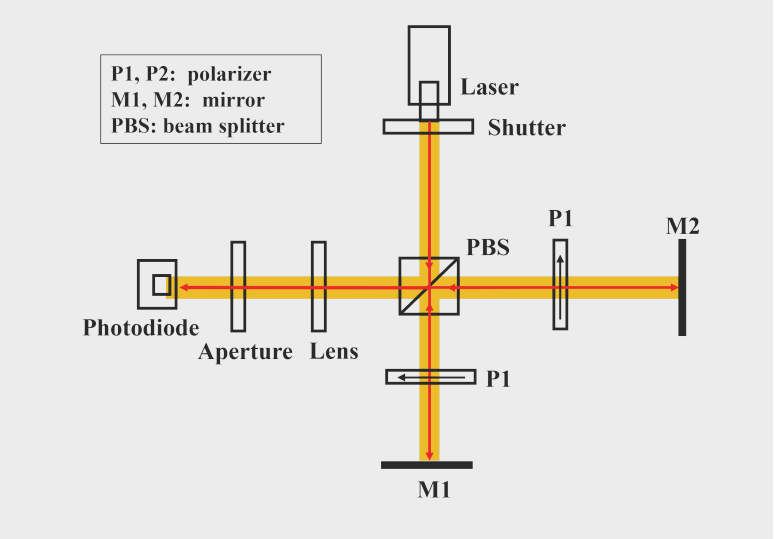

Figure 3.2. A schematic of the Michelson interferometer.

In this work, we focused on a highly precise technique known as phase-shifting interferometry (PSI), which accurately determines phase information while mitigating

environmental effects and has a high resolution. PSI has emerged as one of the most widely used methods for high-resolution phase measurement, which offers accuracy better than 1/100 of the wavelength used [85][90][91]. This technique has been extensively employed in applications such as surface profiling, wavefront sensing, and optical metrology, where precise measurements of distance, surface shape, or refractive index variations are critical.

PSI is constructed based on traditional interferometry but introduces a key refinement: the phase of one of the interfering beams is systematically varied linearly over time, which allows multiple interference patterns to be recorded [85][91]-[93]. These patterns contain the necessary information to determine the optical phase modulation. It can be accomplished by several methods to obtain the phase shift with known increments. One of the most commonly used involves the translation of a mirror with a piezoelectric transducer (PZT) [85]. The PZT can move one of the mirrors in the interferometer with a precision speed and position control, thereby generating a changing interference pattern. For example, Jin *et al.* proposed introducing a phase lag by using a PZT-mounted mirror in one path, while placing the LC device under investigation at switching rates of 1 kHz in the other path as the signal beam [86]. The resulting interference pattern, which contains both the incremental phase shift and phase modulation information, is recorded and converted into an intensity signal by a photodiode. The optical phase modulation can then be computed smoothly and precisely from the recorded data. However, the periodic nature of the moving mirror's control system imposes a limitation on the continuity of the signal.

Several studies have proposed various refinements of PSI for optical phase measurement. Another alternative method was proposed in [94], wherein the authors constructed a system based on a Homodyne Michelson interferometer to dynamically measure the phase in the time

domain. Two acousto-optic frequency shifters (AOFSs) introduce precise phase shifts between the signal and reference beams, resulting in a carrier frequency signal (200 kHz) through their interference. These phase shifts are synchronized using RF signal generators and controlled to modulate the phase incrementally. The recorded intensity variations are processed using a quadrature demodulation scheme, which extracts phase data encoded in the carrier signal. Digital signal processing is applied to refine and smooth the extracted phase information, ensuring high precision in phase measurement.

There are several algorithms used to determine the phase information in PSI, such as the phase-stepping method (PSM) [92], and Fast Fourier Transform (FFT) method [93][95]. When two plane waves interfere, the interferometer can be adjusted to produce an interference pattern in the form of vertical fringes:

$$I_n = I(1 + m\sin[kx + \delta(P) + n\Delta]) \tag{3-6}$$

where I_n is the intensity of the nth picture, I is the illuminating intensity, m is the modulation index, k is the spatial frequency, $\delta(P)$ is the phase change, caused by the change in the measured quantity P, and Δ is the angle of each phase step.

To extract the phase information, at least three measurements of the intensity distribution at different phases are required. With the evolution of the phase-stepping method, several algorithms for phase calculation have become popular [92]. The most widely used is the four-step algorithm with a phase step of 90º. The phase modulation, δ, can be calculated as:

$$\delta = \tan^{-1}\left(\frac{I_1 - I_3}{I_2 - I_4}\right) \tag{3-7}$$

where I_1, I_2, I_3 and I_4 are the intensities at the phase shifts of 0º, 90º, 180º and 270º, respectively (with numerator $I_1$and I_3 correspond to the sine component, and the denominator I_2 and I_4 correspond to the cosine component). In the numerical implementation, the $arctan2$

function was employed instead of the simple $\tan^{-1}$ to ensure correct phase determination across all four quadrants.

In addition, applying the FFT to the recorded interference signal is also a widely used technique to obtain phase modulation with a high resolution. It is because the data can be obtained in one shot, and FFT is able to process a large amount of the captured interference data. This quick data capture avoids the influences of the background noise and unwanted errors. The application of this method will be detailed in Section 3.4.

In summary, precisely measuring the continuous phase modulation of LC phase modulators in the time domain is essential yet challenging for the development of next-generation SLM technologies. In this chapter, we discuss three methods developed for the work here. The first, based on a transmission measurement, is simple and convenient, allowing for simultaneous observation under a microscope. Following this, I propose two more advanced techniques based on PSI that provide more accurate phase measurements in the time domain. One method involves placing a rotating half-waveplate between two quarter-wave plates to produce a phase ramp with a period of 4 seconds, detailed in Section 3.3. This setup employs the 4-step algorithm to extract the corresponding phase modulation in the time domain. The second approach uses an acousto-optic frequency shifter (AOFS) to introduce a 40 MHz phase shift in one path, with phase modulation extracted using a FFT method, as explained in Section 3.4. Both PSI-based methods offer precise ways to measure dynamic phase shifts in the time domain.

3.2 Transmission Measurement

As an indirect evaluation of optical phase modulation, the transmission-based method includes

two approaches: the one using a microscope to measure the transmission and another employing a laser as the light source.

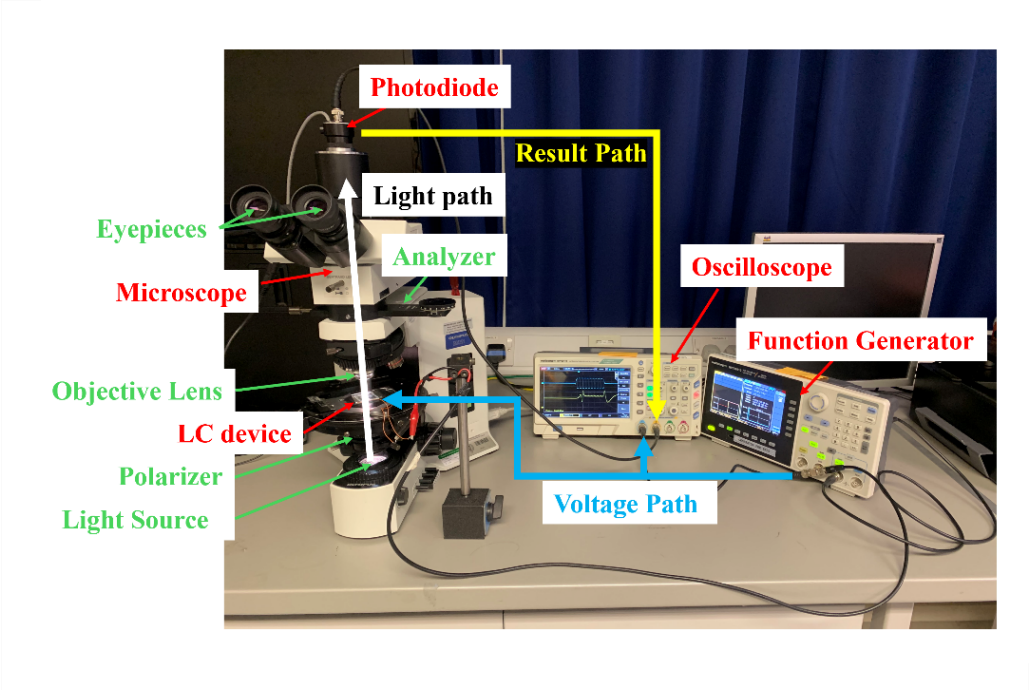

Figure 3.3. Experimental setup for real-time observation and optical phase evaluation using a transmission-based method. The halogen light source comes from the bottom of the microscope and passes through a polarizer to illuminate the liquid crystal (LC) device. The light then travels through an analyser, where optical transmission is captured by a photodiode connected to the microscope. This transmitted signal follows the Result Path (yellow) to an oscilloscope for monitoring. An external function generator supplies the designed voltage waveforms, controlling the LC device and allowing direct observation of transmission curves on the oscilloscope via the Voltage Path (blue). The microscope's eyepiece enables real-time observation of the LC states, providing simultaneous visual information that aids in correlating the optical transmission measurements with the physical state changes in the LC device.

The first setup, as shown in **Figure 3.3**, consists of a microscope, a function generator as well as an oscilloscope. Light from the microscope passes through the LC device, which is placed between the crossed polarizers, with the analyser and polarizer of the microscope set perpendicular to each other. The LC device is modulated and controlled by the external voltage waveforms from the function generator. The transmitted light is received by a photodiode placed at the top of the microscope, and the resulting signal is displayed on the oscilloscope. This arrangement allows us to observe the LC device's real-time performance and assess its

optical characteristics directly from the oscilloscope readings.

The transmission of light through the LC device placed between two crossed polarizers is expressed as:

$$T = \sin^2(2\chi) \cdot \sin^2\left(\frac{\pi \Delta n_{eff} d}{\lambda}\right) \tag{3-8}$$

where χ is the rotation angle of the optic axis relative to the polarizer, Δn_{eff} is the effective birefringence of the LCs, d is the cell gap, and λ is the wavelength of light.

When the LC device is placed at a 45º angle between two orthogonally positioned polarizers, χ equals to 45º, causing the $\sin^2(2\chi)$ term to equal 1. This simplifies the transmission equation to

$$T = \sin^2\left(\frac{\pi \Delta n_{eff} d}{\lambda}\right) \tag{3-9}$$

In this configuration, the transmission behaviour of the LC device is determined solely by the second *sine* function. The phase difference δ between the ordinary and extraordinary waves is given by:

$$\delta = \frac{2\pi d \Delta n_{eff}}{\lambda} \tag{3-10}$$

Thus, the argument of the *sine* function in the transmission equation becomes $\frac{\delta}{2}$. The transmission can then be expressed as:

$$T = \sin^2\left(\frac{\delta}{2}\right) \tag{3-11}$$

This means that the transmission behaviour varies periodically with δ, repeating every increase of 2π rad in δ, corresponding to a full phase modulation cycle. Therefore, between two adjacent peak points in the transmission curve, the phase difference δ changes by 2π rad, indicating a 2π rad phase modulation. This relationship allows phase modulation to be estimated by analysing the transmission characteristics as a function of time or voltage.

For example, for the LC modulator discussed later in Chapter 4, our goal is to detect the optical phase modulation of the symmetric H (Hs) state in the LC device. Since the Hs state is transient and exists only for a few milliseconds, it is crucial to confirm that the measured phase corresponds specifically to this state. To ensure this, we measure the transmission while simultaneously observing the LC device's behaviour under the microscope using the setup in Fig. 3.3. This dual approach enables us to verify that sufficient phase modulation has been achieved and that it indeed corresponds to the Hs state before placing it into a more accurate phase measurement system where the internal state cannot be directly observed.

Figure 3.4 (a) presents the waveform of the voltage applied to the LC device. The driving voltage is a burst driving voltage designed to induce the Hs state. It begins with a priming stage, where a 1 kHz square wave at 10 Vrms is applied continuously for 5 ms to initialize the device. During this stage, the voltage remains unmodulated, facilitating the transition of the device from the splay state to the Hs state. This is followed by a modulation stage, in which the driving signal alternates between 1 ms "on" and 1 ms "off" periods. This cyclic on-off driving signal enables the formation of the transient Hs state. Finally, the relaxation stage ensues, during which no voltage is applied, allowing the device to return to its ground state (splay state).

Figure 3.4(b) illustrates the corresponding transmission curve during this voltage sequence. According to theory and Eq. (3-11), the phase difference (δ) changes by 2π rad when the transmission curve completes a full cycle, indicating a full 2π rad phase modulation. During the initial 5 ms priming stage, the transmission curve exhibits more than one full cycle before stabilizing. This suggests the device transitions from the splay state to the Hs state, with an estimated optical phase modulation of approximately 2.4π rad during the priming stage. After this, the device enters the modulation stage, where the voltage alternates between "on" and

"off" for 1 ms. Finally, during the relaxation stage, the device gradually reverts to the splay state.

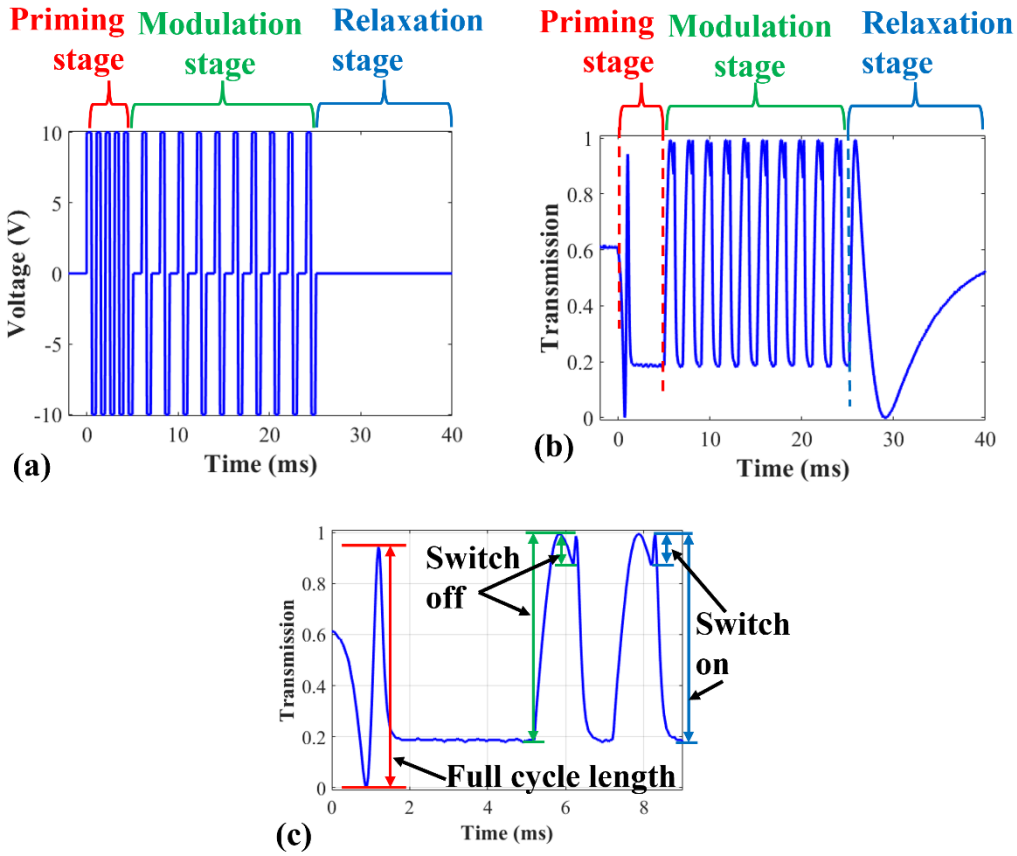

Figure 3.4. The voltage waveform and corresponding transmission curve for a Hs device. (a) An illustration of the burst driving voltage with the amplitude of 10 Vrms and (b) the corresponding normalized transmission curve and (c) the zoomed-in figure of (b) containing only 2 modulations (note: the driving frequency during the burst is 1 kHz).

Figure 3.4(c) provides an enlarged section of the transmission curve in Fig. 3.4(b) during the 1 ms "on" and "off" periods in the modulation stage. The switch-off process (marked in green) and the switch-on process (marked in blue) each span approximately half the length of the full cycle observed during the priming stage. This corresponds to a phase shift of approximately π radians, demonstrating the phase modulation characteristics of the Hs state in 1 ms scale. This behaviour aligns with the expected phase modulation during the voltage-off period, as detailed in Chapter 4.

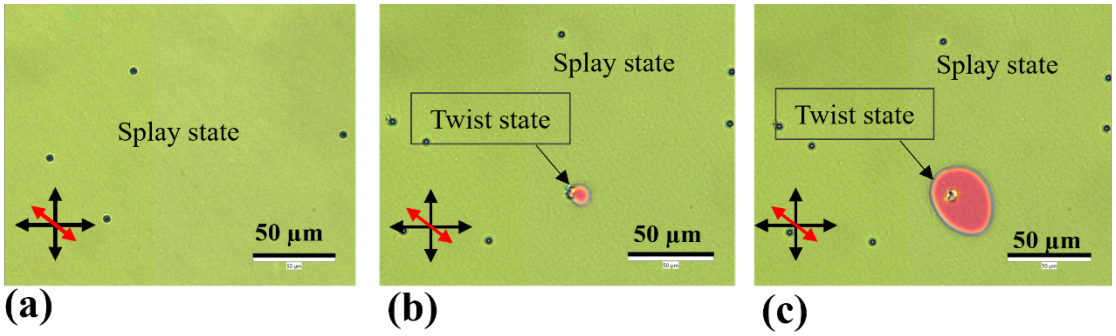

Figure 3.5. Representative polarizing optical microscope (POM) images of switching states in a nematic pi-cell under the burst driving voltage. (a) the splay state of the device under no applied voltage (the black dots in the image are the spacer beads distributed throughout the cell to obtain a unform cell gap). (b, c) The switch off state of the device, where the V state relaxes to T state (the pink area) while Hs state relaxes to the H state (the green area). In (b), the formation of the V state is observed under a burst voltage of 10 Vrms for 25 ms, and (c) demonstrates the growth of the V state under a repeating burst voltage of 10 Vrms for 50 ms. The transformation of states mentioned is shown in Fig. 3.6. The crossed double-headed black arrows represent the orientations of the transmission axes of the polarizer and the analyzer, and the double-headed red arrow represents the rubbing direction of the alignment layers.

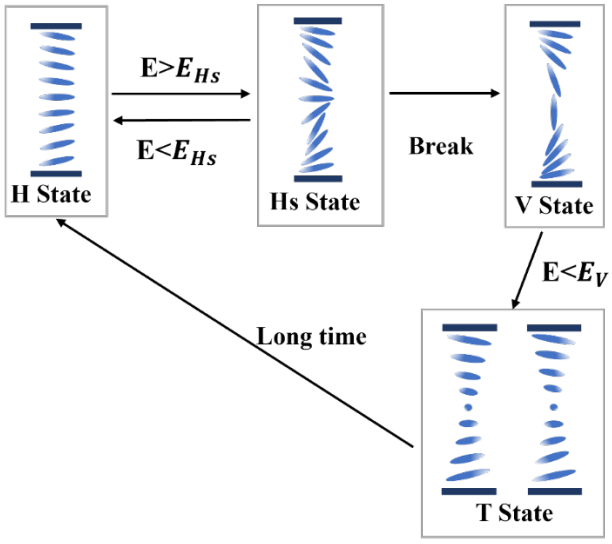

Figure 3.6. The switching states of a nematic pi-cell. An illustration showing the transitions of a nematic pi-cell under different electric field conditions.

Figure 3.5 presents the performance of the LC device observed under the microscope during this period. Fig. 3.5(a) represents the ground state of the device, while Fig. 3.5(b) and (c) depict the device in mixed states including the splay states and twist states (T state) during the voltage off period. This can indicate the presence of the Hs state and V state during the

voltage-on period. Capturing an image of the transient Hs state is challenging due to its short duration; however, by analysing the state transformations observed during the switch-off, we can confirm its presence. **Figure 3.6** illustrates the states transition about Hs state happened in pi-cell under different conditions. After Hs transitions to the V state, the device requires several seconds to relax back to its ground state. In Fig. 3.5(b) and (c), we could distinguish the appearance of V state by observing the shrinking area when we switch off the voltage.

This combination of transmission measurements and microscopic observations allows us to directly correlate the optical behaviour with the physical state changes within the device. Based on these observations, we conclude that the device could achieve about π rad phase modulation in 1 ms under 10 Vrms using the Hs state and is ready to be measured in the optical phase measurement system for precise quantitative analysis. This transmission method is particularly significant when measuring devices with complex and transient states, where we may be unsure which states contribute to the observed phase modulation in the setup. By combing the transmission measurement with the microscopic observations, we obtain solid verification of the states involved.

The second setup used to measure transmission employs a laser as the light source to provide a more accurate evaluation of the optical phase modulation, compared to the bright light used as light source in the previous setup. Using a laser offers several advantages, including a coherent and monochromatic light source with a well-defined wavelength, which is critical for precise phase modulation measurements. As shown in **Figure 3.7**, light from the laser (IEC 60825-1:2014, wavelength = 635 nm, continuous wave) passes through a polarizer and then through the LC device, which encodes phase information onto the light. Subsequently, the light passes through a second polarizer, placed perpendicularly to the first and known as

the analyser, before being detected by a photodiode.

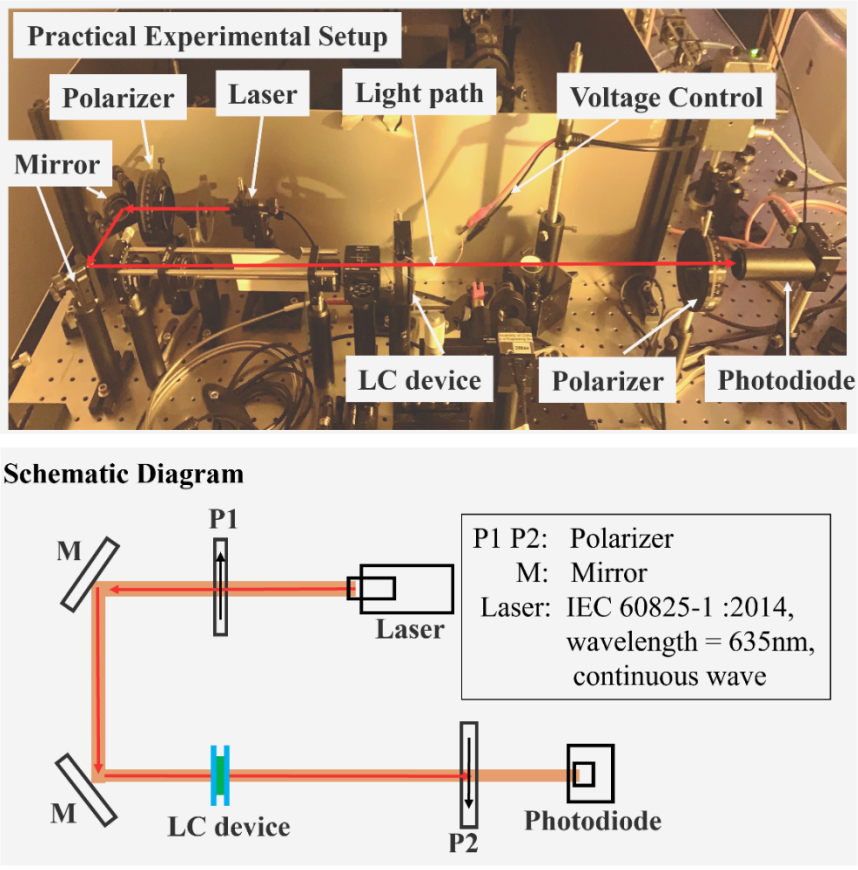

Figure 3.7 Experimental setup and schematic diagram for laser-based transmission measurement of the LC device. The upper panel shows the practical experimental setup, where a laser source emits the light that is directed by two mirrors and passes through the LC device. It then passes a second polarizer, positioned perpendicularly to the initial polarizer, before reaching the photodiode for detection. An external function generator provides voltage control of the LC device. The lower panel presents a simplified schematic of the optical layout, illustrating the light from the laser, through the mirrors, polarizers, LC device, and finally to the photodiode.

The LC device is controlled by a function generator that can be managed by an external PC to apply continuously increasing voltage increments, producing the desired waveform. This setup allows us to obtain the transmission behaviour in both the time domain and the voltage domain. To be specific, this setup allows us to obtain the transmission in the time domain, analysing the dynamic phase modulation of the LC device. The transmission-time behaviour can quickly provide us with an estimate of the phase modulation. Additionally, the arrangement can also determine the response of an LC device to a slowly increasing voltage. The transmission-voltage curve can then be measured to confirm the device thickness and other

relevant parameters. The advantage of this method lies in its simple alignment and more accurate simulation of the practical optical phase modulation due to the laser light source, providing a better evaluation of the device as well as phase performance.

For example, when a pi-cell is placed in the setup and the burst driving voltage is applied to the device, as shown in Fig. 3.4(a), a transmission-time curve can be obtained, similar to that depicted in Fig. 3.4(b). The received intensity I can be described by Eq. 3.8, and the phase modulation is related to this intensity, as indicated in Eq. 3.11. According to the evaluation method described above, the optical phase retardation δ of the device changes by a full 2π rad radians when the transmission goes through the full cycle. Theoretically, this setup allows for a more accurate evaluation of the phase modulation of the pi-cell compared to the first setup. However, it does not provide insight into the internal performance of the LC device.

Notably, this setup can be used for voltage-domain measurements, which could provide crucial information about the device's response to varying voltages. For instance, a continuous square waveform with a frequency of 1 kHz was applied to the device, with the voltage gradually increasing from 0.1 Vrms to 5 Vrms, as shown in **Figure 3.7**(a). An enlarged section of this waveform is presented in Fig. 3.7(b). The external PC controlled the function generator to increment the voltage in specific steps. We also sent the received signal to the PC, which allows us to plot the voltage-transmission curve, as shown in Fig. 3.7(c), and compared it with the simulation results (the simulation methodology will be discussed in Section 4.3). By adjusting the LC layer thickness parameter in the simulation to match the experimental data, we are able to determine that the practical thickness of the LC layer in the device is approximately 3.73 μm. As can be seen from Fig. 3.7(c), the simulated results are consistent with the measured transmission-voltage curve, validating our simulation model and providing

confidence in the accuracy of the device parameters used. In addition, the phase modulation can be determined as voltage increases, based on Eq. (3-11). As the voltage approaches infinity, the phase is set to 0 rad. The voltages corresponding to phase shifts of π and 2π rad can also be identified at the highest and lowest point of the curve. This indicates that the device has the potential to achieve a maximum phase modulation of 8 rad. Furthermore, as the voltage increases from 0 to 1.2 V (the bottom point of the curve), the phase shift is estimated to be approximately 1.72 rad.

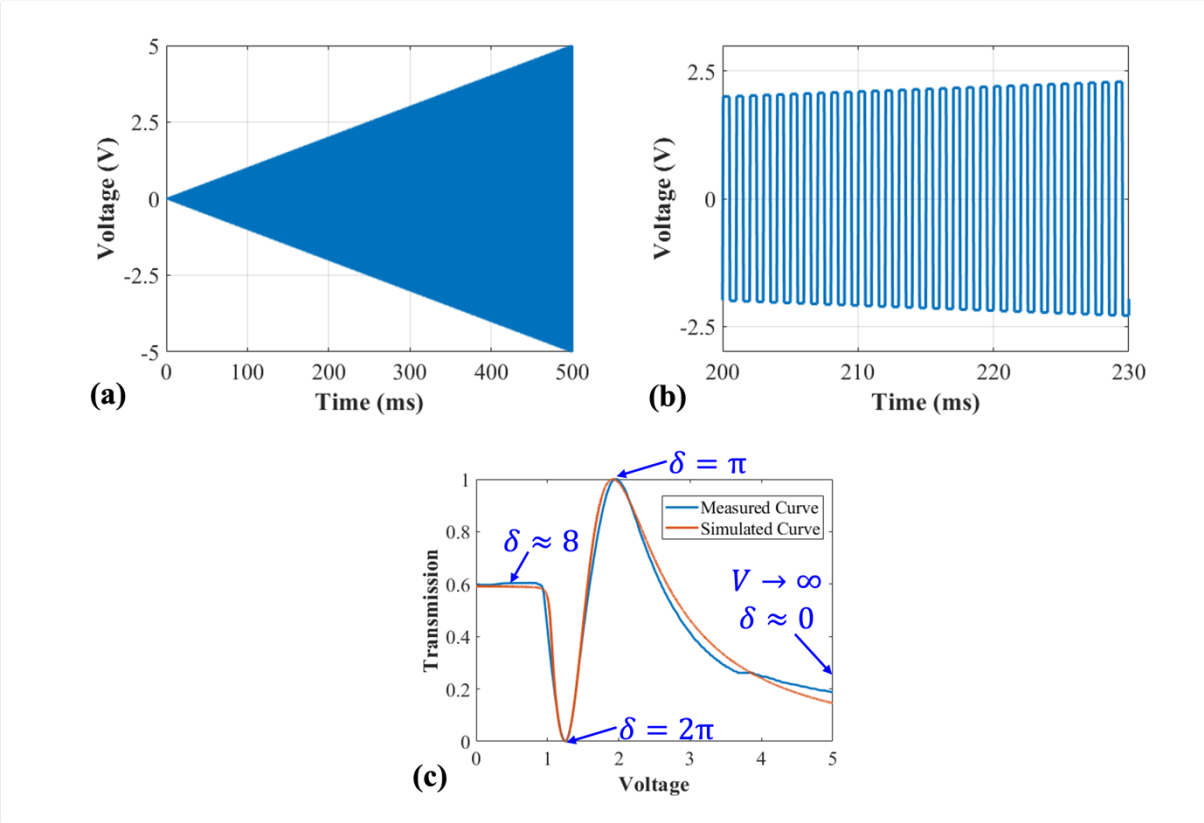

Figure 3.7. Voltage-transmission results measured by placing the nematic LC pi-cell at 45° relative to two orthogonally aligned polarizers: (a) the waveform of the applied continuous square wave with a frequency of 1 kHz and continuously increasing amplitude from 0 to 5 Vrms; and (b) enlarged section of (a) and (c) corresponding transmission result in a normalized form.

In conclusion, both methods provide an estimation of the phase modulation of the LC device using relatively simple experimental setups. The primary advantage of the microscope-based setup is that it enables simultaneous microscopic observation of the LC device's

performance while predicting its phase modulation. The second method is advantageous because it combines the precision of laser-based measurements with straightforward experimental setup and alignment. By using a laser light source, we minimize errors due to chromatic dispersion and incoherence, which are common when using broad-spectrum light sources. Therefore, the first microscope-based setup is more suitable when microscopic observation is required; if observation under a microscope is not necessary, the second method provides more accurate results, which is essential for the estimation of the device thickness in practical applications.

While this transmission-based phase estimation method is simple and straightforward, it has certain limitations. It cannot provide a precise quantitative value of the phase modulation because it relies on indirect estimation via light transmission. Moreover, this method is generally applicable only to simple devices with planar switching, where the LC director reorients uniformly in a single plane. In devices with more complex switching mechanisms or non-uniform director profiles, this approach may not accurately reflect the true optical phase modulation. Therefore, when precise quantitative data are required, a more accurate phase modulation measurement system is necessary, and the results from this indirect evaluation should be interpreted with caution. Therefore, this method is most suitable for preliminary testing, which requires the simplicity and direct visual confirmation as the purpose.

3.3 Phase-shifting Twyman Green Interferometer

In this section, we introduce a newly designed phase-shifting interferometry technique, which was designed to enhance measurement accuracy while minimizing the impact of environmental factors such as vibrations and air turbulence. By systematically varying the phase using a rotating half-wave plate and capturing multiple interference intensities at different phase shifts,

we can accurately and efficiently reconstruct the optical phase modulation of the device under test. This design not only improves the overall precision of phase measurements but also enables robust and repeatable results even in less-controlled environments.

Figure. 3.8 depicts the design of the phase-shifting Twyman Green interferometer, which is a modified form of the Michelson interferometer optimized for optical testing. Light from a helium–neon laser with a wavelength of 632.8 nm (Thorlabs, HNL050L) passed through a neutral density filter to reduce its intensity and then entered a non-polarizing beam splitter, which divided the light into two paths: the signal path and the reference path. The LC device under test was placed in the signal path and driven by a function generator (Multicomp PRO, MP750510). By applying a suitable voltage driving waveform, as illustrated in **Figure 3.9**(a), the device exhibited a continuous optical phase response. This phase modulation is represented through intensity modulation, as shown in Fig. 3.9(b), with the relationship between phase modulation and intensity described by Eq. 3-11. Specifically, the device was driven into the desired state, with the phase modulated in 1 ms pulses repeated every 1 second. This phase modulation was then encoded onto the signal beam, which allows us to extract the LC device's dynamic phase modulation in the time domain.

In the reference path, a half-wave plate was placed between two quarter-wave plates. This half-wave plate was smoothly rotated using a motorized rotation stage (Thorlabs, PRM1Z8/M), rotating it by 90° over a period of 4 seconds. This rotation produced a continuous phase shift in the reference beam, resulting in a 2π rad phase shift period over 4 seconds, illustrated in Figure 3.9(c). By introducing a known and controllable phase shift in the reference arm, we effectively implemented phase-shifting interferometry, which is essential for precise phase measurements. A Jones matrix approach is used below to illustrate the optical phase-

shifting behaviour of the reference path, which could demonstrate how mechanically rotating the half-wave plate between two quarter-wave plates produces a continuous phase ramp. This theoretical framework supports our experimental design and aids in interpreting the interference patterns obtained.

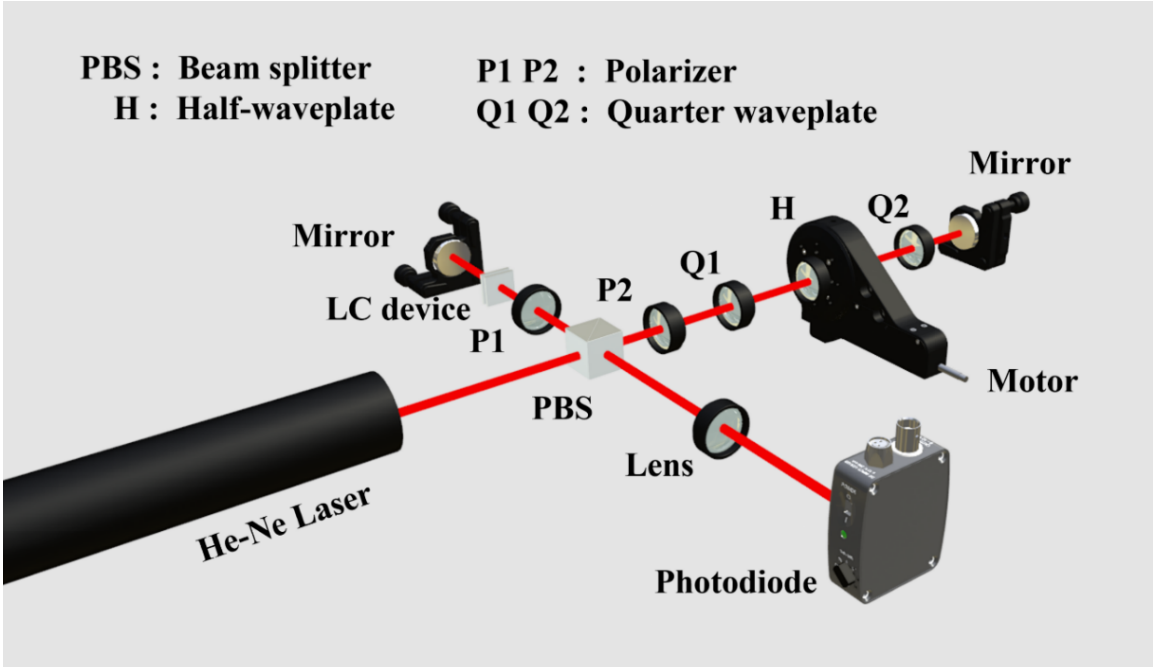

Figure 3.8. A phase-shifting Twyman Green interferometer was used to measure the optical phase modulation. One path of the interferometer contained the LC device to produce the phase delay to be measured, while the other path included two quarter-wave plates and a rotating half-wave plate to produce a continuous phase ramp.

The optical field, E'_{out}, at the output of a single optical path—comprising a polarizer (P2), a quarter-wave plate (Q1) oriented at $\frac{\pi}{4}$, a rotating half-wave plate (H) at an angle φ, and another quarter-wave plate (Q2) also at $\frac{\pi}{4}$ - can be expressed using Jones matrix formalism:

$$\mathbf{E'_{out}} = \mathrm{Q_2}\left(\frac{\pi}{4}\right)\ \mathrm{M}(\varphi)\ \mathrm{Q_1}\left(\frac{\pi}{4}\right)\ \mathrm{P}\ \mathbf{E_{in}} \tag{3-12}$$

where $\mathbf{E_{in}}$ is the Jones vector of the input light, which is linearly polarized along the vertical direction.

The matrix $\mathrm{M}(\varphi)$ represents the rotating half-wave plate and is given by:

$$\mathrm{M}(\varphi) = \mathrm{R}(-\varphi)\,\mathrm{H}\left(\frac{\pi}{2}\right)\,\mathrm{R}(\varphi) \tag{3-13}$$

where:

- $\mathrm{R}(\varphi)$ is the rotation matrix accounting for the rotation of the optical axis by an angle φ: $\mathrm{R}(\varphi) = \begin{pmatrix} cos\varphi & sin\varphi \\ sin\varphi & -cos\varphi \end{pmatrix}$
- $\mathrm{H}\left(\frac{\pi}{2}\right)$ is the Jones matrix of a half-wave plate: $\mathrm{H}\left(\frac{\pi}{2}\right) = \begin{pmatrix} \cos\left(\frac{\pi}{2}\right) & -\sin\left(\frac{\pi}{2}\right) \\ \sin\left(\frac{\pi}{2}\right) & \cos\left(\frac{\pi}{2}\right) \end{pmatrix} = \begin{pmatrix} 0 & -1 \\ 1 & 0 \end{pmatrix}$
- $\mathrm{Q1}(\frac{\pi}{4})$ and $\mathrm{Q2}(\frac{\pi}{4})$ are the Jones matrices for the quarter-wave plates oriented at $\frac{\pi}{4}$ relative to the vertical axis: $\mathrm{Q}_1\left(\frac{\pi}{2}\right) = e^{-i\frac{\pi}{4}}\begin{pmatrix} 1 & 0 \\ 0 & i \end{pmatrix}$
- P is the linear polarizer: $\mathrm{P} = \begin{pmatrix} 1 & 0 \\ 0 & 0 \end{pmatrix}$
- $\mathbf{E_{in}}$ represent the vertical polarized incident light: $\mathbf{E_{in}} = \begin{pmatrix} 1 \\ 0 \end{pmatrix}$

Multiplying out the terms in Eq. (3-12) and assuming that all components are ideal (lossless and perfectly aligned), the output field simplifies to:

$$\mathbf{E'_{out}} = \mathbf{E_{in}}\, e^{j2\varphi}\,. \tag{3-14}$$

This result indicates that the effect of the rotating half-wave plate, sandwiched between the two quarter-wave plates, is to introduce a phase shift of 2φ to the optical field.

In the reference path of the interferometer, the light passes through these components, is reflected by a mirror, and then passes through them a second time, effectively doubling the optical path and the phase shift. The optical field, $\mathbf{E_{out}}$, at the output after this double-pass is given by:

$$\mathbf{E_{out}} = \mathbf{E_{in}}\, e^{j4\varphi}\,, \tag{3-15}$$

This demonstrates that rotating the half-wave plate by an angle φ results in a phase shift of 4φ in the reference beam.

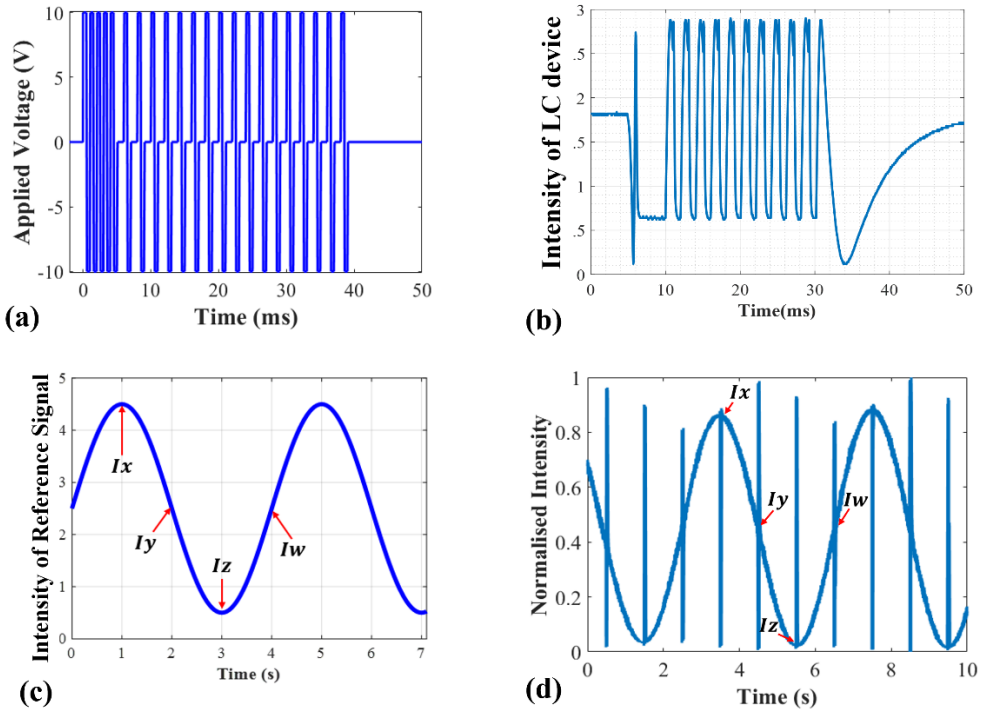

Figure 3.9. The interference signal of an LC device. (a) The burst driving voltage applied to the LC device, consisting of a 40 ms operating period repeated every 1 second. (b) The phase response of the LC device, represented by its intensity. (c) The phase shift introduced by the rotating half-wave plate, illustrated through intensity variations in the reference wave. (d) The interference pattern resulting from the combination of the reference wave and the signal wave, which reflects the phase response of the LC device.

The continuous rotation of the half-wave plate produces a continuous phase ramp in the reference wave. In our study, rotating the half-wave plate by 90° per second results in a total phase shift of 360° (or 2π rad). This generates a full cycle in the interference signal with a period of 4 seconds, as illustrated in Fig. 3.9(c).

The light from the two paths of the interferometer were then re-combined by the beam splitter to generate an interference signal that was recorded by a photodiode (Thorlabs,

PDA36A-EC, Si Amplified Detector 350 - 1100 nm). The interference signal results are from the superposition of the two beams: one containing the phase modulation introduced by the LC device (modulated every 1 second) and the other containing the continuous phase shift from the rotating half-wave plate (with a period of 4 seconds). Within each "period" of the reference wave there are four places where the phase shift from the burst driven applied on the device can be observed. With an analogue-to-digital (A2D) converter, the received light intensity can be acquired, shown in Fig. 3. 9(d).

The interference light signal received by the photodiode can be expressed as:

$$E = A(t)\cos(\omega t + kt) + B(t)\cos(\omega t + \delta(t) + \Delta), \tag{3-16}$$

and the resulting intensity can be expressed as:

$$I = \frac{(A(t))^2}{2} + \frac{(B(t))^2}{2} + A(t)B(t)\cos(kt + \delta(t) + \Delta) \tag{3-17}$$

where ω is the angular frequency of the light, k is the effective wave number of the phase shift in the reference light wave, kt represents the continuous phase shift produced by the rotating half-wave plate, $\delta(t)$ is the phase modulation induced by the LC device, Δ represents the optical path difference between the two arms and the environmental influences, both of which are poorly defined and can vary over time (e.g., due to minor air movement etc.), $A(t)$ is the amplitude of the reference beam path and is near constant, and $B(t)$ is the amplitude of signal light beam, which has a residual amplitude modulation caused by the LC device. In expressing the resulting intensity, it is assumed that we can ignore components at optical frequencies – this will then be the signal from the photodiode.

Our goal is to extract the phase modulation δ(t), introduced by the LC device. However, the term, $kt + \Delta$, needs to be known, which can be challenging as Δ is non-measurable and will deteriorate the accuracy of the phase results. To avoid this issue, we utilize the **four-step**

phase-shifting algorithm, which is a widely adopted technique in interferometry [82][89]. By using known phase shifts between successive intensity measurements, it provides a robust means of calculating the unknown phase difference caused by the sample under test. This approach is particularly useful in our setup because it mitigates the impact of environmental disturbances and uncertainties in the optical path length.

By selecting four specific time points where the phase term, $kt + \Delta$, takes on known values—specifically, nπ and $\frac{\pi}{2} + n\pi$ (with n being an integer) — we eliminate the dependence on Δ. These points correspond to phase shifts where the cosine function simplifies, allowing us to solve for δ(t) without knowledge of Δ. Within each 4-second period of the reference wave, there are four instances where the phase condition, $kt + \Delta$, are equal to $n\pi$, $\frac{\pi}{2} + n\pi$, $\pi + n\pi$, and $\frac{3\pi}{2} + n\pi$ rad. The intensities at these four points are labelled I_x, I_y, I_z, and I_w in Fig. 3.10(d), corresponding to phase shifts of:

$kt + \Delta =$ nπ:

$$I_x(t) = \frac{A(t)^2}{2} + \frac{B(t)^2}{2} + A(t) \cdot B(t) \cos\big(\delta(t)\big) \tag{3-18}$$

$kt + \Delta = \frac{\pi}{2} +$ nπ:

$$I_y(t) = \frac{A(t)^2}{2} + \frac{B(t)^2}{2} - A(t) \cdot B(t) \sin\big(\delta(t)\big) \tag{3-19}$$

$kt + \Delta =$ π + nπ:

$$I_z(t) = \frac{A(t)^2}{2} + \frac{B(t)^2}{2} - A(t) \cdot B(t) \cos\big(\delta(t)\big) \tag{3-20}$$

$kt + \Delta = \frac{3\pi}{2} +$ nπ:

$$I_w(t) = \frac{A(t)^2}{2} + \frac{B(t)^2}{2} + A(t) \cdot B(t) \sin\big(\delta(t)\big) \tag{3-21}$$

By combining the four intensity measurements, as shown in **Figure 3.10**(a), with an enlarged section shown in Fig. 3.10(b), the optical phase modulation, $\delta(t)$, can be extracted using the following equation:

$$\delta(t) = \arctan\left[\frac{I_w(t)-I_y(t)}{I_x(t)-I_z(t)}\right] \tag{3-22}$$

where I_x, I_y, I_z, and I_w represent the intensity at the four chosen points. The extracted optical phase modulation result is shown in Fig. 3.10(c) with an enlarged section shown in Fig. 3.10(d).

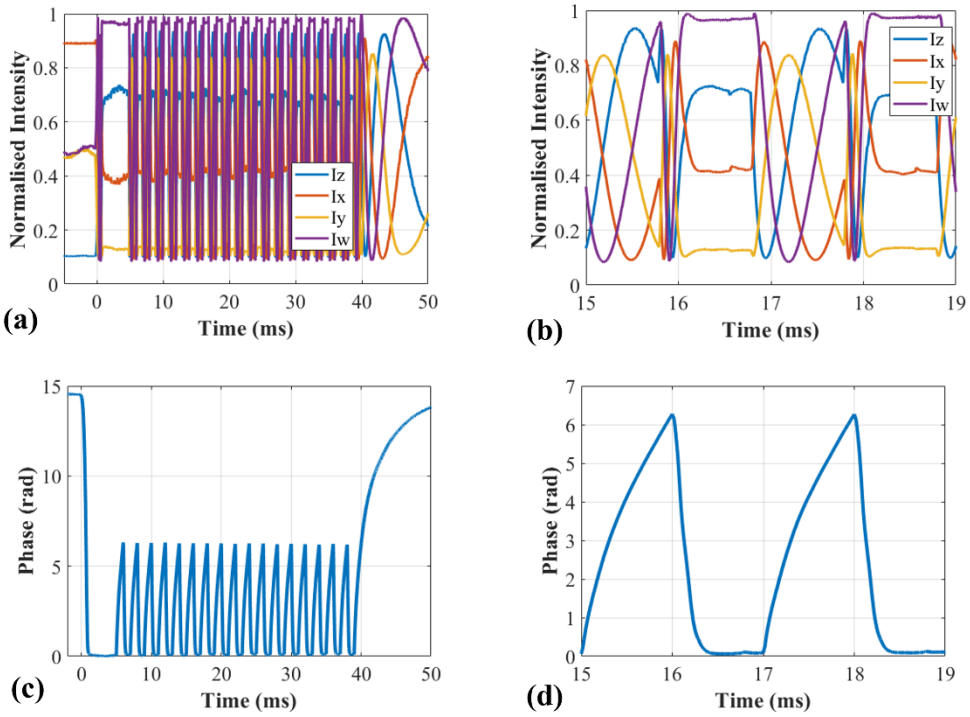

Figure 3.10. Extracting the phase modulation of an LC device. (a) The extracted signal at four specific positions (I_x, I_y, I_z, and I_w) along the phase ramp shown in Fig. 3.9(d). (b) The enlarged section of (a) from 15 ms to 19 ms. (c) The extracted phase modulation result calculated using Eq. (3-22), and (d) the enlarged section of (c) from 15 ms to 19 ms.

By utilizing the four-step phase-shifting algorithm, we effectively eliminate the dependence on the unknown optical path difference Δ, which also contains the unwanted environmental influences, leading to an accurate phase modulation. Besides, this method also eliminates the dependence on any common-mode fluctuations in the amplitudes A(t) and B(t), which further enhances the accuracy. This method allows us to accurately determine the phase

modulation $\delta(t)$ with high precision. The precise timing and synchronization with the phase shifts introduced by the rotating half-wave plate are crucial for the accuracy of the measurements. The data acquisition method ensures that the intensity measurements are captured at the exact moments corresponding to the required phase shifts of nπ and π/2+nπ rad. This synchronization enables the correct application of the phase extraction algorithm and minimizes errors due to environmental disturbances.

It should also be clarified that any intensity fluctuations introduced by small errors in the retardation of the half-wave plate are minimal, owing to the careful selection of the waveplate used. Additionally, the measured amplitude modulation of the LC device is below 4% in our experiments. Therefore, neither of these factors causes a significant error in the calculation of the phase modulation.

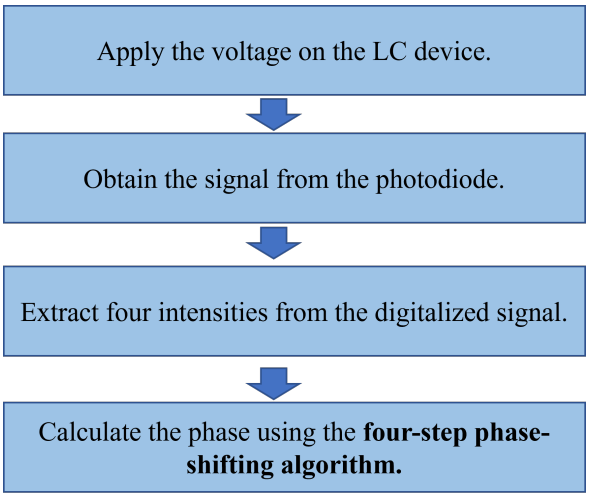

Figure 3.11. The experimental procedure for using a phase-shifting Twyman Green interferometer to measure the optical phase modulation.

Figure. 3.11 illustrates the entire experimental process. We begin by applying the designed voltage waveform (Fig. 3.9(a)) to the LC device using a function generator. This waveform modulates the phase of the light passing through the LC device (Fig. 3.9(b)), which

encodes the phase information onto the signal beam. The rotating half-waveplate in the reference path provides a continuous phase shift with period of 4s, (Fig. 3.9(c)), which was exemplified above using the Jones matrix approach. The photodiode detects the interference signal resulting from the superposition of the signal and reference beams in the interferometer (Fig. 3.9(d)). The digitized data corresponds to the intensity measurements labelled as I_x, I_y, I_z, and I_w. These specific intensity points are chosen according to the four-step phase-shifting algorithm, occurring at known phase shifts introduced by the rotating half-wave plate. After acquiring these intensity measurements (Fig. 3.10(a)-(b)), we apply Equation (3-24) to extract the phase modulation $\delta(t)$ introduced by the LC device (Fig. 3.10(c)-(d)).

In summary, in this section, we adopted a rotating half-wave plate placed between two quarter waveplates to introduce a continuous phase shift in the interferometer aiming to mitigate the impact of minor vibrations and air movement. This approach enhances the stability and accuracy of the phase measurements by providing a smooth and controlled phase shift that is less susceptible to environmental disturbances. This phase-shifting interferometer was utilized for the precise measurement of the switched symmetric H (Hs) state in a nematic pi-cell. The measured results are discussed in Chapter 4 and reported in my published paper [96].

3.4 Phase-shifting Mach–Zehnder Interferometer

In this section, we begin the development of another phase-shifting interferometer, the phase-shifting Mach–Zehnder interferometer, a very useful tool for measuring optical phase changes with high precision. The Mach–Zehnder interferometer is a well-established instrument in optical physics and engineering, renowned for its simplicity and versatility in analysing wavefronts and detecting phase variations. By integrating a phase-shifting methodology into

its design, we enhance its capability to perform accurate dynamic phase measurements, which are essential in applications such as optical metrology, telecommunications, and adaptive optics.

Figure 3.12 illustrates the full assembly of the phase-shifting Mach–Zehnder interferometer used in our experiments. Light from a helium–neon laser (Thorlabs, HNL050L) emitting at a wavelength of 633 nm serves as the coherent light source. A non-polarizing beam splitter divides the laser beam into two paths: the signal path and the reference path. In the signal path, the beam passes through the LC device under test, which is placed between two parallel polarizers. The LC device modulates the phase of the transmitted light in response to an applied voltage, provided by an external function generator (Multicomp PRO, MP750510). This applies a periodic burst driving voltage to the LC device, as illustrated in **Figure 3.13**(a). By applying this waveform, the device is driven into an appropriate state, with phase modulation occurring in 1 ms pulses repeated every 1 s.

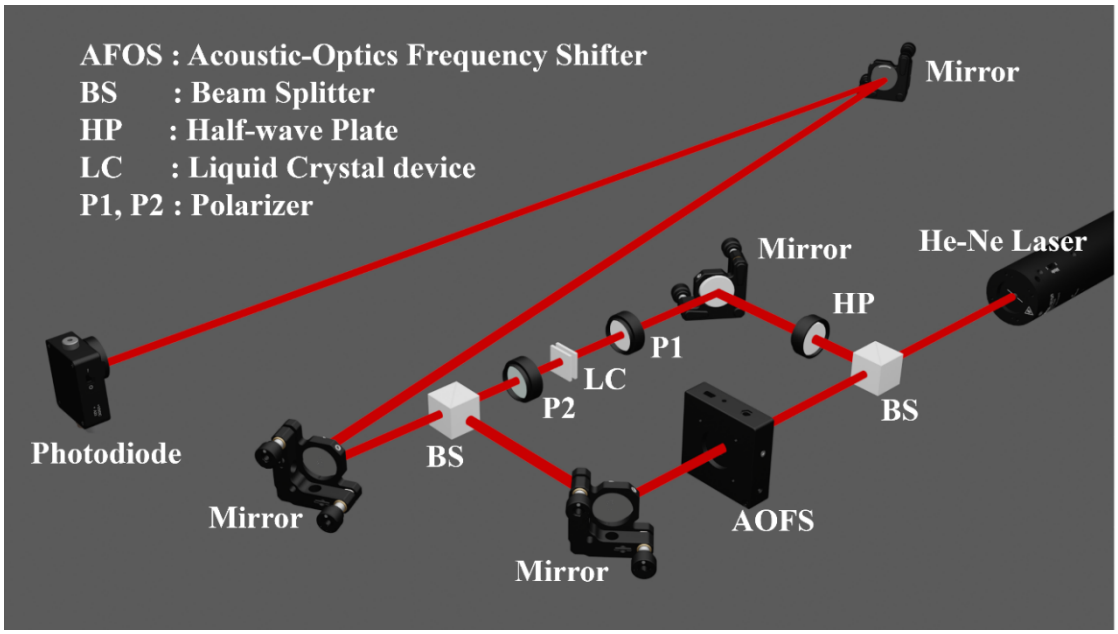

Figure 3.12. A schematic of the phase-shifting Mach–Zehnder interferometer used to measure the phase modulation. One path of the interferometer contained the LC device to produce the phase delay to be measured, and a half-wave plate to rotate the polarization to match that produced by the AFOS placed in the other path to produce a 40 MHz continuous phase shift.

In the reference path, an Acousto-Optic Frequency Shifter (AOFS) introduces a controlled frequency shift of 40 MHz to the reference beam. Operating on the acousto-optic effect, the AOFS diffracts the incoming light using sound waves propagating through an optical crystal, resulting in a frequency shift and, consequently, a phase shift in the diffracted light. By driving the AOFS with a 40 MHz radio frequency (RF) signal, the phase shift is induced in the reference beam. This 40 MHz driving signal, with its continuous phase shift, serves as a reference phase modulation for the phase extraction process, as illustrated in Fig. 3.13(d). The introduced 40 MHz continuous phase shift is essential for the phase-shifting interferometry technique, since it enables rapid data collection while minimizing environmental noise and influences, thereby ensuring highly accurate phase measurement.

Notably, the AOFS splits the input beam into two distinct beams: one that retains its initial frequency and polarization state, and another that is frequency-shifted by 40 MHz. This frequency-shifted beam also exhibits a 4° tilt in its propagation direction and an orthogonal polarization relative to the original beam. To ensure that both the signal and reference paths have consistent polarization, we place a half-wave plate in the signal path, which used to align its polarization with that of the reference path. Additionally, because the AOFS splits the beam, the intensity in the reference path decreases. By using the half-wave plate in the signal path, we achieve polarization consistency without further impacting the reference intensity.

After traversing their respective paths, the signal and reference beams are recombined using a second non-polarizing beam splitter. Mirrors are strategically placed to direct the beams and ensure proper alignment. The recombined beam is then directed onto a photodiode detector (Thorlabs, DET10A/M, Si biased detector), which converts the optical signal into an electrical signal for analysis. The oscilloscope (Multicomp MP720115) is used to collect both the

received and reference signals. With its 1 GS/s sampling rate and a storage RAM capacity of 28M, it can capture the 40 MHz signal effectively. As a result, the signal received by the photodiode, as shown in Fig. 3.13(c), contains both the optical phase modulation induced by the LC device and an additional 40 MHz phase shift introduced by the AOFS.

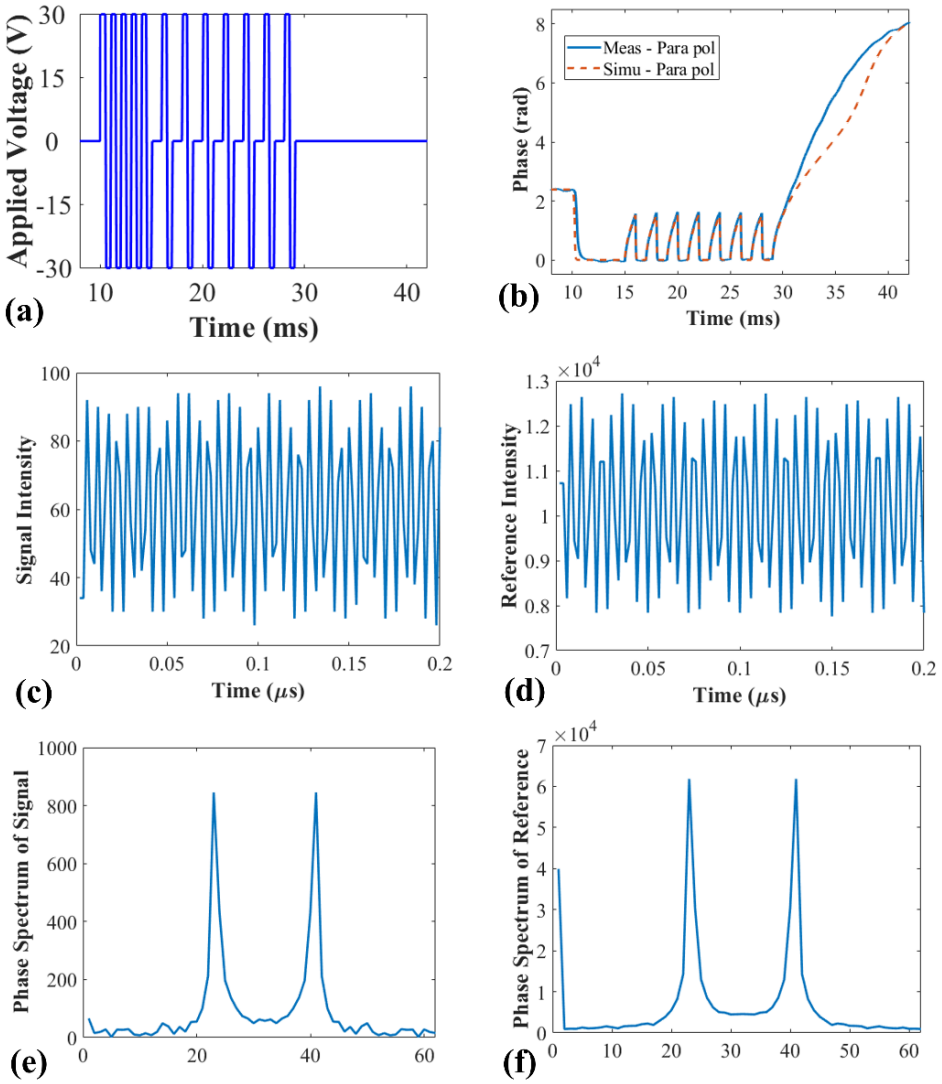

Figure 3.13. The data results during phase extraction process of the phase-shifting Mach–Zehnder interferometer. (a) The burst driving voltage applied to the LC device which consists of a 30 ms operating period repeated every 1 second. (b) Extracted experimental phase modulation using Eq. (3-25) demonstrating that the phase results are stable and show good consistency with the simulated results (the simulation techniques will be discussion in Chapter 5). (c) The intensity of the signal obtained from the photodiode. (d) The intensity of the 40 MHz driving signal as the reference signal. (e) and (f) are the spectrum of the signal and the reference data after applying FFT.

To extract the optical phase modulation information from the received signal, a Fast Fourier Transform (FFT) method was employed [93][95], which can efficiently determine the phase information from the signal by converting the time-domain signals into complex spectra in the frequency-domain. The interference signal $I(t)$ detected by the photodiode can be expressed as:

$$I(t) = I_S + I_R + 2\sqrt{I_S I_R}\cos(\delta_{LC}(t) - \delta_{AOFS}(t) + \Delta) \quad (3\text{-}23)$$

where I_S and I_R are the intensities of the signal and reference beams, respectively, δ_{LC} is the phase modulation introduced by the LC device, δ_{AOFS} is the continuous phase shift due to the AOFS with frequency of 40 MHz, and Δ is any initial phase difference due to path length differences and environmental influences.

The reference signal $I_R(t)$ collected by the oscilloscope can be expressed as:

$$I_R(t) = I_R\cos\big(\delta_{AOFS}(t)\big) \quad (3\text{-}24)$$

By performing an FFT on the time-domain interference signal $I(t)$ and the reference signal $I_R(t)$ simultaneously, as shown in Fig. 3.13 (e) and (f), we can transform both into the frequency domain, obtaining their amplitude and phase information at each frequency component. The received signal, $I(t)$, contains both the LC device's phase modulation $\delta_{LC}(t)$ and the 40 MHz continuous phase shift $\delta_{AOFS}(t)$, while the driving signal $I_R(t)$ contains a stable and continuous reference phase shift, $\delta_{AOFS}(t)$. Therefore, the phase modulation of the device is obtained by subtracting the phase of the reference signal from that of the received signal:

$$\delta_{LC}(t) = \theta_{received}(40\text{ MHz}) - \theta_{reference}(40\text{ MHz}) \quad (3\text{-}25)$$

To ensure accuracy, it is crucial to use phase unwrapping when dealing with values exceeding the [−π, π rad] range. In this work, the unwrapping was performed in MATLAB using the built-in unwrap function, which corrects for phase discontinuities by detecting jumps greater than π radians and adding or subtracting appropriate multiples of 2π rad. As a result, phase information can be efficiently extracted from the detected signals. Additionally, applying the FFT enhances the resolution of the phase modulation results by using a high sampling rate on the original data.

Extracting phase information from two waves of the same frequency with different phase shifts can also be achieved using other methods, such as data-fitting and dot product (quadrature detection). Data-fitting methods involve modelling the interference signal and reference signal and fitting them to a standard mathematical function to extract phase parameters. The interference signals *I(t)* in our case can be modelled as a sinusoidal function:

$$I(t) = A\cos(\omega t + \delta) + B \tag{3-26}$$

where A is the amplitude of the signal, ω is the angular frequency of the wave ($\omega = 2\pi f$, with f = 40 MHz in our case), δ is the phase shift we want to extract, and B is a constant offset due to background light or detector bias.

By fitting the measured interference signal to this model, we can extract the phase parameter δ along with the amplitude A and offset B. Data-fitting methods directly estimate parameters, which enables precise determination of phase shifts. They are flexible, accommodating complex signal models, and can be robust against noise and outliers with proper implementation. However, in our experiment, data-fitting is impractical due to its computational intensity. High-frequency signals like our 40 MHz interference require high sampling rates and generate large datasets, which makes iterative nonlinear fitting too time-

consuming for real-time analysis. Additionally, sensitivity to initial parameter guesses can lead to slow convergence or incorrect results, complicating the analysis and hindering the tracking of rapid phase changes introduced by the LC device.

Dot product methods, also known as quadrature detection, involve multiplying the measured signal with reference sine and cosine waves at the same frequency and integrating the results over a specific time interval to obtain the in-phase ($D_{in_{phase}}$) and quadrature ($D_{\text{quadrature}}$) components:

$$D_{in_{phase}} = \frac{2}{T}\int_{t_0}^{t_0+T} I(t)\cos(\omega t)\,dt \tag{3-27}$$

$$D_{\text{quadrature}} = \frac{2}{T}\int_{t_0}^{t_0+T} I(t)\sin(\omega t)\,dt \tag{3-28}$$

The phase shift δ is then calculated as:

$$\delta = \text{arctan2}\left(D_{\text{quadrature}}, D_{in_{phase}}\right) \tag{3-29}$$

where $I(t)$ is the measured signal, ω is the angular frequency of 40 MHz, T is the integration time, ideally an integer multiple of the signal's period ($T = N\ \frac{2\pi}{\omega}$, with N being an integer), and $\text{arctan2}\left(D_{\text{quadrature}}, D_{in_{phase}}\right)$ is the two-argument arctangent function.

The dot product method is straightforward and computationally efficient, which makes it suitable for real-time processing. It enables immediate phase calculation without requiring a transformation of the signal into the frequency domain, which is particularly advantageous when computational resources are limited or for lower-frequency applications. However, at higher frequencies like 40 MHz, the method faces significant challenges due to its reliance on precise synchronization and sensitivity to noise. These challenges become more pronounced when processing large amounts of data over extended time intervals, as completing the integration and phase extraction demands substantial computational capability.

Therefore, applying the FFT method to the phase extraction process offers significant advantages, particularly in computational efficiency and the ability to handle high-frequency signals. The entire experimental procedure is illustrated in **Figure 3.14**. We begin by applying the designed voltage waveform (Fig. 3.13(a)) to the LC device using a function generator. This waveform modulates the optical properties of the LC device, resulting in a phase modulation of the light passing through it and encoding the phase information onto the signal beam. Simultaneously, the AOFS in the reference path generates a continuous phase shift at a frequency of 40 MHz (Fig. 3.13(d)). This continuous phase shift serves as a reference phase modulation in the data extraction process. The interference between the signal beam (modulated by the LC device) and the reference beam (modulated by the AOFS) is detected by a photodiode (Fig. 3.13(c)). The resulting interference signal contains both the phase modulation from the LC device and the known phase shift from the AOFS.

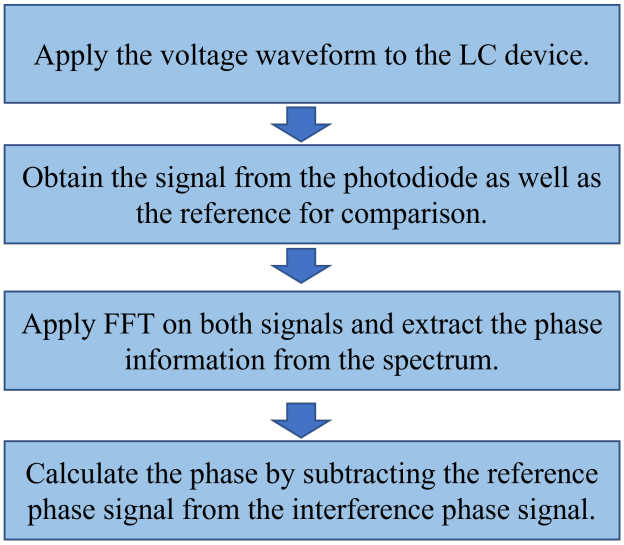

Figure 3.14. The experimental procedure of using the phase-shifting Mach-Zehnder interferometer to measure the optical phase modulation.

The interference signal is digitized by sampling it with a high-speed oscilloscope, ensuring that the sampling rate is sufficient to capture the 40 MHz modulation accurately. We then apply a FFT algorithm to both the interference signal and the reference signal, obtaining

their frequency spectra as depicted in Fig. 3.13(e) and (f), respectively. By selecting the frequency component corresponding to the 40 MHz modulation in each spectrum, we extract their phase information separately. Then, based on Eq. 3-25, we subtract the phase of the reference signal from that of the interference signal and eliminate the common phase shift introduced by the AOFS. As a result, the phase modulation $\delta(t)$ introduced by the LC device is extracted, as depicted in Fig. 3.13(b). This process allows us to accurately determine the dynamic phase changes induced by the LC device under the applied voltage waveform, which demonstrates the effectiveness of the FFT method in our phase extraction procedure.

In summary, in this section, we have discussed the use of an AOFS to introduce a continuous 40 MHz phase shift in the reference path of the interferometer for the purposes of PSI interferometry. This design enhances the accuracy by capturing the received data in a single shot, which effectively eliminates the influences of air disturbances or mechanical vibrations. Additionally, it improves the resolution of phase measurements by employing FFT for detailed phase extraction. This optical phase measurement setup overcomes limitations imposed by the length of the applied voltage on the LC device, as encountered in the interferometer setup designed in Section 3.3. It also eliminates the need for complex mechanical adjustments or stabilization techniques. With faster data acquisition and advanced phase extraction, this approach is particularly suited for applications requiring both high precision and real-time monitoring.

This interferometer was applied to measure the switched twisted symmetric H state in a STN-LC device, with the results presented and analysed in Chapter 5, which is further reported in my published paper. Xue, L., Elston, S. J., & Morris, S. M. (2025). Polarization-independent nematic liquid crystal phase modulators. *ACS Photonics*.

3.5 Summary

In this chapter, three methods have been introduced that were developed to evaluate dynamic optical phase modulation and perform accurate phase measurements of LC devices, which are essential for studying LC-based optical phase modulation devices.

In Section 3.2, we introduced a technique based on the optical transmission response of LC devices. By combining the measurement system with a microscope, we can observe the performance of an LC device in real time while measuring the optical transmission. This allows for an initial estimation of phase modulation and ensures that the measured phase corresponds to the desired states. This approach is particularly useful for capturing transient states, where LC devices change their status rapidly under applied voltages. Additionally, another transmission-based setup uses a laser as the light source, combined with external voltage control that provides precise phase steps. This setup enables accurate measurement of voltage-transmission curves, which can be used to predict the thickness of the LC layer. This method is especially valuable for estimating LC device parameters in detail by analysing its electro-optical response.

To achieve higher precision, we applied phase-shifting interferometry (PSI) to traditional Twyman Green interferometer to address environmental disturbances that affect measurement precision and to improve resolution. The PSI-based Twyman Green interferometer introduces a known phase shift in one beam path by employing a rotating half-wave plate placed between two quarter-wave plates, which creates a periodic phase shift with a 4-second period. This continuous phase variation enables the four-step phase-shifting algorithm to extract phase data accurately from interference patterns. This method significantly improves measurement accuracy by eliminating the impact of environmental factors and

residual phase offsets in the system. While this method is relatively simple and provides precise measurements, it limits the applied voltage waveform to non-continuous forms due to synchronization constraints with the fixed phase shift period. Specifically, continuous voltage modulation cannot be used, making this method unsuitable for applications requiring dynamic or continuous voltage waveforms. This method is applied to measure the optical phase modulation performance in the symmetric H state of a pi-cell LC device, which will be discussed in detail in Chapter 4.

To overcome the limitations of the PSI-based Twyman Green interferometer, we developed a PSI-based Mach–Zehnder interferometer incorporating an Acousto-Optic Frequency Shifter (AOFS). The AOFS introduces a continuous high-frequency phase shift of 40 MHz in the reference beam path, as described in Section 3.4. This setup utilizes a fast Fourier transform (FFT) method for phase extraction, enabling efficient and accurate analysis of interference signals. The rapid data acquisition provided by this method significantly eliminates the impact of environmental noise and system errors, thereby improving the accuracy of phase extraction. Additionally, the continuous phase shift generated by the AOFS enables the measurement of continuous phase modulation, effectively overcoming the voltage waveform limitations associated with the PSI-based Twyman Green interferometer. Furthermore, the ability to process large datasets using FFT ensures high-resolution phase measurements, making this method highly suitable for studying dynamic optical phase modulation. This PSI-based Mach–Zehnder interferometer was designed to evaluate the dynamic optical phase modulation performance in the twisted symmetric H state of a super-twisted nematic (STN) LC device, with detailed results presented in Chapter 5.

4. Fast Analogue 2π rad Phase Modulator Using a Pi-Cell

In this chapter, we investigate the optical phase modulation potential of a nematic liquid crystal (LC) pi-cell operating in the so-called symmetric H (Hs) state. The stability of the Hs state is limited and is obtained by employing a short burst voltage to drive the LC pi-cell into the Hs state. This is investigated by adjusting the amplitude of the applied voltage and the duration of the voltage burst. Experimental results of the optical phase modulation are obtained using a phase-shifting Twyman Green interferometer (presented in Section 3.3) and compared with results from simulations carried out using Ericksen-Leslie continuum theory. The device is able to achieve a full 2π rad phase modulation with 1 ms timescale in a reflective geometry (akin to that of a spatial light modulator), which shows excellent phase modulation capability, and the experimental results are found to be in good agreement with the results from simulations.

The work presented in this chapter has been published in the journal article: Xue, L., Jin, Y., Elston, S. J., & Morris, S. M. (2023). Fast analogue 2π phase modulation using a liquid crystal Pi-Cell. *Optics & Laser Technology,* 167, 109773.

4.1 Literature Review

The need for high performance displays [97] and image projection [98] has been a key driver in the development of LC spatial light modulator (SLM) technology for applications requiring high frame rate and analogue 2π rad phase modulation at low driving voltages [99]. For nematic LC-based SLM technologies, previous developments in this field have typically resulted in response times of the order of milliseconds, limited for the most part by the viscoelastic

response of the nematic LC [100]. To enable SLM technology to be used in a wider range of applications, it is of great significance to investigate a better performance mode. To enable SLM technology to be used in a wider range of applications, such as LiDAR and optical beam steering [101], super-resolution optical microscopy [14][102], optically probing of biological systems [103] and holography [9][15], improving the switching speed, while maintaining access to the full 2π rad range is of great necessity.

Currently, LC-based SLMs typically employ either a ferroelectric liquid crystal (FLC) or a nematic LC (NLC) to modulate the optical phase. However, both FLC and NLC technologies have their pros and cons. For example, FLC-based SLM technology exhibits a fast response time (generally of the order of sub-milliseconds), but the phase modulation is usually only binary [78][104], which requires sophisticated optical configurations to generate a continuous phase modulation [79][80]. Nematic SLM technology, on the other hand, does exhibit multi-level analogue phase modulation, but at the expense of a slower response time. Other LC modes do exist that can exhibit both fast response and analogue phase modulation, but such modes have not yet been successfully commercialized. For example, both the flexoelectro-optic effect in chiral nematic LCs and the electro-optic switching in nematic pi-cells have the potential for both fast response and full 2π analogue phase modulation.

In the case of the flexoelectro-optic effect in chiral nematic LCs, fast sub-millisecond response times can be observed when the pitch (p) of the helix is short ($p \approx 300$ - 400 nm) [29]. In the uniform lying helix (ULH) geometry, flexoelectric coupling to an applied electric field results in a tilt of the optic axis of the chiral nematic LC in the plane of the device. This rotation of the optic axis can then be manifested as a phase modulation when the LC layer is sandwiched between quarter-wave plates, as demonstrated in [105]. To observe flexoelectro-

optic switching, a ULH alignment is required when conventional transverse electric fields are employed (the electric field is aligned along the normal of the device substrates). However, the formation of the ULH alignment is nontrivial [106] and polymer stabilization is often employed to stabilize the alignment, albeit with varying degrees of success [107]. Furthermore, while analogue 2π rad phase modulation with 1 millisecond response time has been observed using this electro-optic mode, the device had to be operated at relatively high temperatures more than 100 °C [108].

Fast-switching electro-optic effects in nematic LCs can be achieved using the pi-cell configuration, which features parallel rubbed planar alignment layers. In this setup, the LC molecules are anchored as anti-parallel pretilt angles at the surfaces by the alignment layers while forming a bend-like shape in the middle region under high voltages, where they remain vertically aligned (perpendicular to the plates). This symmetric bend configuration, known as the optically compensated bend (OCB) mode or the vertical state (V-state), was first introduced by Bos and Koehler/Beran in 1984 [50]. In this arrangement, the nematic LC can achieve response times on the order of a few milliseconds or less by virtue of the symmetric LC director profile and the absence of backflow during director reorientation [50]. Its fast response times make the pi-cell particularly valuable for nematic LC display applications.

To obtain the OCB mode, a voltage exceeding a specific threshold must be applied [86][110]. However, a significant challenge arises from the topological differences between the relaxed state and the electric field-driven bend state required for OCB operation. Transitioning to the bend state involves a slow nucleation process, often requiring several seconds. Additionally, the applied voltage must be sufficiently high to maintain the bend state and prevent the LC from transitioning into the twisted state (T-state). In order to maintain the

required state, and achieve suitable response times, researchers have proposed the use of polymer stabilization [67][111]. or alternatively an increase in the pretilt angle at the substrates of the device [112][113]. However, polymer stabilization usually also results in an unwanted increase in the switching voltage, and both approaches reduce the overall range of optical phase modulation.

Pi-cell devices exhibit an array of different director configurations when subjected to an electric field and as a result can be operated in different 'modes'. One such mode that has received little attention for potential optical phase modulation applications is the transient symmetric H (Hs) state, which can be obtained by applying a sudden step increase in the voltage across a pi-cell. This potentially exhibits continuous (analogue) phase modulation together with sub-millisecond response times at moderate driving voltages [50][114]. It also exhibits a symmetric LC director profile, which avoids backflow during director reorientation. These characteristics make it a promising candidate for use as an optical phase modulator, and it is this mode that is the focus of the present chapter. While many of the characteristics are favourable for phase modulation, the effective lifetime of the Hs state is typically of the order of a hundred milliseconds, which is rather short, and potentially restricts its practical application.

Figure 4.1 illustrates the typical transformations between the different states of a pi-cell with a low pretilt angle ($\approx 4 \sim 5°$). With no applied voltage, the LC director forms a stable splay (H) state, which has the minimum energy level. When the applied voltage is above a critical voltage V_{th} (Freed) (V_{th} (Freed) $\approx$ 1 Vrms), then the internal field is above that required to switch to an asymmetric state ($E > E_{\mathrm{Ha}}$) and a Fréedericksz transition occurs, and the director profile transforms into one of the asymmetric H (Ha) states. Alternatively, if a sudden voltage above

a higher threshold voltage (V_{th} (Hs)) is applied to the H state, then the internal field is above that required to switch to a symmetric state ($E > E_{Hs}$), and the transient Hs state is obtained – this state will tend to drift into the Ha state(s), or transform to the bend state, also termed the vertical (V) state directly for a higher applied voltage.

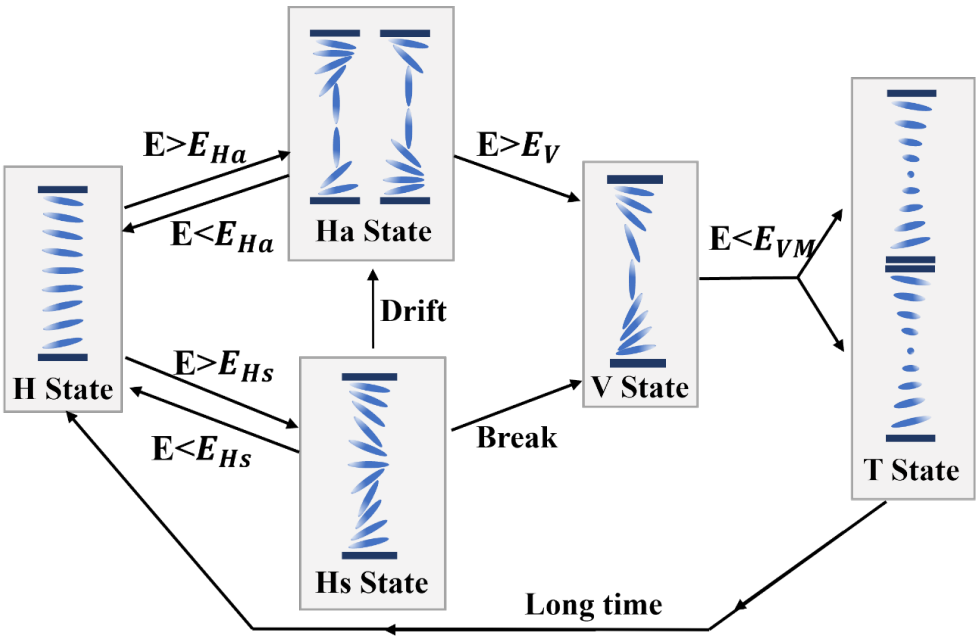

Figure 4.1. The switching states of a nematic pi-cell. An illustration showing the transitions of a nematic pi-cell under different electric field conditions.

As the operating voltage is increased above the threshold for the V state, V_{th} (V), then the internal field is increased above that required to switch to a V state ($E > E_V$), and both Hs and Ha states will transform to the V state because the V state is energetically favourable at high voltages. It is worth noting that the transition speed from the Hs state to the V state is much faster than that from the Ha state to the V state due to the larger energy difference between the two states [115], which contributes to the short lifetime of the Hs state. When the voltage is removed and the device is in either the Ha or Hs state, the director alignment will return to the H state directly; on the contrary, if the voltage is removed while the device is in the V state, or if the retaining voltage for the V state falls below the threshold voltage ($E >$

E_{VM}), then a twisted state (T state) forms and the device gradually returns to the H state via domain growth over the course of a few seconds.

Additionally, it can be seen from the schematic in Fig. 4.1 that in the Hs state the LC director in the middle of the device is aligned parallel to the substrates, and the whole device could be regarded as two half thickness Fréedericksz devices stacked together, as illustrated in **Figure 4.2**. Consequently, the threshold voltage for the Hs state is double that of the Fréedericksz (antiparallel rubbed alignment layers) device (V_{th} (Hs) $\approx$ *2* $\times$ V_{th} (Freed)). Furthermore, because the response time of Fréedericksz devices is proportional to the square of the LC layer thickness ($\tau \epsilon d^2$), the response time of the Hs state is more than 4 times faster than the Ha state when considering the additional effects of flow-reorientation coupling [114]. With such potential for fast switching, it is important to investigate the potential of the Hs state in optical phase modulation, but also essential to investigate the stability and the lifetime of the Hs state.

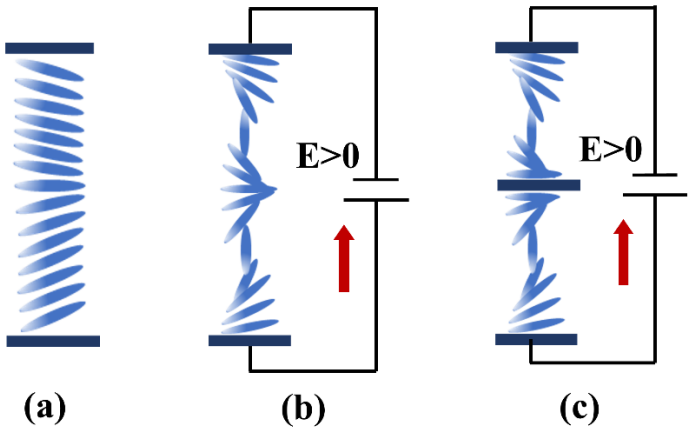

Figure 4.2. Schematics of a pi-cell in the splay state and Hs state: (a) the splayed ground state when V = 0 and (b) the symmetric H state when V > Vth (Hs) and (c) two half-thickness Fréedericksz cells as a simplified view of the Hs state.

To prolong the lifetime of the Hs state, researchers have proposed that with higher operating voltage, the lifetime of the Hs state will increase [109][116]. This is because large

applied voltages produce a high tilt director distribution which assists the bulk decoupling from the effects of any asymmetric surface pretilts, as depicted in **Figure 4.3**(a). Asymmetric surface pretilts can be the main cause for the director profile collapsing into one of the Ha states, as illustrated in Fig. 4.3(b). The LC director in the middle layer drift towards one surface due to the asymmetry in the surface pretilt. Therefore, higher voltages weaken the impact from any asymmetric surface condition and enable the device potentially to remain in the Hs state longer, and the lifetime of the Hs state will in principle be indefinite if the pretilts of the device are ideally symmetrical.

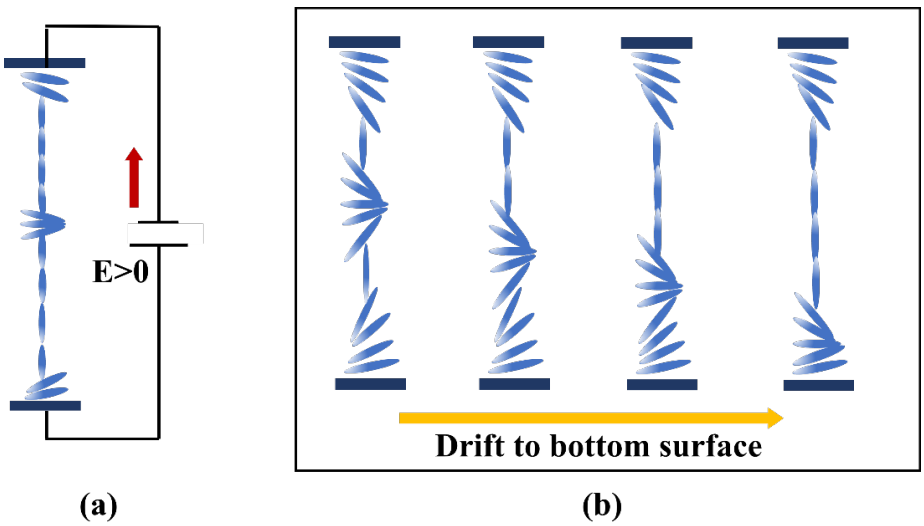

Figure 4.3. An illustration of the formation of the Hs state under different scenarios: (a) The Hs state formed under a very high voltage, with the bulk director profile decoupled from the surface boundary layers. (b) Schematic depiction of the Hs to Ha transition at $V > V_{th}$ (Fréedericksz threshold), where the central region of the director profile appears initially decoupled from the surface boundaries but gradually drifts toward the lower substrate over time.

However, as can be seen in Fig. 4.1, the Hs state can transition to the V state even without progressing to the Ha state, which further contributes to its short lifetime. Ru Yang *et al.* have pointed out that under higher applied voltages the V state would tend to rapidly nucleate and cause the device to transition to the OCB mode [117]; therefore, the authors suggested a burst driving method composed of an operating time period and a relaxation time period in order to obtain the Hs state, and the existence of the symmetric profile of the LC director in the Hs state

was confirmed by stroboscopic conoscopic imaging [117]. The operating time of the burst driving method must be long enough to switch the device into the Hs state but short enough to avoid the device breaking down to the Ha state or transitioning to the V state, while the relaxation time allows a complete recovery to the ground H state (splay state).

4.2 The Hs state Pi-Cell Phase Modulator

As noted above, the transient Hs state is obtained by applying a sudden voltage above its threshold, (V_{th} (Hs)). To prevent the Hs state from collapsing into the Ha state or nucleating into the V state, a burst driving method is employed. During the operating period, when the voltage is applied, the Hs state is formed and stabilized while avoiding transitions to other states. The subsequent relaxation period, when no voltage is applied, allows the system to recover to the ground H state. By periodically repeating this burst voltage cycle, the Hs state is regularly obtained. The amplitude and duration of the operating burst voltage significantly influence the lifetime of the Hs state. Therefore, it is important to study the stability of the Hs state in order to determine its stable operational lifetime.

4.2.1 Appearance of Hs State

The pi-cell device used in the experiment reported here consisted of glass substrates that were coated with indium tin oxide (ITO) electrodes and parallel rubbed polyimide alignment layers. The surface pretilts were typically within 4° to 5° and the cell gap was 3.7 μm. The nematic LC mixture, E7 (Synthon Ltd.), which has been extensively characterized in terms of its physical properties was capillary filled into the pi-cell device. To distinguish the transformation between different states, the device was positioned between crossed polarizers on a polarizing optical microscope (POM) (Olympus BX51), with the rubbing direction (optic axis) aligned at 45° to the polarizer and analyser pair.

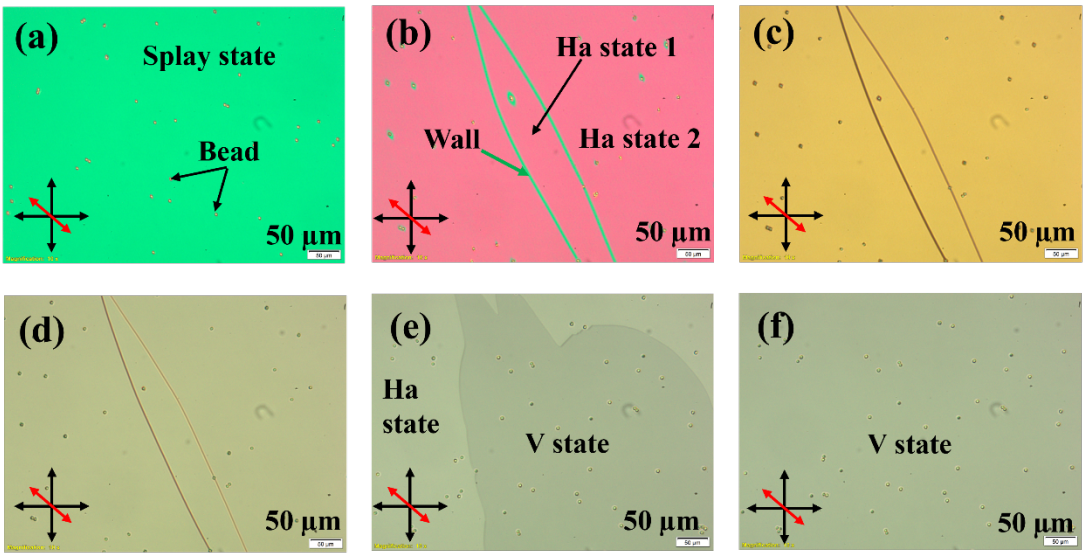

Figure 4.4. Representative polarizing optical microscope (POM) images of a pi-cell device under continuous square waveform voltage: (a) the splay state of the device under no applied voltage (the black dots in the image are the spacer beads distributed throughout the cell to obtain a unform cell gap). Mixture of Ha state 1 and Ha state 2 when the device was driven by a square voltage of (b) 1.4 Vrms, (c) 3.2 Vrms, and (d) 4.5 Vrms. (e) The formation of the V state under the voltage of 6 Vrms, and (f) the V state under the voltage of 10 Vrms. The double-headed black arrows represent the orientations of the polarizer and analyser. The double-headed red arrows represent the rubbing direction.

Figure 4.4 demonstrates the switching processes in a pi-cell along with exemplar POM images of the various states under a continuous square driving voltage. When the voltage was applied, the Ha and V states were observed at lower and higher voltages, respectively, but the transient Hs state could not be captured due to its short lifetime. Both the Ha and V states generally exhibit a uniform colour in the microscope image, with the colour changing as the voltage increased. Due to imperfect surface alignments, two distinct formations of Ha states are observed, along with the presence of several domain walls, as shown in Figs. 4.4(b) - (d). These domain walls represent the interface between regions inside and outside the domains, that is where the LC director has drifted in opposite directions to the device surfaces [120]. As the voltage increased, changes in the observed colour were directly linked to variations in the effective birefringence of the LC layers.

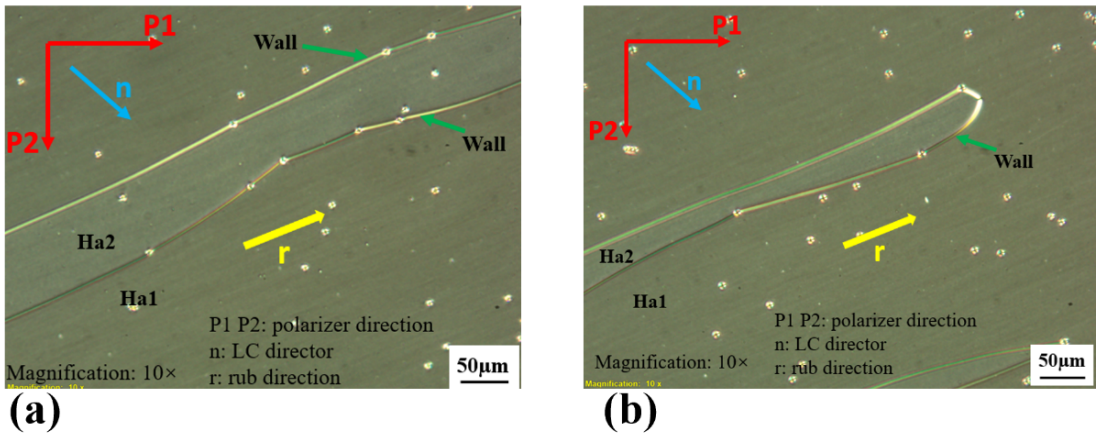

Figure 4.5. Domain wall formations in the Ha state under an applied voltage of 2.7 Vpp. (a) Domain wall along two sides aligned with the rubbing direction. (b) Domain wall with one end oriented perpendicular to the rubbing direction.

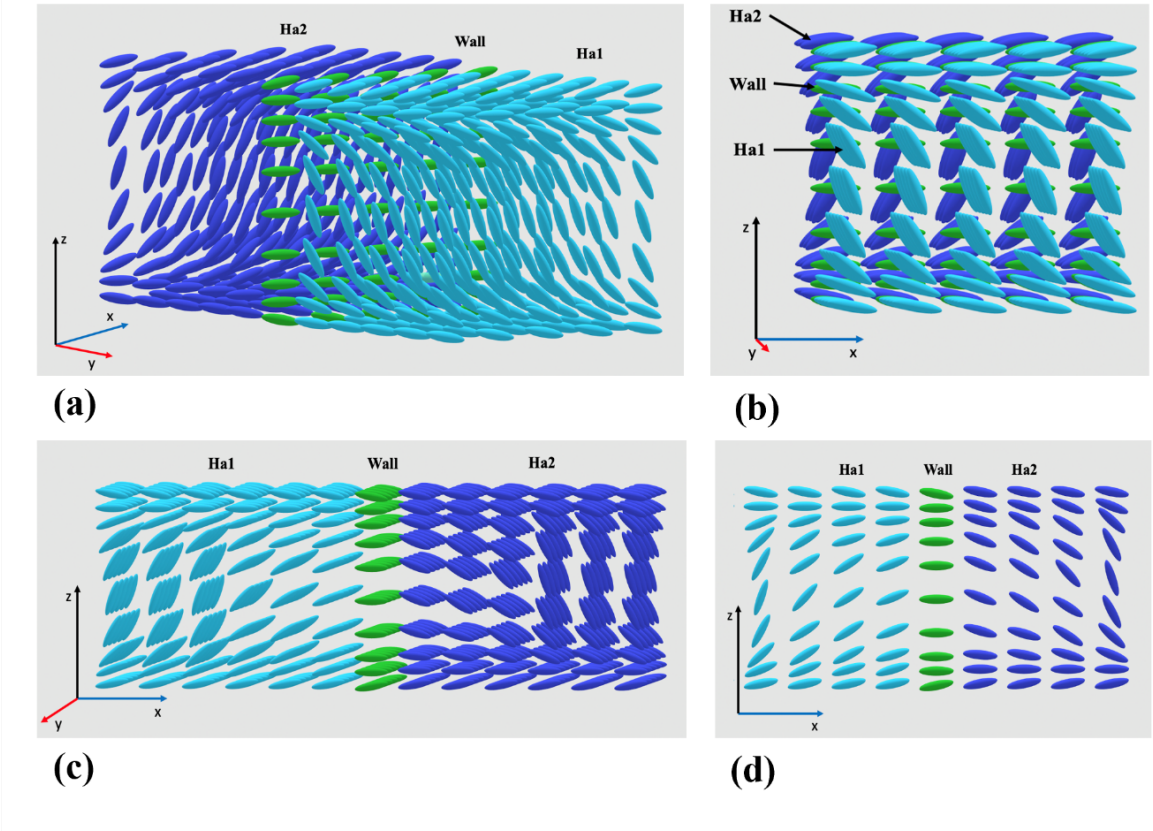

Figure 4.6. Visualization of the formation of two types of domain walls between Ha states: (a) 3D model of the wall on the sides, illustrating twist distortion; (b) zoomed view of the side wall showing detailed twist distortion; (c) 3D model of the wall at the end; and (d) zoomed XOZ view of the end wall showing a splay-bend distortion.

Figure. 4.5 depicts a zoomed view of a domain wall, where its alignment predominantly follows the rubbing direction. Specifically, Fig. 4.5(a) shows a domain wall along two sides aligned with the device's rubbing direction, while Fig. 4.5(b) depicts a domain wall at an end perpendicular to the alignment. This behaviour can be attributed to the differing orientations of the LC director between two Ha states, as illustrated in **Figure 4.6**. Walls parallel to the alignment direction exhibit strong twist distortion, as shown in Figs. 4.6(a)–(b), while walls perpendicular to the alignment direction display strong splay-bend distortion, as depicted in Figs. 4.6(c)–(d) [120].

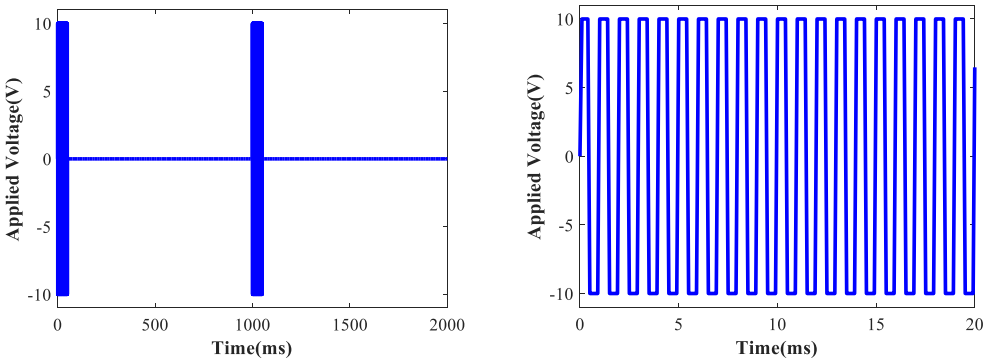

(a) (b)

Figure 4.7. The waveform of an applied burst driving voltage: (a) full view and (b) zoomed view to 20 ms.

To obtain the transient Hs state, a burst driving voltage, as shown in **Figure 4.7**, was applied to the pi-cell. The applied voltage was a square wave of 1 kHz with a variable burst duration repeated every 1 second, as indicated in Fig. 4.7(b). By adjusting the amplitude and burst operating time, the Ha, Hs and V states appear separately, while in some case these states appear together due to the nonuniform conditions of the device substrate surfaces. Since the device contained many spacer beads to maintain a uniform cell gap, most Ha and V states formed and grew around these beads. Variations in the burst driving voltage further complicated the situation, resulting in mixtures of states. When the applied electric energy is low, either due to a lower voltage or a shorter duration, the resulting mixture primarily consists

of Ha and Hs states. Conversely, if the electric energy is high, caused by a higher voltage or a longer duration, the mixture shifts to a combination of V and Hs states.

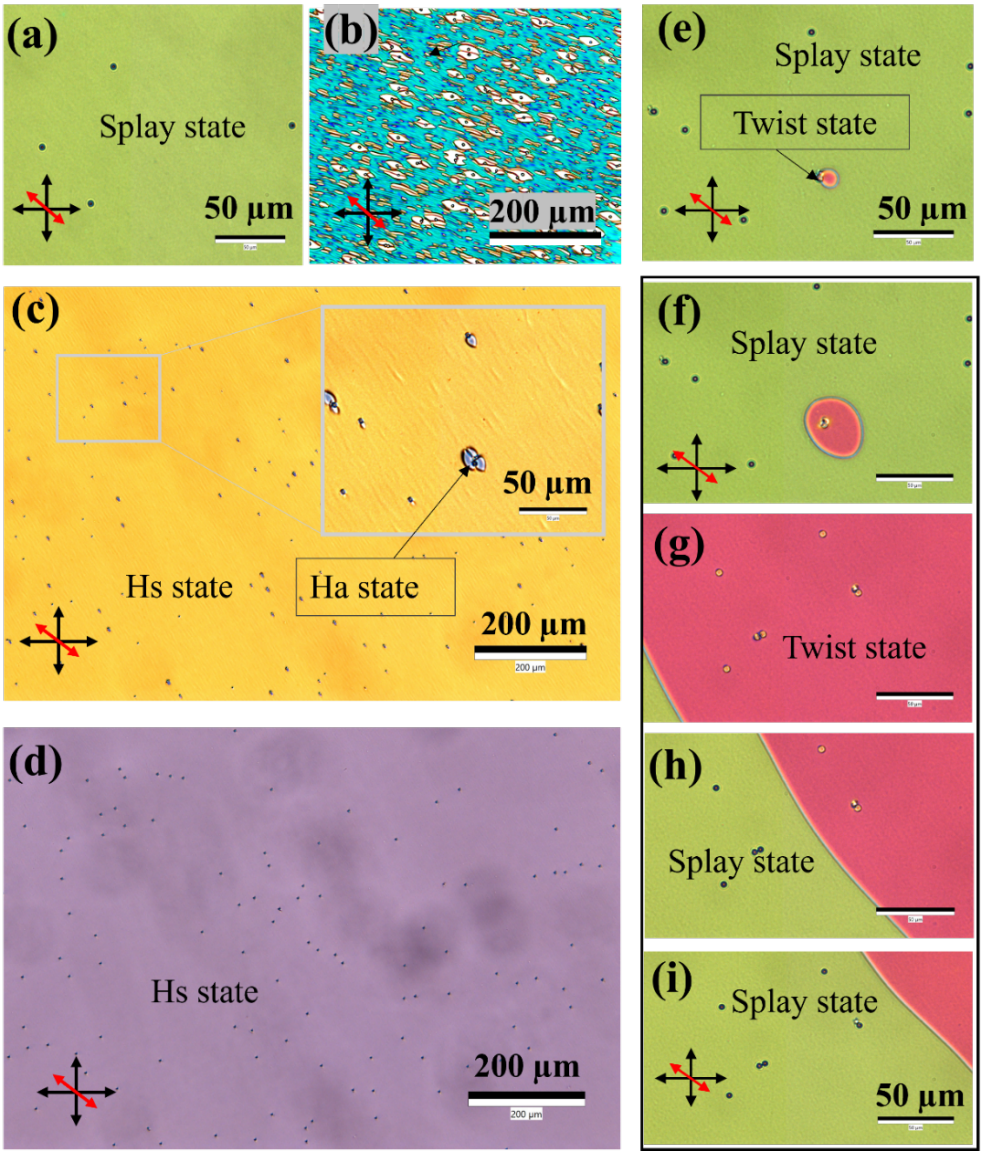

Figure 4.8. Representative polarizing optical microscope (POM) images of (a) the splay state of the device under no applied voltage (the black dots in the image are the spacer beads distributed throughout the cell to obtain a unform cell gap). (b) mixture of Hs state and Ha states when the device was driven by a burst driving voltage of 3 Vrms for 100 ms. (c) Hs state and tiny regions of Ha states when the device was driven by a burst driving voltage of 4 Vrms for 90 ms. (d) the Hs state formed by a burst driving voltage of 7 Vrms for 20 ms. (e) formation of the V state under a burst voltage of 10 Vrms, and during the relaxation period, V state relaxes to T state while Hs state relaxes to the H state, (e) demonstrate the V state under a repeating burst voltage of 10 Vrms for 35 ms. (f)-(i) demonstrate the growth of the V state under a repeating burst voltage of 10 Vrms for 50 ms. The crossed double-headed black arrows represent the orientations of the transmission axes of the polarizer and the analyser, and the double-headed red arrow represents the rubbing direction of the alignment layers.

For example, the investigated pi-cell was initially in the splay state, as shown in **Figure 4.8**(a). When the operating condition was a driving burst voltage of 100 ms duration with an amplitude of 3 Vrms, even though the Ha state can still collapse during the relaxation period between the voltage bursts, the formation of the Ha state was still dominant during the driving burst, which is not appropriate for a phase modulator design based on the Hs state, as shown in Fig. 4.8(b). However, when a burst voltage of 90 ms duration with an amplitude of 4 Vrms is applied, the Hs state, characterized by a yellow colour with some texture in certain areas, became the dominant state in the image of Fig. 4.8(c). The existence of the texture arises from variation in the positions of the central LC director. Specifically, some regions are slightly displaced upwards from the central plane, while others are slightly displaced downwards. This uneven director profile in the device is primarily caused by minor asymmetries in the surface properties of the device. In addition, although it can be seen that the Ha state has also formed, which is evidenced by the small blue regions that exist around some of the spacer beads, this only takes up a very small portion of the area. Under the condition where the Hs state is dominant, the device can still be considered a viable optical phase modulator based on the Hs state.

In addition, under a moderate amplitude voltage and short operating time, the Hs state can be obtained on its own, as shown in Fig. 4.8(d) for a 20 ms duration voltage burst with a voltage amplitude of 7 Vrms. In such a case, very small Ha states may still appear due to the asymmetries introduced by the spacer beads. However, because the total area of any Ha state domains over the whole device is negligible and any Ha states disappear completely by the end of the relaxation period between bursts (due to a decay time of a few milliseconds), any appearance of the Ha states can be ignored. When the driving amplitude was increased to 10 Vrms, the device initially exhibited only the Hs state at the beginning of the burst. However,

as the burst length increased, part of the Hs state transitioned to the V state, which subsequently grew as small regions around the spacer beads. This behaviour is shown in Fig. 4.8(e). It should be noted that if the V state regions during this stage are small and fully collapse during the relaxation period, allowing the device to recover to the ground H state, they have no impact on the formation of the Hs state, or the phase modulator design based on the Hs state.

Furthermore, as the burst length increased (i.e., was longer than 35 ms for an applied voltage of 10 Vrms) then the V states grew significantly. In this case the V/T state then did not collapse between bursts and consequently the V states continued to grow from burst-to-burst and the whole area of the Hs state eventually transitioned to the V state. Since capturing images during the voltage-on phase was challenging due to the transient nature of the Hs state, the images were taken during the voltage-off phase, as shown in Fig. 4.8(f) - (i). Here, the splay state transitions to the Hs state under voltage-on conditions, while the T state becomes the V state under voltage-on conditions. In these images, the V state is observed to dominate, occupying the entire visible area in the eyepiece, leaving the device unsuitable for a phase modulator design based on the Hs state.

4.2.2 Voltage Conditions for a Stable Hs State

In the subsequent work, we apply a burst driving voltage to stimulate the Hs state, and the duration of the burst is required to be long enough to induce the Hs state but short enough to minimize the Ha state regions and prevent significant transition to the V state. The states of the pi-cell are strongly determined by the applied voltage and its duration time. Therefore, it is of great necessity to quantify the effects of burst driving voltage on the device's state and state transitions.

Figure 4.9 presents the characterization of the states of the pi-cell device under various applied voltages and duration of the voltage bursts. These states were determined from observations of the POM images (as illustrated in Figure 4.8) together with the measured time-dependent transmission. The experimental setup used for these measurements is detailed in Section 3.2 (Fig. 3.4). The burst driving voltage applied on the device, illustrated in Fig. 4.9(a), includes an operation period (in this case 30 ms) followed by a relaxation period (in this case 970 ms). Transmission curves corresponding to this burst voltage, obtained with the device placed between crossed polarizers and with the rubbing direction aligned at 45° to the polarizers' transmission axis, are presented in Fig. 4.9(b). From these measurements, together with the images observed through the POM, it can be determined that the flat period in the transmission curve during the operation period corresponds to the Hs state. The constant transmission region during the relaxation period represents the ground H state, which is weakly splayed. The undulating regions of the transmission curve between these states indicate the dynamic switching behaviour of the device.

By repeating these investigations for a range of voltage bursts and durations, the stable operating regime of the Hs state can be determined. This is illustrated in Fig. 4.9(c), where the *x*-axis represents increasing voltage, and the *y*-axis represents the increasing burst duration. The blue areas at the bottom of the bars represent the time taken for the formation of the Hs state (i.e., the time required to reach equilibrium), acquired from the transmission curve(s). These results show that the time needed for the formation of the Hs state is about 0.2 ~ 5.0 ms for the pi-cell device used in this study, depending on the burst driving voltage applied. It can also be seen that as the voltage increases, the time required to form the Hs state becomes shorter. In addition, the green bars indicate the useful lifetime of the Hs state, which tends to decrease as the burst voltage increases. During this time, the formation of a few very tiny Ha

and/or V states might occur around spacer beads, but these are generally small enough to be ignored.

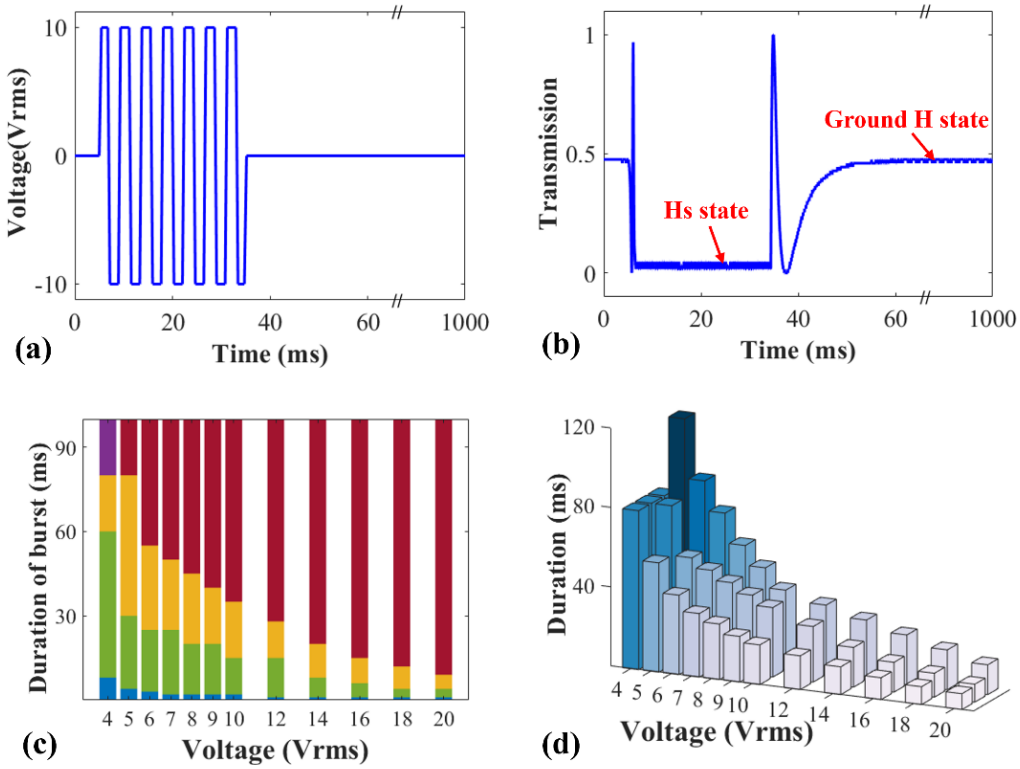

Figure 4.9. Stability of the Hs state. (a) An illustration of the burst driving voltage with the driving frequency during the burst of 1 kHz and (b) corresponding normalized transmission curve. (c) The various states that occur for different driving voltages and duration of the burst (blue – time to equilibrium state, green – Hs state, yellow – mixture of V and Hs states, purple – problematic formation of Ha states, red – growth of the V state). (d) Illustration of how the lifetime of the Hs state can be affected by different repeat periods (the front, middle and back rows represent the periods 0.5 s, 1 s and 2 s, respectively).

The yellow bars indicate where a mixture of Hs and V state tends to occur, since the duration of the driving burst is sufficient to enable the formation and some growth of the V state. However, if the V state domains which have appeared in this region are sufficiently small to collapse completely during the relaxation period between bursts, they will not affect the formation of the Hs state in the next voltage burst. This observation indicates that the voltage burst regime in the region of the bars coloured yellow could also potentially be adopted for phase modulator design based on the formation of the Hs states. Nevertheless, as the drive

voltage increases, the burst duration should decrease to maintain an Hs state that is sufficiently stable to be of use.

Moreover, the red areas in Fig. 4.9(c) indicate the condition when the V state continues to grow as the voltage bursts repeat instead of collapsing between voltage bursts. In this case, the V state gradually overtakes the Hs state, eventually occupying the entire device area and making this regime unsuitable for Hs-based phase modulators. At lower driving voltages, such as with bursts of 4 Vrms, the time for significant growth of the V state tends to be longer (e.g., is more than 100 ms at 4 Vrms). Instead, the Ha state emerges as a greater challenge, tending to dominate the Hs state before the V state becomes dominant. This region is indicated by the purple areas in Fig. 4.9(c). This is not suitable for phase modulator design based on the Hs state; and therefore, implies problematic effects in terms of Ha state formation limiting the useful duration of the stable Hs state. In summary, Fig. 4.9(c) highlights regions where optimal voltage bursts and durations can be selected to maximize the useful lifetime of the Hs state. These regions are represented by the green and yellow bars, which provide the most favourable conditions for designing the Hs-based phase modulator.

Furthermore, we also investigate the effect of the repeating period of the burst voltage on the lifetime of the Hs state. Fig. 4.9(d) illustrates the burst durations required to maintain a stable Hs state across a range of repeating periods, specifically 0.5 s, 1 s, and 2 s. For all three periods the lifetime of the Hs state decreases as the burst driving voltage increases. As the repeat period increases, the time needed for the Hs state formation remains the same, while the potential lifetime of the stable Hs state tends to become slightly longer – this is because any residual Ha and/or V state trapped around the spacer beads was more likely to entirely collapse when the time between burst driving voltage was longer. Therefore, for optical phase

modulation applications, it was necessary to choose an appropriate relaxation period to avoid deleterious growth of the Ha and/or V state within the desired Hs state. In this work, the period of the burst driving voltage and relaxation time were set to 1 s and the duration of the bursts were chosen based on the stable Hs regime shown in Fig. 4.9(c).

4.3 Modelling the Optical Phase Modulation

To estimate the potential response time and phase modulation of the Hs state, we have modelled the LC director reorientation for different applied voltages and pulse duration and have predicted the resulting optical phase modulation based upon the director profiles – the results from these simulations have been used in subsequent sections to make comparisons with experimental results. To determine the LC director reorientation during transient switching of the Hs state in a pi-cell, a computer numerical model was implemented to solve the Ericksen–Leslie continuum equations [39]. There are two key parts to this: (i) the free energy density of the LC layer (which depends on the director configuration, LC elasticity, applied electric field and dielectric permittivity); (ii) the rate of energy dissipation during director reorientation (which depends on the LC viscosities, director reorientation rate and flow within the LC layer).

Here we assume that the LC director remains within one plane and that its orientation is represented by an angle θ(the director tilt angle) which is a function of time and position across the LC layer (defined as the z-coordinate in what follows). As indicated in Section 2.3.1, the free-energy density (due to elastic and dielectric interactions) can then be written in terms of the director $\vec{n}$ based on Eq. (2-11) as

$$f = \frac{1}{2}K_{11}[\nabla \cdot \vec{n}]^2 + \frac{1}{2}K_{33}[\vec{n} \times (\nabla \times \vec{n})]^2 - \frac{1}{2}\Delta\varepsilon\varepsilon_0(\vec{n} \cdot \mathbf{E})^2 \qquad (4-1)$$

where K_{11}, K_{22} and K_{33} are the splay, twist and bend elastic constants, respectively, $\Delta\varepsilon$ is the dielectric anisotropy and **E** is the internal electric field. With the electric field along the z-direction this becomes

$$f = \frac{1}{2}K_{11}\,cos^2\,\theta\left(\frac{\partial\theta}{\partial z}\right)^2 + \frac{1}{2}K_{33}\,sin^2\,\theta\left(\frac{\partial\theta}{\partial z}\right)^2 - \frac{1}{2}\Delta\varepsilon\varepsilon_0\,sin^2\,\theta\,{E_z}^2 \qquad (4-2)$$

where E_z is the local electric field which is determined from the requirement for continuity in the z-component of the electric flux density.

To determine the director behaviour, we then need to solve the Euler-Lagrange equation

$$\frac{\partial}{\partial z}\left(\frac{\partial f}{\partial \theta'}\right) - \frac{\partial f}{\partial \theta} = \frac{\partial \mathcal{D}}{\partial \dot{\theta}} \qquad (4-3)$$

where $\mathcal{D}$ is the dissipation function and the term on the righthand side of Eq. (4-3) can be written as

$$\frac{\partial \mathcal{D}}{\partial \dot{\theta}} = (\alpha_3 - \alpha_2)\dot{\theta} + v_x'(\alpha_3 cos^2\theta - \alpha_2 sin^2\theta) \qquad (4-4)$$

where α_2 and α_3 are the Leslie coefficients and v_x is a non-zero flow term. To solve Eq. (4-4) also requires knowledge of the flow, which is obtained from the Navier-Stokes equation. This leads to

$$\tilde{\sigma}_{zx} = \frac{\partial \mathcal{D}}{\partial v'_x} = \frac{v'_x}{2}[2\alpha_1 sin^2\theta cos^2\theta + \alpha_2(cos^2\theta - sin^2\theta) + 2\alpha_3 cos^2\theta + \alpha_4 + \alpha_5]$$
$$+\dot{\theta}(\alpha_3 cos^2\theta - \alpha_2 sin^2\theta) \qquad (4-5)$$

where $\tilde{\sigma}_{zx}$ is the dynamic portion of the stress tensor, which can be obtained from the non-slip boundary conditions and the knowledge that it is independent of the z-coordinate, α_1, α_2, α_3, α_4 and α_5 are Leslie coefficients.

This system of equations is solved using a simple finite difference approach, with a regular grid in the z-direction. As noted above, non-slip boundary conditions are used for the

flow component. Additionally, the LC director tilt is fixed at the surfaces (here a small symmetric pre-tilt is used). This then allows the simulation of $\theta(z,t)$. To determine the resulting optical phase modulation the local component of the LC refractive index parallel to the rubbing direction is calculated from the director profile

$$n_{effective}(z,t) = \frac{n_e n_o}{\sqrt{n_e^2 \, sin^2\,\theta + n_o^2 \, cos^2\,\theta}} \qquad (4-6)$$

where n_o and n_e are the ordinary and extraordinary refractive indices, respectively. Eq. (4-6) can then be (numerically) integrated across the device thickness to determine a net retardation and hence an optical phase shift

$$\delta = \frac{2\pi}{\lambda} \int_0^d n_{effective}(z,t) \cdot \mathrm{d}z - \delta_0 \qquad (4-7)$$

where δ_0 is a chosen reference phase. The parameter values we used in this study were taken from the literature [39]. Specifically, these parameters were K_{11} = 11.1 pN, K_{33} = 17.1 pN, $\varepsilon_\perp$ = 5.4, $\varepsilon_\parallel$ = 17.4, n_o = 1.5, n_e = 1.72 and the wavelength was set to λ = 632.8 nm. The Leslie coefficients used in the model were α_1 = –21 mPa·s, α_2 = –282 mPa·s, α_3 = –1 mPa·s, α_4 = 225 mPa·s and α_5 = 92 mPa·s, taken from [39].

To estimate the potential optical phase modulation, we consider an LC layer with small symmetric surface pre-tilt which is driven into a transient Hs state by the sudden application of a large electric field – the resulting director profile is then near homeotropic through the bulk of the LC layer, with thin transition regions near each surface and a thin transition region in the centre of the layer. In the limit of very large electric fields, the transition regions become vanishingly thin. When the applied field is removed the director profile begins to relax back towards the ground H state – initially this happens by the growth of boundary layers from each surface, and the growth of boundary layers from the central transition region. This initial behaviour is largely independent of the device thickness. The resulting director profile leads to

a modulation in the optical phase of transmitted light. It is this stage which is critical in understanding the limits in available phase modulation speed because the "switch on" stage can be made fast by being driven with a sufficient electric field amplitude, but the "switch off" stage is limiting due to the balance between elasticity, viscosity and flow in the director reorientation.

For example, in the simulation, a model of an LC layer in the ground H state is driven with a high voltage of 50 Vrms into a director profile of the Hs state, which has very thin transition regions at the surfaces and in the centre of the LC layer – the resulting director profile is mainly homeotropic through the bulk of the cell, as illustrated by the blue line in **Figure 4.10**(a). When the voltage is removed, boundary layers "grow" from the surfaces and cell centre, as illustrated by the transition from the blue line to the brown line (0.08 ms after voltage removal). At later times, the reorientation extends to the bulk of the LC layer, as illustrated by the yellow and purple lines (0.28 ms and 1 ms after voltage removal).

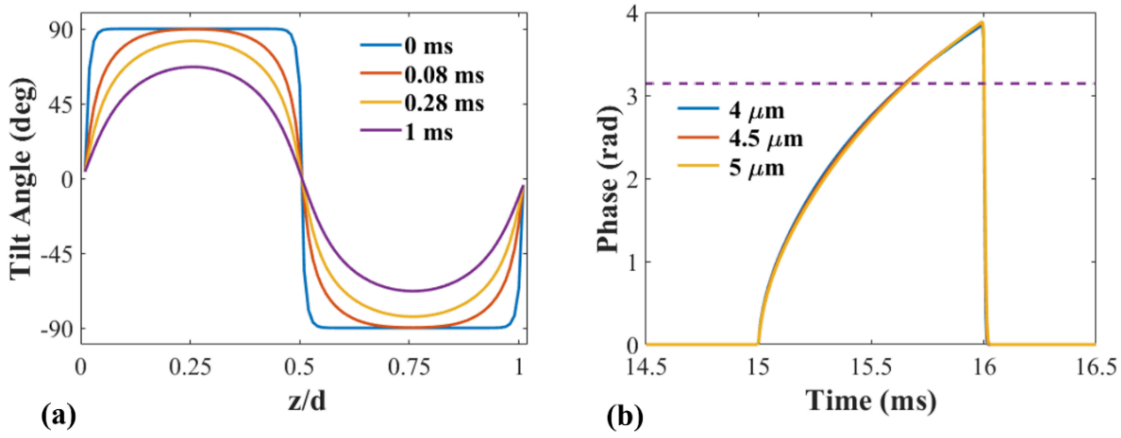

Figure 4.10. Simulation result of the device under a voltage of 50 Vrms and the corresponding phase modulation: (a) director distribution (tilt angle) at different times after the removal of the applied voltage, and the director angle is 4º at the two substrate surfaces due to the pretilt angle (d – LC layer thickness and *z* is a distance along the normal to the substrates); and (b) corresponding optical phase modulation following the voltage removal process – the voltage was removed at 15 ms and the director profile at 1 ms in (a) corresponds to the highest phase modulation at 16 ms in (b). Results are shown for three different LC layer thicknesses.

The resulting optical phase modulation is shown in Fig. 4.10(b). Again, the 50 Vrms driving voltage was applied to the device in order to drive the device into the Hs state discussed above. The voltage was then removed at 15 ms and reapplied at 16 ms. In the 1 ms between 15 ms and 16 ms we can see the optical phase modulation resulting from the director profiles illustrated in Fig. 4.10(a), which describes the relaxation period. In Fig. 4.10(b), we show the modulation effect for LC layer thicknesses of 4 μm, 4.5 μm and 5 μm – this shows that for small device thickness variation around this point, the available optical phase modulation does not substantially vary. As noted above, this is because the behaviour is dominated by the growth of the surface and central boundary layers in this regime. In each case the phase modulation was substantially greater than π-radians, which indicates that a full 2π rad optical phase modulation would potentially be available in a reflective SLM arrangement with switching times on a 1 ms timescale.

In the experiments, before extracting the phase, an initial measurement was conducted to analyse the transmission behaviour during the burst voltage. As discussed in Section 3.2, the transmission-time behaviour can quickly provide us with an estimate of the phase modulation expectation, and a transmission-voltage curve can be measured to confirm the device thickness. The experiment setup was presented in Section 3.2. In this case, the pi-cell was placed between crossed polarizers with the rubbing direction at 45° to the polarizer axis. The light from the laser passed through a polarizer, LC device and another orthogonal polarizer in turn, before it was finally received by the photodiode. By applying the burst driving voltage to the device, a transmission-time curve can be obtained, as illustrated earlier in Fig. 3.5. Similarly, by applying a gradually increasing square wave (1 kHz frequency is used here) and recording the transmission, the transmission-voltage curve can be observed, as presented in Fig. 3.8.

To match the transmission-voltage curve with the simulation by adjusting the LC layer thickness and the pretilt angle of the device, they were set as 3.73 μm and 4º, respectively. Based on the transmission-voltage dependence, it can be noted that between two neighbouring points where the transmission reaches 50%, the optical phase retardation of the device has changed by π rad. Similarly, between two successive points where the transmission is 0% and 100% there is also a change in optical phase retardation of π rad. Therefore, from the measured transmission-time curve of a pi-cell, it was estimated that a phase shift of π rad was achieved in 1 millisecond for the transmission arrangement. The device behaviour shows great consistency with the calculation result; and therefore, it is predictable that this device can exhibit a phase modulation of 2π rad in 1 millisecond in a reflective SLM geometry.

The results outlined above indicate that: (1) the LC layer thickness is 3.73 μm (with a small pre-tilt of around 4°); and (2) by modulating the signal as illustrated in Fig. 3.10(a) a useful level of phase modulation is expected in the Hs state.

We then utilized this simulation model to predict the optical phase modulation of the designed optical phase modulator for this particular device with realistic driving conditions. In the simulation, the burst driving voltage was set to 10 Vrms, as will be illustrated later in Fig. 4.12(a). The LC device was driven into the Hs state at 0 ms and remained stable for 5 ms. Following this, the device transitioned into the modulation stage, which consists of the alternating voltage of 1 ms off and 1 ms on. **Figure 4.11**(a) depicts the simulated dynamic changes in the director profiles during the modulation stage, focusing on the interval from 25 ms to 26 ms. This specifically relates to the optical phase modulation when the voltage is removed. The resulting optical phase modulation is shown in Fig. 4.11(b), where a full phase shift of 2π rad is achieved within 1 millisecond in a reflective geometry. This result aligns well

with the estimation obtained using the transmission method, validating both the simulation and experimental approaches. This consistency between simulation and prior estimations confirms the great potential of this modulator design. Based on this, we anticipate similar outcomes in subsequent experimental measurements, which could further confirm the potential reliability and precision of the burst driving method and the optical phase modulator design.

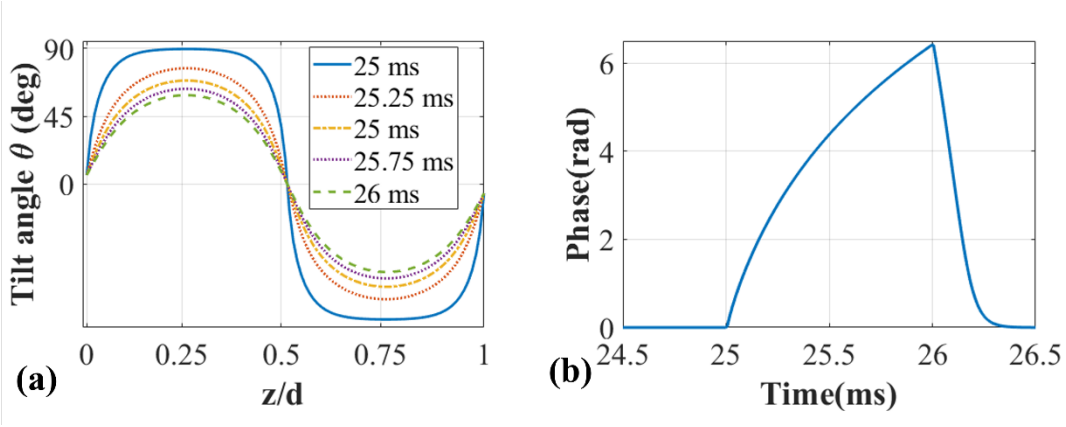

Figure 4.11. Simulation result of the device under a voltage of 10 Vrms: (a) director distribution (tilt angle) at different times after the removal of the applied voltage, and the director angle is 4º at the two substrate surfaces due to the pretilt angle (d – LC layer thickness and *z* is a distance along the normal to the substrates); and (b) corresponding optical phase modulation following the voltage removal process in the reflection geometry – the voltage was removed at 25 ms and the director profiles in (a) results in the phase modulation in (b).

4.4 Experimental Results

We now aim to accurately measure the optical phase modulation of the LC device in the Hs state using the phase-shifting Twyman Green interferometer method outlined in Section 3.3. The applied burst driving voltage consisted of a cyclic 1 second long waveform sequence with "priming stage" of a ±10V 1kHz square wave for 5 ms (which drives the devices into the Hs state) followed by a "modulation stage", where this drive voltage was repeatedly turned on for 1 ms and then off for 1 ms for the next 35 ms, followed by a "relaxation stage" where no voltage was applied for the rest of the 1 second, to allow the LC device to return to the ground H state. This voltage waveform is shown in **Figure 4.12**(a).

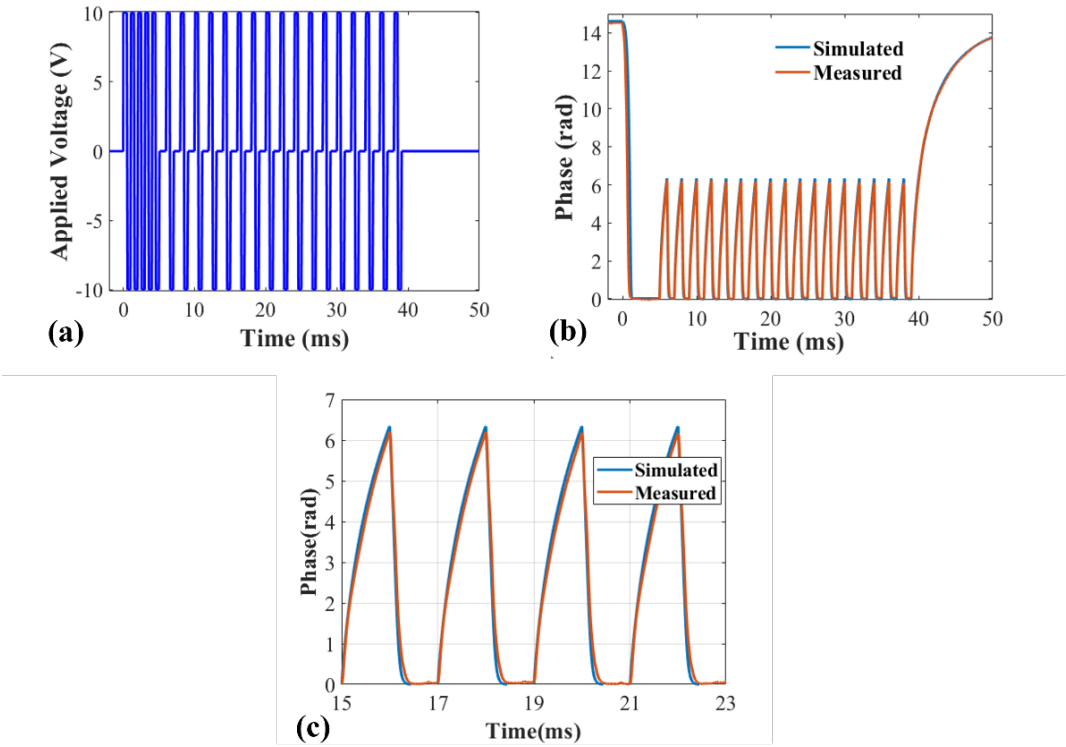

Figure 4.12. (a) The burst driving voltage applied to the nematic pi-cell, which consisted of a 40 ms operating period repeated every 1 second. (b) The corresponding optical phase modulation results of the LC device under voltage shown in (a). (c) An enlarged view of the modulation section from 15 ms to 23 ms of (b).

A four-step phase-shifting algorithm is employed to extract the phase information, represented by Eq. (3-24), as explained in Section 3.3. The phase modulation was then extracted and is shown in Fig. 4.12(b), where the horizontal axis is the time scale, and the vertical axis is the phase modulation from the LC device. Fig. 4.12(c) plots the enlarged section of Fig. 4.12(b) to highlight the detailed phase response under modulation. It is evident that a stable 2π rad phase modulation was achieved in 1 millisecond in the Hs state using the reflection (two-pass) configuration. The measured phase modulation correlates well with our results from simulations for an LC layer thickness of 3.73 μm (the other device parameters were as listed in the modelling in Section 4.3). This agreement highlights the accuracy of our simulation model, which incorporated detailed device parameters including elastic constants, dielectric anisotropy, and pretilt angles as well as validates the reliability and effectiveness of

the experimental setup. In addition, this result further underscores the feasibility of the burst driving method in reliably maintaining the Hs state while achieving precise optical phase control, demonstrating its practical applicability for high-speed optical phase modulator design.

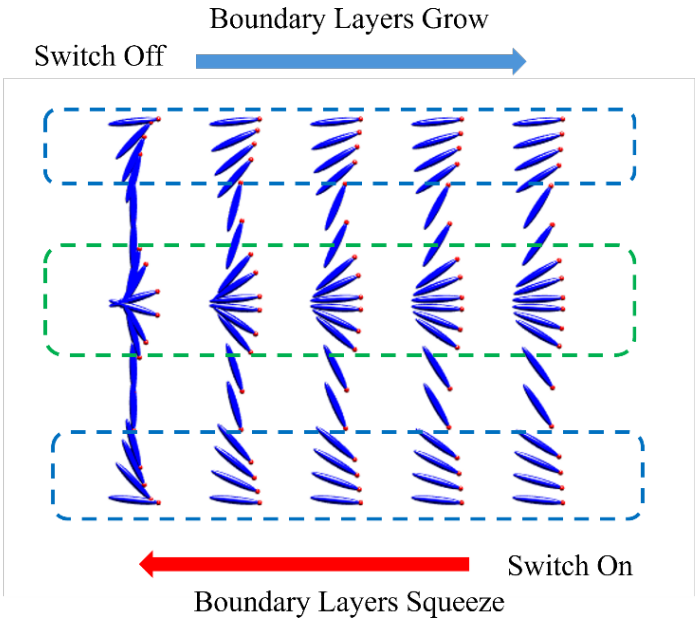

Figure 4.13. Simulation of the LC device director distribution during phase modulation under a voltage of 10 Vrms with 1 ms pulse. This illustrates the dynamic behaviour of LC molecules at various time points after the removal of the applied voltage from the left to the right (or after reapplication of the voltage from the right to the left in 1 ms). The boundary layers grow outward from the surfaces and the centre of the LC layer during the relaxation process, while compressing in response to the applied electric field.

The behaviour of the LC director within the device during the modulation process is depicted above in Fig. 4.11(a) using curves representing the changes of tilt angle θ, while **Figure 4.13** provides a detailed illustration of the dynamic director profiles during the 1 ms relaxation process. Both visualizations are based on simulation insights and highlight the intricate molecular dynamics that determines the optical phase modulation. During the relaxation period, when the applied voltage is removed, the boundary layers grow outward from the surfaces and the centre of the LC layer, allowing the LC director to gradually return to the ground state alignment. However, since 1 ms is far too short for the LC director to fully reach the ground state, the voltage is reapplied long before complete relaxation occurs.

Conversely, during the reapplication period, the boundary layers are compressed as the LC director reorients in response to the electric field. This repeat between boundary layer growth and compression is the key mechanism in generating phase modulation in the device. The director reorientations produce precise and controllable optical phase modulation. This understanding, derived from the simulation, underscores the effectiveness of burst voltage driving in achieving rapid and stable phase modulation for high-speed optical phase modulation applications.

To further explore the phase modulation capability of the nematic pi-cell in the Hs state, the following experiments were conducted. Firstly, since the available phase modulation is related to the amplitude of the applied voltage, it was necessary to investigate the relationship between the driving voltage and the optical phase response of the device in the Hs state. To do this, a driving signal of the same form as that illustrated in Fig. 4.12(a) was used, with a priming stage of a 1 kHz square wave, followed by a modulation stage where the driving signal was repeatedly on for 1 ms and then off for 1 ms, followed by a relaxation stage with no voltage signal applied. By adjusting the amplitude of the 1 kHz voltage from 6 Vrms to 20 Vrms, the corresponding phase modulation during the voltage modulation stage was measured, as shown in **Figure 4.14**(a). Since the lifetime of the Hs state is significantly shorter at 20 Vrms, the voltage applied to the device was adjusted for only achieving two modulation cycles before transitioning out of the Hs state. In each case the resulting optical phase modulation signal is offset to zero for the equilibrium Hs state present after the priming stage.

Fig. 4.14(b) presents an enlarged section of Fig. 14(a) to provide a clearer view of the phase modulation during the pulses. It can be observed that as the driving amplitude increases, the phase modulation depth also increases and the switching on speed also becomes faster. The

increased available phase modulation at higher voltage is because of the fact that, when a larger voltage is applied, the internal electric field then leads to a larger region of the LC director aligning parallel to the electric field. Consequently, the transition regions (boundary layers) at the surfaces and in the centre of the device in the Hs state become thinner – when the field is removed this then produces a larger phase modulation within 1 ms.

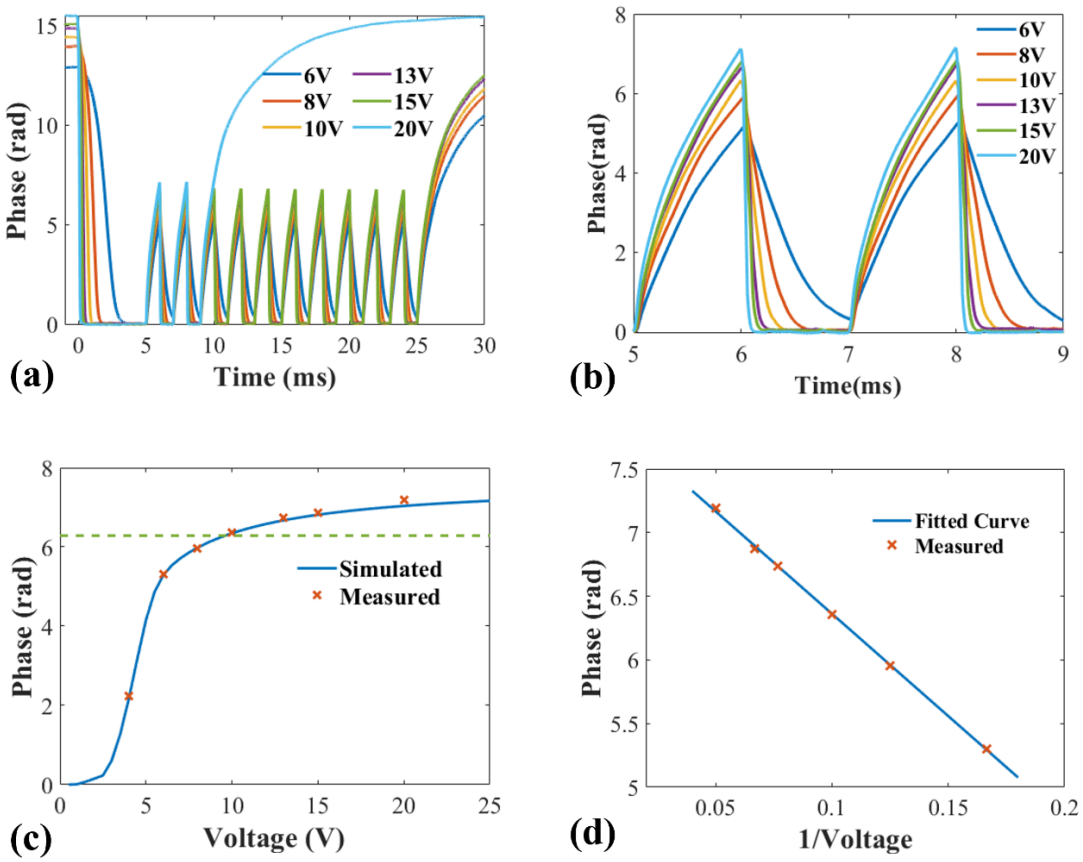

Figure 4.14. Measured results: (a) phase modulation response as a function of time for various applied voltages with a 25 ms operation time (under 10 ms for 20 Vrms) and (b) enlarged section of (a) from 5 ms to 9 ms and (c) simulation and measured results illustrating the relationship between the applied voltage and phase modulation during relaxation process within 1 ms time scale. (d) the 1 ms phase modulation at higher voltage is linearly dependent on the inverse of the applied voltage.

The resulting available phase modulation as a function of voltage within the period of the 1 ms pulse is plotted in Fig. 4.14(c), together with the simulated response. The optical phase modulation at 4 Vrms is not shown in Fig. 4.14(a) due to the space constraints. It can be seen

that the available phase modulation increases as the voltage increases, apparently tending towards an asymptote at higher voltages. Importantly, 2π rad optical phase modulation within 1 ms is available with a driving voltage of 10 Vrms, and when the voltage is above 10 Vrms the corresponding phase modulation is larger than 2π rad in 1 millisecond. However, it is also important to note that when the applied voltage is higher, the lifetime of the Hs state is reduced due to the rapid growth of the V state, limiting the potential to exploit the optical phase modulation response (for example, here when the voltage is 20 Vrms, the useful Hs state lifetime becomes less than 10ms). It is also interesting to observe that for higher drive voltages a plot of the available phase modulation in 1 ms as a function of the inverse of the voltage leads to a straight-line behaviour, as seen in Fig. 4.14(d). This is likely to be due to the fact that the LC electric coherence length is inversely related to the electric field strength, which then dictates how thin the boundary layers at the surfaces are and how thin the transition region in the centre of the Hs layer is, with a corresponding influence on the available optical phase modulation.

To demonstrate the potential for addressing multiple optical phase levels using switching in the Hs state, the optical phase after 1 ms can be maintained by choosing a suitable hold voltage. In this case, after the priming period required to establish the Hs state, the switching waveform in the operating period consists of driving, relaxing, and holding in turn. The driving voltage (fixed at 10 Vrms) initiates the Hs state. The relax voltage is applied after driving to allow the LC director to settle into a specific intermediate configuration corresponding to the desired phase level within 1 ms. This voltage determines how much the LC director relaxes, thus controlling the optical phase modulation. Following this, the hold voltage is applied to stabilize the LC director profile, ensuring the LC device maintains the achieved phase level for an additional 1 ms. By varying the relax voltage (from 0 Vrms to 10 Vrms) and selecting the

corresponding hold voltage, the system enables precise and stable phase control. The resulting measured and simulated phase modulation curves are shown in **Figure 4.15**(a) and (b), together with a plot of the rms voltage applied in Fig. 4.15(c) and (d). This demonstrates that the optical phase can be precisely set at any arbitrary chosen point within the range of 0 to 2π rad.

Further validation of the optical phase modulation capability of the Hs state was conducted by applying various relax-hold voltage combinations. The root-mean-square (RMS) voltage waveforms corresponding to these combinations are shown in Fig. 4.15(g) and (h). The resulting phase modulation, presented in Fig. 4.15(e) and (f), remained stable on the millisecond timescale and demonstrated good controllability. These results confirm that the optical phase can be continuously and precisely modulated to any desired level, depending on the applied voltage. Importantly, the measured results show excellent agreement with the simulation, confirming the accuracy of the approach. This demonstrates that precise, controllable optical phase modulation over a full range of 0 to 2π rad can be achieved on millisecond time scales with a nematic LC pi-cell in the Hs state. If it is required for longer time scales of modulation, the device is also capable of holding the phase within the operation period.

Figure. 4.16 plots the relationship between the hold voltage required and the relax voltage, as well as the optical phase state obtained as a function of the relax voltage. By choosing different hold voltages as the relax voltages change, a flat and stable phase level can be maintained for 1 ms, as seen in Fig. 4.15. In Fig. 4.16 (a), the hold voltage is plotted against the relax voltage. Notably, when the relax voltage exceeds 6 Vrms for the device under investigation, the required hold voltage becomes equal to the relax voltage. This indicates that equilibrium is reached during the 1 ms relaxation period at higher relax voltages, allowing the

hold voltage to equal the relax voltage, simplifying the modulation scheme. Additionally, the experimentally determined hold voltage aligns closely with the simulated values, demonstrating the accuracy of both experimental and simulation. Fig. 4.16(b) depicts the relationship between the resulting phase modulation and the relax voltage. The phase modulation of 0 rad corresponds to condition where the relax voltage is 10 Vrms, indicating no additional phase modulation. The phase modulation demonstrates a continuous 2π rad phase range as the relax voltage is varied, which underscores the effectiveness of the relax-hold voltage scheme in achieving controllable and stable phase modulation over a wide range. The measured data shows great agreement with the simulated results, which further demonstrates the reliability and accuracy of both the simulation model and measurement system. This continuous phase response highlights the potential of this modulation method for applications requiring precise and repeatable optical phase control.

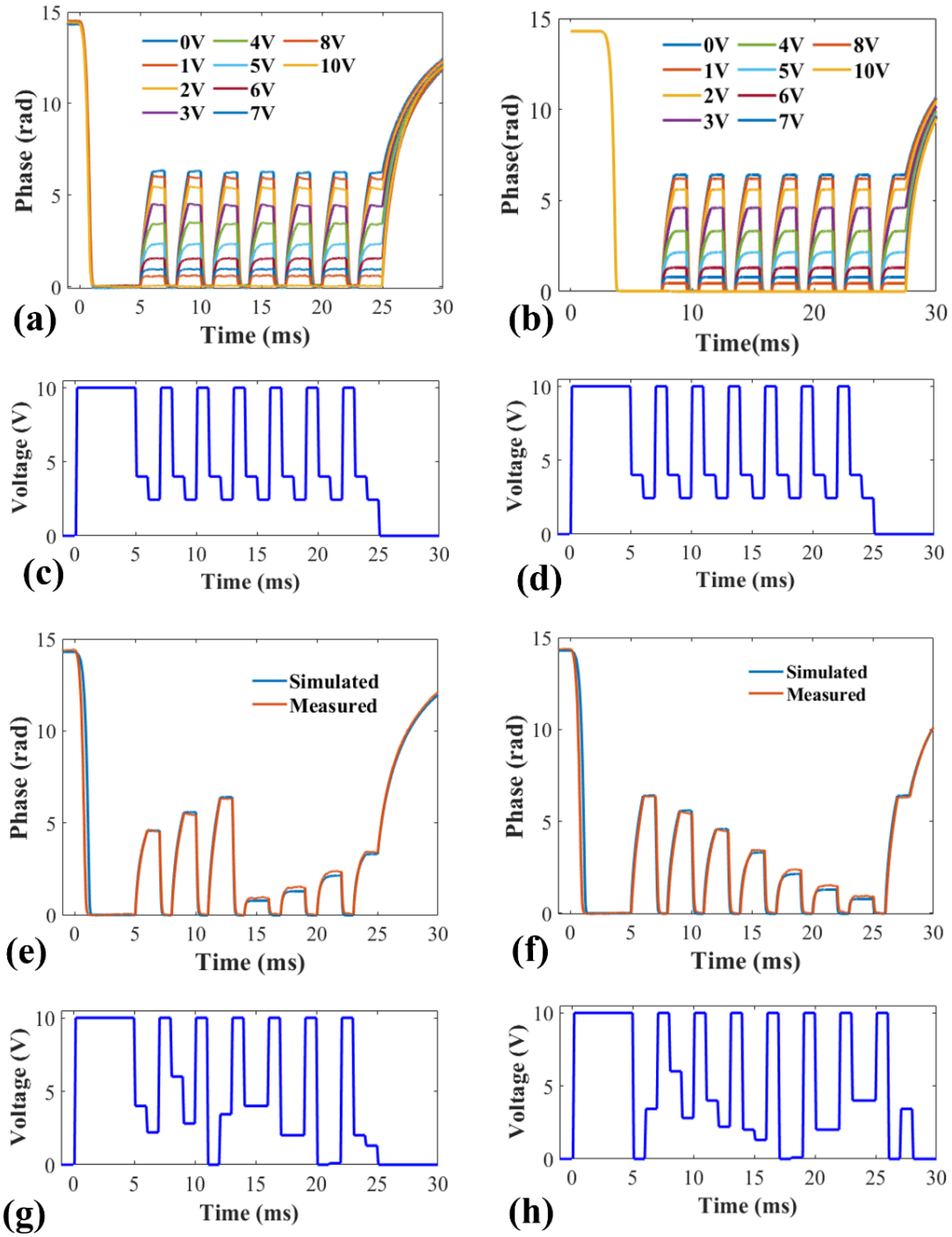

Figure 4.15. Demonstration of the multiple optical phase levels achieved by the LC device under various operating conditions: (a) measured and (b) simulated phase modulation curves changes under the increasing relax and hold voltages combination. (c) and (d) are corresponding applied voltage waveforms for (a) and (b), respectively, and within the modulation range, the voltage is same during each modulation. (e) and (f) show measured and simulated phase modulation results under varying relax-hold voltage combinations, and (g) and (h) present the applied corresponding voltage waveforms for (e) and (f), respectively. The voltage is different during each modulation within the modulation range in (g) and (h).

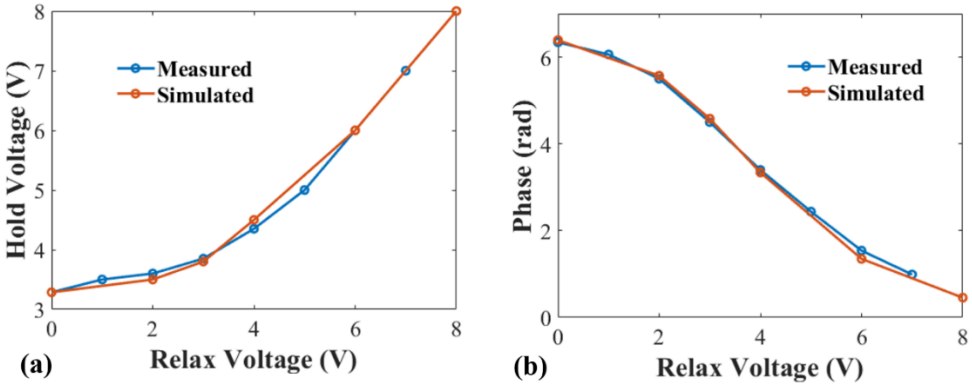

Figure 4.16. Modulation results: (a) the relationship between the hold and relax voltages and (b) phase modulation under various relax voltages.

4.5 Conclusions

In this chapter, we use a burst driving method to obtain the Hs state in a nematic LC and investigate the effects of the amplitude and operating time on the stability for use as an optical phase modulator. The switching transition to the Hs state, and the required conditions for its stability are illustrated. Modelling based on Ericksen-Leslie theory indicated that useful optical phase modulation could be obtained in the Hs state on a 1 ms timescale. To verify the model, a nematic LC (E7) was capillary filled into a pi-cell device. A phase measurement system based on a phase-shifting Twyman Green interferometer was employed to enable time-dependent optical phase measurements. The experimental results revealed that the Hs state can achieve a 2π rad optical phase modulation in 1 millisecond under a burst voltage of 10 Vrms at room temperature in a reflective device configuration (as commonly implemented in SLM technology). Further, multiple optical phase levels were achieved under various applied relax-hold voltage combinations. However, as the stability of the Hs state is limited, it cannot provide a truly continuous phase modulation with time, and thus further work is required to stabilize and preserve the Hs state, which would then provide a route to significantly enhance the capability of nematic based optical phase modulators.

5. Polarization-independent Phase Modulator Design

In this chapter, we investigate the potential of achieving polarization-independent phase modulation using super-twisted nematic (STN) liquid crystal (LC) devices. Here, we describe the use of a burst driving voltage applied to a 180° STN LC device to obtain a twist symmetric H (T-Hs) state, which enables simultaneous modulation of light for all polarizations, demonstrating a polarization-independent characteristic. To the best of the author's knowledge, this is the first demonstration of using a T-Hs state to achieve polarization-independent optical phase modulation. Additionally, we consider a 90° twisted nematic (TN) LC device for comparison as this can also exhibit polarization-independent characteristics.

Simulations were carried out using a numerical model based on the Ericksen–Leslie continuum equations [39], which was employed in conjunction with Jones calculus described in Section 2.5.2 to simulate the optical properties of the device. The time-dependent optical phase modulation of the device was subsequently measured using a phase-shifting Mach–Zehnder interferometer, as introduced in Section 3.4. The experimental results demonstrate that an STN device with an 8.9 μm thick LC layer, operating in the T-Hs state, exhibited a π/2 rad optical phase modulation in 1 ms for a burst voltage of 30 Vrms that was found to be independent of the incident polarization. These measurements were obtained at room temperature in a single optical path configuration and were found to be in good agreement with the results from simulations.

This work has been written up and published on a peer-reviewed journal: Xue, L., Elston,

S. J., & Morris, S. M. (2025). Polarization-independent nematic liquid crystal phase modulators. ACS Photonics.

5.1 Literature review

As discussed in Section 1.1, Spatial Light Modulators (SLMs) are crucial components in modern optics and photonics, offering precise and dynamic control over the properties of light such as phase, amplitude, and polarization. By exploiting the unique electro-optic properties of liquid crystals (LCs), LC-based SLMs enable real-time manipulation of incident light with incredible flexibility and precision, shaping optical wavefronts for a variety of applications including beam shaping[7], microscopy [14], holography[15][16], and optical communication systems [121]. Therefore, SLMs that are capable of high frame rates, analogue 2π rad phase modulation, and low driving voltages are in high demand.

To further improve the versatility and efficiency of optical systems, polarization independence is a highly desirable feature in the design and application of LC-based SLMs as it ensures consistent performance in real-world scenarios where the incident light may exhibit unpredictable or changing polarization characteristics. Polarization-independent SLMs would allow incident light to pass through the device without changing the polarization state, which eliminates the need for additional optical components, such as polarizers, to manage varying polarization states. This streamlines the optical system, enhances the optical efficiency, and reduces the financial cost.

Broadly, three different techniques have been considered for polarization-independent performance using LC based devices. The first technique is to configure the surface alignment of the LC device at the two opposing substrates to be orthogonal to one another, as exemplified

by Twisted Nematic (TN)-LC devices, enabling polarization independence to be achieved while maintaining optical phase modulation with an applied voltage [53][122][123]. In a TN-LC device, the LC director near the substrate surfaces aligns parallel to the surface alignment, while in the bulk, the director twists uniformly by 90º due to the boundary conditions in the absence of an applied voltage. When a voltage is applied, the LC director in the middle of the layer orients along the electric field direction, while the director near the substrate surfaces maintain alignment with the surface rubbing direction. At high voltages, the two boundary layers can be regarded as decoupled from the bulk and are oriented along perpendicular directions, allowing for simultaneous optical phase modulation for orthogonal linear polarizations. TN-LC devices have been applied for the purposes of amplitude modulation, phase-only modulation [55] and complex modulation. The latter enables simultaneous control of both the amplitude and phase [124].

Secondly, polarization independence can be achieved by utilizing certain LC phases, such as blue phase LCs (BPLC) [125][126], polymer-stabilized blue phase LCs (PS-BPLCs) [127]-[129], short pitch chiral nematic LCs (CLCs) [130]-[132] and polymer-dispersed LCs (PDLC) [134]-[136]. BPLCs exhibit a three-dimensional periodic lattice structure with spontaneous chirality and are optically isotropic, enabling the uniform optical modulation of light for all polarization states. Additionally, BPLCs exhibit major advantages in terms of millisecond response times, simple fabrication methods (no need for surface alignment layers), a large optical Kerr effect and the ability to perform continuous optical phase modulation, making them a promising candidate for SLM technologies. Towards this end, previous research proposed optimizing the material parameters and cell gap of the BPLC device to achieve a full 2π rad phase shift at a voltage of 26 V [126]. However, BPLCs typically exhibit limited temperature ranges, which has led to innovations such as crosslinked polymer networks to

stabilize the mesophase (PS-BPLCs). Nonetheless, polymer stabilization remains a challenging process and requires a high driving voltage, which increases power consumption. While reducing the operating voltage is possible by increasing $\Delta\varepsilon$, this approach typically results in a higher viscosity and potentially slower response time. Additionally, the prolonged charging time subsequently limits the device's resolution and frame rate [128]. What's more, a PS-BPLC device was found to exhibit a full 2π rad phase shift at 24 Vrms but needed a four-pass optical configuration to achieve this amount of phase modulation [129].

For CLCs with a pitch smaller than the wavelength of light, the uniform standing helix and focal conic states have been exploited to demonstrate polarization independence owing to their anisotropic properties [130]. This attribute arises from the helical macroscopic structures, which possesses circular symmetry, enabling uniform interaction with incident light regardless of the polarization state. CLCs have also been extensively applied in the infrared (IR) band as polarization-independent variable optical attenuators [131] and in the THz band as polarization-independent 2π rad THz phase shifters [132]. PDLCs, on the other hand, have been used to achieve polarization independence by randomly dispersing the orientation of the LC director, ensuring that incident light of any polarization experiences the same effective refractive index, resulting in a consistent phase shift [134]. It has been suggested that these structures can be optimised by making the LC droplets pinned near the glass substrates [135] and using nanometre sized PDLCs [136]. However, PDLCs can suffer from limited phase modulation and unwanted losses due to light scattering.

The third method involves stacking two birefringent layers orthogonally to enable phase modulation in both the *x* and *y* directions independently [137]-[139]. Researchers inserted an ultra-thin polymer film in the middle of two separate orthogonal LC layers resulting in a

polarization-independent phase modulation with a 2π rad phase shift at 9 Vrms and an 8.1π phase shift at 40 Vrms [139]. Despite the extensive range of different demonstrations and solutions presented to date, the aforementioned approaches are not without their drawbacks and undesirable properties such as limited optical phase modulation, complicated fabrication procedures and device architectures, and/or the need for specialised LC compounds.

In this chapter, we present an innovative approach to achieving polarization-independent optical phase modulation by applying a burst driving voltage to a 180º super-twisted nematic (STN) LC device to make use of the twist symmetric H (T-Hs) state. STN-LCs, characterized by their greater twist compared to TN-LCs, have also been employed in LC displays [140]-[142] and SLM technology for both amplitude modulation and phase modulation. For instance, the use of 180º-twist STN-LC in a pi-cell is known to form a π-twist state [143][144], which has the advantage of inducing a fast and uniform transition to the bend state without the need for nucleation. This transition exhibits a much lower voltage threshold when compared to a conventional nematic pi-cell design. In this work, we use a combination of simulations and experiments to demonstrate that accessing the T-Hs state in an STN-LC using a burst driving voltage can result in polarization-independent phase modulation. For comparison, simulations are also conducted for a TN-LC device, which is capable of polarization-independent phase modulation, but suffers from limitations that are not exhibited in the T-Hs state of an STN-LC device.

This chapter is structured as follows. With the aid of simulations, we begin by considering the behaviour for a 90º TN and the STN devices with different alignment conditions. Results indicate that both the 90º TN device and the T-Hs state found in the 180° STN planar-aligned LC device have the potential to exhibit polarization-independent phase

modulation, with the latter showing more promise in terms of device performance. In Section 5.2, we present the phase modulator concept that exploits the T-Hs state and introduce the practical method used to obtain it, followed by a study of the switching regimes in the 180° STN planar LC device. In Section 5.3, results are presented from our simulation model that has been used to predict the polarization-independent behaviour of the LC devices considered in this work. The penultimate section, Section 5.4, presents experiment results of the phase modulation of the 180°-twist STN planar LC device using a phase-shifting Mach–Zehnder interferometer to measure the optical phase in the time domain. The measured optical phase modulation of the T-Hs state is then analysed and compared with results from simulations. Finally, Section 5.5 concludes the work.

5.2 Polarization-independent Phase Modulator Design

Figure 5.1 illustrates two different 90° TN-LC device configurations while **Figure 5.2** illustrates two different 180° STN-LC device configurations with potential for showing polarization-independent characteristics. The director distribution was determined using a methodology that will be described in further detail in Section 5.3a. These configurations are based on 90°-twist TN LC devices and 180°-twist STN LC devices. For the 90°-twist TN LC device, the director in the middle of the LC layer is either tilted (referred to as a tilted LC device) or aligned parallel to the surface (referred to as a planar LC device). The 180º STN-LC devices were fabricated by doping a chiral additive to a nematic LC host. By precisely controlling the chiral dopant, the pitch of the LC mixture can be set to be twice the thickness of the LC layer, creating a 180º twist state within the device. By filling the LC mixture into a pi-cell (anti-parallel pretilt angles on both surfaces), the director in the middle of the LC layer becomes tilted; referred to herein as a tilted STN device. Conversely, when filled into a

Fréedericksz device (parallel pretilt angles on both surfaces), the LC director in the middle of the layer aligns parallel to the surface, we refer to this as a planar STN device.

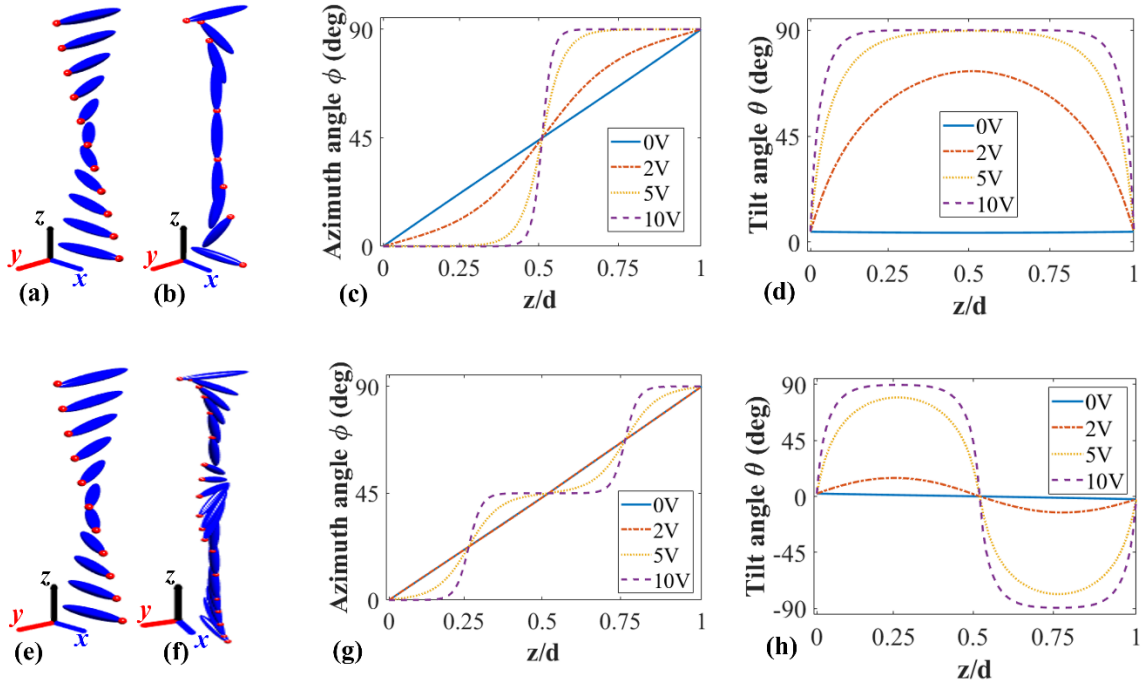

Figure 5.1. Simulations of the director distribution for include a 90° TN-LC device with the central director tilted relative to the surface plane (tilted 90° TN-LC device), a 90° TN-LC device with the central director parallel to the surface plane (planar 90° TN-LC device). Visualization of the director distribution of the tilted 90° TN-LC device: (a) the ground state with no voltage applied and (b) the twisted vertical state under an applied voltage of 10 Vrms. (c) and (d) show the azimuth angle (the angle between the projection of the director on the *xy*-plane and *x*-axis) and the tilt angle (the angle between the director direction and the *xy*-plane) of the LC director, respectively, as a function of the position within the LC layer for different applied voltages, showing the formation of 90° twisted vertical state. Visualization of director distribution of the planar 90° TN-LC device under a sudden voltage: (e) the ground state with no voltage applied and (f) the 90° twisted Hs state under a burst driving voltage of 10 Vrms. (g) and (h) are director profiles under different applied voltages showing the formation of 90° twisted Hs state.

Fig. 5.1(a) – (d) illustrate the change in director configuration for the tilted 90° TN-LC device with and without an applied voltage. Fig. 5.1(a) shows the director profile in the voltage-off state. In this case, when the LC device is placed between parallel polarizers, no light is transmitted at zero voltage. However, if placed between crossed polarizers, all light passes through, demonstrating a so-called polarization rotation effect. When an electric field above

the threshold is applied to the device, the LC director in the bulk tends to reorient in the direction parallel to the applied electric field (as shown in Fig. 5.1(b)), which coincides with the light propagation direction. In this case the polarization rotation effect gradually diminishes allowing for light transmission through parallel-aligned polarizers. The evolution in the director profile (in terms of the azimuth and tilt angle) with an increase in the applied voltage is shown in Fig. 5.1(c) and (d). At high voltages, this reorientation induces the same changes in the effective birefringence within two boundary layers along the *x* and *y* directions, leading to a consequential phase shift in the two directions simultaneously. Notably, in this state the optical characteristics of the outgoing light will not be affected by the LC layer for any initial polarization state of the incoming light, regardless of whether the polarization is along the x-axis or y-axis. As a result, at high voltage the TN-LC device exhibits polarization-independent characteristics.

When applying a sudden voltage to the planar 90° TN-LC device, whose voltage off state is shown in Fig. 5.1(e), the device can form two extra boundary layers in the middle of the device at 45° relative to the alignment direction, as shown in Fig. 5.1(f). This state is a transient state with a lifetime of around a few tens of milliseconds. The director profiles for the whole process as the voltage increases are shown in Fig. 5.1(g) (azimuth angle) and (h) (tilt angle). Unfortunately, the two extra boundary layers that are formed do not help with the polarization independence. However, this configuration motivated us to consider the transient state in the planar 180° STN-LC device, *vide-infra*.

The tilted 180° STN-LC device is commonly used in the design of optical phase modulators, typically using the so-called π-twist state [143][144]. In the voltage off state, it exhibits a 180º twist of the LC director across the device, as shown in Fig. 5.2(a). When a

voltage is applied, the LC director gradually reorients to align with the external electric field direction, forming a bend-like state known as the twisted vertical (T-V) state or π-twist state, as shown in Fig. 5.2(b). In this process, as the LC director begins to untwist, amplitude modulation is achieved when the LC is placed between polarizers. The untwisting results in a change in the effective birefringence of the device, leading to a continuous phase change. The director profile simulated for this device under applied voltages are shown in Fig. 5.2(c) and (d) for the azimuth and tilt angle, respectively.

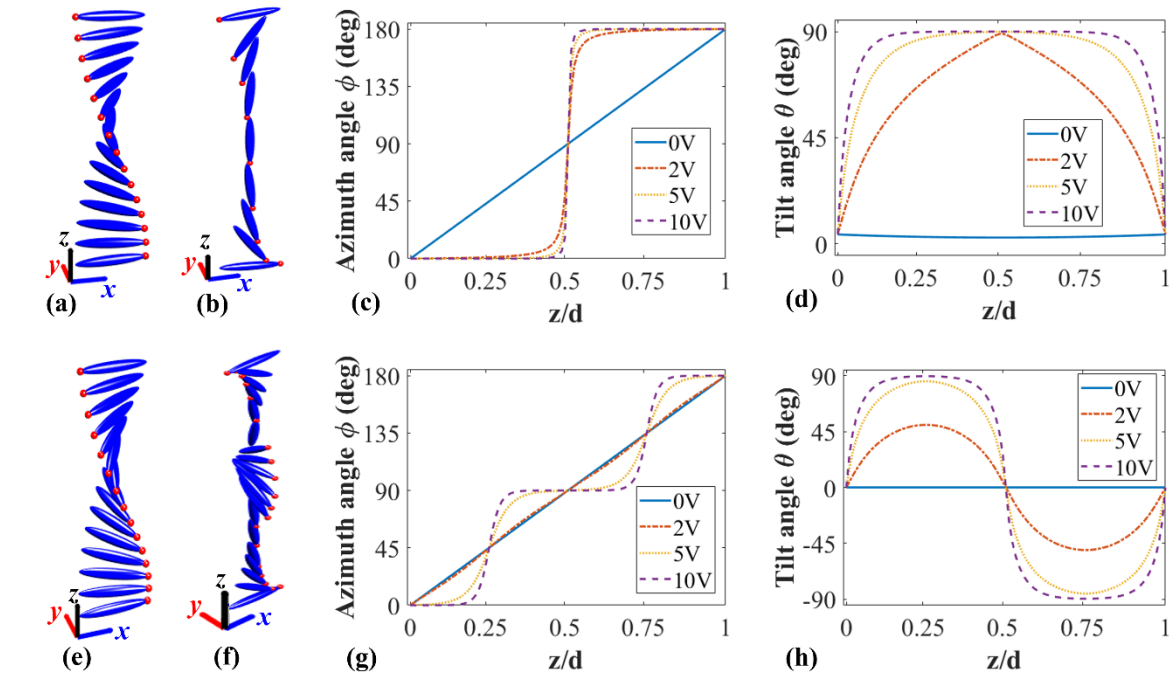

Figure 5.2. Simulations of the director distribution for a 180° STN device with anti-parallel pretilt alignment (tilted 180° STN-LC device), and a 180° STN device with parallel pretilt alignment (planar 180° STN-LC device). Visualization of the director distribution of the tilted 180° STN-LC device: (a) the ground state with no voltage applied and (b) the twisted vertical state under an applied voltage of 10 Vrms and (c) show the azimuth angle (the angle between the projection of the director on the *xy*-plane and *x*-axis) and (d) the tilt angle (the angle between the director direction and the *xy*-plane) of the LC director, respectively, as a function of the position within the LC layer for different applied voltages, showing the formation of a 180° twisted vertical state. Visualization of the director distribution of the planar 180° STN-LC device under a sudden voltage: (e) the ground state with no voltage applied and (f) the 180° twisted Hs state under a voltage of 10 Vrms. (g) and (h) are the director profiles under different applied voltages showing the formation of 180° twisted Hs state.

Figures 5.2(e) – (h) illustrate the corresponding behaviour of the planar 180° STN-LC device. In the voltage off state, it exhibits a 180º twist of the LC director across the device, as shown in Fig. 5.2(e). When we apply a sudden voltage to the LC, it undergoes a distinct transformation, forming two layers in the middle of the device with directions that are oriented perpendicular to the surface alignment, as illustrated in Fig. 5.2(f). This is referred to as the twisted Hs state (T-Hs). The two boundary layers next to the surface are along the *y*-direction and the newly formed boundary layers in the centre of the device are along the *x*-direction. This dual-layer configuration enables the device to simultaneously generate phase modulation in both the *x* and *y* directions, exhibiting a potentially polarization-independent performance for a sudden applied voltage. Like the planar TN configuration, this state is also transient, with a lifetime of only a few tens of milliseconds. The director profiles for different applied voltages are depicted in Fig. 5.2(g) and (h). In comparison to the conventional 90° TN-LC device, which forms only one boundary layer in each direction, the planar 180° STN-LC device forms two boundary layers in each direction. As a result, this allows the T-Hs state in the planar 180° STN-LC device to achieve double the phase modulation of that observed for the 90° TN-LC device.

The simulations presented in Figure 5.2 indicate that the planar 180° STN-LC device warrants further investigation in terms of its potential for polarization-independent phase modulation. Towards this end, **Figure 5.3** illustrates the typical transformations between the different states of a planar 180° STN-LC device, similar to the transformations observed in the nematic pi-cell studied previously (illustrated in Section 4.1). With no applied voltage, the LC director continuously twists 180° within the device, forming the planar twisted-twist (T-T) state with LC director in the middle of the layer aligns parallel to the surface. When the applied voltage is above a critical voltage $V_{th}(TT)$ ($V_{th}(TT) \approx 1.8$ Vrms), the internal electric field is

sufficient to switch the device to a twisted asymmetric H (T-Ha) state ($E > E_{T\text{-}Ha}$). The director profile then transforms into one of the T-Ha states, which is analogous to the Ha state in a conventional nematic pi-cell, but with the director continuously twisted. Alternatively, a transient twisted Hs (T-Hs) state is obtained if a sudden voltage above a higher threshold voltage (V_{th}(T-Hs)) is applied to the T-T state, then the internal field is above that required to switch to a symmetric state ($E > E_{T\text{-}Hs}$).

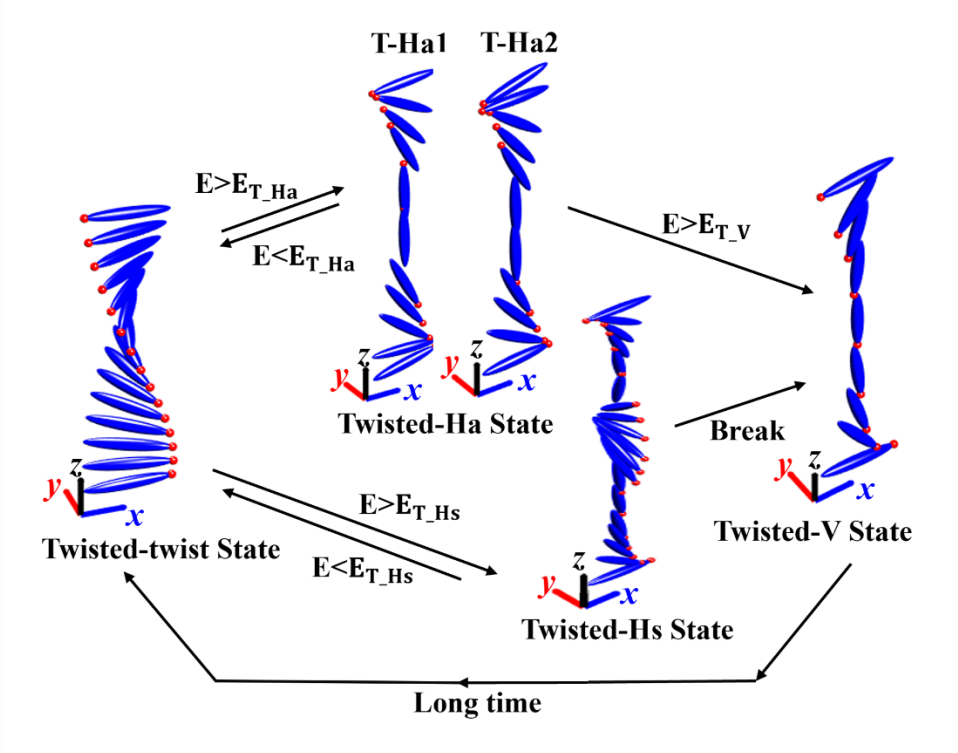

Figure 5.3. An illustration showing the transitions of a planar 180° STN-LC device into different states for different applied electric field conditions. Further details are provided in the text.

The T-Hs state is a transient state that tends to drift into the T-Ha state(s) or transform to the T-V state directly under a higher applied voltage. As the operating voltage is increased above the threshold for the T-V state, V_{th}(T-V), which is approximately 5.8 Vrms for the device under investigation, the internal field is increased above that required to switch to a T-V state ($E > E_V$), and both the T-Hs and T-Ha states will transform to the T-V state because the T-V state is energetically favourable at high voltages. The T-Hs state can persist for a few

milliseconds even under a high voltage exceeding V_{th} (T-V). In this investigation, the device maintained the T-Hs state for approximately 35 ms under an applied voltage of 30 Vrms. For very high voltages, the T-V state shows very little twist. Moreover, when the voltage is removed and the device is in either the T-Ha or T-Hs state, the director alignment will return to the T-T state directly; on the contrary, when removing the voltage in the T-V state, the device gradually returns to the T-T state via domain growth over the course of a few seconds.

To obtain the transient T-Hs state in practice, a burst driving method is typically required [96]. The burst driving voltage consists of an operating period, where the voltage is applied to stimulate the formation of the T-Hs state, and a relaxation period, where no voltage is applied, ensuring the device fully recovers to the T-T state. The operation period needs to be long enough to switch the device to the T-Hs state but short enough to avoid it collapsing to either the T-Ha state or nucleating to the T-V state. By repeating the burst voltage periodically, a stable T-Hs state can be regularly obtained.

The device used in the experiment consisted of glass substrates that were coated with indium tin oxide (ITO) electrodes and antiparallel rubbed polyimide alignment layers, referred to in this work as a Fréedericksz cell. The surface pretilts were typically 4° to 5° and the cell gap was 8.9 μm. The LC mixture was prepared by adding the chiral dopant R811 (a low twisting power chiral dopant sourced from Merck KGaA) (a concentration by weight of 0.48 wt.%) into the nematic LC mixture, E7 (Synthon Ltd.) so as to form a chiral nematic LC with a long pitch of 17.8 μm. By capillary filling into the Fréedericksz cell, a planar 180° STN-LC device was obtained. In addition to the twist profile due to the chiral dopant, the LC director also exhibits a minor tilt in opposite directions influenced by the pretilt angle for the two different surface alignments. This leads to the director in the middle of the LC layer aligning

perpendicular to the surface alignment direction, while maintaining a tilt angle of 0°, parallel to the surface. To distinguish the transformation between the states, the device was positioned between crossed polarizers on a polarizing optical microscope (POM) (Olympus BX51), with the rubbing direction (optic axis) aligned at 45° to the polarizer and analyser pair. The applied voltage was a square wave of 1 kHz with a variable burst duration repeated every 1 s.

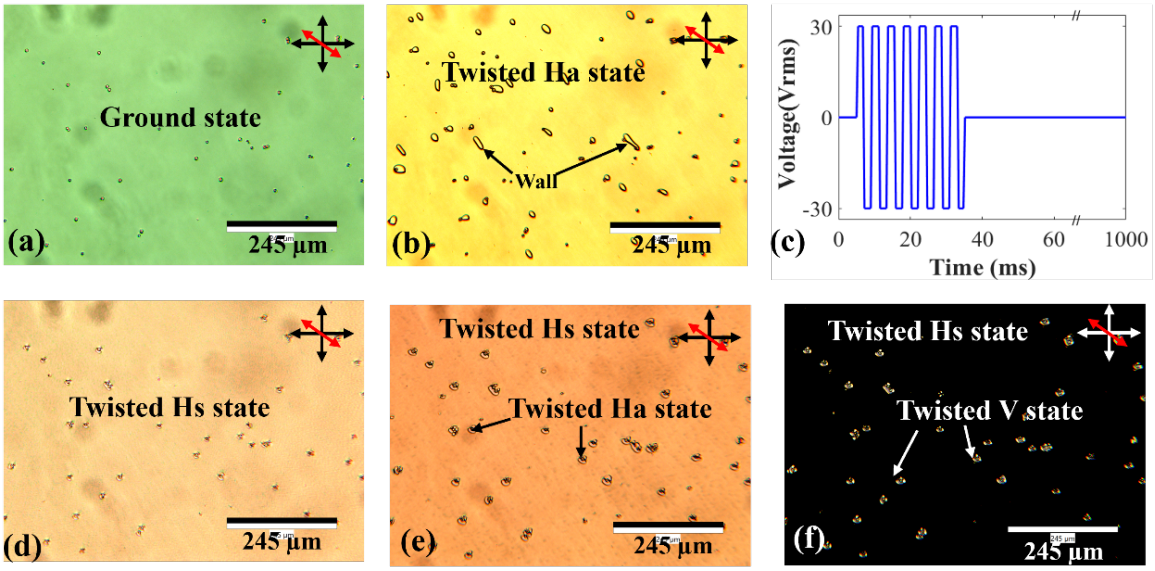

Figure 5.4. Representative polarizing optical microscope images of the switching states of a planar 180° STN-LC device: (a) the planar twisted-twist (T-T) ground state of the device under no applied voltage (the black dots in the image are the spacer beads distributed throughout the cell to obtain a uniform cell gap); (b) the twisted Ha state formed under a continuous driving voltage of 4 Vrms; (c) the waveform of the burst driving voltage without modulation used to apply on the device to capture the T-Hs state; (d) the twisted Hs state formed for a burst driving voltage of 5 Vrms for 50 ms; (d) a mixture of twisted Hs states and twisted Ha states under a burst driving voltage of 3.5 Vrms for 90 ms, and (e) mixture of twisted Hs states and twisted V states under a burst driving voltage of 10 Vrms for 70 ms. The crossed double-headed black arrows (white double-headed arrows in (e)) represent the orientations of the transmission axes of the polarizer and the analyser, and the double-headed red arrows represent the rubbing direction of the alignment layers.

Figure 5.4 demonstrates the voltage switching processes in a planar 180º STN-LC device with the aid of exemplar POM images of the various states. In Fig. 5.4(a), the device exhibits the twist ground state with no applied voltage. When a continuous driving waveform was applied to the device, the T-Ha and T-V states could be observed for lower and higher voltages, respectively, but the T-Hs could not be observed due to its transient lifetime. Both

the T-Ha and T-V states generally exhibit a uniform colour in the image. T-Ha states can be distinguished since several domain walls formed in the field of view when a voltage was applied, as shown in Fig. 5.4(b). These domain walls form due to the opposite reorientation of the LC director in adjacent regions, leading to the formation of two distinct states: T-Ha1 and T-Ha2. The primary difference between these states lies in whether the LC director tilt distortions accumulate predominantly at the top surface or the bottom surface of the device. This behaviour is analogous to the well-known Ha1 and Ha2 states observed in a nematic π-cell [96]. Despite their structural differences, the T-Ha1 and T-Ha2 states exhibit similar birefringent properties, making them challenging to differentiate based on optical effects alone. The domain wall serves as the interface between these two regions, where the LC director is parallel to the surface in the centre of the wall [120]. In Fig. 5.4(b), T-Ha states can be seen as a yellow colour with domain walls formed under a continuous driving voltage of 4 Vrms.

To generate the T-Hs state, we applied a burst driving voltage to the device, which results in a more complex scenario due to a mix of states arising from imperfect surface alignments. The waveform of the burst driving voltage without modulation is shown in Fig. 5.4(c). The image of the T-Hs state was captured during the voltage on operation period, during which the T-Hs state remains stable and for higher drive voltages typically exhibits a uniform dark colour, as expected for a polarization-independent phase modulator. However, in some cases, when a burst driving voltage with lower amplitude is applied, the T-Hs state appears coloured rather than dark, as shown in Fig. 5.4(d) and (e)– this state would not be suitable for polarisation independent phase modulation. This phenomenon occurs because twisted director remains within the device, and boundary layers remain coupled, which prevents complete polarization independence and leads to colour variations in the image. Fig. 5.4(d) depicts the T-Hs state as an orange colour for a burst driving voltage of 5 Vrms for 50 ms. Very small T-

Ha states are present around the beads but can be ignored. A mixture of states appears when we adjust the amplitude and duration of the operating burst voltage. For example, Fig. 5.4(e) depicts the mixture of T-Hs and T-Ha states for a burst driving voltage of 3.5 Vrms for a duration of 90 ms. The T-Hs state appears as uniform regions of orange colour, while the T-Ha state has also formed, as indicated by small regions around certain spacer beads or defects due to imperfect surface alignment. However, the T-Ha state consistently collapses during the relaxation period between voltage bursts. When the T-Ha region remains small relative to the total T-Hs area, and the T-Hs state maintains its polarization-independent characteristics (appearing dark under POM with crossed polarizers), the device still meets the design requirements for a polarization-independent phase modulator based on the T-Hs state.

As voltage increases, Fig. 5.4(f) depicts the mixture of the T-Hs and T-V states for a burst driving voltage of 10 Vrms for 70 ms, with the image taken during this 70 ms voltage on period. The T-Hs state appears as the black regions which dominate the image. This is because the T-Hs state exhibits polarization-independent characteristics, which means it does not alter the polarization of the incident light after passing through the polarizer on the microscope. Therefore, when the device is placed between crossed polarizers, the image appears black. In addition, the T-V state is also observed in the image, emerging where parts of the T-Hs state have evolved into the T-V state, particularly around the spacer beads. During this stage, the regions of the T-V state are small and fully collapse to the ground state between bursts, leaving no impact on the T-Hs state formation and phase modulator design. However, if the amplitude and duration of the burst driving voltage are further increased, the T-V states will then dominate and replace all of the T-Hs states, making the device unsuitable for a polarization-independent phase modulator.

The above characterization shows that the T-Hs state can be obtained by applying a burst driving voltage to the planar 180° STN-LC device, notwithstanding the potential mixture of various states due to the imperfect surface alignment. However, the conditions for utilizing the T-Hs state as a polarization-independent phase modulator are stringent. To ensure effective polarization-independent phase modulation, several criteria must be met. First, proportion of the T-Ha states in the mixture of T-Ha and T-Hs states is not detrimental, and the formed T-V state fully collapses during the relaxation between repeated voltage bursts. Additionally, the boundary layers within the device must be decoupled, ensuring that the device exhibits a dark image under POM with crossed polarizers, which is indicative of polarization independence. When these conditions are satisfied, the device is particularly promising for use in optical phase modulation that requires polarization-independent performance. In the following section, results are presented to confirm the polarization-independent properties.

5.3 Simulation of Phase Modulator

a) The Model

To demonstrate the intricate dynamics of the T-Hs state, we developed a simulation method to first estimate the transient switching behaviour of the LC director before then employing Jones calculus to determine the potential polarization independence and the optical phase modulation performance based on the obtained director profiles.

The transient switching dynamics of the twisted LC device were investigated using a numerical model similar to that described in Section 4.4. This is designed to solve the Ericksen–Leslie continuum equations. The key difference is that the simulation in the STN model accounts for both angular orientations, whereas the model in Chapter 4 considers the LC director orientation only in one dimension. This approach provides valuable insights into the

reorientation of the LC director during transient switching events. The free-energy density considered in the simulations is the composite of elastic, electrostatic, and dielectric contributions, which are the core factors influencing the director behaviour. Here, we deliberately disregard the internal flow within the LC and the chiral factor (q), since they have a secondary impact on the calculation results, but their removal can greatly streamline the calculation process.

The general form of the Frank elastic energy density, f_d, can be written in terms of the director $\vec{n}$, as indicated in Eq. (2-11) in Section 2.3.1, and is presented again here for convenience as

$$f_d = \frac{1}{2}K_{11}[\nabla \cdot \vec{n}]^2 + \frac{1}{2}K_{22}[\vec{n} \cdot (\nabla \times \vec{n})]^2 + \frac{1}{2}K_{33}[\vec{n} \times (\nabla \times \vec{n})]^2 \quad (5-1)$$

where K_{11}, K_{22} and K_{33} are the splay, twist and bend elastic constants, respectively. The electrostatic energy density f_e takes the form

$$f_e = -\frac{1}{2}\Delta\varepsilon\varepsilon_0\left(\vec{n} \cdot \vec{E}\right)^2 \quad (5-2)$$

where $\Delta\varepsilon$ is the dielectric anisotropy, ε_0 is the permittivity of free space, and $\vec{E}$ is the internal electric field.

We define the director in modified spherical polar coordinates, where the LC orientation is represented by an angle θ (the director tilt angle out of the surface plane) and φ (the director twist angle around the z-axis), as shown in **Figure 5.5**(a). Both are a function of time and position across the LC layer (defined as the z coordinate in what follows). In this case, the director can be expressed as:

$$\vec{n} = \begin{pmatrix} cos\,\theta\, cos\varphi \\ cos\,\theta\, sin\varphi \\ sin\theta \end{pmatrix} \quad (5-3)$$

The applied electric field $\vec{E}$ is along the z-direction and the total energy density, L, is given by:

$$L = f_d + f_e = \frac{1}{2}K_{11}\cos^2\theta\left(\frac{\partial\theta}{\partial z}\right)^2 + \frac{1}{2}K_{22}\cos^4\theta\left(\frac{\partial\varphi}{\partial z}\right)^2 + \frac{1}{2}K_{33}[\sin^2\theta\left(\frac{\partial\theta}{\partial z}\right)^2$$

$$+ \sin^2\theta\cos^2\theta\left(\frac{\partial\varphi}{\partial z}\right)^2] - \frac{1}{2}\Delta\varepsilon\varepsilon_0\sin^2\theta\,{E_z}^2 \qquad (5-4)$$

where E_z is the local electric field that is determined from the requirement for continuity in the z-component of the electric flux density. To determine the director behaviour, we then need to substitute Eq. (5-4) into the Euler-Lagrange equations, as explained in Section 2.4. This results in two dissipation equations, one for each of the angular deformations θ and φ:

$$\frac{\partial}{\partial z}\left(\frac{\partial L}{\partial \theta'}\right) - \frac{\partial L}{\partial \theta} = \frac{\partial \mathcal{D}}{\partial \dot{\theta}} \qquad (5-5)$$

$$\frac{\partial}{\partial z}\left(\frac{\partial L}{\partial \varphi'}\right) - \frac{\partial L}{\partial \varphi} = \frac{\partial \mathcal{D}}{\partial \dot{\varphi}} \qquad (5-6)$$

where $\mathcal{D}$ is the dissipation function.

The total energy density, L, can then be substituted into Equations (5-5) and (5-6) to give:

$$\frac{\partial \mathcal{D}}{\partial \dot{\theta}} = \left(\frac{\partial\varphi}{\partial z}\right)^2(K_{33}\sin^2\theta - K_{33}\cos^2\theta + 2\,K_{22}\cos^2\theta)\cos\theta\sin\theta$$

$$+\left(\frac{\partial\theta}{\partial z}\right)^2(K_{33}-K_{11})\cos\theta\sin\theta + \frac{\partial^2\theta}{\partial\theta^2}(K_{11}\cos^2\theta + K_{33}\sin^2\theta)$$

$$+ \Delta\varepsilon\varepsilon_0\cos\theta\sin\theta\,{E_z}^2 \qquad (5-7)$$

$$\frac{\partial \mathcal{D}}{\partial \dot{\varphi}} = -2\frac{\partial\varphi}{\partial z}\frac{\partial\theta}{\partial z}\cos\theta\sin\theta\,[2\,K_{22}\cos^2\theta + K_{33}(\sin^2\theta - \cos^2\theta)]$$

$$+ \frac{\partial^2\varphi}{\partial\varphi^2}\cos^2\theta\,(K_{22}\cos^2\theta + K_{33}\sin^2\theta) \qquad (5-8)$$

which are then solved using a finite difference approach, with a regular grid in the z-direction. As noted above, flow components were not considered. Additionally, the LC director tilt is fixed at the surfaces, with the tilt angle specified as 4°, which allows for the computation of $\theta(z,t)$ and $\varphi(z,t)$.

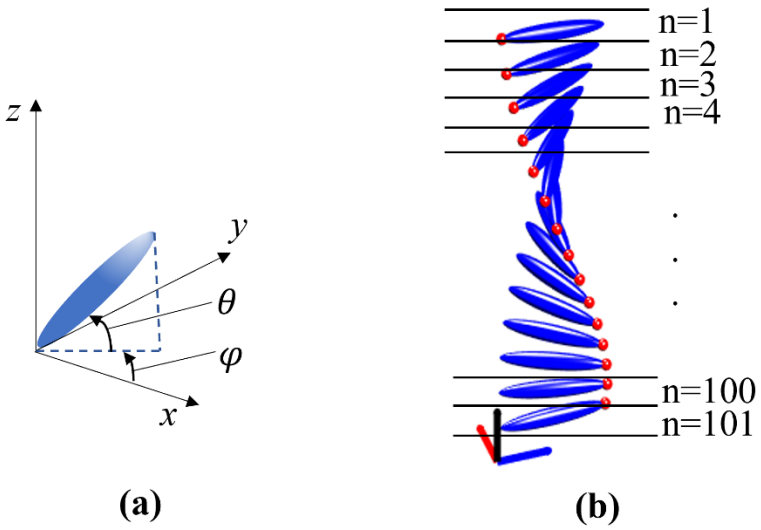

Figure 5.5. Illustration of the LC director: (a) angular orientation of the director, defined by the polar angle (θ) and azimuthal angle (φ) in modified spherical polar coordinates and (b) schematic of the simulation model used for a super-twisted nematic LC device, regarded as a layer-by-layer orientated LC plate along the z-axis.

To determine the optical performance of the TN and STN-LC devices, Jones calculus was used to extract the optical phase modulation from the obtained director profiles. By considering that the light is travelling along the positive z-direction through the LC device, the electric field for the outgoing light, $\mathbf{E_{out}}$, can then be expressed as:

$$\mathbf{E_{out}} = \mathbf{J_{LC}}\,\mathbf{E_{in}} \qquad (5-9)$$

where $\mathbf{E_{in}}$ is the electric field of the incident light and $\mathbf{J_{LC}}$ is the LC phase retarder.

To represent the entire LC device, we conceptualize the device, with a thickness of d, as being comprised of $N_z = 101$ distinct slices, illustrated in Fig. 5.5(b). Each slice is akin to a plate characterized by specific angles $\theta(z,t)$ and $\varphi(z,t)$. The internal 99 slices have a thickness of $\frac{d}{N_z-1}$, while the two surface slices each have a half-thickness of $\frac{d}{2(N)_z-1}$ to accurately model the surface layer performance. The total optical effect is obtained by multiplying the Jones matrices of all individual slices. The whole LC device can then be expressed as:

$$\mathbf{J_{LC}}(V,t) = \mathbf{J_{N_z}}\,\mathbf{J_{N_z-1}}\cdots\mathbf{J_2}\,\mathbf{J_1} = \begin{bmatrix} Ae^{i\delta_x} & B \\ C & De^{i\delta_y} \end{bmatrix} \qquad (5-10)$$

where $\mathbf{J_{LC}}(V,t)$ is the Jones matrix for the entire LC device under an applied voltage *V* at time *t*. $\mathbf{J_1}$ and $\mathbf{J_{N_z}}$ are two surface slices with a thickness of $\frac{d}{2(N)_z-1}$, while $\mathbf{J_2}$ to $\mathbf{J_{N_z-1}}$ are the internal slices with a thickness of $\frac{d}{N_z-1}$. *A* and *D* represent the amplitude ratios for the horizontal and vertical polarization components in the output light to those in the input light, respectively, while δ_x and δ_y refer to the phase shift for these polarization components. Additionally, *B* and *C* refer to the conversion ratio between one polarization component in the input light to another one in the output light.

The Jones matrix for the surface slices ($n = 1$ or $n = N_z$) is expressed as:

$$\mathbf{J_n} = R(-\varphi)MR(\varphi) =$$

$$\begin{bmatrix} cos\varphi & -sin\varphi \\ sin\varphi & cos\varphi \end{bmatrix} \begin{bmatrix} e^{\frac{2\pi}{\lambda}n_{eff}\frac{d}{[\![2(N]\!]_z-1)}} & 0 \\ 0 & e^{\frac{2\pi}{\lambda}n_o\frac{d}{[\![2(N]\!]_z-1)}} \end{bmatrix} \begin{bmatrix} cos\varphi & sin\varphi \\ -sin\varphi & cos\varphi \end{bmatrix} \qquad (5-11)$$

For the internal slices ($2 \le n \le N_z - 1$), the Jones matrix is:

$$\mathbf{J_n} = R(-\varphi)MR(\varphi) =$$

$$\begin{bmatrix} cos\varphi & -sin\varphi \\ sin\varphi & cos\varphi \end{bmatrix} \begin{bmatrix} e^{\frac{2\pi}{\lambda}n_{eff}\frac{d}{N_z-1}} & 0 \\ 0 & e^{\frac{2\pi}{\lambda}n_o\frac{d}{N_z-1}} \end{bmatrix} \begin{bmatrix} cos\varphi & sin\varphi \\ -sin\varphi & cos\varphi \end{bmatrix} \quad (5-12)$$

The effective birefringence, n_{eff}, is given by:

$$n_{eff} = \frac{n_e n_o}{\sqrt{n_e^2 \sin^2\theta + n_o^2 \cos^2\theta}} \quad (5-13)$$

where n_o and n_e are the ordinary and extraordinary refractive indices, respectively. The angles $\theta(z,t)$ and $\varphi(z,t)$ define the orientation of the LC director within each layer, contributing to the overall transmission properties. $\theta(z,t)$ controls the optical phase delay while $\varphi(z,t)$ determines the rotation angle. The transformation of polarization states as light passes through the device can be expressed as:

$$\begin{pmatrix} E_{x_o}(V,t) \\ E_{y_o}(V,t) \end{pmatrix} = \begin{bmatrix} Ae^{i\delta_x} & B \\ C & De^{i\delta_y} \end{bmatrix} \begin{pmatrix} E_{x_i} \\ E_{y_i} \end{pmatrix} \quad (5-14)$$

where E_{x_o} and E_{y_o} are the electric fields for the outgoing light for the *x* and *y* polarizations, respectively, and E_{x_i} and E_{y_i} are the electric fields for the incoming light for *x* and *y* polarizations, respectively.

The optical phase at various time intervals or applied voltages can be extracted from the matrix expression in Eq. (5-14). This enables us to determine the dynamic phase modulation, offering valuable insights into the dynamic behaviour of the LC devices under different operating conditions. Notably, the elements of the leading diagonal in the matrix of $\mathbf{J_{LC}}(V,t)$ represent the amplitude and phase changes for light that remains polarized in the same direction as the incident light. On the other hand, the off-diagonal elements of the Jones matrix $\mathbf{J_{LC}}(V,t)$ denote the amplitude and phase changes for light that becomes polarized in a direction

orthogonal to the incident light. Therefore, for an ideal polarization-independent LC device, the leading diagonal elements would be same, showing simultaneous modulation for both polarizations, and the off-diagonal components are negligible, indicating that the device does not convert the polarization state into an orthogonal state.

b) planar 180° STN-LC Device

Figure 5.6 presents the simulation results for the planar 180° STN-LC device to further investigate its potential for optical phase modulation and polarization independence. Also shown are results for the tilted 90° TN-LC device for the purposes of comparison. The parameters used in the simulation were K_{11} = 11.1 pN, K_{22} = 6.5 pN, K_{33} = 17.1 pN, $\varepsilon_{\perp}$ = 5.4, $\varepsilon_{\parallel}$ = 17.4, n_o = 1.5, n_e = 1.72 and the wavelength was set to λ = 632.8 nm.

To begin our discussion, we consider first the results for the tilted 90° TN-LC device. Fig. 5.6(a) and 5.6(b) present the optical magnitude and phase modulation, respectively, for a 90° TN-LC device with thickness of 5 µm placed between parallel polarizers. The outgoing light shows the same behaviour for the two orthogonal polarizations. The results indicate a relatively low magnitude when the voltage is below 2.0 Vrms, reaching an ideal magnitude of 1 when the voltage surpasses this threshold. This transition signifies a critical operational range where the magnitude values become conducive (approximately 1) for polarization-independent phase modulation capability. Here, a magnitude of 1 corresponds to 100% transmittance. For voltages below 2.0 Vrms, the TN-LC device exhibits polarization transformation behaviour, where the amplitude and phase are coupled. As the applied voltage increases from 2.0 Vrms to 10.0 Vrms, the polarization-independent optical phase modulation of this TN LC device changes from 1.5 rad to 0.25 rad. Within this voltage range, the liquid crystal directors become

perpendicular to the surfaces, and the two surface boundary layer regions are effectively decoupled.

Simultaneous consideration of magnitude and phase modulation is vital for a comprehensive analysis for the optical phase modulators. To facilitate this evaluation, we employ the use of a polar plot, which offers a useful visualization where the radius corresponds to the magnitude and the polar angle represents the achieved phase modulation. Fig. 5.6(c) shows that the TN-LC device can attain about π/2 rad polarization-independent phase modulation as the applied voltage changes from 1.8 Vrms to 10.0 Vrms. A noteworthy aspect of this observation is the consistent phase modulation between the two orthogonal directions, which indicates that the device exhibits the same optical phase modulation characteristics for both the *x* and *y* polarized incident light simultaneously. This highlights the device's polarization-independent characteristics at high voltages. The corresponding LC director distribution was shown previously in Figures 5.1(a) - (d).

We now move on to the simulation results for the planar 180° STN-LC device when switched into the T-Hs state. Fig. 5.6(d) and (e) plot the computed optical magnitude and phase modulation results of the device placed between two parallel polarizers, respectively, and Fig. 5.6(f) presents these combined results as a polar plot. As the voltage changes from 4 Vrms to 15 Vrms, the two polarization curves are consistent, and the magnitude approaches 1, indicating decoupling between the amplitude and phase performance. Within this operational range, the device exhibits successful polarization-independent optical phase modulation of π/2 rad when switched in the T-Hs state. The corresponding LC director distribution was shown previously in Figures. 5.2(e) - (h).

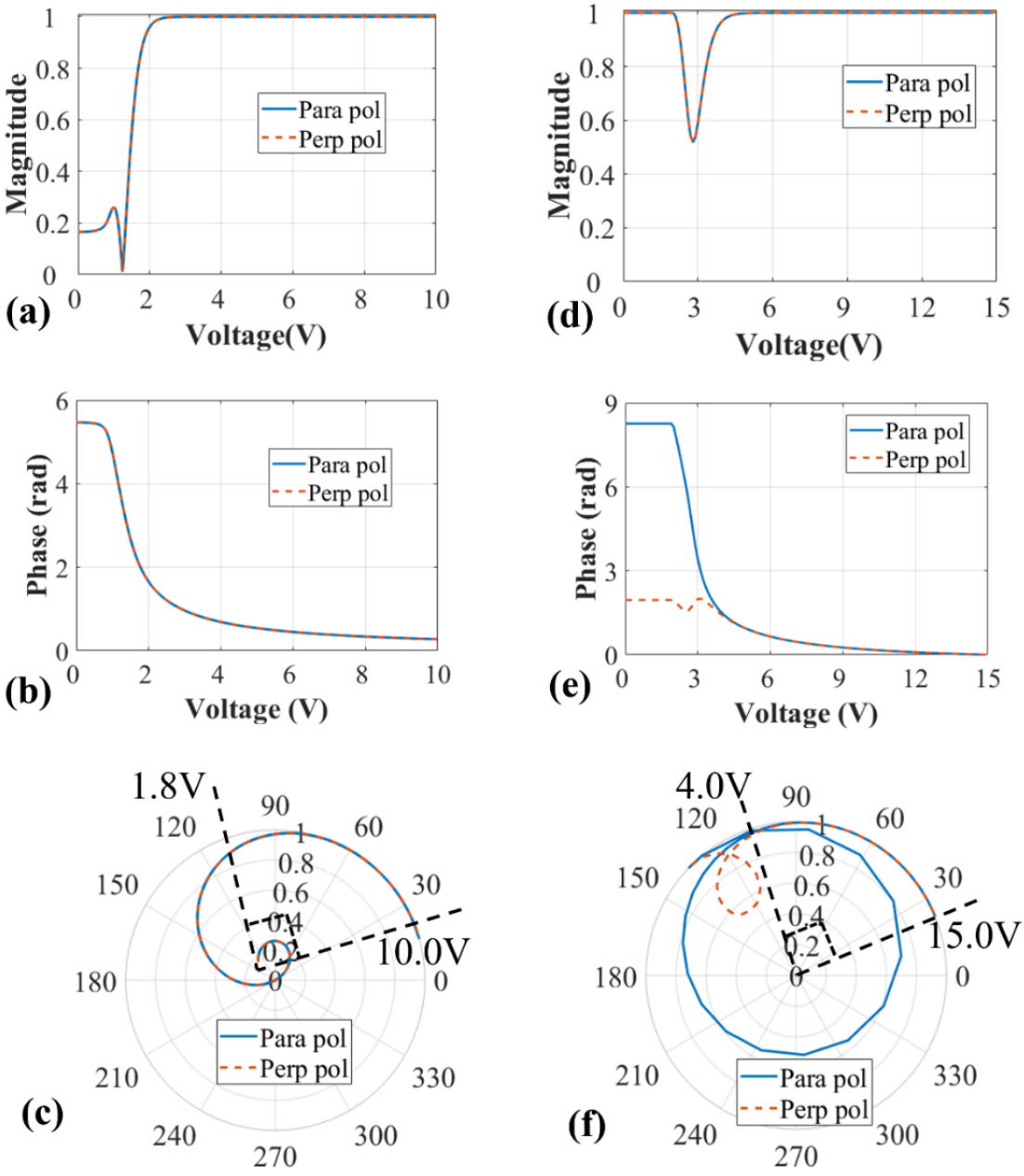

Figure 5.6. Simulation results showing the polarization-independent performance for the tilted 90° TN-LC device (a-c) and the planar 180° STN-LC device switched into the T-Hs state (d-f), both with LC layer thicknesses of 5 µm. (a, d) the magnitude and (b, e) the optical phase modulation as a function of applied voltage for the two orthogonal linear polarization states. (c, f) magnitude and phase represented as a polar plot for different applied voltages and the two polarization states. In the legend, for the 90° TN-LC device, "Para pol" refers to the polarization component parallel to the alignment direction of the bottom surface (*x* direction in Fig. 5.1(a)-(b)), and 'Perp pol' is the polarization component parallel to the alignment direction of the top surface (*y* direction in Fig. 5.1(a)-(b)). For the 180° STN-LC device, "Para pol" refers to the polarization component parallel to the device's alignment directions (*x* direction in Fig. 5.2(e)-(f)), and "Perp pol" refers to polarization component perpendicular to the device's alignment direction (*y* direction in Fig. 5.2(e)-(f)).

In practical applications, a planar 180° STN-LC device with a thin LC layer thickness, such as the 5μm thick device in Figures. 5.6(d) - (f), is incapable of achieving a polarization-independent T-Hs state. Within a constrained space, the LC director in the bulk remains in a continuous twisted condition, instead of forming decoupled boundary layers along the *x* and *y* directions necessary for phase modulation during the switch 'on' and 'off' switching processes. Consequently, the continuously twisted director profile changes the polarization of incident light to its orthogonal direction, undermining the polarization-independent characteristics. To address this issue, the thickness of the planar STN-LC device must be increased, which enables the boundary layers to be decoupled in the T-Hs state during the dynamic switching process, facilitating polarization-independent performance as well as sufficient optical phase modulation.

To demonstrate the enhanced phase modulation capability, **Figure 5.7** presents the phase modulation results for planar STN-LC devices with a thickness of 30 μm. The applied burst driving voltage is shown in Fig. 5.7(a). The results correspond to the transmission mode, where light passes through the device once, as illustrated in Figures 5.7(b)–(d). The polar plot in Fig. 5.7(b) highlights the phase modulation characteristics of the T-Hs state within a specific voltage range, where the magnitude approaches an ideal value of 1, and the two polarization curves remain consistent, indicating polarization independence. Notably, the device achieves a full 2π rad phase modulation as the applied voltage increases from 4.7 to 15.0 Vrms. The dynamic performance, shown in Fig. 5.7(c), reveals that the device attains an optical phase modulation of 1.21 rad within 1 ms during both the switch-on and switch-off processes. Fig. 5.7(d) presents the polar plot about the behaviour of the device in the relaxation process from 29 ms to 47.2 ms. The results indicate that the transmittance remains close to 1, confirming stable polarization-independent performance. Furthermore, the phase modulation curve

exhibits a half-circle trajectory, corresponding to the π rad phase modulation achieved in 5.3 ms, and a full-circle trajectory, illustrating the completion of 2π rad phase modulation in 18.2 ms.

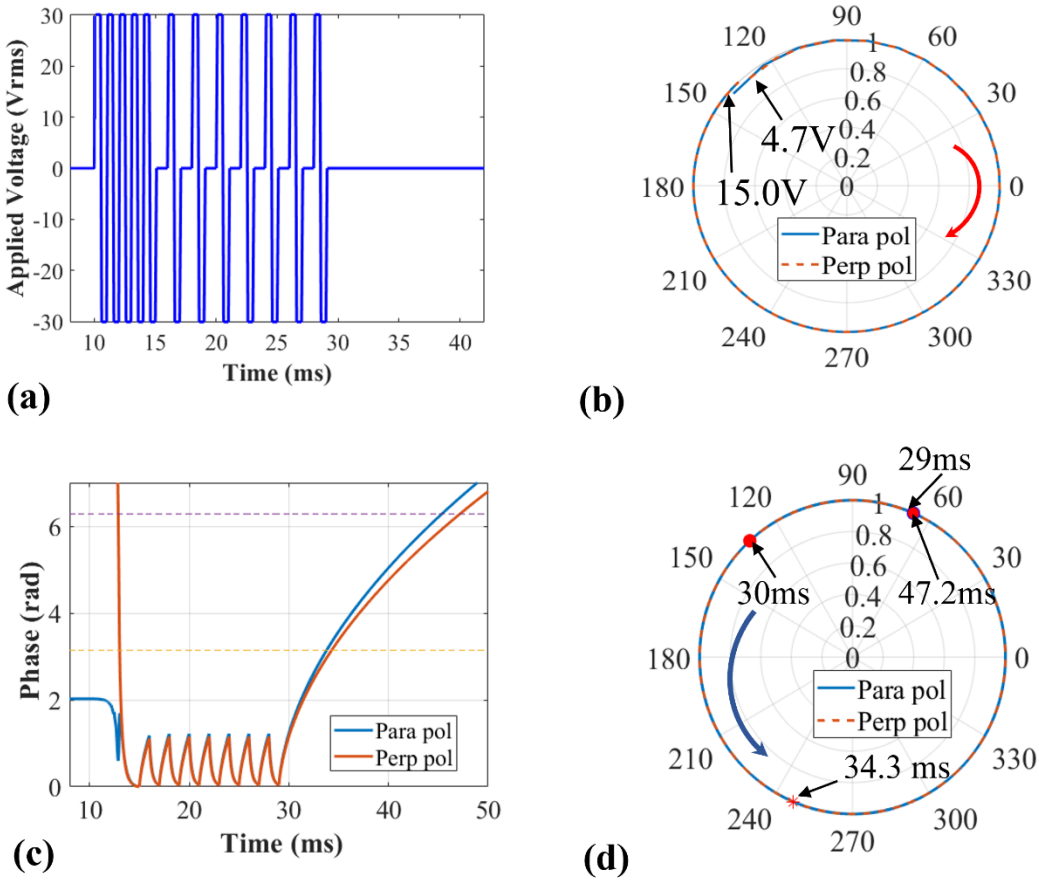

Figure 5.7. Simulation results demonstrating the polarization-independent performance of the planar 180° STN-LC device in the T-Hs state with an increased thickness of 30 μm. (a) the waveform of the burst driving voltage including modulation inside and (b) phase modulation performance as a function of applied voltage, ranging from 4.7 V to 15.0 V and (c) dynamic response under burst voltage of 30 Vrms, and the two horizontal dashed lines indicate π and 2π rad phase modulation, respectively and (d) polar plot representation of the dynamic performance from 29 ms to 47.2 ms, extracted from (b). In the legend, "Para pol" refers to the polarization component parallel to the device's alignment direction (*x* direction in Fig. 1(m)-(n)), and "Perp pol" refers to polarization component perpendicular to the device's alignment direction (*y* direction in Fig. 1(m)-(n)).

These results confirm that the device maintains polarization independence in the T-Hs state while being capable of achieving nearly full 2π rad optical phase modulation, albeit with an extended response time. Thus, while increasing the device thickness enhances phase

modulation, it introduces trade-offs, as thicker devices require higher driving voltages and exhibit slower switching speeds in certain voltage regimes [145].

5.4 Experimental Results and Discussion

The measurement is conducted with the phase-shifting Mach–Zehnder interferometer, described in Section 3.4. To evaluate the polarization-independent performance of the LC device, it is initially placed between two parallel polarizers to assess its response to incident light aligned with its alignment direction. Subsequently, the LC device is rotated by 90º to measure its response to light from the orthogonal direction. If the LC device exhibits the same response in both directions, it can be considered polarization-independent This approach ensures high measurement efficiency, as losses are primarily limited to the interferometric system and minimal losses from the optical components. Additionally, to ensure measurement accuracy, the interferometric system is rigorously calibrated. The designed PSI enables single-shot acquisition of interference data, effectively minimizing the impact of external environmental noise and other disruptive factors. Moreover, applying a FFT method to extract data enhances the resolution of the phase modulation results by enabling a high sampling rate of the original data. This measurement allows for precise representation of phase modulation with very short time intervals.

Figure 5.8 presents the experimental results for the performance of a planar 180° STN-LC device switched into the twisted Hs state at room temperature. The device, with thickness of 8.9 μm, was switched to the T-Hs state using a burst driving voltage, enabling the investigation of its performance within the limited existence of the transient state. As shown in Fig. 5.8(a), the designed voltage waveform consists of two stages: a priming stage and a modulation stage. During the priming stage, a 1 kHz square wave at 30 Vrms is applied for 5

ms (10 - 15 ms) without modulation, ensuring that the device fully transitions into the T-Hs state. This is followed by the modulation stage where the driving signal alternates between an "on" state for 1 ms and an "off" state for 1 ms. Subsequently, a relaxation stage followed with no voltage signal applied, which enables the device fully recovered to the ground state.

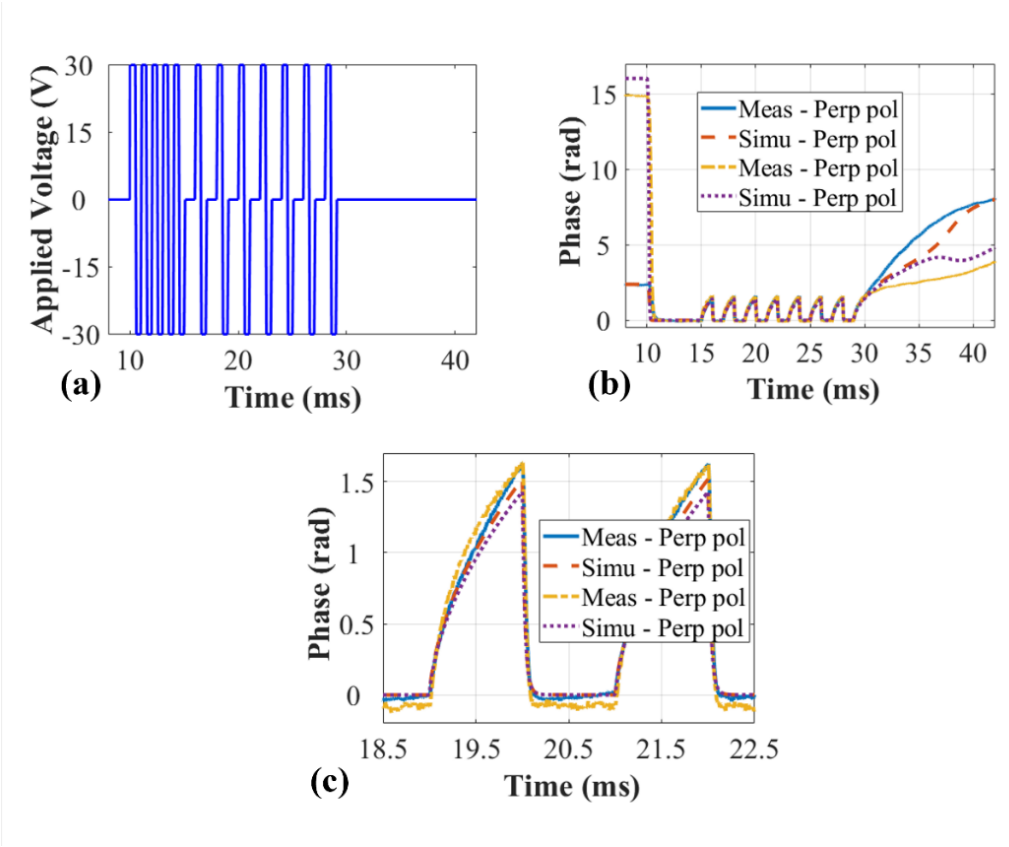

Figure 5.8. The optical phase modulation results of a planar 180° STN-LC device switched into the T-Hs state at room temperature. (a) The burst driving voltage applied to the device, which consisted of a 20 ms operating period repeated every 1 s. (b) The measured and simulated optical phase modulation for two polarization states of the device: parallel ('Para pol') and perpendicular ('Perp pol') to the surface alignment. (c) enlarged section of (b) to illustrate the consistency between experiments and simulations.

Figure 5.8(b) and (c) depict the measured and simulated optical phase modulation results, respectively, for both polarizations extracted for a single-pass configuration (i.e., light passed through the device only once in transmission during the measurement) for the experimental setup described in Section 3.4. During the voltage-on periods (e.g., 16–17 ms, 18–19 ms, 20–21 ms), the device rapidly transitions into the T-Hs state within approximately

0.15 ms, leading to a nearly flat phase response curve. This rapid switching is attributed to the high voltage amplitude, which induces an almost instantaneous transition to the T-Hs state. Conversely, during the voltage-off periods (e.g., 15–16 ms, 17–18 ms, 19–20 ms, etc.), the relaxation process is significantly slower due to the viscosity of the LC, resulting in a gradually changing phase response curve. Under these conditions, the device achieves a $\frac{\pi}{2}$ phase shift within 1 ms for both polarizations in a single-pass setup, confirming its polarization-independent characteristics. With a four-pass configuration, the device achieves a full 2π rad phase modulation with polarization-independent performance within 1 ms during the relaxation process. The consistency between the measurement and simulation results further validates the accuracy of the simulation model as well as our understanding of the switching process. As indicated in Figure 5.7, the 30-μm-thick LC device achieves 2π rad phase modulation within 5.3 ms in reflection mode and 18.2 ms in transmission mode during the relaxation period under the voltage of 30 Vrms.

For future applications, the device can switch between multiple phase levels while maintaining stability within a $\frac{\pi}{2}$ range for extended time duration in the existence of T-Hs state. The requirement for a blackout period (standard for all phase modulator applications) when switching between two phase levels within a π/2 rad phase is 1 ms for this device. Additionally, the 50% duty cycle for switch-on and switch-off states can be modulated through the control scheme. It is worth noting that the device's intrinsic twisted structure makes it sensitive to the illumination angle, which may limit its applicability as a phase modulator in scenarios requiring large-angle incidence. However, in most applications, where the incident light is predominantly normal to the surface, this angular dependence has minimal impact on performance. Moreover, the burst driving scheme restricts its applicability in matrix-addressed systems. A potential

solution to stabilize the transient T-Hs state involves creating a thin polymer layer at the device's midplane using direct laser writing techniques.

Figure 5.9 presents the dynamic director distribution during the 1 ms relaxation process, based on the simulation insights. The boundary layers in the *x* and *y* directions grow over time and are decoupled from the bulk. The device must be sufficiently thick to allow these boundary layers to remain decoupled which is crucial for maintaining polarization-independent performance. As shown in Fig 5.8 (b) between 29 ms and 31 ms, the device begins to exhibit polarization dependence at approximately 30.4 ms, which is around 1.4 ms into the relaxation process. At this point, the phase modulation reaches its maximum polarization-independent value of approximately 1.76 radians, after which the curves for parallel and perpendicular polarizations begin to diverge. This behaviour is intrinsic to the twisted LC structure, where prolonged relaxation causes the boundary layers to couple with each other, leading to the observed polarization dependence. It is expected that using a thicker LC layer (greater than 8.9 μm) and applying specific voltages would enable greater polarization-independent phase modulation, as predicted in Fig. 5.7. To achieve this goal in a single-pass setup within the time domain, potential strategies include: (1) increasing the LC layer thickness to expand the phase modulation range while preserving polarization independence; and (2) optimizing the LC material properties, such as adjusting viscosity or elastic constants, to facilitate faster switching and achieve greater phase modulation under similar driving conditions.

Figure. 5.10 illustrates the dynamic director profiles during the above switching process. The tilt angle θ changes at different time points, which reflects the growth of the boundary layers. Meanwhile, the azimuth angle, φ, remains stable during the process, which

signifies the decoupling of the four boundary layers. This stability and the decoupling imply that the LC director responsible for phase modulation maintains a consistent orientation without twisting during the switching time. Since a twisted LC director typically contributes to polarization transformation, its absence ensures polarization-independent phase modulation. This characteristic ensures successful polarization-independent phase modulation with the transient T-Hs state of the planar 180° STN device.

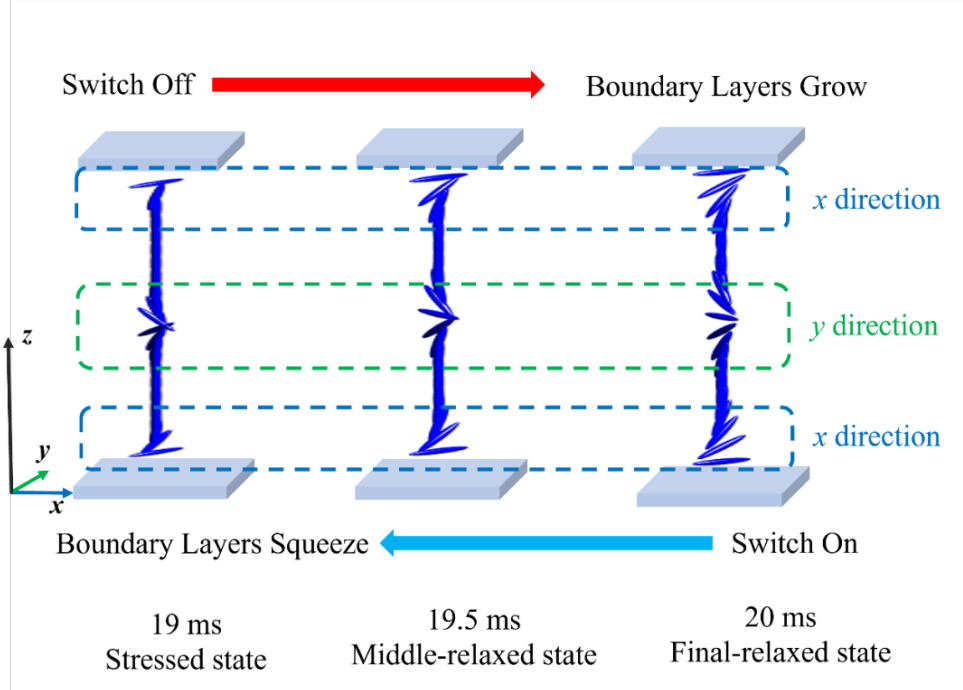

Figure 5.9. Illustration of the director distribution during the switch on and switch off process in 1 ms: the left-to-right sequence represents the process of switch on, while the right-to-left represents the process of switch off, both occurring within 1 ms timescale.

Lastly, **Figure 5.11**(a) and (b) depict polar plot representations of the simulated dynamic switching process for the 8.9 μm device during the 1 ms 'on' and 1 ms 'off' cycles, respectively. The plots consistently maintain a magnitude of 1, indicating phase-only modulation. The similarity between the 'switch-on' and 'switch-off' processes suggests a smooth growth and compression of the decoupled boundary layers. Additionally, the consistent

phase modulation curves for both polarizations confirm a polarization-independent phase modulation of π/2 rad within 1 ms, with no amplitude modulation present.

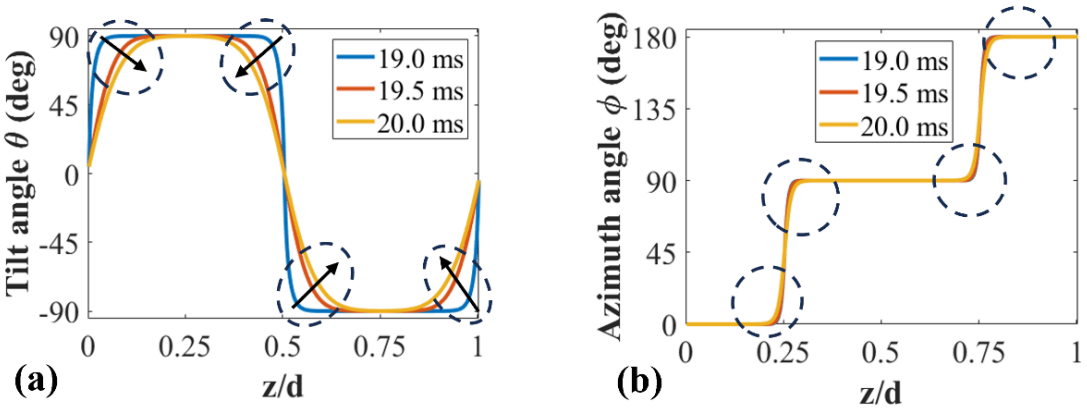

Figure 5.10. Illustration of the director distribution during the relaxation process in 1 ms: (a) the tilt angle and (b) the azimuth angle of the director orientation at different times during the switching process.

Additionally, Fig. 5.8(b) reveals an interesting observation that at t = 29 ms, the two polarization curves remain consistent for only 2 ms before diverging. This suggests that this device can maintain polarization independence for just 2 ms after the 30 Vrms voltage is removed. To explore this further, Fig. 5.11(c) and (d) simulate the 'switch-on' and 'switch-off' process lasting for 15 ms. The results shows that the start point of the 'switch-on' process is aligned with the end point of the 'switch-off', as the LC director in the device completely relaxes at this time. Moreover, in the middle of the switching process, the curves for the 'switch-on' are quite different from those of the 'switch-off'. This discrepancy can be attributed to the growth of boundary layers during this period and the onset of coupling to the bulk, resulting in a continuous structure with the LC director orientation angle φ changing along different paths during the 'switch-on' and 'switch-off' processes [146]. This inconsistency leads to varying phase modulation curves, indicating inconsistent polarization dependent performance during this switching period.

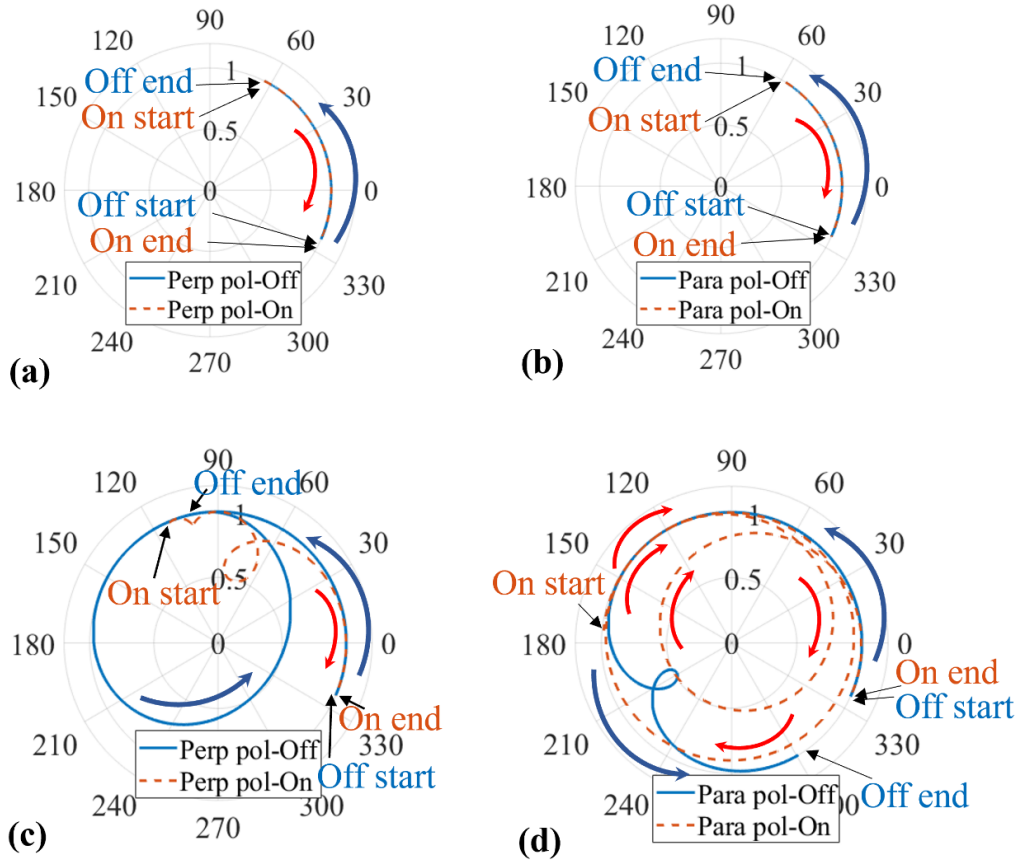

Figure 5.11. The simulated optical phase performance for the 'switch-on' and 'switch-off' processes in 1 ms for polarizations perpendicular (a) and parallel (b) to the surface alignment for the 8.9 µm planar 180° STN LC device. The simulated optical phase performance for the 'switch-on' process and 'switch-off' process in 15 ms for polarizations perpendicular (c) and parallel (d) to the surface alignment.

5.5 Summary

In this chapter, we have investigated the potential for achieving polarization-independent characteristics using twisted nematic LCs and highlight the potential of planar 180° STN devices for use as polarization-independent optical phase modulators. It is shown that to achieve polarization-independent behaviour requires the formation of the so-called twist symmetric H state (T-Hs) using a burst driving voltage. The T-Hs state is distinguished by the formation of central boundary layers that orient perpendicular to the alignment direction at the substrate surfaces. Together, these two newly formed LC boundary layers, along with the two

layers formed originally along the alignment direction, enable the device to modulate light for two perpendicular polarizations simultaneously, thus achieving optical polarization independence.

Experiments were carried out using a phase-shifting Mach–Zehnder interferometer, which enabled the time-dependent optical phase variation to be obtained by employing FFT analysis. The device used in the experiments was a nematic LC Fréedericksz device with an LC layer thickness of 8.9 μm, filled with a long-pitch chiral nematic LC mixture to form a planar 180° STN device. The experimental results revealed that this device switched into the T-Hs state can achieve polarization independence as well as a π/2 rad optical phase modulation in 1 ms under a burst voltage of 30 Vrms at room temperature in a transmission configuration. The measurement results show good consistency with the simulation results that were based upon a combination of the Ericksen–Leslie continuum equations to determine the dynamic director profile and then Jones calculus to compute the phase and polarization properties.

6. Optimizing the Optical System Architecture

This chapter introduces the development and application of an optimization algorithm designed to explore the optimal combination of nematic liquid crystal (LC) devices, including nematic Fréedericksz cells and 90° twisted nematic (TN) devices, with waveplates, such as quarter-waveplates and half-waveplates. The aim is to determine configurations that meet practical application requirements, which are often unattainable with a single LC device. The optimization targets two key performance criteria: achieving polarization-independent phase modulation and maximizing the phase modulation depth for a single polarization. For example, whether a nematic Fréedericksz device combined with waveplates can be optimized to achieve polarization-independent phase modulation is investigated, as well as whether this combination improves single-polarization phase modulation. Similarly, for the 90° TN LC device, the inherent polarization independence at higher voltages is further optimized to extend the phase modulation range with minimal trade-offs in amplitude performance when it is in combination with waveplates. Also, 90° TN LC is explored to determine whether it can achieve enhanced single-polarization phase modulation when combined with waveplates.

The optimization is conducted in two domains: the voltage domain and the time domain. In the voltage domain, the objective is to ensure consistent behaviour across a broad voltage range, which is expected to achieve stable and predictable phase modulation. In the time domain, the focus is on the dynamic response, particularly within the rapid 1 ms relaxation process, to optimize temporal performance and ensure fast switching characteristics. These efforts are critical for improving the performance of optical systems in dynamic and practical environments where precise control of polarization and phase modulation is required. This optimization of the LC device with waveplates offers several advantages, including enhanced

adaptability of device performance, increased flexibility to accommodate diverse optical environments, making it a robust framework for advanced optical systems.

This chapter is structured into four sections. First, the optical configuration to be optimized is described, followed by an introduction to the algorithm and verification of the optimization technique using a well-established optical principle. Next, the optimization method is applied to the nematic Fréedericksz device, which operates under single polarization along its alignment direction. The investigation focuses on two objectives: achieving polarization-independent phase modulation and maximizing phase modulation of a single polarization, both in the voltage and time domains. These four aspects are systematically discussed. Other single-polarization operated devices, such as certain states in Pi-cells, are not explored in detail, as they follow similar principles as the Fréedericksz device. Furthermore, the potential of the 90° twisted nematic (TN) device is examined for polarization independence and enhanced phase modulation along a single polarization in both the voltage and time domain. Other twisted nematic LC devices, including the 180° super-twisted nematic (STN) device, are not investigated, as they follow a similar optimization methodology. Finally, the chapter concludes with a summary of the findings.

6.1 Optimization Algorithm Demonstration

6.1.1 System Introduction

This section details the implementation of the optimization process, which integrates precise optical simulations of LC devices and waveplates with the appropriate application of an advanced optimization algorithm. The optical system to be optimized comprises three key components: the first waveplate, the LC device, and the second waveplate, as depicted in **Figure 6.1**. The optimization aims to adjust key system parameters, including the retardances

and rotation angles of the waveplates and rotation angles of the LC device, to achieve target optical performance. These parameters are accurately integrated to provide a robust representation of the system through Jones matrix formalism. Specifically, the first waveplate is characterized by its retardance (Pa_1) and rotation angle (Pa_2), while the second waveplate is defined by its retardance (Pa_3) and rotation angle (Pa_4). The LC device is represented by its Jones matrix derived from above mentioned simulation (in Section 4.3 and Section 5.3), where its phase modulation and polarization state can be extracted. To introduce more degrees of freedom, the rotation angle (Pa_5) of the LC device is also included in its positioning within the optical system.

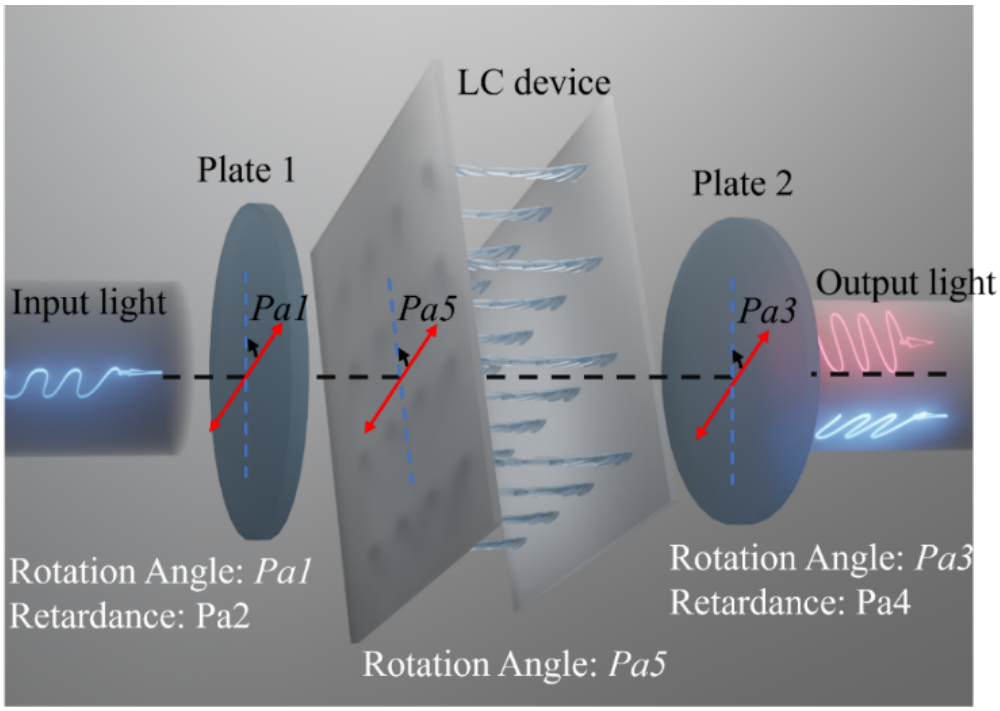

Figure 6.1. Schematic of the optical path configuration comprising two waveplates and a LC device placed in the middle. The optimization parameters include the retardance (Pa_1) and rotation angle (Pa_2) of the first waveplate, as well as the retardance (Pa_3) and rotation angle (Pa_4) of the second waveplate. The rotation angle of the LC device (Pa_5) is also considered in the optimization process. The Jones matrix of the LC device is derived from prior simulations. This figure illustrates the system using a Fréedericksz LC device as an example, with a single-polarized incident light and both *x*- and *y*-polarized components in the outgoing light, which demonstrates the polarization-independent modulation capability of the Fréedericksz device in combination with the two waveplates.

As light propagates through the system, it interacts first with the first waveplate, then the LC device, and finally exits through the second waveplate. The optical behaviour of the system is mathematically expressed as:

$$\mathbf{E_{out}} = \mathbf{J_{P2}} \cdot \mathbf{J_{LC}} \cdot \mathbf{J_{P1}} \cdot \mathbf{E_{in}} \qquad (6-1)$$

where $\mathbf{J_{P1}}$ and $\mathbf{J_{P2}}$ represent the Jones matrices of the first and second waveplates, respectively, characterized by their retardances and rotation angles (Pa_1 Pa_2, Pa_3, and Pa_4). $\mathbf{J_{LC}}$ represents the Jones matrix of the LC device at the rotation angle (Pa_5). $\mathbf{E_{in}}$ and $\mathbf{E_{out}}$ are the input and output light vectors, respectively.

The Jones matrices of the waveplates are typically determined by their retardances (η) and rotation angles (θ). A waveplate without rotation can be expressed as a diagonal phase matrix:

$$\mathbf{WP} = \begin{bmatrix} 1 & 0 \\ 0 & e^{i\eta} \end{bmatrix} \qquad (6-2)$$

When rotation effects are included, the rotated waveplate is expressed as:

$$\mathbf{J_P} = \mathbf{MRM} \cdot \mathbf{WP} \cdot \mathbf{RM} \qquad (6-3)$$

where the rotation matrices are defined as:

$$\mathbf{MRM} = \begin{pmatrix} cos\theta & -sin\theta \\ sin\theta & cos\theta \end{pmatrix} \qquad (6-4)$$

$$\mathbf{RM} = \begin{pmatrix} cos\theta & sin\theta \\ -sin\theta & cos\theta \end{pmatrix} \qquad (6-5)$$

Using these definitions, the Jones matrices for the two waveplates, J_{P1} and J_{P2}, are explicitly expressed as:

$$\mathbf{J_{P1}} = \begin{pmatrix} \cos(Pa_2) & -\sin(Pa_2) \\ \sin(Pa_2) & \cos(Pa_2) \end{pmatrix} \cdot \begin{bmatrix} 1 & 0 \\ 0 & e^{i(Pa_1)} \end{bmatrix} \cdot \begin{pmatrix} \cos(Pa_2) & \sin(Pa_2) \\ -\sin(Pa_2) & \cos(Pa_2) \end{pmatrix} \qquad (6-6)$$

$$\mathbf{J_{P2}} = \begin{pmatrix} \cos(Pa_4) & -\sin(Pa_4) \\ \sin(Pa_4) & \cos(Pa_4) \end{pmatrix} \cdot \begin{bmatrix} 1 & 0 \\ 0 & e^{i(Pa_3)} \end{bmatrix} \cdot \begin{pmatrix} \cos(Pa_4) & \sin(Pa_4) \\ -\sin(Pa_4) & \cos(Pa_4) \end{pmatrix} \qquad (6-7)$$

For the LC device, its Jones matrix $\mathbf{M_{LC}}$ is derived from simulation results and incorporates rotation effects using the same transformation matrices:

$$\mathbf{J_{LC}} = \mathbf{MRM} \cdot \mathbf{M_{LC}} \cdot \mathbf{RM} \qquad (6-8)$$

where MRM and RM are the rotation matrices in Eq. (6-4) and Eq. (6-5). Substituting these into the expression gives:

$$\mathbf{J_{LC}} = \begin{pmatrix} \cos(Pa_5) & -\sin(Pa_5) \\ \sin(Pa_5) & \cos(Pa_5) \end{pmatrix} \cdot \boldsymbol{M_{LC}} \cdot \begin{pmatrix} \cos(Pa_5) & \sin(Pa_5) \\ -\sin(Pa_5) & \cos(Pa_5) \end{pmatrix} \qquad (6-9)$$

Substituting all terms in Eq. (6-1), the Jones matrix of the whole system can be obtained, which enables the extraction of the corresponding phase modulation and amplitude variations for each polarization state. The combined optical effects of the system, which consists of the two waveplates and the LC device, can be expressed using the total Jones matrix as:

$$\mathbf{J_T} = \mathbf{J_{P1}} \cdot \mathbf{J_{LC}} \cdot \mathbf{J_{P2}} = \begin{bmatrix} A\mathrm{e}^{i\delta_x} & B \\ C & D\mathrm{e}^{i\delta_y} \end{bmatrix} \qquad (6-10)$$

where δ_x and δ_y represent the phase modulation for the *x*- and *y*-polarized components, respectively, the elements *A* and *D* correspond to the amplitude modulation of the *x*- and *y*-polarized components, while the off-diagonal elements *B* and *C* describe the coupling between polarization states, indicating polarization transformation effects within the system.

The LC device's behaviour is modelled across varying voltages or over different time intervals. By substituting a series of Jones matrices for the LC device - each representing its characteristics at different voltage levels or time points - the optimization process effectively captures the device's dynamic performance. Within the optimization algorithm, this is implemented using a loop that iterates through multiple voltage values or time steps, calculating the optical response at each instance. As a result, the obtained phase modulations

(δ_x and δ_y), the amplitude responses (*A* and *D*), and the off-diagonal elements (*B* and *C*) are evaluated over a defined voltage range or time period.

To be specific, when the LC device is optimized in the voltage domain, its behaviour is represented by a series of Jones matrices corresponding to different voltage levels:

$$\mathbf{M}_{\mathbf{LC_{vol}}} = \left[\boldsymbol{M}_{\boldsymbol{LC_{V1}}}, \boldsymbol{M}_{\boldsymbol{LC_{V2}}}, \boldsymbol{M}_{\boldsymbol{LC_{V3}}}, \ldots \boldsymbol{M}_{\boldsymbol{LC_{VN}}}\right] \quad (6-11)$$

Similarly, if the LC device is optimized in the time domain, its behaviour is characterized by a series of Jones matrices at different time points:

$$\mathbf{M}_{\mathbf{LC_{time}}} = \left[\boldsymbol{M}_{\boldsymbol{LC_{t1}}}, \boldsymbol{M}_{\boldsymbol{LC_{t2}}}, \boldsymbol{M}_{\boldsymbol{LC_{t3}}}, \ldots \boldsymbol{M}_{\boldsymbol{LC_{tN}}}\right] \quad (6-12)$$

By calculating the LC device's performance across multiple voltages and time points, a set of results is obtained for Eq. (6-10). The corresponding phase modulation (δ_x and δ_y), amplitude performance (*A* and *D*), and off diagonal elements (*B* and *C*) in the voltage domain are expressed as:

$$\boldsymbol{\delta}_{\boldsymbol{x_{vol}}} = \left[\delta_{\boldsymbol{x}_{V1}}, \delta_{\boldsymbol{x}_{V2}}, \delta_{\boldsymbol{x}_{V3}}, \ldots \delta_{\boldsymbol{x}_{VN}}\right] \quad (6-13)$$

$$\boldsymbol{\delta}_{\boldsymbol{y_{vol}}} = \left[\delta_{\boldsymbol{y}_{V1}}, \delta_{\boldsymbol{y}_{V2}}, \delta_{\boldsymbol{y}_{V3}}, \ldots \delta_{\boldsymbol{y}_{VN}}\right] \quad (6-14)$$

$$\mathbf{A_{vol}} = \left[\mathrm{A}_{V1}, \mathrm{A}_{V2}, \mathrm{A}_{V3}, \ldots \mathrm{A}_{VN}\right] \quad (6-15)$$

$$\mathbf{D_{vol}} = \left[\mathrm{D}_{V1}, \mathrm{D}_{V2}, \mathrm{D}_{V3}, \ldots \mathrm{D}_{VN}\right] \quad (6-16)$$

$$\mathbf{B_{vol}} = \left[\mathrm{B}_{V1}, \mathrm{B}_{V2}, \mathrm{B}_{V3}, \ldots \mathrm{B}_{VN}\right] \quad (6-17)$$

$$\mathbf{C_{vol}} = \left[\mathrm{C}_{V1}, \mathrm{C}_{V2}, \mathrm{C}_{V3}, \ldots \mathrm{C}_{VN}\right] \quad (6-18)$$

Similarly, in the time domain, the phase modulation and amplitude response matrices are given by:

$$\boldsymbol{\delta}_{\mathbf{x_T}} = \left[\delta_{\mathbf{x}_{T1}}, \delta_{\mathbf{x}_{T2}}, \delta_{\mathbf{x}_{T3}}, \ldots \delta_{\mathbf{x}_{TN}}\right] \quad (6-19)$$

$$\boldsymbol{\delta_{\mathbf{y_T}}} = \left[\delta_{\mathbf{y}_{T1}}, \delta_{\mathbf{y}_{T2}}, \delta_{\mathbf{y}_{T3}}, \ldots \delta_{\mathbf{y}_{TN}}\right] \quad (6-20)$$

$$\mathbf{A_T} = [\mathrm{A}_{T1}, \mathrm{A}_{T2}, \mathrm{A}_{T3}, \ldots \mathrm{A}_{TN}] \quad (6-21)$$

$$\mathbf{D_T} = [\mathrm{D}_{T1}, \mathrm{D}_{T2}, \mathrm{D}_{T3}, \ldots \mathrm{D}_{TN}] \quad (6-22)$$

$$\mathbf{B_T} = [\mathrm{B}_{T1}, \mathrm{B}_{T2}, \mathrm{B}_{T3}, \ldots \mathrm{B}_{TN}] \quad (6-23)$$

$$\mathbf{C_T} = [\mathrm{C}_{T1}, \mathrm{C}_{T2}, \mathrm{C}_{T3}, \ldots \mathrm{C}_{TN}] \quad (6-24)$$

In summary, incorporating the Jones matrix of the LC device at multiple voltages or time points, rather than at a single operating condition, enhances the system's adaptability and ensures optimal performance across a broader operational range. This capability enables more practical applications, such as integration into imaging systems where dynamic updates to the imaging process are required.

6.1.2 Algorithm Introduction

The Particle Swarm Optimization (PSO) algorithm [147]-[149] was employed to optimize the system parameters. PSO is a population-based optimization technique inspired by the social behaviour of bird flocks or fish schools. It effectively explores the parameter space and delivers a global optimum solution with high precision while meeting the mathematical criteria established for the system. PSO was chosen over alternative optimization methods due to its robust global search capability, computational efficiency, and suitability for optimizing continuous parameters, such as rotation angles and retardances. Unlike gradient-based methods, which require a differentiable objective function and are not well-suited for complex optical simulations, PSO operates effectively without gradient information. Additionally, while other algorithms such as Genetic Algorithms (GA) [150][151] and Simulated Annealing (SA) [152][153] can be effective, they often exhibit slower convergence rates and require more complex implementation strategies. PSO's strength in avoiding local minima further enhances the reliability of the optimization process, particularly when dealing with multi-modal

objective functions. These attributes collectively establish PSO as an ideal choice for achieving precise and polarization-independent optical performance in this study.

The application of the PSO algorithm in this optimization system is illustrated in the flowchart shown in **Figure 6.2**. This algorithm begins by initializing the optimization constants, including the population size and the maximum number of iterations. For this study, the population size (*popsize*) is set to 100 (could be larger, if necessary, like 200, or 500), which means in one iteration, this would calculate 100 groups $\mathbf{E_{out}}$ derived from different optimization parameters. The iteration count is set to be 100 (could be larger, if necessary, like 200). Also, the Jones matrix of the LC device under voltage or in the time domain are also imported as constants in the algorithm.

The initial population of particles and their velocities in the PSO algorithm are randomly generated within predefined ranges. Each particle represents a potential solution to the optical system, with its position corresponding to a specific set of system parameters. The retardances of the waveplates (Pa_1 and Pa_3) are initialized around $\frac{\pi}{2}$ for quarter-waveplates and around π rad for half-waveplates or set to arbitrary values within the range [0, π rad] to represent arbitrary initiated waveplates with specific phase retardances. The rotation angles (Pa_2, Pa_4, and Pa_5) are randomly assigned values within [0, 360°]. The "velocity" refers to the rate of change of these parameters during optimization, which is used to guide how particles move through the solution space. Initial velocities are assigned random values within [2, 5] to balance exploration and exploitation, which allows particles to explore the parameter space effectively while avoiding abrupt changes. Each particle is then evaluated using the optical simulation system to assess its performance against the optimization objectives, enabling the PSO algorithm to iteratively improve the solution.

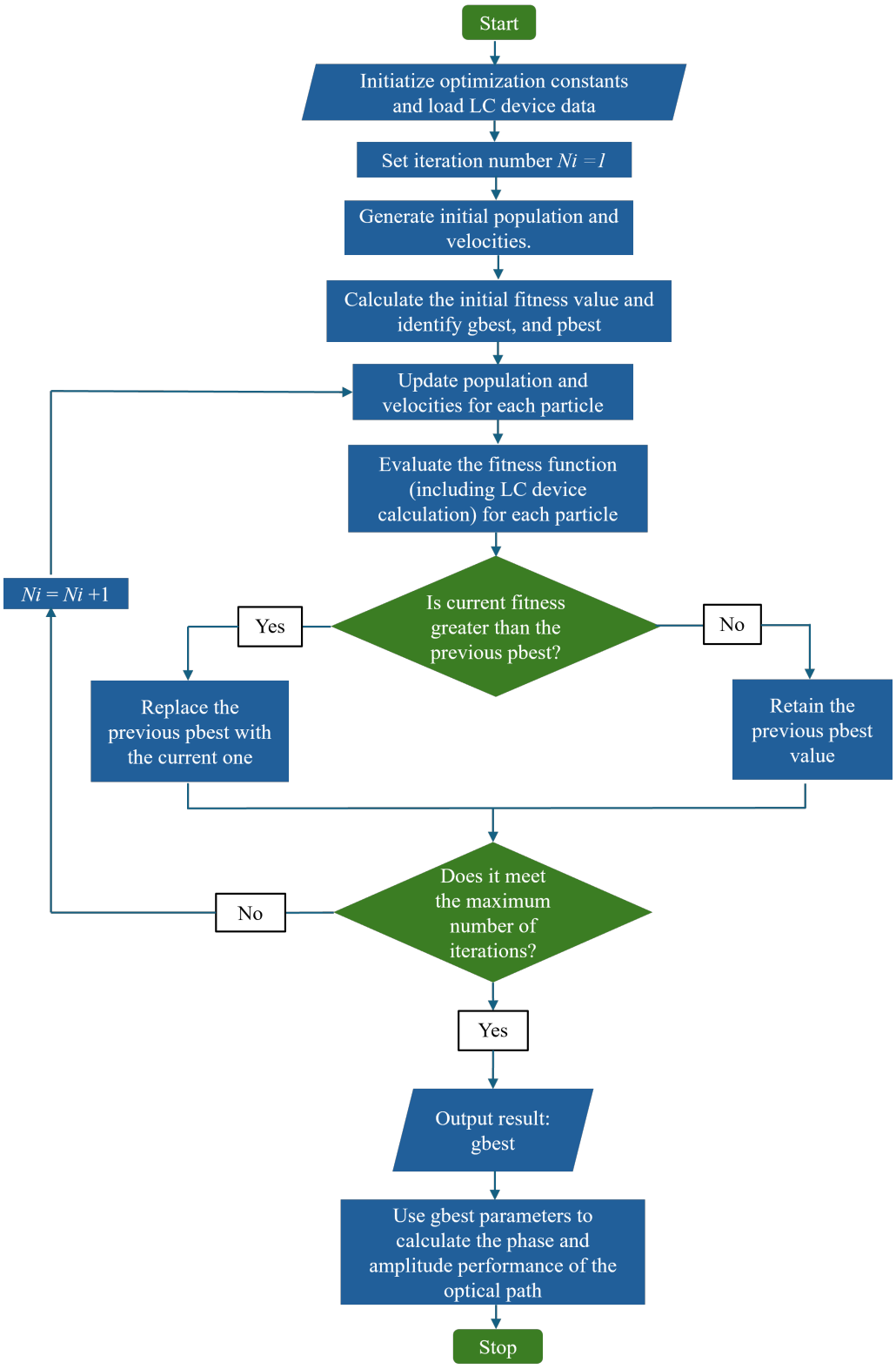

Figure 6.2. Flowchart illustrating the PSO algorithm for optimizing an LC device with two waveplates. The process begins with initializing optimization constants and LC device parameters. The fitness value is computed based on optical calculations, followed by iterative updates of particle positions and velocities. The algorithm continuously updates the global best (*gbest*) and personal best (*pbest*) values until the maximum iteration is reached. The final *gbest* parameters are used to calculate the phase and amplitude performance of the optical system.

The fitness function is a fundamental component for evaluating the optical performance of the system, which is tailored to meet the design objectives. These can include achieving polarization-independent phase modulation and maximizing the phase modulation range of a single-polarized light source.

Settings for Polarization-independent Phase Modulation.

To ensure polarization independence, the phase modulations for two orthogonal polarizations, δ_x and δ_y, are extracted at each voltage level or time point. The optimization objective is to minimize the phase difference between these two polarizations, as this is a key criterion for achieving polarization independence. This objective is defined as Fit_1, where a smaller value of Fit_1 indicates improved consistency between the phase modulations of the two polarizations.

In the voltage domain, Fit_1 is expressed as:

$$Fit_1 = \left|\delta_{x_{V1}} - \delta_{y_{V1}}\right| + \left|\delta_{x_{V2}} - \delta_{y_{V2}}\right| + \cdots + \left|\delta_{x_{VN}} - \delta_{y_{VN}}\right| \qquad (6-25)$$

In the time domain, Fit_1 is similarly defined as:

$$Fit_1 = \left|\delta_{x_{T1}} - \delta_{y_{T1}}\right| + \left|\delta_{x_{T2}} - \delta_{y_{T2}}\right| + \cdots + \left|\delta_{x_{TN}} - \delta_{y_{TN}}\right| \qquad (6-26)$$

Minimizing Fit_1 across all voltage levels or time points ensures a uniform phase response for both polarizations, thus maintaining polarization independence.

Simultaneously, off-diagonal elements, *B* and *C*, in Eq. (6-10) indicate polarization transformation. For polarization-independent performance, these values should be as small as possible. This requirement is quantified by the following optimization metric:

In the voltage domain, the metric is defined as:

$$Fit_2 = \left|B_{V1} + B_{V2} + \cdots + B_{VN}\right| + \left|C_{V1} + C_{V2} + \cdots + C_{VN}\right| \qquad (6-27)$$

In the time domain, it is expressed as:

$$Fit_2 = |\mathrm{B}_{T1} + \mathrm{B}_{T2} + \cdots + \mathrm{B}_{TN}| + |\mathrm{C}_{T1} + \mathrm{C}_{T2} + \cdots + \mathrm{C}_{TN}| \quad (6-28)$$

A smaller value of Fit_2 corresponds to improved polarization independence, which could ensure minimal polarization transformation across different voltage levels or time intervals.

Simultaneously, to maintain high optical efficiency and minimize amplitude loss, the amplitude modulation is designed to be close to 1. The corresponding fitness function Fit_3 in the voltage domain is expressed as:

$$Fit_3 = \sum_{i=1}^{N} |\mathrm{A}_{Vi} - 1| + \sum_{i=1}^{N} |\mathrm{D}_{Vi} - 1| \quad (6-29)$$

Similarly, in the time domain, the corresponding fitness function Fit_3 is defined as:

$$Fit_3 = \sum_{i=1}^{N} |\mathrm{A}_{Ti} - 1| + \sum_{i=1}^{N} |\mathrm{D}_{Ti} - 1| \quad (6-30)$$

A lower value of Fit_3 indicates improved amplitude performance, which leads to higher optical efficiency and minimized amplitude loss. This is critical for optimizing the device's performance.

The overall fitness function is defined as:

$$Fit = Fit_1 + Fit_2 + Fit_3 \quad (6-31)$$

where the objective is to minimize the value of Fit. If significant differences exist among Fit_1, Fit_2, and Fit_3, appropriate weights factors (W_1, W_2, and W_3) are introduced to balance their contributions:

$$Fit = W_1 \cdot Fit_1 + W_2 \cdot Fit_2 + W_3 \cdot Fit_3 \quad (6-32)$$

Settings for Enhanced Phase Modulation of Single-polarized Light

To maximize the phase modulation range of single-polarized light, the objective is to maximize the phase difference of a single polarization. For *x*-polarized light in the voltage domain:

$$Fit\_\mathrm{m}_1 = \delta_{x\_V\_max} - \delta_{x\_V\_min} \quad (6-33)$$

In the time domain:

$$Fit\_\mathrm{m}_1 = \delta_{x\_T\_max} - \delta_{x\_T\_min} \quad (6-34)$$

Here, $\delta_{x\_V\_max}$ and $\delta_{x\_T\_max}$ present the maximum phase modulation in the voltage domain and time domain, respectively. Similarly, $\delta_{x\_V\_min}$ and $\delta_{x\_T\_min}$ present the minimum phase modulation in the voltage domain and time domain, respectively, for the *x*-polarized light. A larger value of Fit_{m_1} indicates a larger phase modulation range and an enhanced modulation capability.

Simultaneously, the amplitude is optimized to remain as close to unity as possible. This is achieved by minimizing the deviation of the amplitude from 1, which ensures high optical efficiency. The formulation is expressed as follows:

In the voltage domain:

$$Fit_{m_2} = \sum_{i=1}^{N} |\mathrm{A}_{Vi} - 1| \quad (6-35)$$

In the time domain:

$$Fit_{m_2} = \sum_{i=1}^{N} |\mathrm{A}_{Ti} - 1| \quad (6-36)$$

A lower value of Fit_{m_2} indicates reduced deviation and ensures that the amplitude remains near the desired level, which also indicates a low amplitude modulation as well as a low amplitude loss.

Since the optimization involves both phase modulation (Fit_{m_1}) and amplitude performance (Fit_{m_2}), weighting factors (W_{m_1} and $W_{(m2}$) are introduced to balance their contributions in the overall fitness function, defined as:

$$\mathrm{Fit}_m = -W_{m_1} \cdot Fit_{m_1} + W_{m_2} \cdot Fit_{m_2} \qquad (6-37)$$

The negative sign associated with W_{m_1} ensures that Fit_{m_1} is maximized, whereas Fit_{m_2} is minimized, when the algorithm is optimized the Fit_m to have the minimum value. This formulation ensures that the optimization process prioritizes maximizing the phase modulation range while maintaining the amplitude close to unity, with appropriate weighting factors to achieve a balanced trade-off between these two objectives.

The PSO algorithm proceeds iteratively until the maximum number of iterations is reached, which is set to 100 in this case. In each iteration, the positions and velocities of particles are updated based on their personal best (*pbest*) and global best (*gbest*) values. The fitness value of each particle is evaluated using Eq. (6-32) or Eq. (6-37), and the new *pbest* values are determined by comparing the fitness values within the swarm. The *gbest* value is subsequently updated by comparing the current fitness values with the previous ones. Since the objective is to minimize the fitness value, a newly generated *pbest* that is smaller than the current *gbest* replaces it as the new *gbest*. If the new *pbest* does not improve upon *gbest*, the algorithm continues to the next iteration, maintaining the previous *gbest* value and repeating the comparison process. This iterative procedure continues until either the maximum iteration limit is reached, or the fitness values converge.

To ensure practical optimization results, it is essential to impose appropriate parameter constraints after each parameter update. If the two waveplates are designed to function as quarter-wave plates, the parameters Pa_1 and Pa_3 are restricted to a small range around $\frac{\pi}{2}$,

specifically within the interval $\left[\frac{\pi}{2} - 0.005,\ \frac{\pi}{2} + 0.005\right]$, where the margin 0.005 accounts for potential errors. Similarly, the parameters Pa_2, Pa_4, and Pa_5 are constrained within the range [0, 360°] to ensure physically meaningful solutions.

At the end of the optimization process, both the final optimization results and the convergence behaviour of the fitness function should be analysed. To evaluate convergence, the evolution of the *gbest* value over iterations is plotted. A properly converging optimization process should yield a curve that gradually flattens as iterations increase. If the curve does not exhibit this behaviour, it may be necessary to adjust the optimization parameters and re-run the optimization. Once convergence is achieved, the final *gbest* value and the corresponding optimal parameter set (Pa_1 to Pa_5) are obtained. The final performance of the optimized configuration is then computed by substituting these parameters back into the calculation.

6.1.3 System Verification

To validate the reliability of this computational framework, a systematic verification process was conducted before applying it to practical optimization problems. As a test case, a rotating half-waveplate was used to represent the LC device awaiting optimization. As discussed in Section 3.3, when a half-waveplate is placed between two quarter-waveplates with their optical axes oriented at 45°, it can generate continuous phase modulation. Theoretically, the induced phase modulation is twice the rotation angle of the half-waveplate. A mathematical derivation of this relationship is presented below.

The Jones matrix for a single rotating half-waveplate is expressed as:

$$\mathbf{J_{HWP}} = \begin{bmatrix} \cos(2\varphi) & \sin(2\varphi) \\ \sin(2\varphi) & -\cos(2\varphi) \end{bmatrix} \qquad (6-38)$$

where φ represents the rotation angle of the half-waveplate, varying within the range [0, 360º]. In this verification, 101 discrete values of φ were used to evaluate the system response.

For an x-polarized incident light, the input electric field vector is:

$$\mathbf{E_{in}} = \begin{bmatrix} 1 \\ 0 \end{bmatrix} \qquad (6-39)$$

After passing through the half-waveplate, the output electric field is given by:

$$\mathbf{E_{out}} = \mathbf{J_{HWP}} \cdot \mathbf{E_{in}} = \begin{bmatrix} \cos(2\varphi) \\ \sin(2\varphi) \end{bmatrix} \qquad (6-40)$$

This result indicates that a single rotating half-waveplate does not induce phase modulation, as the output polarization changes as the rotation angles increases, while the amplitude varies according to $\cos(2\varphi)$ and $\sin(2\varphi)$. **Figure 6.3**(a)-(c) illustrates the performance of a single rotating half-waveplate. The amplitude modulation plot in Fig. 6.3(a) illustrates the variations in the parallel and perpendicular polarization components as a function of φ. The phase modulation plot in Fig. 6.3(b) confirms that there is no phase shift variation with φ. Additionally, the polar plot in Fig. 6.3(c) further validates the absence of phase modulation over a full 360° rotation.

When the half-waveplate is placed between two quarter-waveplates, the Jones matrix for the system becomes:

$$\mathbf{E_{out}} = \mathbf{J_{QWP}} \cdot \mathbf{J_{HWP}} \cdot \mathbf{J_{QWP}} \cdot \mathbf{E_{in}} \qquad (6-41)$$

where the Jones matrix of a quarter-waveplate (QWP) with its optical axis at 45° is:

$$\mathbf{J_{QWP}} = \frac{1}{\sqrt{2}} \begin{bmatrix} 1 & -i \\ -\mathrm{i} & 1 \end{bmatrix} \qquad (6-42)$$

Substituting the matrices and solving for E_{out}, the output light field is obtained as:

$$\mathbf{E_{out}} = \begin{bmatrix} \cos(2\varphi) - i\sin(2\varphi) & 0 \\ 0 & -\cos(2\varphi) - i\sin(2\varphi) \end{bmatrix} \cdot \mathbf{E_{in}} = \begin{bmatrix} \cos(2\varphi) - i\sin(2\varphi) \\ 0 \end{bmatrix} \quad (6-43)$$

This result confirms that an *x*-polarized incident light propagating through the system remains *x*-polarized. The performance of the output light is illustrated in Fig. 6.3(d)–(f). The amplitude of *x*-polarized light remains constant as the rotation angle increases, while the phase shift follows a linear relationship with φ, resulting in a total phase shift of 720° for a full 360° rotation. The *y*-polarized component remains zero as the rotation angle changes. This agrees with theoretical predictions.

To verify this behaviour within the algorithm, the Jones matrix of a rotating half-waveplate was employed to imitate the LC device model. The two waveplates were initially assigned arbitrary retardances, while the rotation angles of all three components were randomly initialized within the range [0, 2π rad]. The cost function, as defined in Section 6.1.2, aimed to maximize the phase modulation range for single-polarized light. After multiple iterations, the optimized results indicate that the system parameters converge to two quarter-waveplates with retardances of 1.57 and rotation angles of 135° and 315°, which ensures a relative angle of 45° to the input and output polarization. The rotation angle of the half-waveplate is 155.68°; however, since it continuously rotates, its initial placement angle does not influence the final system performance. The results of the optimized system are identical as those presented in Fig. 6.3(d)–(e). Specifically, the amplitude of the *x*-polarized light remains constant at 1 regardless of the rotation angle, while the phase shift exhibits a linear dependence, demonstrating a 720° phase shift for a full 360° rotation. This confirms the expected twofold relationship predicted by Eq. (6-43).

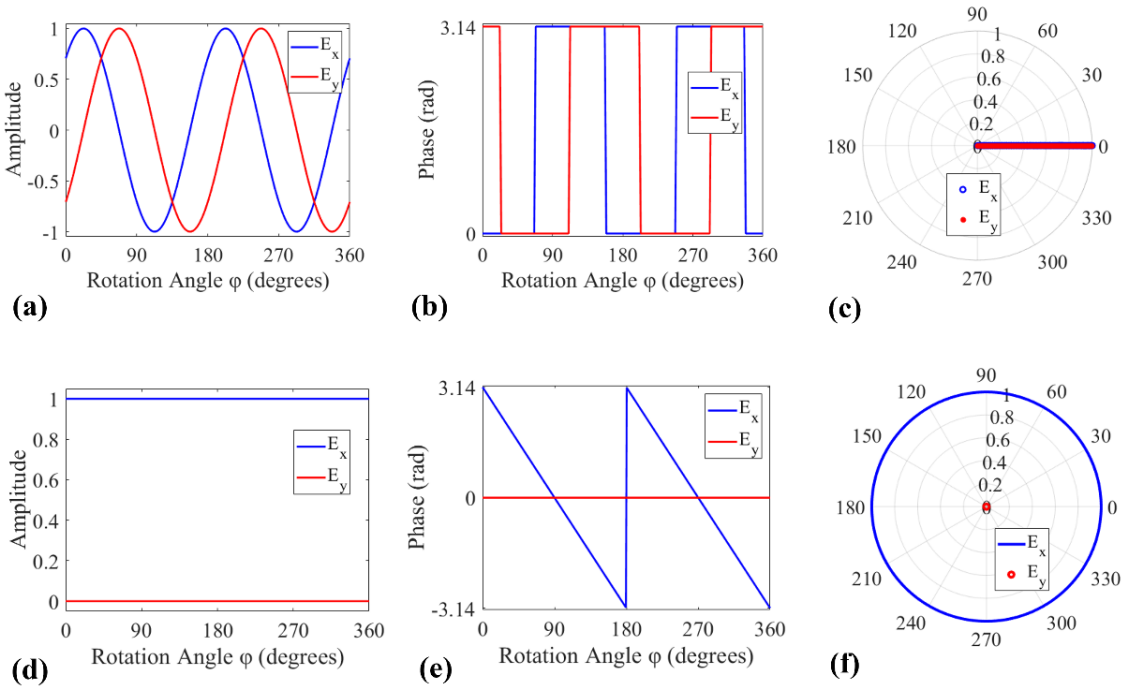

Figure 6.3. Verification of the optimization algorithm by simulating a rotating half-waveplate representing the LC device placed between two waveplates with arbitrary retardances. Performance of a single rotating half-waveplate: (a) amplitude modulation, (b) phase modulation, and (c) polar plot. Rotating half-waveplate positioned between two quarter-waveplates with optical axes oriented of 45º: (d) amplitude modulation, (e) phase modulation, and (f) polar plot. 'E_x' refers to the *x* polarization input light, while 'E_y' refers to the *y* polarization input light.

This verification establishes the reliability of the proposed optimization algorithm. By representing LC devices using Jones matrices, the method effectively captures dynamic optical behaviour over a specified voltage range and time period. The results validate the efficiency of the framework in rapidly identifying the optimal configuration for the LC-waveplate system based on a given optimization objective. This framework provides a robust foundation for designing advanced optical systems. In the following section, this approach is extended to the optimization of widely used LC devices, focusing on achieving polarization-independent operation or maximizing their phase modulation range.

6.2 Optimization for Fréedericksz LC device

6.2.1 Polarization independence in the voltage domain

The optimization of the Fréedericksz LC device begins by initiating the values of the optical parameters of the LC device and two waveplate with arbitrary values. The retardance values of the waveplates are randomly assigned within the range [0, π rad], while their rotation angles are distributed within the range [0, 2π rad]. The primary goal was to achieve the polarization-independent phase modulation while simultaneously maximizing phase modulation. Key optimization parameters, such as population size and initial velocities, are adjusted to achieve optimal performance.

Figure 6.4 presents the performance of a single 5 μm thick Fréedericksz device filled with nematic LC in its original state prior to optimization. In this configuration, only parallel polarization exhibits a phase modulation of 193.12º as voltage increases from 2.0 to 10.0 V, while the perpendicular polarization remains unchanged, which indicates zero phase modulation. This highlights the device's inherently anisotropic behaviour, which serves as the baseline for subsequent optimization efforts. The optimization range for this device begins from 2.0 V, rather than 0 Vrms, due to practical considerations for reflective SLM applications. In such scenarios, a phase shift of approximately 2π rad in reflection (equivalent to π rad in transmission) is commonly required. Therefore, the voltage range of 2.0 to 10.0 V is selected to achieve around π rad phase modulation for the 5 μm-thick LC device under a driving voltage of 10 Vrms.

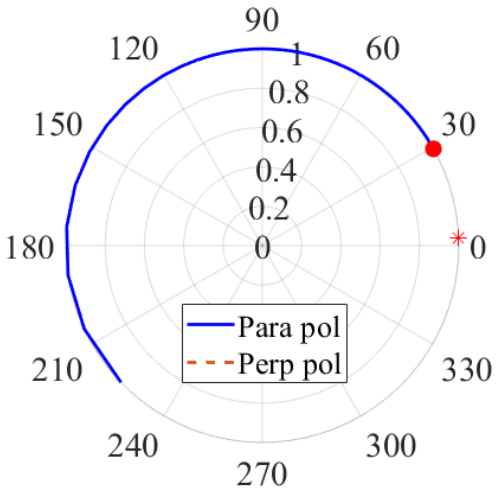

Figure 6.4. Performance of a single nematic Fréedericksz LC device in the voltage domain as the voltage changes from 2.0 V to 10.0 V, with the red point marking the phase modulation at 10.0 V. 'Para pol' refers to the polarization parallel to the input light's polarization, which also corresponds to the device alignment. 'Perp pol' refers to the polarization perpendicular to the input light's polarization, also corresponding to the device alignment.

Results of Arbitrary Retardance Optimization

Using the optimization algorithm described above, setting the retardances of the two waveplates to arbitrary values within the range [0, π rad] can yield multiple configurations that achieve satisfactory polarization-independent phase modulation to a different extent. The configurations summarized in **Table 6.1** demonstrate polarization-independent performance through different mechanisms, as illustrated in **Figure 6.5**. Table 6.1 presents the exact values of the five key parameters along with evaluation metrics, including the phase modulation under two amplitude constraints. The constraint of 0.99 indicates that the amplitude at both polarizations of the outgoing light reaches 0.99, which demonstrates high polarization purity, with the corresponding cross-polarization (polarization transformation) amplitude being only 0.14. This indicates the intensity of polarization transformation of 1.96%. Similarly, the 0.9 constraint corresponds to a lower outgoing amplitude of 0.9 for both polarizations, with a significantly higher cross-polarization amplitude of 0.43, which indicates the intensity of

polarization transformation of 18.49%. The results are further visualized as polar plots, where the radius represents amplitude modulation, and the angle corresponds to phase modulation.

As shown in Fig. 6.5, configurations (a) to (c) demonstrate achieved phase modulation behaviours under two constraints as the voltage increases. Each configuration exhibits polarization-independent performance within a specific voltage range, while polarization transformation occurs beyond that range. This indicates that polarization independence is only maintained under limited operational voltages. Table 6.1 presents that the achieved phase modulation is significantly reduced compared to that of a single device operating under a single polarization, which reaches 193.12° as the voltage increases from 2.0 to 10.0 V.

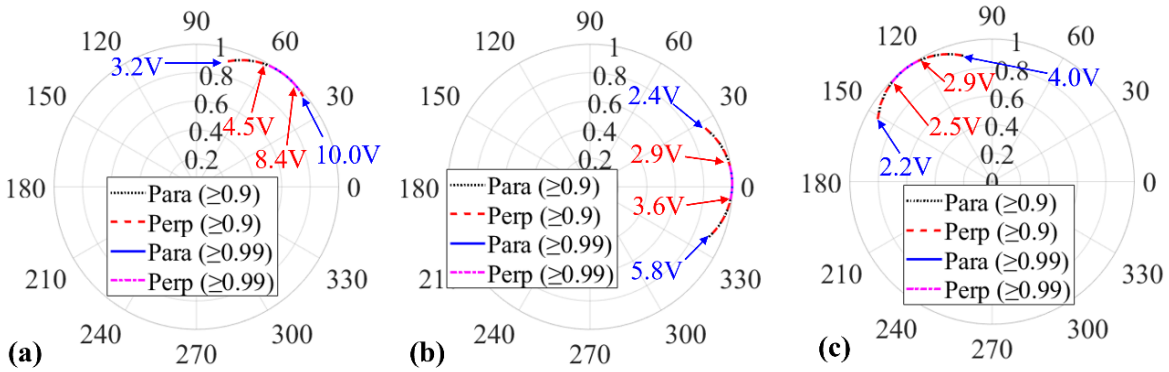

Figure 6.5. The polarization-independent phase modulation performance of a nematic Fréedericksz LC device placed between two waveplates with arbitrary retardances in the voltage domain. The corresponding phase retardances and rotation angles are listed in Table 6.1. The amplitude constraints are of 0.9 and 0.99, respectively. 'Perp pol' refers to the polarization perpendicular to the input light's polarization, which also corresponds to the device alignment. 'Para pol' refers to the polarization parallel to the input light's polarization, also corresponding to the device alignment.

Despite this limitation, the optimized results exhibit expected polarization-independent performance with all configurations, which demonstrates the effectiveness of the optimization algorithm. A single Fréedericksz device can only achieve phase modulation along one single polarization, while if placed between waveplates, polarization-independent phase modulation

can be achieved, though the phase modulation is quite limited. To address this limitation, the device thickness can be increased to enhance phase modulation performance. Moreover, all solutions remain within the physically feasible retardance range [0, π rad], which ensures their practical applicability in real-world device implementations.

Table 6.1. Parameters of the configurations corresponding to the performance shown in Figure 6.5.

	Pa1 (rad)	**Pa2 (deg)**	**Pa3 (rad)**	**Pa4 (deg)**	**Pa5 (deg)**	**Phase (>0.99) (deg)**	**Phase (>0.9) (deg)**
(a)	0.65	44.79	0.20	225.71	225.02	16.15	35.67
(b)	2.08	45.20	2.46	224.88	315.06	13.91	50.39
(c)	0.12	58.59	2.08	224.54	226.19	13.74	48.85

In addition, one optimization algorithm generates multiple favourable results are possibly due to the intrinsic nature of the PSO algorithm, which explores multiple regions in the solution space and provides several near-optimal solutions. This is evident in the results, where configurations (a)-(c) all achieve good performance. The cost function combines amplitude and phase modulation metrics, introducing a trade-off by balancing the weight numbers. While some solutions excel in one aspect (e.g., amplitude uniformity), they may slightly underperform in another (e.g., phase range). This highlights the importance of carefully defining the cost function based on specific application needs. Since this is a multi-objective optimization problem, more rigorous cost function constraints and weight adjustments are needed to achieve better results.

Re-Optimization with A Single Half-Waveplate

A second re-optimization was conducted using a single half-waveplate in combination with the LC device. The retardance values were set to be π rad and 0 to imitate this system. Minor deviations are introduced to simulate fabrication errors of waveplates. In this system, rotation angles of the waveplate and the LC device are set as optimization parameters. The results, presented in **Figure 6.6**, demonstrate polarization-independent phase modulation, where both polarizations exhibit identical phase modulation with amplitude exceeding constraints of 0.9 and 0.99. The optimized rotation angles for configuration (a) are -45º for the half-waveplate and 45.00º for the LC device, whereas for configuration (b), they are -45.00º for the half-waveplate and 135.00º for the LC device. Notably, the rotation angles of the LC device in these two configurations are oppositely oriented, and the phase modulation performance illustrated in Figure 6.6 exhibits opposite symmetry as well. The achieved phase modulation for both configurations (a) and (b) is identical, which is 7.07° under the constraint of 0.99 and increasing to 44.92° under the relaxed constraint of 0.9.

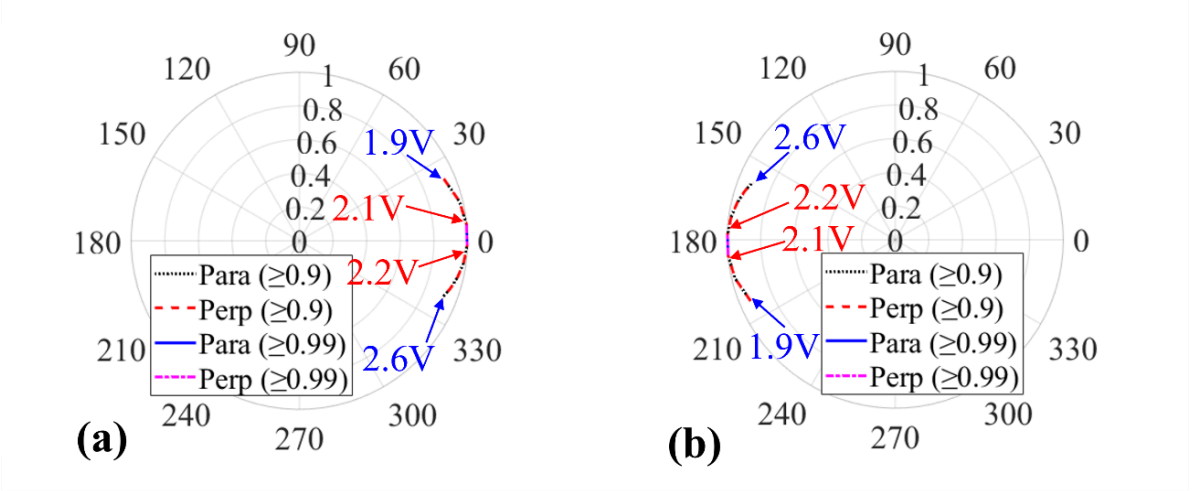

Figure 6.6. Performance of a nematic Fréedericksz LC device in the configurations where the LC device is placed with a single half-waveplate. The amplitude constraints are of 0.9 and 0.99, respectively. Perp pol' refers to the polarization perpendicular to the input light's polarization, which also corresponds to the device alignment. 'Para pol' refers to the polarization parallel to the input light's polarization, also corresponding to the device alignment.

The configuration that combines a single half-wave plate with a Fréedericksz nematic LC device successfully achieves polarization-independent phase modulation. However, the modulation is rather limited under strict amplitude constraint of 0.99 for a pure polarization-independent performance. When the phase modulation is improved by reducing this constraint, polarization transformation is simultaneously introduced.

6.2.2 Polarization independence in the time domain

Demonstrating the operation of the optimized system in the time domain is essential, as it highlights the practicality of this optimization methodology in fast switching applications. This section applies the optimization algorithm to investigate the dynamic performance of the LC-waveplate system and focuses on achieving either polarization-independent phase modulation over time. As shown in **Figure 6.7**, a single Fréedericksz LC device achieves a phase modulation of 69.53° for parallel polarization within a 1 ms timescale, with amplitude performance close to 1. The perpendicular polarization remains at 0, which underscores the anisotropic nature of the Fréedericksz device and its inherent limitation in achieving polarization-independent applications.

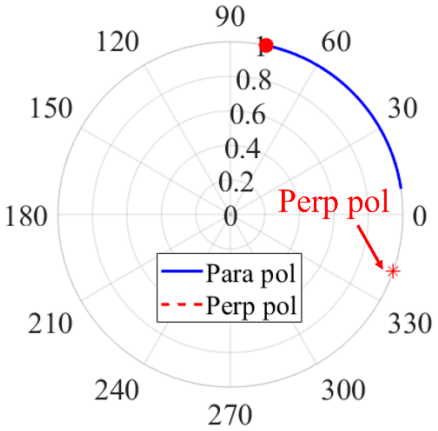

Figure 6.7. Performance of a single nematic Fréedericksz LC device in the time domain during the relaxation process within 1 ms.

When optimizing the system in which a Fréedericksz device is placed between two waveplates with arbitrary retardances, the Jones matrix of the LC device in the time domain was incorporated into the optimization framework. The waveplates were initialized with arbitrary retardances within the range [0, π rad]. The optimized results are presented in **Figure 6.8**, with amplitude constraints (as explained in Section 6.2.1) to be 0.9 and 0.99, respectively. The corresponding performance are summarized in **Table 6.2**. Under constraint of 0.99, all configurations demonstrate consistent phase modulation for both perpendicular and parallel polarizations, with polarization transformation limited to only 2% of the light intensity. This indicates the pure polarization-independent capability of the optical system across all evaluated time points. However, the achieved phase modulation remains limited, as shown in the last column of Table 6.2.

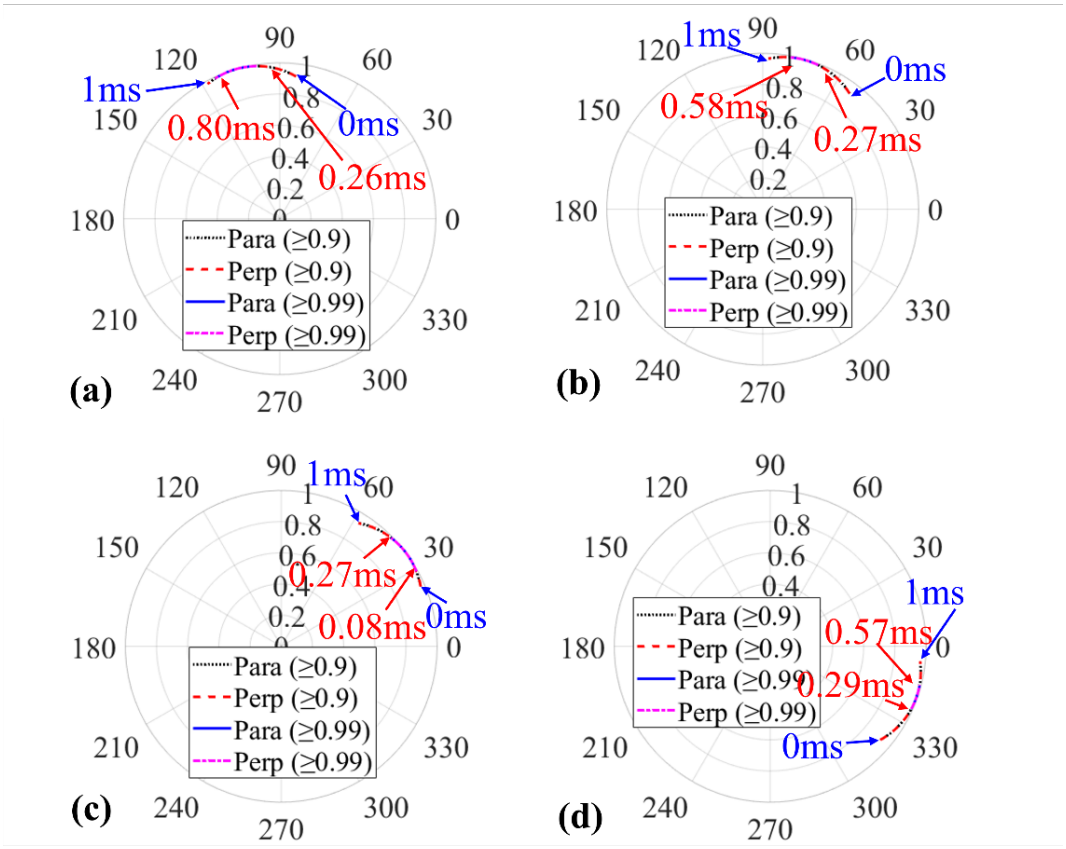

Figure 6.8. Time-domain performance of a single nematic Fréedericksz LC device placed between two waveplates with arbitrary retardances during the 1 ms relaxation process. The red point indicates the end of the 1 ms period, while the two overlapping curves represent the behaviour of the parallel and perpendicular polarizations. The parameters of each configuration are listed in Table 6.2.

When the amplitude constraint is relaxed to 0.9, the polarization-independent phase modulation can extend to 1 ms, though the system exhibits a higher degree of polarization transformation, with approximately 20% of the output intensity attributed to cross-polarization. In this case, the achieved phase modulation reaches 34.77°, roughly half the value attained by a single LC device operating under a single polarization (69.53°) over the same timescale (1 ms). This reduction highlights the inherent trade-off between achieving polarization independence and maximizing phase modulation depth. Additionally, all configurations under this relaxed constraint show minimal amplitude loss—approximately 0.07—over the 1 ms time scale.

Table 6.2. Parameters of the configurations corresponding to the performance shown in Figure 6.8.

	Pa1 (rad)	**Pa2 (deg)**	**Pa3 (rad)**	**Pa4 (deg)**	**Pa5 (deg)**	**Phase (>0.99) (deg)**	**Phase (>0.9) (deg)**
(a)	2.2	225.01	0.9	315.02	44.55	16.08	34.76
(b)	0.42	238.95	1.62	137.73	310.63	10.57	34.76
(c)	0.93	226.88	0.07	12.47	44.55	15.69	34.76
(d)	2.72	223.8	2.34	47.38	316.08	9.41	34.76

These results validate that a single-polarized Fréedericksz LC device, when combined with waveplates of optimized retardance, can achieve polarization-independent phase modulation during its 1 ms relaxation process. Although minor polarization transformation occurs over some time points, the overall polarization independence is largely maintained under loose constraint. The limited phase modulation could be improved if the standalone LC device were capable of producing a greater phase shift. Additionally, it is worth noting that

other single-polarization configurations, such as specific states in the Pi-cells, are not explored in this section. These are expected to exhibit similar performance based on the same optimization framework.

6.2.3 Single polarization phase modulation in the voltage domain

To investigate the potential for achieving greater phase modulation with a single Fréedericksz LC device, the optimization algorithm was modified by adjusting its cost function while following a similar optimization process. The performance of a standalone nematic Fréedericksz LC device, shown in Figure 6.4, exhibits a phase modulation of 193.12° as the voltage increases from 2.0 V to 10.0 V for the parallel polarization. The optimization algorithm was designed to maximize the phase difference while allowing a constant level of amplitude loss. The initial retardances were set to arbitrary values within the range [0, π rad].

The optimized results, presented in **Figure 6.9**, indicate that all configurations which incorporate additional waveplates do not demonstrate any improvement in phase modulation compared to a single LC device. Even with optimized retardances for the waveplates, phase modulation remains unchanged compared to a single Fréedericksz device. This suggests that the standalone Fréedericksz device already operates near its maximum phase modulation capacity during switching. The parameters of these configurations are detailed in **Table 6.3**. As the voltage increases from 2.0 V to 10.0 V, both the unoptimized and optimized setups achieve the same phase modulation of approximately 194.54°, with amplitude maintained at 1, which is quite identical to the performance of a single Fréedericksz device.

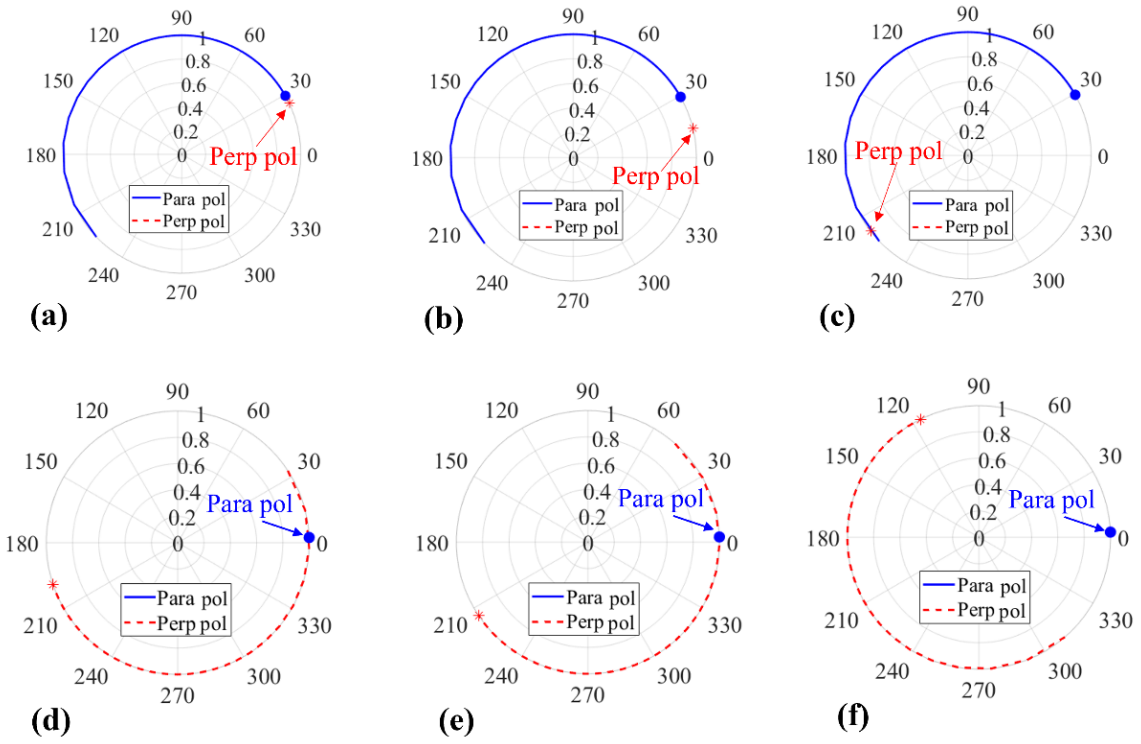

Figure 6.9. Voltage domain performance of a nematic Fréedericksz LC device placed between two waveplates with optimal retardances. The corresponding phase retardances and rotation angles are listed in Table 6.3. The voltage range is from 2.0 V to 10.0 V, with the red point marking the phase modulation at 10.0 V. 'Perp pol' refers to the polarization perpendicular to the input light's polarization, which also corresponds to the device alignment. 'Para pol' refers to the polarization parallel to the input light's polarization, also corresponding to the device alignment.

Table 6.3. Parameters of the configurations corresponding to the performance shown in Figure 6.9.

	(a)	**(b)**	**(c)**	**(d)**	**(e)**	**(f)**
Pa1/(rad)	0.12	0.10	0.80	0.86	0.18	1.45
Pa2/(deg)	0.00	0.00	0.00	180.00	0.00	0.00
Pa3/(rad)	0.28	0.10	2.96	2.09	3.04	0.06
Pa4/(deg)	0.00	0.00	0.00	0.00	0.00	0.00
Pa5/(deg)	0.00	0.00	0.00	270.00	90.00	90.00
Phase/(deg)	194.59	194.59	194.59	194.59	194.59	194.59

Additionally, in configurations (a)–(c), the waveplates remain in the same positions, with rotation angles of 0°, which causes no change in phase modulation performance. Specifically, the parallel polarization remains unchanged, while the perpendicular polarization exhibits zero modulation, which is consistent with the behaviour of a standalone Fréedericksz device. In contrast, configurations (d)–(f) exhibit the opposite behaviour: while the parallel polarization remains static, the perpendicular polarization begins to exhibit dynamic changes as voltage increases. This behaviour is attributed to the 90° rotation of the LC device, as indicated in Table 6.3.

These results highlight the intrinsic limitations of the Fréedericksz device, which achieves a phase modulation of 194.54° with high amplitude performance (1.0) but cannot further enhance dynamic phase modulation through the addition of extra waveplates.

6.2.4 Single polarization phase modulation in the time domain

To evaluate the time-domain performance of the Fréedericksz LC device, various configurations incorporating additional waveplates were optimized to investigate the possibility of larger phase modulation for a single polarization. The simulation performance of a standalone Fréedericksz LC device, as shown in Figure 6.7, demonstrates a phase modulation of 69.53° within a 1 ms timescale under parallel polarization, while maintaining an amplitude close to unity. The initial retardances of the waveplates were set to arbitrary values within [0, π rad].

The optimized results, illustrated in **Figure 6.10**, indicate that incorporating additional waveplates (configurations (a)–(f)) does not improve amplitude or phase modulation compared to a standalone Fréedericksz device. Even when the retardances of the waveplates were

optimized, the system achieved the same phase modulation performance of approximately 69.54°, with no improvement in phase modulation, which confirms that the Fréedericksz device already operates at its maximum phase modulation capacity. The parameters of these configurations are detailed in **Table 6.4**. In configurations (a)–(c), the performance of the parallel polarization remains unchanged, while the perpendicular polarization exhibits zero modulation, consistent with the behaviour of a standalone Fréedericksz device. These configurations correspond to an LC device with a rotation angle of 0°. In contrast, in configurations (d)–(f), dynamic changes occur in the perpendicular polarization within the 1 ms timescale, while the parallel polarization remains static. This behaviour is attributed to a 90º rotation of the LC device, as detailed in Table 6.4.

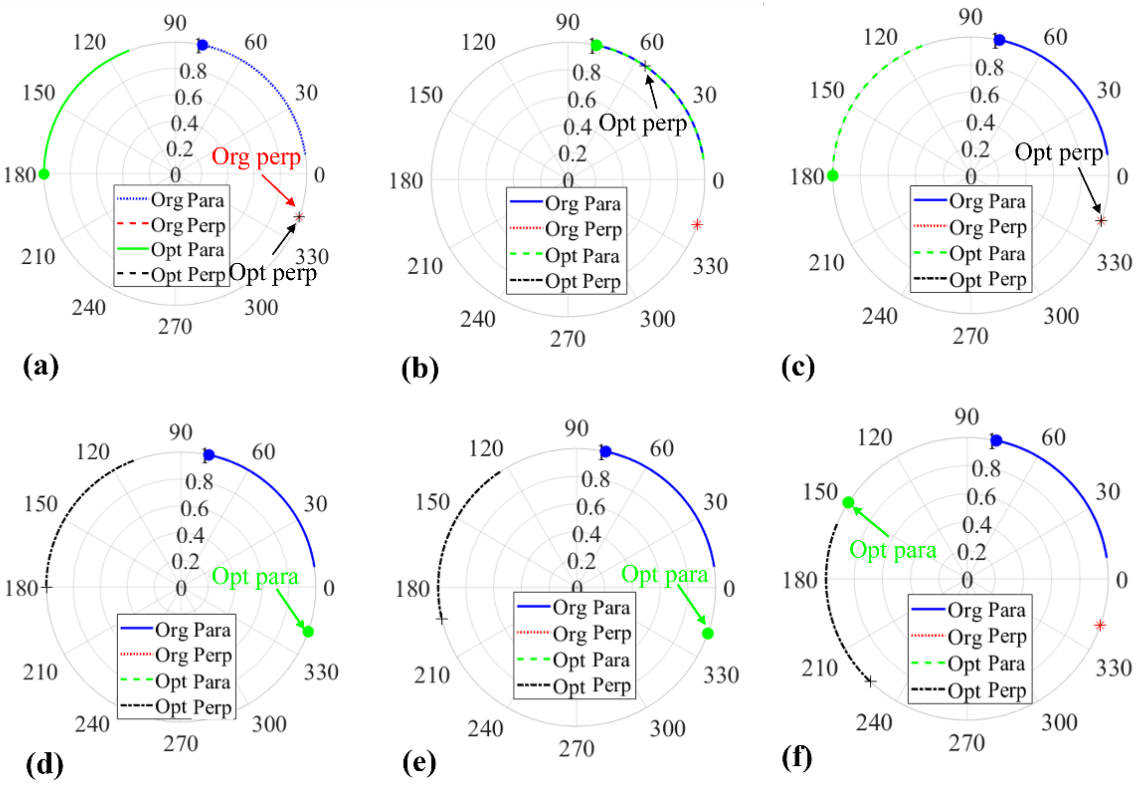

Figure 6.10. Time-domain performance of a single nematic Fréedericksz LC device placed between two waveplates with arbitrary retardances during the 1 ms relaxation process. The red point indicates the end of the 1 ms period. 'Perp pol' refers to the polarization perpendicular to the input light's polarization, which also corresponds to the device alignment. 'Para pol' refers to the polarization parallel to the input light's polarization, also corresponding to the device alignment. The parameters of each configuration are listed in Table 6.4.

Table 6.4. Parameters of the configurations corresponding to the performance shown in Figure 6.10.

	(a)	(b)	(c)	(d)	(e)	(f)
Pa1/(rad)	1.78	1.31	0.00	1.78	0.00	2.91
Pa2/(deg)	270.00	0.00	0.00	0.00	0.00	90.00
Pa3/(rad)	0.00	0.00	1.78	0.00	2.01	2.60
Pa4/(deg)	0.00	0.00	270.00	0.00	0.00	0.00
Pa5/(deg)	0.00	0.00	0.00	90.00	90.00	270.00
Phase/(deg)	69.53	69.53	69.53	69.53	69.53	69.53

6.3 Optimization for 90° TN device

6.3.1 Polarization independence in the voltage domain

In this section, the performance of the 90° TN LC device is examined. TN LC device exhibits polarization-independent behaviour at high applied voltages, as discussed in Section 5.1. The optimization algorithm is applied trying to increase its polarization-independent phase modulation in the voltage domain. The simulation performance of a single 5μm thick 90° TN device is presented in **Figure 6.11**(a), where both polarizations exhibit consistent phase modulation. The amplitude constraints are explained in Section 6.2.1. Under the amplitude constraint of 0.9, the single TN LC device achieves a polarization-independent phase modulation of approximately 92.28°, as the voltage increases from 1.86V to 10.0V. Under a stricter constraint of 0.99, the device achieves a polarization-independent phase modulation of approximately 62.55° as the voltage changes from 2.3 V to 10V.

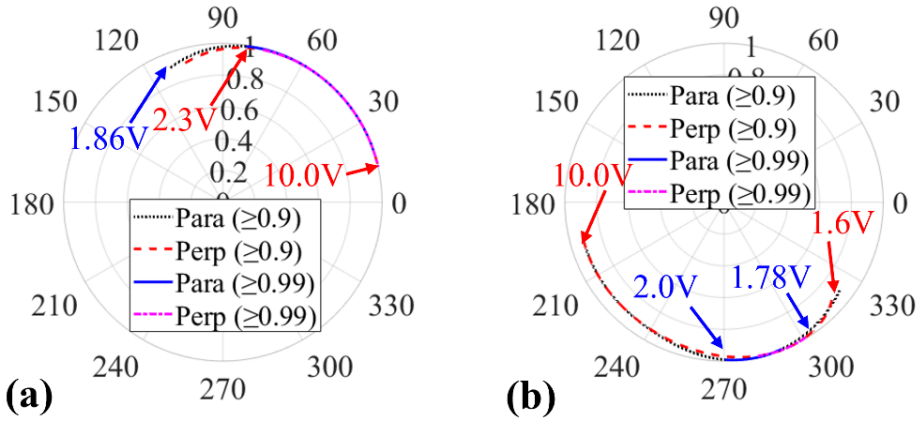

Figure 6.11. Voltage-domain performance of (a) a single 90° TN-LC device and (b) its optimized configurations for improved polarization-independent phase modulation, achieved by combining with two half-waveplates. The voltage range extends are labelled in the figure. The results are plotted by using two amplitude constraints of 0.9 and 0.99. Perp pol refers to the polarization perpendicular to the input light's polarization, corresponding to the device alignment, while Para pol refers to the polarization parallel to the input light's polarization, also aligned with the device orientation.

The optimal configuration consists of a 5 μm thick TN LC device positioned between two half-wave plates, with the waveplates oriented at rotation angles of 343° and 61.59°, respectively. The performance of this optimized configuration is illustrated in Fig. 6.11(b). Under an amplitude constraint of 0.9, the device achieves a polarization-independent phase modulation of approximately 126.69° as the applied voltage increases from 1.6 V to 10.0 V. This presents a significant improvement in phase modulation compared to a single TN LC device. When the amplitude constraint is tightened to 0.99, the optimized configuration achieves a phase modulation of approximately 21.25° over a narrower voltage range of 1.78 V to 2.0 V. This modulation is reduced relative to the 62.55° achieved by a single TN LC device under the same strict constraint. The optimized configuration exhibits enhanced polarization-independent phase modulation under the lower amplitude constraint and reduced phase modulation under the stricter constraint.

6.3.2 Single polarization phase modulation in the voltage domain

In certain applications, the 90° TN LC device is utilized for phase modulator for a single polarized light. The performance of a single 5 μm 90° TN device is presented in **Figure 6.12**(a). It shows that both polarizations exhibit consistent phase modulation of approximately 110° with amplitude exceeds 0.8 as the voltage increases from 1.7V to 10.0V. The device maintains an amplitude variation of 0.2 and an average amplitude of 0.99.

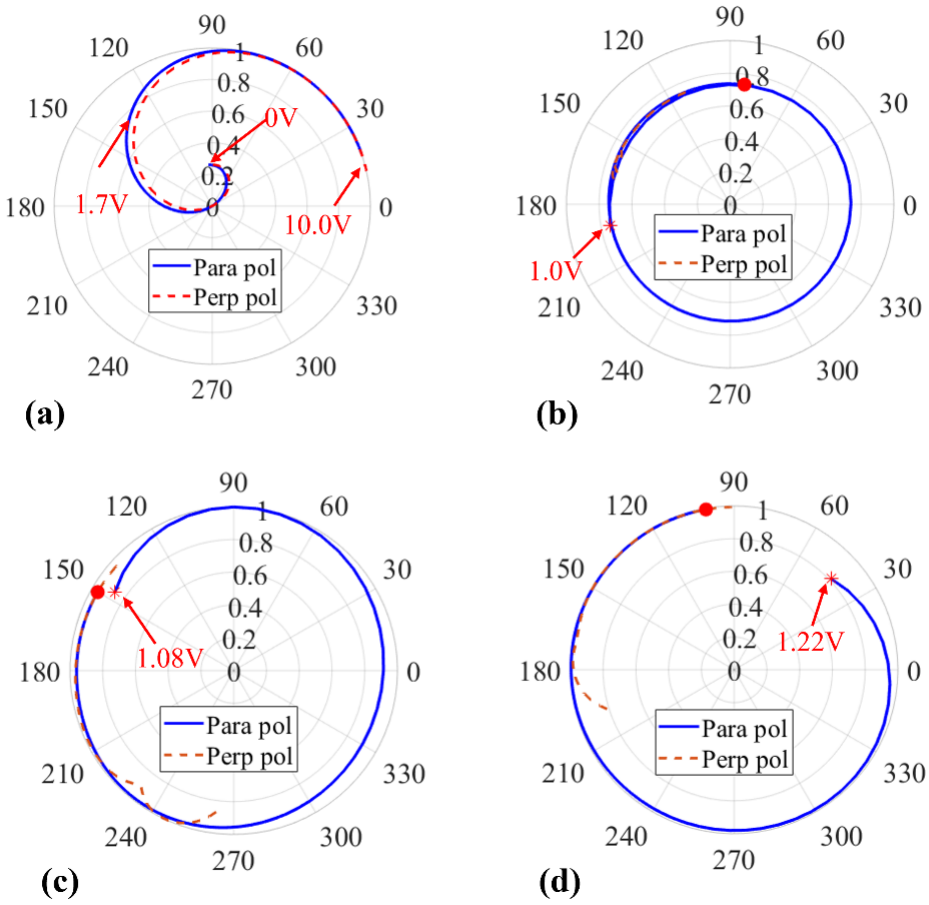

Figure 6.12. Voltage-domain performance of (a) a single 90° TN-LC device and (b), (c) and (d) its optimized configurations for improved phase modulation range, achieved by combining with waveplates of different arbitrary retardances. The corresponding phase retardances and rotation angles are detailed in Table 6.5. The voltage range extends different and marked in the figures, and the red points indicate the phase modulation at 10.0 V. Perp pol refers to the polarization perpendicular to the input light's polarization, corresponding to the device alignment, while Para pol refers to the polarization parallel to the input light's polarization, also aligned with the device orientation.

To maximize phase modulation in a single polarization, the optimization algorithm was applied to the TN LC–waveplate system with a focus on extending the phase modulation range for one polarization, rather than maintaining identical performance across both polarizations. The optimized results are presented in Fig. 6.12(b)–(d). All configurations exhibit a significantly enhanced phase modulation range compared to a standalone 90° TN LC device. The amplitude remains constant across the voltage range, while a slight reduction in amplitude is observed due to the optimization trade-offs. The detailed configuration parameters and corresponding performance metrics are summarized in **Table 6.5**.

Table 6.5. Parameters of the configurations corresponding to the performance shown in Figure 6.12 of the configuration containing 90° TN-LC device.

	(a)	**(b)**	**(c)**	**(d)**
Pa1/(rad)	0	2.11	1.96	1.28
Pa2/(deg)	0	142.53	156.79	144.77
Pa3/(rad)	0	0.66	2.48	1.49
Pa4/(deg)	0	239.04	242.63	236.90
Pa5/(deg)	0	79.59	0.00	186.96
Average amplitude	0.99	0.74	0.96	0.99
Amplitude difference	0.20	0.03	0.13	0.19
Phase/(deg)	110.09	466.64	356.41	303.20

Among the configurations, configuration (b) achieves the maximum phase modulation at parallel polarization, reaching 466.64° as the voltage increases from 1.0V to 10.0V. The amplitude modulation remains minimal at 0.03, with the average amplitude of 0.74. This phase

modulation enhancement is nearly four times greater than that of a single-polarized light. Configuration (c) exhibits a full 2π rad phase modulation as the voltage increases from 1.08 V to 10.0 V, but it has a better amplitude performance than (a), with a slight amplitude variation. What's more, configuration (d) exhibits the best amplitude performance as it is close to 1 with nearly 0 amplitude variation but sacrifices its phase modulation range to 303.20° as the voltage increases. The comparison between the three configurations reflects trade-offs between parameters. These findings indicate that by carefully optimizing the LC-waveplate system parameters, it is possible to substantially enhance phase modulation in a single polarization with TN LC device.

6.4 Summary

This chapter presents a systematic investigation of the optimization method applied to LC device–waveplate architectures. The objective is to achieve polarization independence and enhance phase modulation performance across the voltage and time domains. The LC devices analysed include the Fréedericksz nematic LC device, which represents anisotropic LC devices (such as pi-cells), and the 90° twisted nematic (TN) LC device, which represents twisted nematic configurations (such as super-twisted nematic LC devices).

Section 6.1 introduces the system architecture, where an LC device is positioned between two waveplates, and describes the optimization algorithm, which integrates the Jones matrix formalism with the particle swarm optimization (PSO) algorithm. A thorough system verification is conducted to validate the reliability of the algorithm, laying the groundwork for subsequent optimization processes.

Section 6.2 explores the optimization of a configuration consisting of a Fréedericksz LC device positioned between two waveplates and evaluates its potential for achieving polarization-independent phase modulation in both the voltage and time domains as an initial step. The results demonstrate the configuration's feasible polarization-independent phase modulation; however, the achievable phase modulation remains relatively limited. Further optimization targeting enhanced phase modulation for a single polarization yields no significant improvement, even with optimized waveplate configurations, highlighting the intrinsic limitations of the Fréedericksz device. Nonetheless, these findings demonstrate that a single-polarization device can be extended to achieve polarization-independent phase modulation through appropriate optimization strategies.

Section 6.3 focuses on TN LC devices, using the 90° TN LC configuration as a representative example. A standalone 90° TN LC device demonstrates polarization-independent performance at high voltages. To extend the polarization-independent phase modulation range, the optimization algorithm is applied to a configuration in which the TN LC device is placed between two waveplates. The results reveal improved phase modulation performance, though this enhancement comes at the cost of minor polarization transformation under a relatively loose amplitude constraint of 0.9. Furthermore, the algorithm is also employed to maximize the phase modulation range for a single polarization. The optimized configurations achieve significantly enhanced phase modulation (three times improvement) and constant amplitude performance, though at the expense of a modest decrease in amplitude.

7. Conclusions and Future Work

7.1 Conclusion for Each Chapter

This thesis presents a systematic investigation into liquid crystal (LC) based optical phase modulators, focusing on enhancing their response time, phase modulation depth, and polarization independence while maintaining low voltage operation. Through a combination of theoretical modelling, experimental validation, and numerical optimization, this research explores the performance of two nematic LC devices - a pi-cell based phase modulator, and a super-twisted nematic (STN) LC based polarization-independent modulator. Furthermore, this thesis also explores ways of optimising the optical system configuration (the combination of LC device and fixed waveplates) for improved optical phase modulation. The optimized optical phase modulator can be applied to advanced SLM design, which paves the way for next-generation optical modulators with applications in adaptive optics, beam steering, holography, and display technologies.

Chapter 1 introduces the motivation and objectives of the research, which highlights the key challenges in LC-based optical phase modulation, such as the need for fast response times (<1 ms), full 2π rad phase modulation, low operating voltages (≤ 15 V_{rms}), and polarization independence. The fundamental trade-offs between response time, phase modulation depth, and voltage constraints are discussed, which provides the foundation for the research focus.

Chapter 2 provides the theoretical foundation for understanding LC physics and its simulation methods in optical phase modulation. It introduces the fundamental properties of LCs, including phase transitions, order parameter theory, and molecular alignment, followed

by a discussion of elastic properties and continuum theory, where Frank continuum theory and Ericksen-Leslie theory describe LC deformations and hydrodynamics. These principles form the basis for modelling LC reorientation under external fields, particularly in phase modulation applications. The director model and finite difference method are introduced as numerical tools for solving LC configurations. Additionally, birefringence and the Jones matrix formalism are explored to describe how LCs modulate light polarization and phase, particularly in twisted nematic (TN) LC devices. The chapter also examines dielectric energy and the Fréedericksz transition, which determine the voltage required for LC switching.

Additionally, the chapter briefly introduces polymer stabilization as a method to enhance LC performance and mentions chiral and smectic ferroelectric LCs as promising candidates for optical phase modulators, though they are not the focus of this thesis. Overall, this chapter establishes the theoretical and numerical framework that supports the design, simulation, and optimization of LC-based phase modulators in the following chapters.

Chapter 3 presents three phase measurement techniques for evaluating LC-based phase modulation in the time domain. A transmission-based method is employed for preliminary assessment, particularly when combined with microscopy, allowing transient states to be observed and confirmed. Phase-shifting interferometry is used for high-resolution and precise phase modulation measurements. The phase-shifting Twyman Green interferometer developed utilizes a rotating half-waveplate to introduce controlled phase shifts, with a four-step phase extraction algorithm applied to determine the corresponding phase modulation accurately. Additionally, a phase-shifting Mach–Zehnder interferometer incorporates an Acousto-Optic Frequency Shifter (AOFS) to generate a continuous 40 MHz phase shift, with Fast Fourier Transform (FFT) analysis used for phase extraction. These techniques provide high-resolution,

time-resolved phase measurements, and enable continuous and accurate characterization of the dynamic optical response of LC devices. In addition, it is worth mentioning that the transmission-based method, which uses a laser as the light source, can provide an accurate transmission curve that varies with voltage changes in controllable steps. This method can be used to evaluate the thickness of the device when compared with simulation results.

Chapter 4 investigates a pi-cell-based optical phase modulator. It demonstrates that a short burst voltage can drive the device into the symmetric H-state (Hs state), which has a doubled phase modulation due to the formation of additional boundary layers. The stability of this transient Hs state is examined under a microscope. Optical phase modulation simulations are conducted by deriving the free-energy density and solving the Euler-Lagrange equations to model the director behaviour, followed by phase modulation calculations based on effective birefringence. Dynamic phase measurements using the phase-shifting Twyman Green interferometry confirm that a 3.7 μm thick device achieves full 2π rad phase modulation within 1 ms in reflection configuration under 10 Vrms, with experimental results closely matching simulations. However, the Hs state exhibits limited stability, where polymer-stabilized LC structures could help to improve its lifetime and long-term usability.

This chapter combined with Section 3.3 have been published in a peer-reviewed journal: Xue, L., Jin, Y., Elston, S. J., & Morris, S. M. (2023). Fast analogue 2π phase modulation using a liquid crystal Pi-Cell. *Optics & Laser Technology*, 167, 109773.

Chapter 5 explores polarization-independent phase modulator based on a super-twisted nematic (STN) LC device. Applying a burst driving voltage to a 180° STN LC device induces the twisted Hs (T-Hs) state, where additional perpendicularly aligned boundary layers enable

polarization-independent operation. The stability of this transient T-Hs state is examined under a microscope. For optical simulations, Jones calculus is employed to compute phase and amplitude performance based on the director profile for both polarizations. Experimental validation using phase-shifting Mach–Zehnder interferometry shows excellent agreement with numerical simulations. The results confirm that the T-Hs state enables simultaneous modulation for both polarizations, achieving polarization-independent 2π rad phase modulation in an 8.9 μm thick device within 1 ms under 30 Vrms using a four-pass geometry. However, the stability limitations of the T-Hs state may restrict its practical applications.

This Chapter combined with Section 3.4 have been published in a peer-reviewed journal: Xue, L., Elston, S. J., & Morris, S. M. (2025). Polarization-independent nematic liquid crystal phase modulators. *ACS Photonics.*

Chapter 6 presents an optical optimization algorithm that integrates Jones matrix formalism and particle swarm optimization (PSO) to determine the optimal combination of LC devices with waveplates. It aims to optimize the retardances and rotation angles of waveplates as well as the rotation angle of the LC device to achieve polarization-independent or enhanced phase modulation across varying voltages or time. The optimization results indicate that for a Fréedericksz nematic LC device, optimized configurations are able to achieve polarization independence across different voltages and over time. However, the phase modulation remains limited. Additionally, it fails to improve single-polarization phase modulation for a Fréedericksz nematic LC device due to its inherent material limitations. In addition, for a 90° TN LC device, the optimized configuration extends the polarization-independent phase modulation range under minor trade-offs of polarization transformation. Furthermore, the optimized configuration is able to achieve a phase modulation range up to three times larger

compared to a single LC device. The multi-objective optimization framework successfully identifies locally optimal solutions, which indicates its applicability to the strategic design of the LC-waveplate optical system for enhanced modulation performance.

In conclusion, this thesis provides a robust foundation for the advancement of high-performance LC-based optical phase modulators, addressing fundamental trade-offs between response time, phase modulation depth, voltage constraints, and polarization independence. Through a combination of experimental validation, theoretical modelling, and numerical optimization, this work has provided a comprehensive framework for improving LC phase modulation performance. The findings of this research contribute to the development of next-generation LC-based optical modulators with applications in adaptive optics, high-speed holography, beam shaping, and AR/VR display technologies. While challenges remain - such as improving the stability of the Hs state in pi-cells and the T-Hs state in a STN device and refining the optimization framework - this thesis lays the groundwork for further advancements in LC phase modulation, and aims to play a crucial role in shaping the future of photonics, optical communications, and dynamic wavefront control technologies.

7.2 Future Work

Based on the findings and challenges outlined in this thesis, several promising research directions are proposed to further enhance LC-based optical phase modulators and explore their practical applications.

Enhancing Hs state & THs- State Stability

The stability of the Hs state in pi-cells and the T-Hs state in 180º STN devices limits the long-term usability of these modulators. To address this, polymer-stabilized nematic LCs present a promising solution by introducing a thin polymer layer at the centre of the device, as shown in **Figure 7.1** (a)-(c). Since this thin polymer layer would drop horizontally in the device, several perpendicular polymer walls are also required to serve as anchoring points, as presented in Fig. 7.1 (d), which ensures the stability of these thin layers within the device. This structural reinforcement prevents the middle layers from drifting or breaking under high voltages, while still allowing them to function as additional boundary layers, contributing to enhanced phase modulation and polarization independence. Future research will focus on optimizing polymer concentrations and cross-linking techniques to achieve a balance between stability and response time. Additionally, different experimental methods should be studied to ensure the formation of an ideal thin polymer layer within a micro-thick LC device. If successfully implemented, this approach could lead to continuous and stable phase modulation, which would make these devices more viable for high-speed and analogue optical applications.

Low-Voltage STN Devices for Polarization Independence

The high voltage requirement (30 V_{rms}) for STN devices operating in the T-Hs state poses a challenge for practical applications, particularly due to the limitations of silicon backplane technology. Reducing this voltage is essential for real-world implementation and broader adoption in low-power optical systems. Future work could explore alternative LC mixtures with lower elastic constants and optimized birefringence, which would enable phase modulation at reduced driving voltages. Additionally, the use of dual-frequency LCs materials or those exhibiting dielectric anisotropy may further reduce the operation voltage while maintaining fast response times.

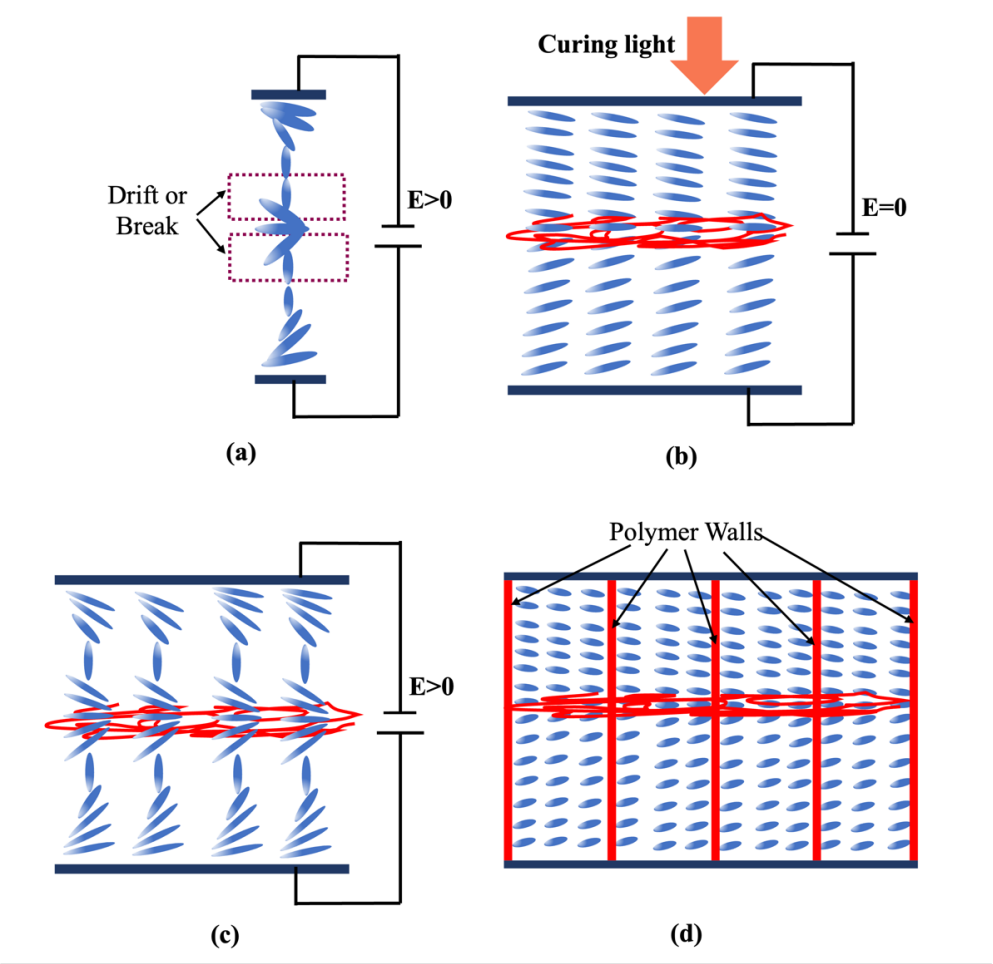

Figure 7.1. The illustration of the stabilization process for the Hs state. (a) A single pi-cell LC device switched into the Hs state, where central flat-lying molecules are prone to drift toward the surface, which makes the Hs state unstable. (b) The stabilization process involves applying the laser source onto the device to induce the formation of a thin polymer layer that can lock the central molecules in place when the device is under zero voltage. (c) The polymer-stabilized device exhibits fixed central layers after switching into the Hs state, which exhibits a stable Hs state. (d) Schematic illustration of the polymer walls.

Advanced Optical Optimization Framework

The PSO-based optimization framework introduced in this thesis provides a foundation for determining the optimal LC-waveplate architecture, but further refinements could enhance both efficiency and robustness. Expanding the current PSO-based approach by integrating deep learning based optimization could enable faster and more complex multi-objective optimizations. This can be achieved by training machine learning models to predict optimal configurations. Additionally, using alternative optimization algorithms alongside PSO - such

as genetic algorithms or gradient-based methods - could provide independent validation of results, which can help to confirm the accuracy and reliability of the optimized configurations. This cross-validation approach would reduce the risk of local minima trapping and improve the convergence of solutions. Additionally, applying the optimized designs to experimental setups is a crucial next step to assess their feasibility in real-world conditions.

Integration with Commercial LCOS SLMs

To validate the practical utility of the optimized LC devices, future research should focus on their integration into commercially available LCOS spatial light modulators. While this thesis primarily evaluates phase modulation depth, response time, and polarization independence in a single-pixel device, scaling these properties to an SLM requires achieving uniform phase and amplitude performance across an entire pixel array. This necessitates fabricating a test array with multiple independently addressable pixels and systematically measuring phase response uniformity, diffraction efficiency, and long-term stability under real-world conditions.

Chiral LCs and Ferroelectric LCs for High-Speed Optical Modulation

Future research could explore chiral nematic (cholesteric) and smectic ferroelectric liquid crystals (FLCs) to develop even faster analogue 2π rad optical phase modulators. While conventional nematic LCs provide tuneable birefringence, their response time is fundamentally constrained by viscoelastic relaxation. In contrast, chiral nematic LCs and ferroelectric smectic LCs exhibit microsecond switching times, making them strong candidates for high-speed phase modulation. Chiral nematic LCs, with their helical structures, can be optimized for fast polarization control and broadband optical response. Meanwhile, smectic ferroelectric LCs, which utilize spontaneous polarization switching, achieve microsecond response times, making them highly suitable for real-time applications such as dynamic holography and high-speed

beam steering. What's more, the recent discovered ferroelectric nematic LCs present ferroelectric properties without the need for smectic layering, and early studies suggest they can also switch quickly because their molecular reorientation responds directly to electric fields. Future work could integrate these materials with optimized voltage waveforms, surface alignment techniques, tailored LC mixtures, and polymer-stabilized layers to achieve both high-speed response and stable phase control, paving the way for next-generation ultrafast optical modulators.

8. References

[1] Khalil, K., Sabry, Y. M., Hassan, K., Shebl, A., Soliman, M., Eltagoury, Y. M., & Khalil, D. (2016). In-line optical MEMS phase modulator and application in ring laser frequency modulation. *IEEE Journal of Quantum Electronics*, 52(8), 1-8.

[2] Lazarev, G., Hermerschmidt, A., Krüger, S., & Osten, S. (2012). LCOS spatial light modulators: trends and applications. *Optical Imaging and Metrology: Advanced Technologies*, 1-29.

[3] Francis, T. S., Jutamulia, S., & Tanone, A. (1997, October). Applications of liquid-crystal spatial light modulators to optical information processing systems. In *Liquid Crystals* (Vol. 3143, pp. 92-101). SPIE.

[4] Lechner, B. J., Marlowe, F. J., Nester, E. O., & Tults, J. (1971). Liquid crystal matrix displays. *Proceedings of the IEEE,* 59(11), 1566-1579.

[5] Ambs, P., Otón, J., Millán, M. S., Jaulin, A., & Bigué, L. (2007, June). Spatial light modulators for information processing: applications and overview. In *AIP Conference Proceedings* (Vol. 949, p. 226). IOP Institute of Physics Publishing Ltd.

[6] Zou, J., Yang, Q., Hsiang, E. L., Ooishi, H., Yang, Z., Yoshidaya, K., & Wu, S. T. (2021). Fast-response liquid crystal for spatial light modulator and LiDAR applications. *Crystals*, 11(2), 93.

[7] He, Z., Gou, F., Chen, R., Yin, K., Zhan, T., & Wu, S. T. (2019). Liquid crystal beam steering devices: principles, recent advances, and future developments. *Crystals,* 9(6), 292.

[8] Wang, M., Zong, L., Mao, L., Marquez, A., Ye, Y., Zhao, H., & Vaquero Caballero, F. J. (2017, March). LCoS SLM study and its application in wavelength selective switch. In *Photonics* (Vol. 4, No. 2, p. 22). MDPI.

[9] Jesacher, A., Maurer, C., Schwaighofer, A., Bernet, S., & Ritsch-Marte, M. (2008). Near-perfect hologram reconstruction with a spatial light modulator. *Optics Express*, 16(4), 2597-2603.

[10] Wang, S., Jiang, S., Hu, Y., Wang, D., & Zhang, P. (2019, November). Novel liquid-crystal computer-generated hologram based on spatial light modulator interference exposure method. In *Optical Design and Testing IX* (Vol. 11185, pp. 35-41). SPIE.

[11] Pérez, J. O., & Ambs, P. (2006, June). Characterization and applications of a pure phase reflective liquid crystal spatial light modulator. In *Seventh International Conference on Correlation Optics* (Vol. 6254, pp. 181-194). SPIE.

[12] Matsushima, T., Kimura, S., & Komura, S. (2021). Fast response in‐plane switching liquid crystal display mode optimized for high‐resolution virtual‐reality head‐mounted display. *Journal of the Society for Information Display*, 29(4), 221-229.

[13] Yin, K., Hsiang, E. L., Zou, J., Li, Y., Yang, Z., Yang, Q., ... & Wu, S. T. (2022). Advanced liquid crystal devices for augmented reality and virtual reality displays: principles and applications. *Light: Science & Applications,* 11(1), 161.

[14] Maurer, C., Jesacher, A., Bernet, S., & Ritsch‐Marte, M. (2011). What spatial light modulators can do for optical microscopy. *Laser & Photonics Reviews*, 5(1), 81-101.

[15] Zhang, Z., You, Z., & Chu, D. (2014). Fundamentals of phase-only liquid crystal on silicon (LCOS)

devices. *Light: Science & Applications,* 3(10), e213-e213.

[16] Reichelt, S., Häussler, R., Fütterer, G., Leister, N., Kato, H., Usukura, N., & Kanbayashi, Y. (2012). Full-range, complex spatial light modulator for real-time holography. *Optics Letters,* 37(11), 1955-1957.

[17] Hansford, D. J., Jin, Y., Elston, S. J., & Morris, S. M. (2021). Enhancing laser speckle reduction by decreasing the pitch of a chiral nematic liquid crystal diffuser. *Scientific Reports*, 11(1), 4818.

[18] Jin, Y., Hansford, D. J., Elston, S. J., & Morris, S. M. (2021). Laser speckle reduction using a liquid crystal diffuser enhanced with redox dopants. *Advanced Photonics Research*, 2(6), 2000184.

[19] Liu, J., & Wang, J. (2015). Demonstration of polarization-insensitive spatial light modulation using a single polarization-sensitive spatial light modulator. *Scientific Reports*, 5(1), 9959.

[20] Zhu, Z., Wen, Y., Li, J., Chen, Y., Peng, Z., Li, J., ... & Yu, S. (2023). Metasurface-enabled polarization-independent LCoS spatial light modulator for 4K resolution and beyond. *Light: Science & Applications*, 12(1), 151.

[21] Tang, M., Huang, K., Zhang, Y., & Lu, J. (2024). Polarization-independent liquid-crystal phase modulator with multi-microdomain orthogonally twisted photoalignment. *Light: Advanced Manufacturing,* 4(4), 404-409.

[22] Hyman, R. M., Lorenz, A., Morris, S. M., & Wilkinson, T. D. (2014). Polarization-independent phase modulation using a blue-phase liquid crystal over silicon device. *Applied Optics*, *53*(29), 6925-6929.

[23] Huang, Y., Liao, E., Chen, R., & Wu, S. T. (2018). Liquid-crystal-on-silicon for augmented reality displays. *Applied Sciences*, 8(12), 2366.

[24] Suslick, K. S. (2001). Encyclopedia of Physical Science and Technology. *Sonoluminescence and Sonochemistry, 3rd edn. Elsevier Science Ltd, Massachusetts*, 1-20. (Chapter 4)

[25] Singh, S. (2000). Phase transitions in liquid crystals. *Physics Reports*, *324*(2-4), 107-269.

[26] Meyer, R. B., Liebert, L., Strzelecki, L., & Keller, P. (1975). Ferroelectric liquid crystals. *Journal de Physique Lettres*, *36*(3), 69-71.

[27] Jones, J. C. (2015). On the biaxiality of smectic C and ferroelectric liquid crystals. *Liquid Crystals*, 42(5-6), 732-759.

[28] Huang, Y., He, Z., & Wu, S. T. (2017). Fast-response liquid crystal phase modulators for augmented reality displays. *Optics Express*, 25(26), 32757-32766.

[29] Patel, J. S., & Meyer, R. B. (1987). Flexoelectric electro-optics of a cholesteric liquid crystal. *Physical Review Letters,* 58(15), 1538.

[30] Tsvetkov, V. (1942). Acta Physicochim. (USSR), 16, 132–147.

[31] Stefan Marti, Liquid Crystal, MIT Media Lab, https://web.media.mit.edu/~stefan/liquid-crystals/node2.html (accessed 7 May 2025).

[32] Mayer, J. C., & Oversteegen, L. G. (2003). Continuum theory. In *Encyclopedia of general topology* (pp. 299-303). Elsevier.

[33] Stewart, I. W. (2019). The static and dynamic continuum theory of liquid crystals: a mathematical introduction. *CRC Press*.

[34] Oseen, C. W. (1933). The theory of liquid crystals. *Transactions of the Faraday Society*, *29*(140), 883-899.

[35] Frank, F. C. (1958). I. Liquid crystals. On the theory of liquid crystals. *Discussions of the Faraday Society*, *25*, 19-28.

[36] Doi, M. (2013). *Soft Matter Physics.* Oxford University Press.

[37] Leslie, F. M. (1968). Some constitutive equations for liquid crystals. *Archive for Rational Mechanics and Analysis*, *28*, 265-283.

[38] Parodi, O. (1970). Stress tensor for a nematic liquid crystal. *Journal de Physique*, *31*(7), 581-584.

[39] P. Brimicombe, L. Parry-Jones, S. Elston, E. Raynes, Modeling of dual frequency liquid crystal materials and devices, *Journal of Applied Physics*, 98 (2005) 104104.

[40] Miesowicz, M. (1946). The three coefficients of viscosity of anisotropic liquids. *Nature*, *158*(4001), 27-27.

[41] Dhara, S., Balaji, Y., Ananthaiah, J., Sathyanarayana, P., Ashoka, V., Spadlo, A., & Dabrowski, R. (2013). Active and passive viscosities of a bent-core nematic liquid crystal. *Physical Review E—Statistical, Nonlinear, and Soft Matter Physics*, *87*(3), 030501.

[42] Dark, M. L., Moore, M. H., Shenoy, D. K., & Shashidhar, R. (2006). Rotational viscosity and molecular structure of nematic liquid crystals. *Liquid Crystals*, *33*(1), 67-73.

[43] Hird, M. (1997). *Introduction to liquid crystals chemistry and physics*. Taylor & Francis.

[44] Nehring, J., & Saupe, A. (1971). On the elastic theory of uniaxial liquid crystals. *The Journal of Chemical Physics*, *54*(1), 337-343.

[45] Jones, R. C. (1941). A new calculus for the treatment of optical systems I. Description and discussion of the calculus. *Journal of the Optical Society of America*, *31*(7), 488-493.

[46] Takatoh, K., Sakamoto, M., Hasegawa, R., Koden, M., Itoh, N., & Hasegawa, M. (2005). Alignment technology and applications of liquid crystal devices. *CRC Press*.

[47] Serati, S. A., Xia, X., Mughal, O., & Linnenberger, A. (2003, August). High-resolution phase-only spatial light modulators with submillisecond response. In *Optical Pattern Recognition XIV* (Vol. 5106, pp. 138-145). SPIE.

[48] Bauchert, K. A., Serati, S. A., & Furman, A. (2002, March). Advances in liquid crystal spatial light modulators. In *Optical Pattern Recognition XIII* (Vol. 4734, pp. 35-43). SPIE.

[49] Yang, B. R., Elston, S. J., Raynes, P., & Shieh, H. P. D. (2007). Investigation of the transient symmetric H state in a pi-cell. *Applied Physics Letters*, 91(7).

[50] Bos, P. J., & Koehler/Beran, K. R. (1984). The pi-cell: a fast liquid-crystal optical-switching device. *Molecular Crystals and Liquid Crystals*, 113(1), 329-339.

[51] Schadt, M., & Helfrich, W. (1971). Voltage-dependent optical activity of a twisted nematic liquid crystal. *Applied Physics Letters*, 18(4), 127-128.

[52] Fergason, J. (1973). *U.S. Patent* No. 3,731,986. Washington, DC: U.S. Patent and Trademark Office.

[53] Patel, J. S., & Lee, S. D. (1991). Electrically tunable and polarization insensitive Fabry‐Perot étalon with a liquid‐crystal film. *Applied Physics Letters*, 58(22), 2491-2493.

[54] Luis Martinez, J., Moreno, I., Davis, J. A., Hernandez, T. J., & McAuley, K. P. (2010). Extended phase modulation depth in twisted nematic liquid crystal displays. *Applied Optics*, 49(30), 5929-5937.

[55] Mahmud, M. S., Naydenova, I., & Toal, V. (2008). Implementation of phase-only modulation utilizing a twisted nematic liquid crystal spatiallight modulator. *Journal of Optics A: Pure and Applied Optics*, 10(8), 085007.

[56] Durán, V., Lancis, J., Tajahuerce, E., & Fernández-Alonso, M. (2006). Phase-only modulation with a

twisted nematic liquid crystal display by means of equi-azimuth polarization states. *Optics Express*, 14(12), 5607-5616.

[57] Chen, S. H., & Yang, C. L. (2002). Dynamics of twisted nematic liquid crystal pi-cells. *Applied Physics Letters,* 80(20), 3721-3723.

[58] Chen, T. J., Cheng, Y. H., & Wu, S. M. (2008). Twisted liquid crystal pi-cell stabilized by polymer-sustained alignment. *Applied Physics Letters*, 93(22).

[59] Pande, M., Tripathi, P. K., Misra, A. K., Manohar, S., Manohar, R., & Singh, S. (2016). Dielectric and electro-optical properties of polymer-stabilized liquid crystal system. *Applied Physics A*, 122, 1-9.

[60] Chien, C. Y., Hsu, C. J., Chen, Y. W., Tseng, S. H., & Sheu, C. R. (2016). Holographic polymer networks formed in liquid crystal phase modulators via a He-Ne laser to achieve ultra-fast optical response. *Optics Express*, 24(7), 7534-7542.

[61] Kim, S. H., & Chien, L. C. (2004). Electro-optical characteristics and morphology of a bend nematic liquid crystal device having templated polymer fibrils. *Japanese Journal of Applied Physics*, 43(11R), 7643.

[62] Sun, J., & Wu, S. T. (2014). Recent advances in polymer network liquid crystal spatial light modulators. *Journal of Polymer Science Part B: Polymer Physics,* 52(3), 183-192.

[63] Li, Y., Yang, Z., Chen, R., Mo, L., Li, J., Hu, M., & Wu, S. T. (2020). Submillisecond-response polymer network liquid crystal phase modulators. *Polymers*, 12(12), 2862.

[64] Peng, F., Chen, H., Tripathi, S., Twieg, R. J., & Wu, S. T. (2015, March). Fast-response IR spatial light modulators with a polymer network liquid crystal. In *Emerging Liquid Crystal Technologies X* (Vol. 9384, pp. 91-98). SPIE.

[65] Huang, C. Y., Fung, R. X., & Lin, Y. G. (2007). Effects of curing conditions on electrooptical properties of polymer-stabilized liquid crystal pi-cells. *Japanese Journal of Applied Physics*, 46(8R), 5230.

[66] Asakawa, Y., Takahashi, T., & Saito, S. (2007). Transient response characteristics of polymer stabilized bend alignment state of nematic liquid crystal in Pi-cell. *Japanese Journal of Applied Physics*, 46(12R), 7774.

[67] Brimicombe, P. D., Elston, S. J., & Raynes, E. P. (2007). Dynamic properties of polymer stabilised pi-cells. *Molecular Crystals and Liquid Crystals*, 476(1), 165-411.

[68] Huang, C. Y., Lai, P. C., Hsieh, C. T., Chang, C. W., & Tian, C. J. (2010). Modification of symmetric H state lifetime in splayed nematic cells. *Japanese Journal of Applied Physics*, 49(11R), 110203.

[69] Manohar, R., Misra, A. K., & Srivastava, A. K. (2010). Polymer‐induced improvements in ferroelectric liquid crystal. *Polymer Composites*, 31(10), 1776-1781.

[70] Rudquist, P., Komitov, L., & Lagerwall, S. T. (1998). Volume-stabilized ULH structure for the flexoelectro-optic effect and the phase-shift effect in cholesterics. *Liquid Crystals*, 24(3), 329-334.

[71] Meyer, R. B. (1969). Piezoelectric effects in liquid crystals. *Physical Review Letters*, 22(18), 918.

[72] Rudquist, P., Komitov, L., & Lagerwall, S. T. (1994). Linear electro-optic effect in a cholesteric liquid crystal. *Physical Review E*, 50(6), 4735.

[73] Wang, X., Fells, J. A., Yip, W. C., Ali, T., Lin, J. D., Welch, C., ... & Elston, S. J. (2019). Fast and low loss flexoelectro-optic liquid crystal phase modulator with a chiral nematic reflector. *Scientific Reports,* 9(1), 7016.

[74] Corbett, D. R., & Elston, S. J. (2011). Modeling the helical flexoelectro-optic effect. *Physical Review E—Statistical, Nonlinear, and Soft Matter Physics,* 84(4), 041706.

[75] Fells, J. A., Welch, C., Yip, W. C., Elston, S. J., Booth, M. J., Mehl, G. H., ... & Morris, S. M. (2019). Dynamic response of large tilt-angle flexoelectro-optic liquid crystal modulators. *Optics Express*, 27(11), 15184-15193.

[76] Wang, X., Fells, J. A., Shi, Y., Ali, T., Welch, C., Mehl, G. H., ... & Elston, S. J. (2020). A Compact Full 2π Flexoelectro‐Optic Liquid Crystal Phase Modulator. *Advanced Materials Technologies*, 5(12), 2000589.

[77] Varanytsia, A., & Chien, L. C. (2017). Giant flexoelectro-optic effect with liquid crystal dimer CB7CB. *Scientific Reports,* 7(1), 41333.

[78] Clark, N. A., & Lagerwall, S. T. (1980). Submicrosecond bistable electro‐optic switching in liquid crystals. *Applied Physics Letters*, 36(11), 899-901.

[79] Pertuis, V., & Patel, J. S. (1993). Twisted smectic structure for gray scale modulator. *Ferroelectrics,* 149(1), 193-205.

[80] Fünfschilling, J., & Schadt, M. (1989). Fast responding and highly multiplexible distorted helix ferroelectric liquid‐crystal displays. *Journal of Applied Physics*, 66(8), 3877-3882.

[81] Abdulhalim, I. (2012). Highly promising electrooptic material: Distorted helix ferroelectric liquid crystal with a specific tilt angle. *Applied Physics Letters*, 101(14).

[82] Pozhidaev, E. P. (2001, June). Electro-optical properties of deformed-helix ferroelectric liquid crystal display cells. In *Advanced Display Technologies: Basic Studies of Problems in Information Display* (FLOWERS 2000) (Vol. 4511, pp. 92-99). SPIE.

[83] Otón, J., Ambs, P., Millán, M. S., & Pérez-Cabré, E. (2009). Dynamic calibration for improving the speed of a parallel-aligned liquid-crystal-on-silicon display. *Applied Optics*, 48(23), 4616-4624.

[84] Zhang, Z., Lu, G., & Francis, T. S. (1994). Simple method for measuring phase modulation in liquid crystal televisions. *Optical Engineering*, 33(9), 3018-3022.

[85] Creath, K. (1988). V phase-measurement interferometry techniques. In *Progress in Optics* (Vol. 26, pp. 349-393). Elsevier.

[86] Jin, Y., Elston, S. J., Fells, J. A., Chen, B., Li, M., Kamal, W., ... & Morris, S. M. (2022). Backflow-assisted time-resolved phase modulation in nematic liquid crystal Pi-Cells. *Optics & Laser Technology*, 156, 108596.

[87] Fells, J. A., Elston, S. J., Booth, M. J., & Morris, S. M. (2018). Time-resolved retardance and optic-axis angle measurement system for characterization of flexoelectro-optic liquid crystal and other birefringent devices. *Optics Express*, 26(5), 6126-6142.

[88] Sandford O'Neill, J. J., Fells, J. A., Welch, C., Mehl, G., Yip, W. C., Wilkinson, T. D., ... & Morris, S. M. (2019). Robust measurement of flexoelectro-optic switching with different surface alignments. *Journal of Applied Physics*, 125(9).

[89] Li, R., & Cao, L. (2019, September). A comparison of calibration methods for phase-only LCoS spatial light modulators. In *Photonic Fiber and Crystal Devices: Advances in Materials and Innovations in Device Applications XIII* (Vol. 11123, pp. 52-57). SPIE.

[90] Brock, N., Hayes, J., Kimbrough, B., Millerd, J., North-Morris, M., Novak, M., & Wyant, J. C. (2005,

August). Dynamic interferometry. In *Novel optical systems design and optimization VIII* (Vol. 5875, pp. 101-110). SPIE.

[91] Phillion, D. W. (1997). General methods for generating phase-shifting interferometry algorithms. *Applied Optics*, 36(31), 8098-8115.

[92] Stoilov, G., & Dragostinov, T. (1997). Phase-stepping interferometry: five-frame algorithm with an arbitrary step. *Optics and Lasers in Engineering*, 28(1), 61-69.

[93] Morimoto, Y., & Fujisawa, M. (1994). Fringe pattern analysis by a phase-shifting method using Fourier transform. *Optical Engineering*, 33(11), 3709-3714.

[94] Fells, J. A., Salter, P. S., Welch, C., Jin, Y., Wilkinson, T. D., Booth, M. J., ... & Morris, S. M. (2022). Dynamic phase measurement of fast liquid crystal phase modulators. *Optics Express*, 30(14), 24788-24803.

[95] Goldberg, K. A., & Bokor, J. (2001). Fourier-transform method of phase-shift determination. *Applied Optics,* 40(17), 2886-2894.

[96] Xue, L., Jin, Y., Elston, S. J., & Morris, S. M. (2023). Fast analogue 2π phase modulation using a liquid crystal Pi-Cell. *Optics & Laser Technology*, 167, 109773.

[97] Johnson, K. M., McKnight, D. J., & Underwood, I. (2002). Smart spatial light modulators using liquid crystals on silicon. *IEEE Journal of Quantum Electronics*, 29(2), 699-714.

[98] Wu, S. T., & Lackner, A. M. (1994). Mylar‐film‐compensated π and parallel‐aligned liquid crystal cells for direct‐view and projection displays. *Applied Physics Letters*, 64(16), 2047-2049.

[99] Lee, Y. H., Franklin, D., Gou, F., Liu, G., Peng, F., Chanda, D., & Wu, S. T. (2017). Two-photon polymerization enabled multi-layer liquid crystal phase modulator. *Scientific Reports*, 7(1), 16260.

[100] Wu, S. T., & Wu, C. S. (1989). High-speed liquid-crystal modulators using transient nematic effect. *Journal of Applied Physics*, 65(2), 527.

[101] He, Z., Gou, F., Chen, R., Yin, K., Zhan, T., & Wu, S. T. (2019). Liquid crystal beam steering devices: principles, recent advances, and future developments. *Crystals,* 9(6), 292.

[102] Deng, Y., Huang, C. H., Vinoth, B., Chu, D., Lai, X. J., & Cheng, C. J. (2020). A compact synthetic aperture digital holographic microscope with mechanical movement-free beam scanning and optimized active aberration compensation for isotropic resolution enhancement. *Optics and Lasers in Engineering,* 134, 106251.

[103] Woltman, S. J., Jay, G. D., & Crawford, G. P. (2007). Liquid-crystal materials find a new order in biomedical applications. *Nature Materials*, 6(12), 929-938.

[104] Srivastava, A. K., Chigrinov, V. G., & Kwok, H. S. (2015). Ferroelectric liquid crystals: Excellent tool for modern displays and photonics. *Journal of the Society for Information Display*, 23(6), 253-272.

[105] Fells, J. A., Wang, X., Elston, S. J., Welch, C., Mehl, G. H., Booth, M. J., & Morris, S. M. (2018). Flexoelectro-optic liquid crystal analog phase-only modulator with a 2π range and 1 kHz switching. *Optics Letters*, 43(18), 4362-4365.

[106] Salter, P. S., Elston, S. J., Raynes, P., & Parry-Jones, L. A. (2009). Alignment of the uniform lying helix structure in cholesteric liquid crystals. *Japanese Journal of Applied Physics*, 48(10R), 101302.

[107] Yu, C. H., Wu, P. C., & Lee, W. (2022). Polymer stabilization of uniform lying helix texture in a bimesogen-doped cholesteric liquid crystal for frequency-modulated electro-optic responses. *Materials,*

15(3), 771.

[108] Wang, X., Fells, J. A., Ali, T., Lin, J. D., Welch, C., Mehl, G. H., ... & Elston, S. J. (2020). Transmissive flexoelectro-optic liquid crystal optical phase modulator with 2π modulation. *AIP Advances*, 10(5).

[109] Tartan, C. C., & Elston, S. J. (2015). Asymmetric director structures and flexoelectricity in nematic pi-cell devices. *Applied Physics Letters*, 107(8).

[110] Lee, S. H., Kim, T. J., Lee, G. D., Yoon, T. H., & Kim, J. C. (2003). Geometric structure for the uniform splay-to-bend transition in a π-cell. *Japanese Journal of Applied Physics*, 42(10A), L1148.

[111] Kikuchi, H., Yamamoto, H., Sato, H., Kawakita, M., Takizawa, K., & Fujikake, H. (2005). Bend-mode liquid crystal cells stabilized by aligned polymer walls. *Japanese Journal of Applied Physics*, 44(2R), 981.

[112] Yeung, F. S. Y., & Kwok, H. S. (2006). Fast-response no-bias-bend liquid crystal displays using nanostructured surfaces. *Applied Physics Letters,* 88(6).

[113] Yeung, F. S., Li, Y. W., & Kwok, H. S. (2006). Pi-cell liquid crystal displays at arbitrary pretilt angles. *Applied Physics Letters*, 88(4).

[114] Brimicombe, P. D., & Raynes, E. P. (2005). The influence of flow on symmetric and asymmetric splay state relaxations. *Liquid Crystals*, 32(10), 1273-1283.

[115] Lee, C. H., Raynes, E. P., & Elston, S. J. (2010). The effect of high voltage on the bend transition in Pi-cells. *Applied Physics Letters*, 97(15).

[116] Brimicombe, P. D., & Raynes, E. P. (2006). Symmetric H state lifetime in splayed nematic liquid crystal devices. *Applied Physics Letters*, 89(3).

[117] Yang, B. R., Elston, S. J., Raynes, P., & Shieh, H. P. D. (2007). Investigation of the transient symmetric H state in a pi-cell. *Applied Physics Letters*, 91(7).

[118] Shagam, R. N., & Wyant, J. C. (1978). Optical frequency shifter for heterodyne interferometers using multiple rotating polarization retarders. *Applied Optics*, 17(19), 3034-3035.

[119] Creath, K. (1988). V phase-measurement interferometry techniques. In *Progress in Optics* (Vol. 26, pp. 349-393). Elsevier.

[120] Elston, S. J. (2008). Flexoelectricity in nematic domain walls. *Physical Review E—Statistical, Nonlinear, and Soft Matter Physics,* 78(1), 011701.

[121] Ahderom, S., Raisi, M., Lo, K., Alameh, K. E., & Mavaddat, R. (2002, July). Applications of liquid crystal spatial light modulators in optical communications. In *5th IEEE International Conference on High Speed Networks and Multimedia Communication* (Cat. No. 02EX612) (pp. 239-242). IEEE.

[122] Honma, M., & Nose, T. (2003). Polarization-independent liquid crystal grating fabricated by microrubbing process. *Japanese journal of applied physics*, 42(11R), 6992.

[123] Huang, Y., Wen, C. H., & Wu, S. T. (2006). Polarization-independent and submillisecond response phase modulators using a 90 twisted dual-frequency liquid crystal. *Applied physics letters*, 89(2).

[124] Hsieh, M. L., Chen, M. L., & Cheng, C. J. (2007). Improvement of the complex modulated characteristic of cascaded liquid crystal spatial light modulators by using a novel amplitude compensated technique. *Optical Engineering*, 46(7), 070501-070501.

[125] Sun, C., & Lu, J. (2019). A polarization-independent blue phase liquid crystal on silicon with low operation voltage. *Scientific Reports*, 9(1), 16900.

[126] Yan, J., Guo, Z., Xing, Y., & Li, Q. (2015). Investigation of fringing electric field effect on high-resolution blue phase liquid crystal spatial light modulator. *Applied optics*, 54(24), 7169-7174.

[127] Polarizer-free and fast response microlens arrays using polymer-stabilized blue phase liquid crystals. *Applied Physics Letters*, 96(11).

[128] Huang, Y., Chen, H., Tan, G., Tobata, H., Yamamoto, S. I., Okabe, E., ... & Wu, S. T. (2017). Optimized blue-phase liquid crystal for field-sequential-color displays. *Optical Materials Express*, 7(2), 641-650.

[129] Peng, F., Lee, Y. H., Luo, Z., & Wu, S. T. (2015). Low voltage blue phase liquid crystal for spatial light modulators. *Optics Letters*, 40(21), 5097-5100.

[130] Hyman, R. M., Lorenz, A., & Wilkinson, T. D. (2016). Phase modulation using different orientations of a chiral nematic in liquid crystal over silicon devices. *Liquid Crystals*, 43(1), 83-90.

[131] Du, F., Lu, Y. Q., Ren, H. W., Gauza, S., & Wu, S. T. (2004). Polymer-stabilized cholesteric liquid crystal for polarization-independent variable optical attenuator. *Japanese journal of applied physics,* 43(10R), 7083.

[132] Wang, C. T., Wu, C. L., Zhang, H. W., Lin, T. H., & Lee, C. K. (2016). Polarization-independent 2 pi phase modulation for terahertz using chiral nematic liquid crystals. *Optical Materials Express*, 6(7), 2283-2290.

[133] Yang, J., Zhang, Y., & Lu, J. (2024). Polarization-independent twist liquid crystal phase modulators. *Optics Express*, 32(26), 46014-46020.

[134] Ren, H., Lin, Y. H., Fan, Y. H., & Wu, S. T. (2005). Polarization-independent phase modulation using a polymer-dispersed liquid crystal. *Applied Physics Letters,* 86(14).

[135] Lin, Y. H., & Tsou, Y. S. (2011). A polarization-independent liquid crystal phase modulation adopting surface pinning effect of polymer dispersed liquid crystals. *Journal of Applied Physics*, 110(11).

[136] Lucchetta, D. E., Karapinar, R., Manni, A., & Simoni, F. (2002). Phase-only modulation by nanosized polymer-dispersed liquid crystals. *Journal of Applied Physics*, 91(9), 6060-6065.

[137] He, Z., Lee, Y. H., Gou, F., Franklin, D., Chanda, D., & Wu, S. T. (2017). Polarization-independent phase modulators enabled by two-photon polymerization. *Optics Express*, 25(26), 33688-33694.

[138] Ren, H., Lin, Y. H., & Wu, S. T. (2006). Polarization-independent and fast-response phase modulators using double-layered liquid crystal gels. *Applied Physics Letters*, 88(6).

[139] Lin, Y. H., Ren, H., Wu, Y. H., Zhao, Y., Fang, J., Ge, Z., & Wu, S. T. (2005). Polarization-independent liquid crystal phase modulator using a thin polymer-separated double-layered structure. *Optics Express*, 13(22), 8746-8752.

[140] Ohgawara, M., Tsubota, H., Kuwata, T., Akatsuka, M., Koh, H., Sawada, K., & Matsuhiro, K. (1991). Development of a multicolour super-twisted-nematic display. *Displays,* 12(2), 65-73.

[141] Scheffer, T., & Nehring, J. (1997). Supertwisted nematic (STN) liquid crystal displays. *Annual review of materials science,* 27(1), 555-583.

[142] Takatoh, K., Harima, A., Kaname, Y., Shinohara, K., & Akimoto, M. (2012). Fast-response twisted nematic liquid crystal displays with ultrashort pitch liquid crystalline materials. *Liquid Crystals,* 39(6), 715-720.

[143] Chen, T. J., Cheng, Y. H., & Wu, S. M. (2008). Twisted liquid crystal pi-cell stabilized by polymer-

sustained alignment. *Applied Physics Letters*, 93(22).

[144] Chen, S. H., & Yang, C. L. (2002). Dynamics of twisted nematic liquid crystal pi-cells. *Applied physics letters*, 80(20), 3721-3723.

[145] Wang, H., Nie, X., Wu, T. X., & Wu, S. T. (2006). Cell gap effect on the dynamics of liquid crystal phase modulators. *Molecular Crystals and Liquid Crystals*, 454(1), 285-687.

[146] Li, J., Hoke, C. D. H. C. D., & Bos, P. J. B. P. J. (1996). Studies of the bistability of highly twisted nematics. *Japanese journal of applied physics*, 35(6A), L706.

[147] Wang, D., Tan, D., & Liu, L. (2018). Particle swarm optimization algorithm: an overview. *Soft Computing,* 22(2), 387-408.

[148] Marini, F., & Walczak, B. (2015). Particle swarm optimization (PSO). *A tutorial. Chemometrics and Intelligent Laboratory Systems*, 149, 153-165.

[149] Juneja, M., & Nagar, S. K. (2016, October). Particle swarm optimization algorithm and its parameters: A review. In *2016 International Conference on Control, Computing, Communication and Materials (ICCCCM)* (pp. 1-5). IEEE.

[150] Kumar, M., Husain, D. M., Upreti, N., & Gupta, D. (2010). Genetic algorithm: Review and application. *Available at SSRN 3529843*.

[151] Alam, T., Qamar, S., Dixit, A., & Benaida, M. (2020). Genetic algorithm: Reviews, implementations, and applications. *arXiv preprint arXiv:2007.12673*.

[152] Suman, B., & Kumar, P. (2006). A survey of simulated annealing as a tool for single and multiobjective optimization. *Journal of the Operational Research Society*, 57(10), 1143-1160.

[153] Sibalija, T. (2018). Application of simulated annealing in process optimization: a review. *Simulated Annealing: Introduction, Applications and Theory*, 1-14.